THE UNIVERSITY OF BIRMINGHAM

Ultrafast Dynamics of Photoexcited Carriers in Semiconducting Nano Materials

by

Wei He

A thesis submitted in fulfillment for the
degree of Doctor of Philosophy

in the
Nanoscale Physics Research Laboratory
The School of Physics and Astronomy

June 2015

Acknowledgements

I would like to thank my supervisor Dr. Andrey Kaplan, for giving me such a good opportunity to work in the project described in this thesis at the beginning and always being patient and enthusiastic with this project. The successful completion of this thesis is supported by his continuous encouragement and suggestions.

This work can not be accomplished without collaborating with other colleagues. I appreciate Igor Yurkevich, Thomas Roger, George Barreto, Dimitri Chekulaev and Ammar Zakar for continual support and consultation. Dr. Andreas Frommhold helps me to take SEM images of samples. Dr. James Bowen helps me to use commercial spectroscopic ellipsometry and construct the simulation model. Prof. Leigh T Canham provides porous silicon samples for the research. Prof. Richard Palmer led me into this ultrafast dynamics research work.

I appreciate all the NPRLers and other friends for making my PhD experience great.

Finally, I would like to thank my family members, for all their understanding, support and encouragement.

I acknowledge the University of Birmingham and the China Scholarship Council for the studentships through my PhD study.

Abstract

This thesis presents a systematic study on the characterising ultrafast dynamics of photo excited carriers in hydrogenated nano crystalline silicon (nc-Si:H) and porous silicon (PS) materials using the ultrafast optical pump probe spectroscopy approaches. The work involves the ground state optical property detection and optical model simulation, ultrafast time resolved pump probe measurements and pump probe data analysis processes. Applying the novel pump probe detection methods, the study explores the carriers concentration, carriers recombination property, scattering rate and conductivity of photo excited semiconducting nano materials.

For the nc-Si:H sample, regarding the multilayer structure and dielectric function variation of excited state nc-Si:H material, the shifting of Fabry-Perot interference fringes were detected from the pump probe reflection measurements with scanning probing angles. And the ultrafast parameters plasma frequency ω_p and scattering rate Γ were precisely determined from the optical model fitting. We found that Γ is dependent on ω_p when the carrier-carrier scattering mechanism dominates the scattering process. Moreover, the effective mass m^* of excited carriers is estimated as $m^* \approx 0.17m_e$ through the pump fluence dependent measurements. The recombination property of excited carriers concentration $N_{eh}(t)$ under different pump fluence is then analysed through fitting the decay process of $N_{eh}(t)$ and determining the recombination coefficients. We realised the recombination process is mainly controlled by the quadratic and cubic recombination terms. Meanwhile, the conductivity as a function of pump photon energy is detected and analysed using the Drude conductivity and Boltzmann transport theory. Lastly, the pump probe ellipsometry technique is detailedly introduced and applied to accurately characterise the decay process of dielectric constant and absorption coefficient and conductivity of excited state nc-Si:H material. In researching PS membrane, we simultaneously did the time resolved pump probe transmission and reflection measurements. According to the detected data, we developed a nonuniform optical model based on Wentzel-Kramers-Brillouin (WKB) approach and Drude equation in the analysis procedure. The model permits to retrieve a pump-induced nonuniform complex dielectric function change and excited carriers concentration, along the increasing of membrane depth and time delay. Then, the diffusion coefficient and recombination time of excited carriers in PS membrane are discussed through the simulating of a carrier transport equation.

Contents

List of Figures

List of Tables

Abbreviations

nc-Si:H	Hydrogenated nano crystalline silicon
PS	Porous silicon
SE	Spectroscopic ellipsometry
Nd:YVO_4	Neodymium Yttrium orthovanadate
LBO	Lithium triborate
Ti	Titanium
SPM	Self-phase modulation
α-Si	Amorphous silicon
C-Si	Crystalline silicon
nc-Si	nano crystalline silicon cluster
EMA	Effective medium approximation
MG	Maxwell Garnett
FWHM	Full width at half Maximum
VB	Valence band
CB	conduction band
RCE	Rotating compensator ellipsometry
P	Polariser
C	Compensator
S	Sample
A	Analyser
CCD	Charge coupled device
BR	Bruggeman model

Physical Constants

Speed of Light in vacuum	c	$=$	$2.99792 \times 10^{8}\ m/s$
Plank's constant	h	$=$	$6.62607 \times 10^{-34}\ J \cdot s$
	$\hbar$	$= h/2\pi =$	$1.05457 \times 10^{-34}\ J \cdot s$
Free-space permittivity	ε_0	$=$	$8.85419 \times 10^{-12}\ F/m$
Electron charge	e	$=$	$1.60218 \times 10^{-19}\ C$
Free-electron mass	m_e	$=$	$9.10938 \times 10^{-31}\ kg$
Free-space permeability	μ_0	$=$	$4\pi \cdot 10^{-7}\ H/m$

Symbols

q	Integer number	
ρ	Ellipsometry ratio	
d	Thickness of layer	m
I	Intensity	$W \cdot m^2$
r	Reflection coefficient	
E_i	Incident light electrical field intensity	
E_r	Reflective light electrical field intensity	
N	Complex refractive index	
n	Reflective index (real)	
k	Extinction coefficient (imaginary)	
ε	Complex dielectric constant	
α	Absorption coefficient	m^{-1}
E	Photon energy	eV
θ	Incident angle	degrees
R	Reflectance	
T	Transmittance	
ω	Angular frequency	rad/s
ω_p	Plasma frequency	sec^{-1}
Γ	Damping rate	sec^{-1}
R_0	Reflective signal before pump	
R_t	Reflective signal at t time delay	
F	Pump beam fluence	mJ/cm^2
m_e	Optical mass of excited electron	
m_h	Optical mass of excited hole	
m^*	Optical mass of excited carriers	

λ	Light wavelength	nm
ψ	Arctangent amplitude ratio from reflected p- and s- polarisation	degrees
Δ	Phase difference between reflected p- and s- polarisation	degrees
E_g	Optical energy band gap	eV
K	Electron wave vector	m^{-1}
N_{eh}	Carriers concentration	cm^{-3}
β	Two-photon absorption coefficient	
H	Magnetic field	Wb

Dedicated to my Family and all my Friends...

Chapter 1

Introduction

In the last four decades, the research area of ultrafast carrier dynamics in semiconductor material has presented lots of achievements. Not only involving the basic fundamental interests, the research motivations also focus on the application of semiconductor optoelectronic and electronic devices and the growing need for faster response and processing of information[1]. To continuously develop and optimise microelectronic semiconductor devices, the various dynamical processes in semiconductors need to be understood. So, the excitation of semiconductors into non-equilibrium state (pump) and the subsequent various relaxation processes (probe) need to be precisely explored. As the fast development of the ultrafast lasers, which can produce a few femtoseconds ($1fs = 10^{-15}s$) pulses, the time resolution of time resolved pump-probe technique can be significantly improved. Moreover, the optical spectroscopy is also another powerful technique to investigate electronic and vibrational properties of semiconductor materials. Through the reflection, transmission, luminescence and light-scattering spectroscopies detection approaches, we can realise the invaluable information about such diverse aspects as the electronic band structure, phonons, coupled phonon-plasma modes, single-particle excitation of electrons and holes, and properties of defects, surfaces and interfaces[2]. Therefore, combining the ultrafast pump probe with optical spectroscopic techniques becomes an excellent tool for investigating a wide diversity of ultrafast dynamics phenomena related to relaxation, nonlinear property and transport dynamics in semiconductors.

The developments of ultrafast optical spectroscopy are distinguished in recent few years, such as: high order harmonic generation (HHG) to generate the sub-femtosecond pulse[3], pump probe spectroscopy reflection and transmission and photoluminescence to monitor the optical property of excited state semiconductor[4–8], time resolved optical pump and terahertz spectroscopy probe to realise frequency-dependent conductivity[9–13] and z-scan measurements[14–16] for researching optical nonlinearities etc. In this thesis,

we focus on the characterising ultrafast dynamics of photo excited carriers in semiconducting nano materials, including hydrogenated nano crystalline silicon (nc-Si:H, nano crystalline silicon clusters embedding in amorphous silicon matrix) and porous silicon (PS, void inclusions embedding in nano wires crystalline silicon matrix). Regarding the structure of researched samples and the ultrafast laser system in the lab, we study the optical property of excited state through applying the pump probe spectroscopic reflection[17, 18], transmission[4, 19–21] and ellipsometry[22, 23] approaches. From these measurements, we investigate the relaxation and transportation processes of photo excited carriers. In this chapter, we firstly introduce the research background review about carriers dynamics in semiconductor material. Then, the main research content of this thesis is presented.

1.1 Research Background Review

The hydrogenated nano-crystalline silicon (nc-Si:H), which comprises of the amorphous phase silicon matrix (α-Si) and nano clusters inclusions of crystalline silicon phase (nc-Si), has caused considerable research interests[24, 25] in recent decades. The unique electro-optical properties are exposed about this material, which have already been investigated for application in photovoltaic solar cells[26], nonvolatile memory devices[27], and thin-film transistors[28]. the characterisation and understanding of the excited free carrier properties are important to develop electro-optical applications, which also determines mobility related to carriers concentration and scattering rate. On another hand, the high-frequency conductivity of Si derivative material is also not yet well understood or researched, although it is the most critical property governing the performance of electro-optical devices. In a summary, several crucial questions await understanding and explanation: what happens to the charge carries after they absorb the pump photons; what is the mechanism of the carreirs relaxation and the excess energy release; what physics governs their conductivity.

Investigation of the nano-porous silicon (PS) has also attracted tremendous fundamental research attention and investment into development of applications. In the publication[29], we have indicated that the success of the PS is attributed to a variety of factors, most crucial among them being those related to the wide use of silicon in microelectronics, the well controlled and reproducible dimensions of PS owing to a robust fabrication technology, and the ability to produce quantities on an industrial scale. Moreover, we point out that the potential range of applications spreads over research areas and development activities including the drug and food industry[30], optical sensing

and wave-guiding[31, 32], ion exchange, molecular isolation and purification[33], photonics devices[34–36], antireflection coatings in solar cells[37], and biosensing[38] and many others. Successful development of applications, in the future, requires reliable and verified models describing the optical and conductive properties of the PS[39, 40]. And the transport property of carriers in PS material also need to be accurately characterised.

1.1.1 Excited Carriers Dynamics Procedure

One of the most advanced tools currently available for the investigation of excited carriers relaxation and transport property on extremely short timescales is ultrafast optical pump probe spectroscopy[1]. In brief, the absorption of pump photons with an energy greater than the band gap energy of a semiconductor material generates electron-hole pairs. At sufficiently high concentrations, these charges can be treated as an ambipolar plasma. This free carrier plasma can give an impact on the optical properties of the excited state material and changes the optical response, such as reflectance, transmittance, and polarisability[41–43]. Thus, investigation of the optical response allows indirect access to the properties of the excited carriers forming the plasma, such as the relaxation and recombination times, carrier concentration, carrier temperature and scattering mechanism.

Theoretically speaking, if there is no optical and electrical and other excitation methods, the intrinsic free carriers, including electrons and holes, of a semiconductor material would be distributed in terms of the Fermi-Dirac statistic. Meanwhile, the phonons are used to indicate lattice vibration, which are Bosons and followed by the Bose-Einstein statistic distribution[44, 45]. The energy and momentum are interchanged through carrier-carrier and carrier-phonon interactions, which retain both distributions at a common temperature. Thus, an average momentum of the carrier and phonon systems is zero, and their common temperature represents the carriers and phonons average energies. But when an optical electromagnetic radiation is absorbed by the semiconductor, this equilibrium ground state is perturbed by the excited carriers plasma, which results in different thermal states between carriers and lattice system. However, if the external excitation is stopped, the excited carriers would return back to the original ground state within a short time scale. The average momentum relaxes to zero and the average carrier temperature reaches to equilibrium with the lattice temperature as the excited carriers lose momentum and energy to phonons through variety of scattering and recombination processes.

Figure 1.1 shows a schematic representation of the main processes following photoexcitation of a direct energy band semiconductor with a monochromatic polarised laser

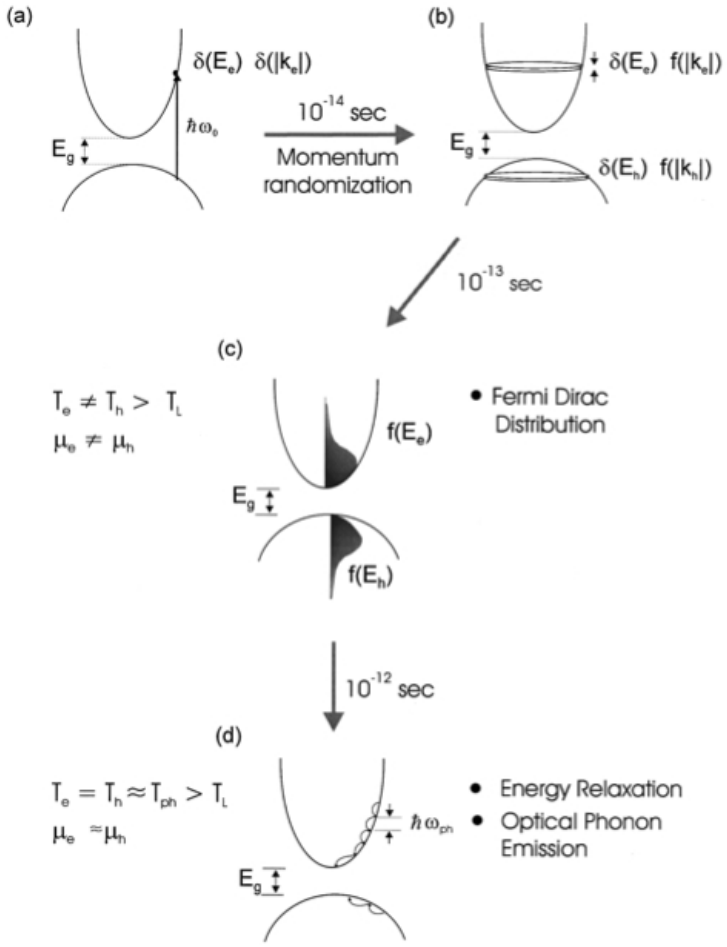

FIGURE 1.1: A schematic diagram illustrating the photo excitation of a semiconductor and subsequent energy relaxation. (a) Initially after photo excitation with polarised light, the carriers will have delta function distribution in momentum and energy space. (b) Within tens of femtoseconds momentum randomisation occurs. (c) Thermalisation of carriers into a certain distribution. (d) As time evolves the hot carriers lose their excess kinetic energy while attempting to reach thermal equilibrium with the lattice through optical phonon scattering. The Figure and Caption are from reference[1].

light. This laser light is assumed to be the ultrashort pulses with a delta function in time. As the photon energy $\hbar\omega_0$ is higher than the band gap energy E_g, the absorption of optical photons can be easily happened. This absorption can lead to the creation of electron-hole pairs with excess kinetic energy corresponding to the residual energy $\hbar\omega_0 - E_g$. This initial excitation by a monochromatic and polarised photon produces the distributions of electron and hole that are narrow in energy, $\delta(E_e)$ and $\delta(E_h)$, respectively, in figure 1.1(a). Then, due to the elastic as well as inelastic scattering events, the randomise momentum process occurs within tens of femtoseconds, as shown in figure 1.1(b).

Actually, the excited electrons will own most of the excess kinetic energy following photo-excitation. This is because the effective mass of excited electrons is much lighter

than that of the holes. Initially, electrons and holes can be considered as separate systems, each with their individual thermal distributions. This indirectly illustrates the electron-hole interactions should be weaker comparing to other carrier-carrier interactions. Meanwhile, the excited carriers concentration can influence electron-electron and hole-hole collisions processes. If the carrier densities were greater than $10^{19} cm^{-3}$ with thermal energy of around $1000K$, these collisions would occur on approximately $10^{-13} s$ time scale and lead to thermalisation of the carriers into an certain static distribution, as shown in figure 1.1(c). This timescale is also the time required to establish a carrier temperature. Subscripts e, h, and L correspond to electrons, holes and lattice, respectively. T and μ describe temperature and chemical potential, respectively[46]. The distribution functions of electrons, $f(E_e)$, and holes, $f(E_h)$, possess different temperatures, which are higher than the lattice temperature. As time evolves the hot carriers lose their excess kinetic energy due to attempt to reach thermal equilibrium with the lattice through various scattering and recombination mechanisms. As shown in Figure 1.1(d), through the carriers relaxation, the population of non-equilibrium optical phonon increases and attempts to thermalise with other lattice modes via phonon-phonon interactions on picosecond timescale. Meanwhile, the carriers recombination process also occurs and transfers the carriers energy to the lattice or emitting photons. If the energy density of carriers is above a certain threshold, this can even induce heating and melting of the lattice[47].

1.1.2 Optical Property of Excited State Semiconductor

As the excited state semiconductor material can be characterised by the pump probe optical spectroscopy methods, a corresponding analysis approach needs to be established to describe the excited state optical property. Generally, the dielectric constant is always used to express the optical property of a researched material. So, the excited carrier dynamics procedure can be related to the variation of material dielectric constant.

In 1983, Shank[41] had started to do the first time resolved pump probe reflectivity measurements to investigate the process of energy transfer to the crystalline silicon lattice. The excited electron-hole plasma contributes to the reflectivity variation of the sample, which was described by Drude expression with neglecting dampening: $n_p = n_0(1-\omega_p^2/\omega^2)^{1/2}$. Here, n_p and n_0 stand for the refractive index of the pumped and unpumped state sample respectively. $\omega_p = (4\pi N_{eh} e^2/m^*_{opt}\epsilon_0)^{1/2}$ is the plasma frequency in CGS unit, which relates to carriers concentration N_{eh} and effective mass m^*_{opt} and ω is the angular frequency of light. m^*_{opt} is the combined optical effective mass. As neglecting the dampening of carriers, the imaginary part of refractive index has been ignored in the analysis.

Sabbah[42] had concluded in his paper that there are mainly two types of linear-response contributions to the measured reflectivity changes: changes in the dielectric function associated with the presence of free-carriers and changes in the dielectric function associated with inter-band transitions. Normally, the Drude model is applied to describe the free-carrier (fc) contribution. And the inter-band contribution is dominated by three separate effects: state filling (sf), lattice temperature changes (lt), and band-gap renormalisation (bgr). In his analysis, when a sample satisfies $\Re(\epsilon) \gg \Im(\epsilon)$ and the change in dielectric function meets $\Re(\Delta\epsilon) \geq \Im(\Delta\epsilon)$ and $|\Delta\epsilon| \ll |\epsilon|$, where ϵ is the dielectric function of sample and $\Delta\epsilon$ is the change of dielectric function, the change of reflectivity can be assumed mainly due to the variation of real part of dielectric constant. So, the normalised change of reflectivity can be formulated only by the real part of refractive index, referring to Fresnel equations:

$$\Delta R/R = \frac{4n_0 cos(\theta)}{(n_0^2 - 1)[n_0^2 - sin^2(\theta)]^{1/2}} \Delta n \ , \tag{1.1}$$

where θ is the incident angle and n_0 is the refractive index of sample and Δn is the change of real part refractive index. But, if the experimental conditions can not fulfil the assumptions, the equation can not be applied anymore to calculate the change of reflectivity.

Moreover, referring to the different contributions on Δn, the total change of refractive index should be written as $\Delta n = \Delta n_{fc} + \Delta n_{sf} + \Delta n_{lt} + \Delta n_{bgr}$. In Sabbah's[42] discussions, the free carrier contribution Δn_{fc} is still expressed using the Drude model, which is mentioned in the previous paragraph. Theoretically, the m^*_{opt} is related with the carrier temperature, which was also taken into account in his discussion. As the carriers temperature can influence the energy band gap and change the distribution of excited carriers in different curvature of energy band, m^*_{opt} is also affected. Then, the state filling effect can be descried by the variation of absorption coefficient $\Delta\alpha_{sf} = K_\alpha \alpha_0$, where K_α is a constant. In general this state filling effect decreases the absorption coefficient for photon energies above the band gap[42], due to the occupation of energy bands by the excited electrons and holes. Δn_{sf} can be estimated out via the Kramers-Kronig relationship from $\Delta\alpha_{sf}$. As for the lattice temperature, which changes the refractive index through a variety of effects including electron-phonon collision, Fermi smearing, and shifts of the band gap energy[48], it can be formulated as $\Delta n_{lt} = (\frac{dn}{dT_l})\Delta T_l$, where $dn/dT_l \approx 3.4 \times 10^{-4} K^{-1}$. Lastly, the band gap renormalisation results from the changes of the single-particle energy of the carriers due to many-body interactions in the excited plasma. In most cases, these changes can be treated as a rigid shift of the band structure resulting in a shrinkage of the energy gap ΔE_{gap}. So, the changes of the optical

properties can be estimated within the rigid band shift model from a corresponding shift of the optical spectra[17, 49]: $\Delta n_{bgr} = n_g(\hbar\omega + \Delta E_{gap}) - n_g(\hbar\omega)$.

However, Sokolowski[17] had demonstrated that the changes of the optical properties are mainly dominated by the response of the free carriers (fc), especially at high densities of excited carriers concentration. Moreover, the variation of imaginary part of complex refractive index also has a great influence on the changes of optical property. So, both real part and imaginary part are need to be considered, which requires the Drude model need to be expressed fully regarding the excited plasma dampening:

$$\Delta\epsilon_{fc} = -\frac{N_{eh}e^2}{\epsilon_0 m^*_{opt}\omega^2}\frac{1}{1+i\frac{1}{\omega\tau_D}} \ . \tag{1.2}$$

There are two important parameters: carrier concentration N_{eh} and damping time τ_D in the Drude model, to define the accurate excited free carrier response on optical property change. The knowledge about these parameters is also crucial for the development of active optical components[50, 51] based on silicon derivative materials. In this thesis, this free carrier response is considered as the main contribution to interpret the pump probe optical spectroscopy measurements for nc-Si:H and PS membrane samples.

In order to precisely determine the dielectric function of excited semiconductor materials and characterise the excited carrier concentration and scattering rate, researchers have designed lots of different detection approaches in pump probe experiments. Roeser[18] employs a dual-angle-of-incidence reflectometry technique to do the time resolved dielectric function measurements with Drude model simulation, which illustrates the merit of dual-angle detection can improve the accuracy of determining the plasma frequency and damping time. And he also proposed that a pump probe ellipsometer may be another ideal device for determining the ultrafast dynamics of multilayer structured sample. Yoneda[52] had applied the ultrashort-pulse laser ellipsometry pump-probe experiments to research the gold targets. They measured time-resolved $p-$ and $s-$polarised reflectivity and the $s-p$ phase difference from ellipsometer detection to realise the plasma expansion and atomic polarisability. In this thesis, referring to the multilayer structured sample nc-Si:H, the multiple incident angle detection method is applied firstly to measure the induced Fabry-Perot interference shifting and simulate out the excited carrier concentration and scattering rate. Furthermore, the pump-probe ellipsometry detection approach is also built up for precise characterisation of the optical properties of excited state nc-Si:H material.

Additionally, Esser[4, 53, 54] presented a study of spectral- and time-resolved pump probe reflectivity and transmission measurements on hydrogenated amorphous silicon (α-Si:H). Moreover, the optical response of photo excited carriers in energy state of

α-Si:H is determined by intra-band transitions. And the Drude formula is also used to describe the microscopic transport properties of excited free carriers in the probing optical frequency range. Then, the non radiative recombination process of excited carriers above $5 \times 10^{19} cm^{-3}$ is fitted by a quadratic process, $dN/dt = \gamma N^2$. He also mentioned that the optical response displays the dynamics expected from a trapping mechanism at lower free-carrier density for α-Si:H material[53]. In our case, the hydrogenated nano crystalline silicon sample is a multilayer structured, opaque sample, which means we can not probe the transmission. And the recombination process of extracted carrier concentration, from Drude model fitting pump probe data, can be analysed by a recombination equation including the linear and quadratic and cubic processes, which supports the discussion of all kinds of carriers recombination mechanisms.

Actually, the ultrafast dynamics of photo excited carriers in hydrogenated nano crystalline silicon had been researched before, but there is still little known about photo induced changes of material[55]. Kudrna[56] measured the differential absorption of sample by a standard pump probe transmission technique. The transmission T_E (T_0) of the sample after (without) the pump excitation monitored by the probe pulse, are connected with the relevant absorbances A_E or A_0 as $T_{E,0} = exp(-A_{E,0})$[56]. The differential absorbance A_D is given as $A_D = A_E - A_0$. Meanwhile, the absorption connected with the excited carriers in material. The excited carriers absorption leads to the positive differential absorbance, but the change of the occupancy of the upper and lower states due to the excitation of carriers across the gap results in the negative differential absorbance (absorption bleaching)[56]. This absorption bleaching has been mentioned above as the state filling effect, and the excited state absorption can be expressed by Drude equation. Moreover, the relationship between transmission and absorbance is also an estimation with ignoring the reflected part of the incident beam. Therefore, if we want to precisely realise the photo-excited carriers dynamics, the reflection needs to be measured as well. Referring to the two different composites in nc-Si:H sample, Barreto[57] combined the pump probe time resolved reflectivity with scattering measurements to extract the characteristic times for charge carrier evolution. They used the 3D Maxwell-Garnett formulae, modified to include the Drude optical response, to model the results, which showed that the recombination times in the nano crystals and in the amorphous matrix were $\sim 4.9ps$ and $\sim 22ps$ respectively[57]. But this research did not regard the probing spectrum influence. Here, we applied the multiple probing angles spectral reflection and spectral ellipsometry detection methods, and focused on the spatially averaged information about the photo excited carrier dynamics.

Moreover, in the optical pump terahertz probe experiments, the researchers not only used the Drude expression to describe the excited free carrier response in terahertz (THz) probing range, they also applied the Lorentz oscillator model[9] or Drude-Smith

model[58] or summed with a Debye relaxator[10] to express a resonance at a finite THz frequency. This is because the THz spectral regime covers many fundamental excitations including rotations, vibrations, and low-lying electronic transitions in molecules and collective modes in condensed matter such as phonons, plasma, magnons, and energy gaps associated with superconductivity as well as intraexcitonic transitions for excitons[9]. In this thesis, we only concentrated on the pump probe visible spectroscopy measurements, so a Drude expression is enough to analyse the experimental data and we ignored the other subordinate influences on optical response. Similarly, the ultrafast dynamics of photo excited carriers in porous silicon material is also revealed by Drude equation under the pump probe visible spectroscopy measurements[59–62].

1.2 Main research content

In this thesis, a detailed report is presented on a systematic ultrafast dynamics study of photo excited carriers in hydrogenated nano crystalline silicon (nc-Si:H) and porous silicon (PS) materials. For the multilayer structured nc-Si:H sample, the multiple incident angles pump probe reflection and pump probe spectroscopic ellipsometry techniques were applied to monitor the optical response decay process after photon excitation. For the PS membrane sample, the pump-probe spectral reflection and transmission techniques are used to characterise the nonuniformly excited carriers along the membrane depth. The thesis is organised as following:

Chapter 2 starts with introducing the basic properties of nc-Si:H and PS materials. The fabrication and characterisation methods are simply reviewed firstly, which illustrates the general morphology of these two novel nano semiconductor materials. Then, the ground state optical properties are presented, which involves the determination approaches and features of absorption coefficients.

Chapter 3 introduces in depth the basic principles of the experimental techniques and data analysis. Firstly, the different optical spectroscopy detection methods, including reflection, transmission and ellipsometry techniques, are discussed. Then, the constructing optical model approach is elucidated with the dispersion relations and effective medium approximation and transfer matrix simulation methods. Using the optical model to fit the optical spectroscopy data, the dielectric constant of unexcited state material can be obtained. Finally, the ultrafast time resolved pump probe spectroscopy approaches are introduced, and the pump probe data analysis method is also detailedly discussed via Drude expression. From the analysis, the carriers concentration and scattering rate can be realised for the excited state material.

In chapter 4, the pump probe reflection and ellipsometry techniques are applied to research the ultrafast dynamics property of nc-Si:H sample. With the help of measurements at multiple probe angles, the plasma frequency ω_p and scattering rate Γ are precisely determined. Γ is dependent on ω_p when the carrier-carrier scattering mechanism dominates the scattering processes. Then, the effective mass m^* of excited carriers is estimated through the pump fluence dependent measurements. Meanwhile, the decay processes of excited carriers concentration $N_{eh}(t)$ are fitted by a recombination equation including linear and quadratic and cubic terms. Furthermore, the high-frequency conductivity as a function of pump photon energy is detected and analysed using the Drude conductivity and Boltzmann transport theory. Finally, the accurate decay processes of dielectric constant and absorption coefficient of excited nc-Si:H material are discussed by pump probe ellipsometry measurements and simulations.

In chapter 5, a free standing PS membrane is researched through the simultaneous pump probe transmission and reflection measurements. In the analysis procedure, we develop a nonuniform optical model based on Wentzel-Kramers-Brillouin (WKB) approach and Drude equation, to fit the transmission and reflection data synchronously. The model permits the retrieval of a pump-induced nonuniform complex dielectric function change and the excited carriers concentration with the increasing of membrane depth and time delay. Thus, lastly the diffusion coefficient and recombination time of excited carriers in PS membrane are discussed through the simulating of the carrier transport equation. Finally, a brief summary follows in Chapter 6.

Chapter 2

Novel Semiconductor Materials

2.1 Introduction

In this thesis, I mainly researched two different types of novel nano semiconductor materials. One is hydrogenated nano crystalline silicon (nc-Si:H), which is crystalline silicon nano clusters embedding into hydrogenated amorphous silicon matrix. Another one is porous silicon (PS) material, which is composed by empty voids and nano wires of crystalline silicon. In order to realise the basic properties of these two different materials, the general fabrication and characterisation methods, optical properties of nc-Si:H and PS materials will be reviewed respectively in this chapter.

2.2 Fabrication and Characterisation of nc-Si:H and PS

Hydrogenated Nano-Crystalline silicon (nc-Si:H)

The material of nc-Si:H used in our study was provided by Sirica DC (Israel), which was fabricated via plasma enhanced chemical vapour deposition (PECVD) and characterised in collaboration with IMT (Institute of Microtechnology, Switzerland).

Hydrogenated microcrystalline silicon was originally introduced by Veprek et al[63–65] through a special kind of plasma-deposition technique. Then, the standard PECVD method for depositing silicon films was gradually formed, which can be seen in publications of S.Usui et al[66] and Spear et al[67]. Nowadays, the PECVD technique has been widely applied to deposit intrinsic silicon films and different doping silicon films. Figure 2.1 is a standard setup of PECVD system. As we can see, a lot of deposition conditions can influence the quality of deposited films, such as substrate temperature, deposition pressure, plasma power and percentage values of silane gas etc. While the

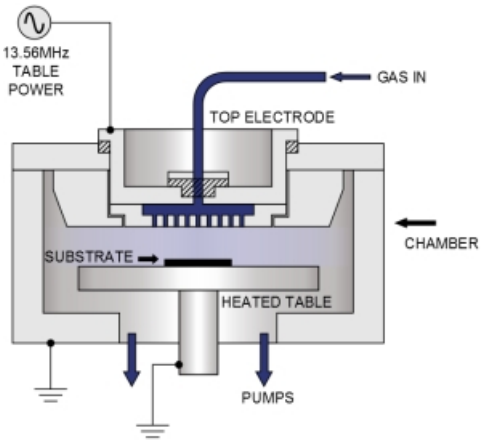

FIGURE 2.1: Standard plasma enhanced chemical vapour deposition (PECVD) setup.

percentage of silane $(SiH_4)/(SiH_4+H_2)$ is one of the most important factors to control the size and morphology of crystalline silicon clusters in deposited film. Figure 2.2 shows the schematic picture of the evolution of crystalline silicon clusters with increasing concentration of silane in hydrogen[68]. The precise details of PECVD technique depositing silicon films can be seen in Shah's publication on depositing nc-Si:H material for solar cell application[26].

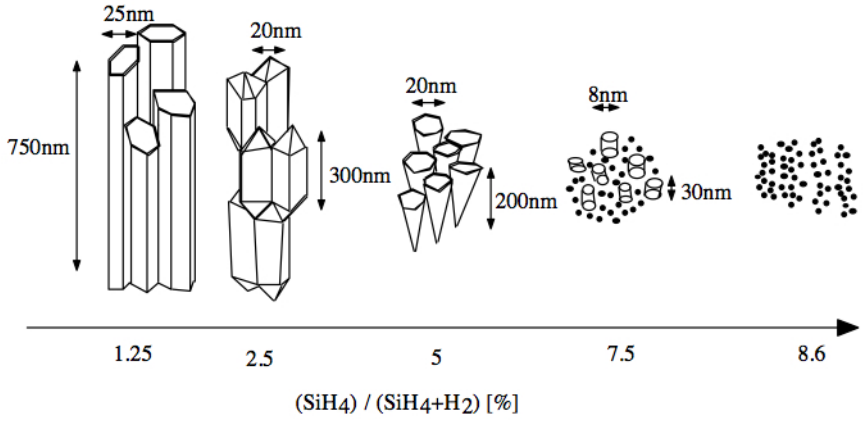

FIGURE 2.2: Schematic evolution of crystalline clusters in nano crystalline silicon film with a variation of hydrogen dilution. Percentage values refer to concentration of silane in total gas flow (hydrogen+silane); this value decreases with increasing hydrogen dilution. The Figure and Caption are from[68].

As for our investigated sample, we firstly estimated the dimensions of the sample layers using cross-sectional scanning electron microscopy (SEM) image, which is shown in Figure 2.3. This is a multilayer structured sample, which consists of a layer of hydrogenated amorphous silicon matrix (α-Si:H) containing nano crystalline silicon clusters (nc-Si). This hydrogenated nano crystalline silicon (nc-Si:H) material is around $480nm$ thick top layer, whereas the underlying silicon oxide film is $\sim 188nm$ thick. The bottom part of the cross section is a bulk crystalline silicon substrate.

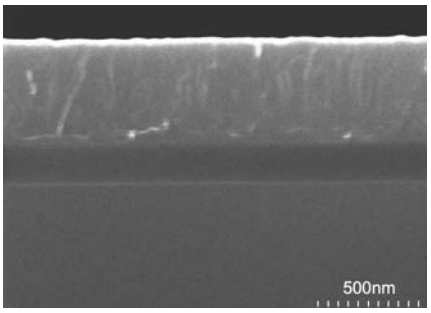

FIGURE 2.3: SEM image of cross section of nc-Si:H sample; the top $480nm$ thick layer is the researching material nc-Si:H, which was grown on a $\sim 188nm$ silicon oxide film (SiO_2) on top of a bulk crystalline silicon substrate. The Figure and Caption are from[69].

Then, the phase composition of the nc-Si:H films was investigated by Raman spectroscopy scattering measurement and analysis of the optical modes[70]. The excitation wavelength is at $532nm$ and we get rid of the background signal from the substrate. In Figure 2.4(a), the experimental Raman data are shown as black circles. Two Gaussian functions with centres around 520 and $480cm^{-1}$ were applied to fit the Raman data. The integrated intensity ratio, $I_{520cm^{-1}}/(I_{520cm^{-1}} + I_{480cm^{-1}})$, can be used to evaluate the crystalline volume fraction in nc-Si:H films[71], where $I_{520cm^{-1}}$ and $I_{480cm^{-1}}$ represent the areas of the respective Gaussians. The fitting results are shown as a red solid line in Figure 2.4(a). The volume fraction of the silicon crystalline phase estimated using this procedure is around 35%, and the rest is amorphous silicon.

The X-ray diffraction (XRD) data shown in Figure 2.4(b) were used to estimate the size of the embedded nano crystalline clusters[72–75]. Using the Scherrer equation[76, 77],

$$\langle a \rangle = \frac{K\lambda}{\beta cos\theta} \tag{2.1}$$

where K is a dimensionless shape factor with a typical value of about 0.9, but slightly varies with the actual shape of crystallite; λ is the X-ray wavelength; β is the diffraction peak broadening at half the maximum intensity (FWHM), after subtracting the instrumental background broadening, in radians; θ is the Bragg diffraction angle; we evaluated the mean diameter as $\langle a \rangle \approx 6nm$. The equation relates the broadening of a peak in a diffraction pattern to the size of the embedded clusters.

Nano Porous Silicon (PS)

Porous silicon (PS) has been known for 40 years and has long been considered as a rather uninteresting side product of electropolishing studies of Si in dilute HF solutions[79]. The first optical studies of PS[80] was performed under the liquid He temperatures and received little attention in scientific research community. Then, after the first publication

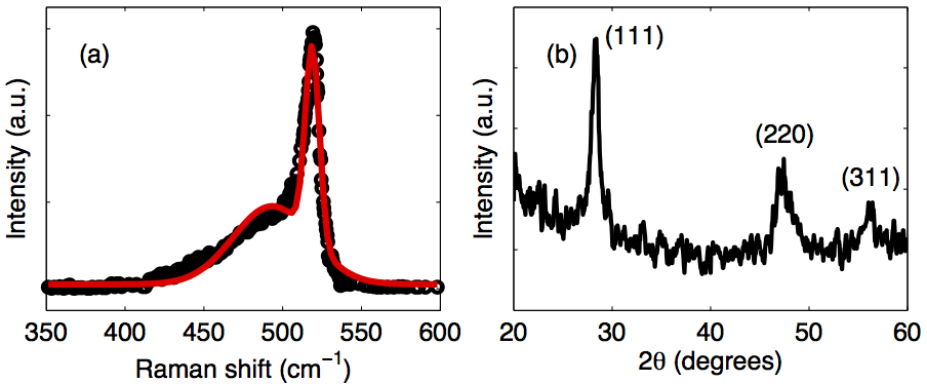

FIGURE 2.4: (a) Experimental Raman spectroscopy measurement data (black circles) of nc-Si:H sample. Red line shows a fit with two Gaussians; (b)X-ray diffraction (XRD) measurement data of nc-Si:H sample, showing three broadened diffraction peaks: (111), (220), (311).

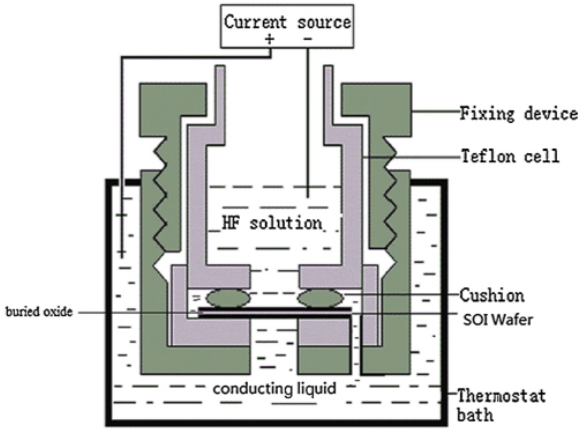

FIGURE 2.5: Schematic of porous silicon etching system. The Figure is from[78].

of efficient room temperature photoluminescence (PL)[81], PS has started to attract intensity research attention. The efficient visible red photoluminescence (PL) from porous silicon can be observed with the naked eye under green or blue laser line excitation[81]. Even though bulk Si has an indirect energy band gap in the infrared light region, the PS structure induces the efficient visible PL. Furthermore, there is also possible application of PS material into the optoelectronic devices within the region of Si technology.

Generally, nano porous silicon is manufactured through the electrochemical etching of a crystalline silicon wafer[81], which can produce a sponge like network with nanometer scale pores ($< 100nm$) and nanometer scale silicon wires with diameter $< 50nm$. This nanometer-scale silicon has a number of unique features, producing a dramatic effect on optical and electrical compared to those of bulk silicon: a large surface area to volume ratio, a pore size smaller than the optical probing wavelength, a modified energy gap, and a constricted free-carrier mean free path. Figure 2.5 illustrates a schematic etching system to producing PS material. As for our research PS samples, the porous

silicon layer was fabricated by electrochemical anodisation of the surface of a 3 inch diameter (100) silicon wafer (B-doped, $5 - 15 m\Omega cm$), using an electrolyte comprised of methanol and 40%HF in the ratio 1:1; a current density of $30 mA/cm^2$ and anodisation time of 11min was chosen to yield a layer with $\sim$ 64% porosity and $\sim 11 \mu m$ depth (calculated gravimetrically). With precisely controlling the anodisation time, different thickness of PS layer can be produced. Then, after anodisation, we can use this PS layer with c-Si substrate sample for research. Moreover, we can also only obtain the PS membrane. We applied a $120 mA/cm^2$ pulse ($10s$) before removed from the electrolyte to get only the PS layer by detaching the underlying c-Si substrate. This free-standing PS membrane was then rinsed in methanol and air-dried. Figure 2.6 (a) and (b) show the cross-sectional SEM images of a PS layer with c-Si substrate and free standing PS membrane, respectively. In our research, we characterised the $\sim 700nm$ PS layer with c-Si substrate sample firstly. Then, we focused on the $\sim 13 \mu m$ thick free standing PS membrane research to avoid the influence from c-Si substrate. Figure 2.6(c) displayed the surface of porous silicon, which illustrates the dimensions of nano pores.

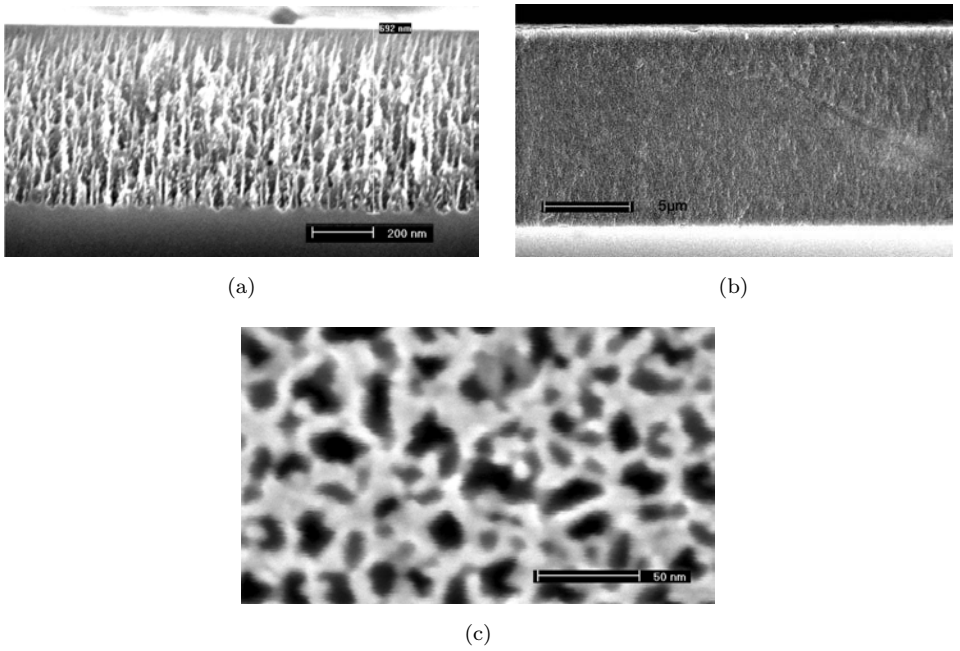

(a) (b)

(c)

FIGURE 2.6: (a) Cross section of SEM image, $\sim 700nm$ PS layer with c-Si substrate; (b) $\sim 13 \mu m$ free standing PS membrane; (c) Surface of PS layer showing dimensions nano pores.

2.3 Optical Property of nc-Si:H and PS

Hydrogenated Nano-Crystalline silicon (nc-Si:H)

As we want to use the spectroscopic pump probe approach to analyse the ultrafast dynamics properties of nc-Si:H material, we need to realise the fundamental optical properties of nc-Si:H sample firstly. Generally, the optical property is represented by the complex refractive index. As long as the complex refractive index N is acquired though the experimental measurements, the complex dielectric constant ϵ and absorption coefficient α of the researched material both can be calculated as well. Intrinsically, N, ϵ and α are correlated with each other. As for nc-Si:H material, absorption coefficient α is an important parameter to be characterised[82], which influences the pump photons absorption. Moreover, the energy band gap E_g of researched material can be approximated out through the relationship between absorption coefficient α and incident photon energy[83]. We can see in Figure 2.7, which illustrates the typical absorption coefficients spectra for the samples of micro/nano crystalline silicon (μc/nc-Si:H), crystalline silicon (c-Si), hydrogenated amorphous silicon (α-Si:H), respectively. These results were measured using the constant photocurrent method (CPM)[84]. As shown, the μc/nc-Si:H closely follows the curve of c-Si, except for a slight red-shift when the photon energy is smaller than $\sim 1.3eV$. The enhanced absorbance in the red region seems to be considered due to the stronger light scattering inside of μc/nc-Si:H material[85], which also related with the crystalline volume fraction of this material. Meanwhile, the amorphous phase fraction contributes to the higher absorption coefficient of μc/nc-Si:H material in the higher photon energy region. Even though the energy gap of α-Si:H, $\sim 1.7eV$ is larger than the c-Si, $\sim 1.12eV$, the direct band gap structure of α-Si:H material improves the absorbance ability in the shorter wavelength region, which can be seen in Figure 2.7. Because of this excellent absorption property in the higher and lower photon energy region, the μc/nc-Si:H has been extensively researched as a novel absorbers in thin film solar cells[26]. In our case, referring to the multilayer structure of nc-Si:H sample, the transmission spectrum of sample can not be detectable due to its opacity. Thus, the CPM method is not suitable any more. To realise the dielectric constant of our opaque sample, spectroscopic reflection and ellipsometry measurements were done and an optical model was built to fit the results. From the optical model fitting, the energy band gap of the researched nc-Si:H material can also be estimated. All these optical properties research and optical model construction will be illustrated in detail in the next chapter.

Nano Porous silicon (PS)

As for the nano porous silicon (PS) material, we also need to fully understand the optical properties before analysing the ultrafast pump probe measurement data. A simple characterisation approach is to measure the spectroscopic reflectance spanning a large spectral region. Figure 2.8(a) displayed the measured reflectance spectra of PS (solid curve) and c-Si (dashed curve) in the photon energy range of $2 - 20eV$ using a

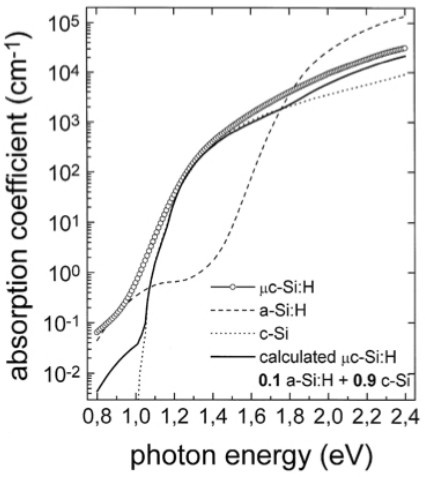

FIGURE 2.7: Optical absorption coefficients (cm^{-1}) of c-Si, μc-Si:H, α-Si:H and calculated α with the help of effective media approximation. The Figure and Caption are from[86].

synchrotron radiation source. Then, the spectral response of the optical constant can be analysed out by the Kramers-Kronig (K-K) relation[87]. The K-K analysis equations are shown as following, which indicates the relationship between real part ϵ_r and imaginary part ϵ_i dielectric constant of a material. This K-K relations are derived based on causality and linearity, which means that light absorption occurs after light enters media[88].

$$\begin{aligned} \epsilon_r(\omega) &= 1 + \frac{2}{\pi} P \int_0^\infty \frac{\omega' \epsilon_i(\omega')}{\omega'^2 - \omega^2} d\omega' \\ \epsilon_i(\omega) &= -\frac{2\omega}{\pi} P \int_0^\infty \frac{\epsilon_r(\omega') - 1}{\omega'^2 - \omega^2} d\omega' \end{aligned} \tag{2.2}$$

Where $\epsilon = \epsilon_r - i \cdot \epsilon_i$ and P in the equation shows the principal value of the integral:

$$P \int_0^\infty d\omega' \equiv \lim_{\delta \to 0} \left(\int_0^{\omega - \delta} d\omega' + \int_{\omega + \delta}^\infty d\omega' \right) \tag{2.3}$$

However, there is also a drawback of this simplest reflectance measurement with K-K analysis approach. As we can see in the K-K Equations 2.2, the integral of photon angular frequency ω is from 0 to ∞, which indicates photon energy should cover a large region, such as $2 - 20eV$, to eliminate the analysis errors. If the photon scanning region is too short, an extending approach should be taken to estimate the reflectance response at other undetected photon energy region. The different extending approaches will give different ϵ results, which leads to the big errors of ϵ. Therefore, some researchers proposed other methods to evaluate the optical properties of PS material.

Another simple method is to evaluate Fabry-Perot interference fringes if they are observed in the reflection or transmission measurements. Figure 2.8(b) shows the measured (solid line) reflectance spectra of a PS sample. Then, a dielectric function model is set

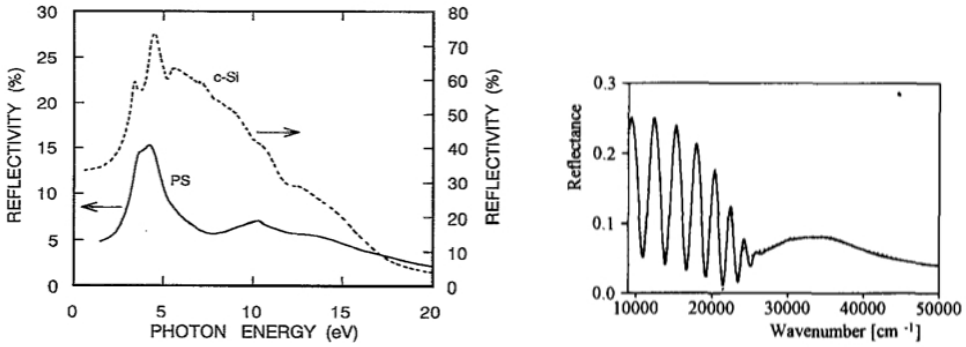

(a) (b)

FIGURE 2.8: (a)Measured reflectance spectra of PS (solid curve) and c-Si (dashed curve) in the photon energy range of $2 - 20eV$ using a synchrotron radiation source. The Figure and Caption are from[87]; (b)Measured (solid line) and calculated (dotted) reflectance spectra of $\sim 70\%$ porosity layer of $1\mu m$ thickness. The Figure is from[89].

up for expressing nano wires c-Si, and an effective medium approximation model is applied to generate the average dielectric response of the whole PS material. Finally, the reflectance or transmittance of the sample can be computed[90]. Through adjusting the parameters of model, including layer thickness and porosity, the experimental spectra can be fitted, which is shown as dotted line in Figure 2.8(b). Apart from these reflection and transmission methods, spectroscopic ellipsometry (SE) can also be applied to evaluate the optical properties of PS sample[80]. As for our researched PS samples, we applied SE method to determine the dielectric function of PS layer on c-Si substrate sample and used spectroscopic transmittance and reflectance measurements to evaluate dielectric function of free standing PS membrane. But, intrinsically, it is same way for both of these applied methods to construct optical model and fit the dielectric constant of PS material, which will be detailedly illustrated in the following chapters. Figure 2.9 gives out the comparison of the absorption coefficient spectra of c-Si, α-Si:H and PS. As we can see, the absorption spectra values of PS falls below that of bulk c-Si and α-Si:H. But there is absorption below the E_g value of bulk c-Si. This electronic absorption tail is definitive proof for the additional (defect) energy states in the middle of energy band gap[91]. In our experiments, the $1.55eV$ photon energy is used to do the ultrafast pump probe measurements for the PS material, of which absorption coefficient corresponds to around $3 \times 10^1 cm^{-1}$. When the free carriers are excited in PS material by pump beam, the higher absorption ability can be observed from the probe beam detection, which will be discussed in the following chapters. This large photo induced absorption has been of considerable interest in view of possible applications in optoelectronics and signal processing[92].

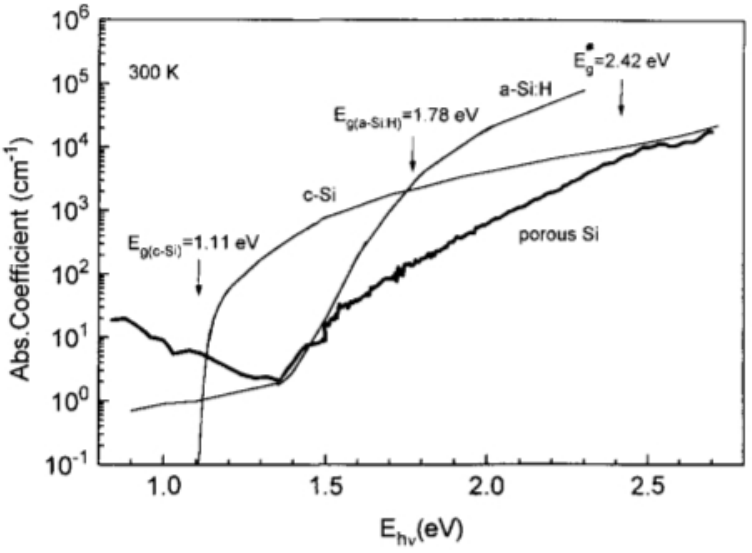

FIGURE 2.9: Comparison of the absorption spectra of c-Si, α-Si:H and PS prepared from p-type ($\sim 1\Omega cm$) Si. The Figure and Caption are from[91].

.

2.4 Summary

In conclusion, the fabrication and characterisation of hydrogenated nano crystalline silicon (nc-Si:H) and nano porous silicon (PS) materials have been simply reviewed firstly, which gives out the general morphology of these two novel nano semiconductor materials. Then, the optical properties of nc-Si:H and PS are introduced respectively, which includes the description of determination methods and features of absorption coefficients. This optical property analysis is also the fundamental step before researching the ultrafast dynamical properties of these two materials.

Chapter 3

Experimental Techniques and Data Analysis

3.1 Introduction

In this chapter, various optical spectroscopy methods are introduced to determine the optical properties of semiconductor samples. They are the reflection, transmission and spectroscopic ellipsometry techniques. The reflection and transmission measurements can acquire the reflectance and transmittance of transparent samples. But, sometimes only detecting the reflected or transmitted signal intensity can not precisely solve out all the optical constant of a sample. Thus, the spectroscopic ellipsometry (SE) is normally applied to improve the determination of optical property. SE is normally based on the reflection measurement. But, the reflected beam is further analysed considering the phase difference between s- and p-polarised states, not only the intensity. Then, with the help of an optical model and applying the transfer matrix method, the dielectric constant of a material can be obtained from fitting the data. Moreover, the structural information of multilayer or multi-phase sample can also be realised, such as film thickness or phase volume fraction. Finally, the ultrafast time resolved pump probe techniques are discussed. As the pump beam excites the material, the reflection, transmission and ellipsometry techniques are applied again for the probe beam to monitor the optical property variation of excited state material. These ultrafast detections can be used to infer the information about the dynamics of excited carriers in the sample. And the discussions detail the principle of time resolved technique, the schematic of pump probe reflection, transmission and ellipsometry setup; the theoretical model for analysing the pump probe data and characterising the ultrafast dynamic.

3.2 Reflection Transmission and Ellipsometry

Even several centuries ago, optical methods have been used to measure the physical properties of materials. Since Huygens correctly concluded that light effectively slowed down on entering more dense media, derived the laws of reflection and refraction and even explained the double refraction of calcite[93], optics have been applied to measure and observe the intrinsic properties of materials in a non-invasive way. The observation by Huygens is fundamental for the reflection and transmission theory. Then, Fresnel conducted a series of experiments to determine the effect of polarisation on interference and went on to evolve a mechanistic description of ether oscillations, which produced his famous formulas about the amplitudes of reflected and transmitted light[93]. Finally, James Clerk Maxwell brilliantly summarised and extended all the empirical knowledge on the subject in a single set of mathematical equations, the famous Maxwell Equations. Starting from this remarkably brief and beautifully symmetrical synthesis, he was able to show *"light was an electromagnetic disturbance in the form of waves"*[93]. Based on these pioneers excellent theories, reflection and transmission techniques were confined to academic laboratories and then began to emerge in industrial applications in the 1960s[94]. The basic principle behind all modern reflection and transmission techniques are not very complicated. A beam of monochromatic light is incident upon a sample. Then, the incident source light and reflected light and transmitted light intensity should be measured accurately. Finally, the ratio between reflected and source light intensity is the sample reflectance; the ratio between transmitted and source light intensity is the sample transmittance for this monochromatic light wave.

In the following sections, these techniques will be discussed on the capability of resolving the important optical parameters for various semiconductor materials. Reflection and transmission measurements will be introduced firstly to see what the obvious information can be obtained directly. To make it simple, we make the assumption that the measurements are performed under the normal incidence condition, which leads to all the cosine terms inside of the Fresnel equations are equal to unity. Furthermore, we also do not need to distinguish the p- (parallel) and s- (perpendicular to the light incident plane) polarisation waves due to the axial symmetry of the measurement at normal incidence. Considering a pure bulk semiconductor sample without films or other material on the surface, such as crystalline silicon, the Fresnel equations are given as following:

$$\begin{aligned} r &= \frac{N_S - N_i}{N_S + N_i} \\ t &= \frac{2N_i}{N_S + N_i} \end{aligned} \tag{3.1}$$

Where N_S is the complex refractive index of bulk material and N_i is the refractive index of the surrounding medium or ambient (normally sample is measured in the air, $N_i = 1 - i \cdot 0$). The bulk sample can also be considered as a semi-infinite thickness substrate. Meanwhile, in the discussion, the transmission is assumed to be detected inside of the bulk material. And the research about films on substrate will be introduced in later sections. As long as the reflection and transmission coefficients are obtained at normal incidence angle, the reflectance and transmittance can be calculated out.

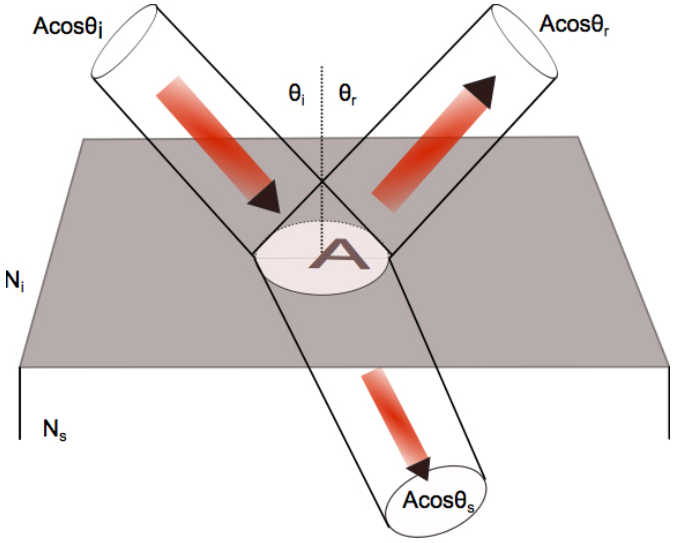

FIGURE 3.1: Reflection and transmission of an incident beam.

As we can see reflection and transmission from Figure 3.1 for an arbitrary incidence angle, part of incident beam is reflected and part of it is transmitted. We define the reflectance R to be the ratio of reflected intensity (or power) to the incident intensity. The light intensity of electromagnetic waves is proportional to magnitude of electrical: $I \propto |E|^2$ and reflection and transmission coefficient are defined as $r = E_r/E_i, t = E_t/E_i$. So, considering the across sectional area of incident and reflected and transmitted beam in Figure 3.1, the reflectance is related to reflection coefficient as following:

$$R = \frac{I_r \cdot Acos\theta_r}{I_i \cdot Acos\theta_i} = \frac{I_r}{I_i} = |\frac{E_r}{E_i}|^2 = |r|^2. \tag{3.2}$$

Where the law of reflection is used to get $\theta_i = \theta_r$ here. And transmittance T is also defined as the ratio of transmitted to incident intensity. But $I_t \propto n_s \cdot |E_t|^2$ should be considered[93, 95],where n_s is the real part of substrate complex refractive index $N_s = n_s - i \cdot k_s$. So the general relation between transmittance and transmission coefficient is as following:

$$T = \frac{n_s \cdot E_t^2 \cdot Acos\theta_s}{n_i \cdot E_i^2 \cdot Acos\theta_i} = (\frac{n_s cos\theta_s}{n_i cos\theta_i}) \cdot |t|^2. \tag{3.3}$$

Because of the normal incident assumption, the reflectance and transmittance for $s-$ and $p-$ polarisation waves are same with each other, which would lead to

$$\begin{aligned} R &= R_s = R_p = (\tfrac{N_s - N_i}{N_s + N_i})^2 \\ T &= T_s = T_p = \tfrac{4 n_s n_i}{(N_s + N_i)^2} \end{aligned} \tag{3.4}$$

As we can measure and calculate the reflectance and transmittance, we should be able to obtain the information about real and imaginary component (n_s, k_s) of bulk material theoretically. However, it is impossible to put the detector inside of bulk material to get transmission signal. All the materials investigated here are assumed to be isotropic structure, which means the complex refractive index of material is not a tensor referring to different directions.

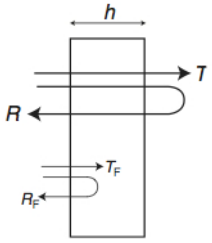

FIGURE 3.2: Partially absorbing slab with plane parallel faces: h, geometrical thickness of the slab; (R, T), intensity reflectance and transmittance overall coefficients of the slab; (R_F, T_F), intensity reflectance and transmittance coefficients of a single face. The Figure and Caption are from[96].

In most cases, the slab structured sample is used to determine the complex refractive index of the material. Enrico Nichelatti[96] proposed an analytical expression to figure out the N_s of a planar slab from normal incidence reflectance and transmittance. As long as one measured (R, T), one can obtain complex refractive index (n_s, k_s) of the slab through following three simple equations:

$$\begin{aligned} R_F &= (2 + T^2 - (1-R)^2 - \{[2 + T^2 - (1-R)^2]^2 - 4R(2-R)\}^{1/2})[2(2-R)]^{-1} \\ k(R,T) &= \tfrac{\lambda}{4\pi h} ln[\tfrac{R_F(R,T)T}{R - R_F(R,T)}] \\ n_{\pm}(R,T) &= \tfrac{1+R_F(R,T)}{1-R_F(R,T)} \pm \{\tfrac{4R_F(R,T)}{[1-R_F(R,T)]^2} - (\tfrac{\lambda}{4\pi h})^2 ln^2[\tfrac{R_F(R,T)T}{R - R_F(R,T)}]\}^{1/2} \end{aligned} \tag{3.5}$$

As we can see the slab schematic Figure 3.2, the analytical procedure is processed as following: firstly $(R, T) \rightarrow R_F$, then $(R, T, R_F(R,T), \lambda, h) \rightarrow (n_s, k_s)$, where λ is incident light wavelength. But there would be inducing two solutions for n_s and both of them are mathematically acceptable. So the proper solution has to be selected on physical grounds, considering practical conditions ($k_s \ll n_s, n_s > 1$). Moreover, from Khashan's[97] and Stezel's[98] discussions on optical constant determination, we can conclude that this is a useful way to obtain the complex refractive index of a material

from $(R(\lambda), T(\lambda))$ measurements. Actually, frankly speaking, the slab sample can definitely be symbolised as $(air/layer/air)$ optical model. In the following sections, we will further talk about how to calculate (R, T) of a multilayer structured sample.

However, it is not always possible to determine optical constants of a material by using reflectance and transmittance measurements. When the sample is very thick, the transmission signal intensity would be very low and absorbance could become stronger, so the detector for transmission can not detect any light. Even though transmitted signal intensity is acquired under this condition, the final results error would also be quite bigger than before. Sometimes, the absorbance of a material can be quite small. From reflected signal and transmitted signal intensity, one still can not get the precise absorbance of sample. Because any fluctuated errors in the detection signal can cover the actual absorbance. This will also increase the difficulty to obtain the optical constant of a material. Moreover, the above discussions are based on the measurements under the special restriction of nearly normal incidence. So in order to resolve the both components of complex refractive index, for all kinds of structured samples, and without special conditions and assumptions, we need to take another different approach.

Spectroscopic ellipsometry is another method to be used to obtain the important optical constants of a material. Ellipsometry measurements are performed by using light of precisely controlled polarisation. The polarised light is reflected from or transmitted through a sample, and then an *analyser* is used in the detection of reflected or transmitted light, ascertaining the change of resultant light polarisation due to its interaction with the sample. Generally, the polarised resultant light often becomes elliptically polarised following reflection or transmission. This is also the reason for the nomenclature 'ellipsometry'. This ellipsometry technique measures two fundamental parameters as a function of light wavelength λ, $(\psi(\lambda), \Delta(\lambda))$. Parameter $tan\psi$ corresponds to the amplitude ratio and Δ represents to the phase difference between the two orthogonal components $p-$ (parallel) and $s-$ (perpendicular) polarised resultant light. Ellipsometry has become an attractive measurement tool due to its non-destructive nature and high sensitivity to small interfacial effects, such as volume fraction of different composed phases material in thin films and thickness identification. And the remarkable features of spectroscopic ellipsometry is typically the high precision measurement (thickness sensitivity: $\sim 0.1\mathring{A}$)[99].

In order to make good use of ellipsometry non-destructive technique, we need to avoid two general restrictions on measurements: surface roughness of sample has to be small and measurement must be performed at oblique incidence[99]. If the roughness of a sample surface exceeds $\sim$ 30%, it would raise difficulty in determining the polarisation sate and measurement errors would also increase. As for the incidence angle, it

influences the sensitivity of measurements and the choices of angle depends on the optical constants of the samples. For crystalline silicon, the incidence angle is typically at around 75°. Around this angle, the amplitude ratio between $p-$ and $s-$ polarised light is at maximum value. So the measurement sensitive is also quite high. When it is normal incidence, the ellipsometry measurement becomes impossible for isotropic materials, since $p-$ and $s-$ polarisation can not be distinguished anymore. But for the anisotropic material, the variation of optical constant at $p-$ and $s-$ directions can still allow the ellipsometry measurement. Apart from the advantages, there is also an inherent drawback for ellipsometry measurements, which is the indirect nature of this characterisation method. Specifically, an optical model is required to analyse ellipsometry data. This optical models need to be constructed, defined by the optical constants and thicknesses information and multi phases volume fraction of the researched sample. Moreover, the characterisation of small absorption coefficients ($\alpha < 100cm^{-1}$) is also rather difficult[99].

The wavelength range of ellipsometry used to scan sample also plays an important role to provide information on different photonic interaction processes. Currently, spectroscopic ellipsometry has been widely applied to evaluate optical constants and monitor the thin film growth processes, especially silicon thin films and microcrystalline silicon thin films[100–109]. For real-time monitoring (*in situ* measurements) , not only characterisation of thin-film growth but also process diagnoses including plasma etching and thermal oxidation can all be performed[110–112]. They also proposed that single wavelength ellipsometry is not sufficient to express the information of the sample in monitoring process. As for our samples, porous silicon and hydrogenated nano crystalline silicon, they all have been manufactured. So, only the *ex situ* measurements can be done. Then, constructing an optical model is necessary to fit (ψ, Δ) and get out optical constants of our samples. As long as complex refractive index $N = n - ik$ is obtained, where n is refractive index and k is extinction coefficient, we can draw out the other optical constants, such as the dielectric function ϵ and absorption coefficient α by simple relations: $\epsilon = N^2$ and $\alpha = 4\pi k/\lambda$.

3.2.1 Principles of Measurements and Terminology

In order to reveal the principles of reflection and transmission spectroscopy and ellipsometry, we first use a simple semi-infinite substrate as an example to discuss the performance of measurement techniques. As we can see in Figure 3.3(a), the incident electric field E_i is distributed between E_{is} and E_{ip} components, which represent the perpendicular and parallel component to incident plane respectively. Meanwhile, (E_{rs}, E_{rp}) and (E_{ts}, E_{tp}) express the $s-$ and $p-$ components of electric vectors of reflected and

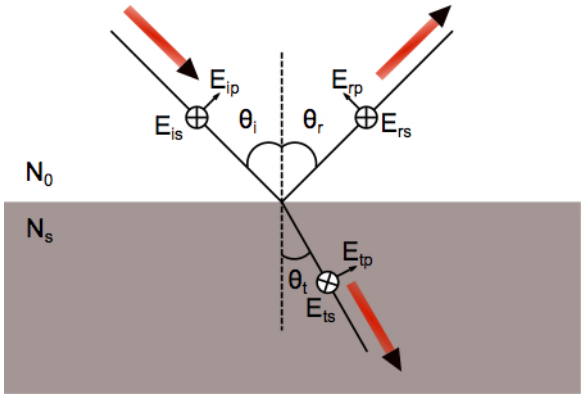

(a)

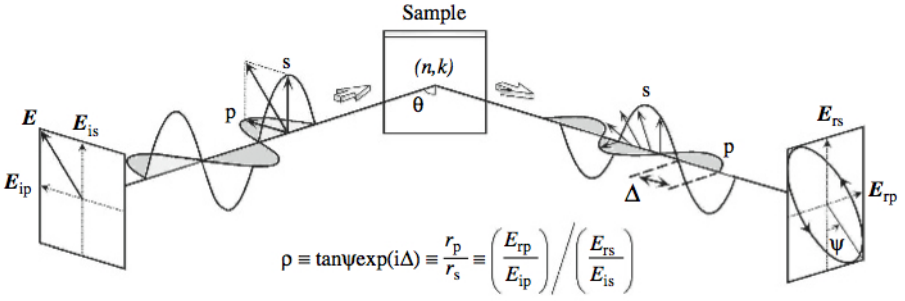

(b)

FIGURE 3.3: (a) Electric field E composed by $p-$ and $s-$ polarisation. E_s is perpendicular and E_p is parallel to the light incident plane. θ_i, θ_r and θ_t are the incident angle, reflective angle and refractive angle respectively. N_0 and N_s are the complex refractive index of the ambient and substrate. (b) Measurement principle of ellipsometry. The Figure and Caption are from[99].

transmitted waves separately. The complex refractive indices of ambient and substrate are N_0 and N_s respectively. According to boundary conditions of Maxwell electromagnetic equations[113, 114], the components of electric filed E and magnetic induction B parallel to the interface are continuous at the boundary. (there is no surface charges for continuous B.) This means the parallel components on the incident side must be equal to that on the transmitted side. Referring to this condition for ambient/substrate interface, the Fresnel equations of reflection and transmission $(s-, p-)$ coefficients can all be derived.

$$r_s = \frac{E_{rs}}{E_{is}} = \frac{N_0 cos\theta_i - N_s cos\theta_t}{N_0 cos\theta_i + N_s cos\theta_t} \qquad r_p = \frac{E_{rp}}{E_{ip}} = \frac{N_s cos\theta_i - N_0 cos\theta_t}{N_s cos\theta_i + N_0 cos\theta_t} \tag{3.6}$$

$$t_s = \frac{E_{ts}}{E_{is}} = \frac{2N_0 cos\theta_i}{N_0 cos\theta_i + N_s cos\theta_t} \qquad t_p = \frac{E_{tp}}{E_{ip}} = \frac{2N_0 cos\theta_i}{N_s cos\theta_i + N_0 cos\theta_t} \tag{3.7}$$

The reflection law $\theta_i = \theta_r$ has been used to derive these equations. Referring to the Snell's law $N_0 sin\theta_i = N_s sin\theta_t$, the Fresnel equations can be rewritten as only depending on the incidence angle θ_i and complex refractive indexes (N_0, N_s). For example, the reflection coefficients can be written as following Equations 3.8. This formulae simplification is also a special feature of the ambient/substrate optical model.

$$r_s = \frac{cos\theta_i - (N_{s0}^2 - sin\theta_i^2)^{1/2}}{cos\theta_i + (N_{s0}^2 - sin\theta_i^2)^{1/2}}, \qquad r_p = \frac{N_{s0}^2 cos_{\theta_i} - (N_{s0}^2 - sin\theta_i^2)^{1/2}}{N_{s0}^2 cos\theta_i + (N_{s0}^2 - sin\theta_i^2)^{1/2}} \tag{3.8}$$

Where $N_{s0} = N_s/N_0$. According to the Figure 3.1 in previous section and definition of reflectance and transmittance, (reflectance is defined as intensity ratio between reflected and incident light, transmittance is the ratio of transmitted to incident intensity), we can obtain the reflectance R and transmittance T as following:

$$R_s = |r_s|^2 \qquad R_p = |r_p|^2 \tag{3.9}$$

$$T_s = \frac{N_s cos\theta_t}{N_0 cos\theta_i} \cdot |t_s|^2 \qquad T_p = \frac{N_s cos\theta_t}{N_0 cos\theta_i} \cdot |t_p|^2 \tag{3.10}$$

If the optical constant of the substrate is to be the complex refractive index $N_s = n_s - ik_s$, this means the reflection and transmission coefficients are all complex values. So, it should be more useful to represent the Fresnel coefficients in the polar coordinate system, which are shown in following Equations 3.11 and 3.12, to conveniently investigate the effect on the amplitude and phase of reflected or transmitted waves separately. As we mentioned earlier, the amplitude ratio and phase difference between $p-$ and $s-$ polarised waves are correlated to the ellipsometry measurement quantities (ψ, Δ).

$$r_s = |r_s| \cdot e^{i\delta_{rs}} \qquad r_p = |r_p| \cdot e^{i\delta_{rp}} \tag{3.11}$$

$$t_s = |t_s| \cdot e^{i\delta_{ts}} \qquad t_p = |t_p| \cdot e^{i\delta_{tp}} \tag{3.12}$$

Figure 3.3(b) illustrates the measurement principle of reflection ellipsometry. The 45° linear polarisation incident light is used to provide equal amplitude components for $p-$ and $s-$ polarised directions. Moreover, $p-$ and $s-$ waves are also both in the same phase, as they are coming from the same source. So, we can define the initial phase for each component $p-$ and $s-$ is zero. After the sample reflection, there are definite changes of amplitude and phase for each components $p-$ and $s-$ polarised waves, in term of the reflection coefficients expressions 3.11. Thus, we can express the phase changes for $p-$ and $s-$ waves as δ_{rp} and δ_{rs} separately. Then, the ellipsometry parameter Δ is

defined to relate with the variations of each component phase by following formula:

$$\Delta = \delta_{rp} - \delta_{rs} \ . \tag{3.13}$$

Therefore, Δ illustrates the phase difference between the $p-$ and $s-$ waves induced by the sample reflection. And this value can vary from $-180°$ to $180°$ or be converted between $0°$ and $360°$ by periodical factor 2π[99, 115]. As for the amplitude changes of $p-$ and $s-$ waves, another ellipsometry parameter ψ is used to express this information, which is defined as the amplitudes ratio of those reflection coefficients in polar coordinate expression 3.11:

$$tan\psi = \frac{|r_p|}{|r_s|} \tag{3.14}$$

Therefore, ψ is the angle, whose tangent is the ratio of the amplitudes of the total reflection coefficients. The value should be in the range from $0°$ to $90°$[99, 115]. To sum up both amplitude and phase information, ρ is defined as the complex ratio between the total $p-$ and $s-$ reflection coefficients:

$$\rho = \frac{r_p}{r_s} = tan\psi \cdot e^{i\Delta} \tag{3.15}$$

Similarity, we can also measure the transmission ellipsometry. This means we can also obtain the amplitude and phase changes due to the transmitting through a sample. And $tan\psi$ would express the amplitude ratio of total $p-$ and $s-$ transmission coefficients and Δ should be the phase difference between transmitted $p-$ waves and $s-$ waves. Then, the ellipsometry parameters are defined as following:

$$\begin{aligned} tan\psi &= \frac{|t_p|}{|t_s|} \\ \Delta &= \delta_{tp} - \delta_{ts} \\ \rho &= \frac{t_p}{t_s} = tan\psi \cdot e^{i\Delta} \end{aligned} \tag{3.16}$$

The amplitude and phase components of ρ is attributed to the tangential and exponential parts of this function respectively[22]. From Maxwell and Fresnel equations to the reflectance R transmittance T and ellipsometry (ψ, Δ), you can see the basic theory behind the measurement and relationships among $R, T, (\psi, \Delta)$. Meanwhile, we also find that $R, T, (\psi, \Delta)$ depend on the external conditions according to above equations, including the complex refractive indexes of the ambient and substrate media and the incidence angle of light. As long as we can measure R, T or (ψ, Δ) and we know the refractive index of the incident medium and incident angle, the material optical constants can be obtained finally from this *Ambient/Substrate* system[22, 100].

3.2.2 Transfer Matrix for a Multilayer System

In the previous section, the theory of Fresnel equations and ellipsometry definition are discussed referring to the basic optical system *Ambient/Substrate*. However, this simple system is not very common in practical world. Moreover, the Fresnel equations can only solve the sample structured with one interface. Normally, the structure of a researched sample is a slabs or a thin film with a substrate, or multilayer films with a substrate. To establish an optical model precisely, we need to understand the basic concepts of thin film, slab and substrate firstly. Generally speaking, a material can be defined as a substrate when the thickness of this material is much bigger comparing to the incident light wavelength and it can also sufficiently absorb incident light. Then, we can ideally coin it as a substrate and we do not need to consider the rear side interface of this medium. Because there will be no light transmitting through this thick and strong absorbance sample, the Fresnel equations can simply solve all the optical parameters for this *ambient/substrate* system using the optical model simulation, which is schematically described in Figure 3.3(a).

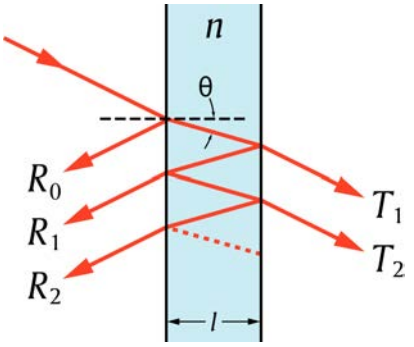

FIGURE 3.4: Interference due to two interfaces reflection and transmission.

However, most samples should be classified into slab category. The thickness value is not very big and it can not totally absorb the incident light. So there is light transmitting through the back interface of the slab, which is depicted in the Figure 3.4. How to obtain the optical constants of the slab has been discussed in detail in some reports[22, 96, 97, 99, 116]. The reflection and transmission of light from a single interface between two mediums can be described by the Fresnel equations 3.6 and 3.7. However, when there are two interfaces, such as a slab in Figure 3.4, the total reflection and transmission intensity include the contributions from front surface and rear surface. Due to the two interfaces effect, the superposition of light waves leads to the optical interference occurs in the spectral reflection and transmission. As for the difference between optical path length and incident light wavelength, these reflections and transmissions can interfere destructively or constructively. The overall reflection and transmission of a slab is the sum of an infinite number of reflections and transmissions.

This will be too cumbersome to calculate. In order to conveniently analyse this kind of sample, we can ideally classify the slab structure as *Ambient/Film/Substrate* optical system, which is shown in Figure 3.5. If the slab is immersed in the air, the optical model actually corresponds to *air/slab/air* system. Here, the substrate is also the air medium. Thus, *Ambient/Film/Substrate* optical system is quite common in the optics research. We need to build the analyse method for this basic system firstly, then we can extend to more complicated optical system, such as multilayer films with a substrate. Basically, even though the Fresnel equations can be improved to use in the multilayer optical system, which has been illustrated in Fujiwara's publication[99] and Thomas's thesis[22], the method is still quite complex and calculation is still quite cumbersome. While the transfer matrix method is a very good approach to resolve the multilayer optical problems easily[93, 95, 117–119]. One transfer matrix can represent the optical property of one layer. So, we will introduce transfer matrix firstly through mathematical treatment of simple *ambient/layer/substrate* optical system. Then, a simple and practical example will be used to illustrate the usefulness of transfer matrix. Finally, we will apply the transfer matrix to analyse a multilayer structured sample.

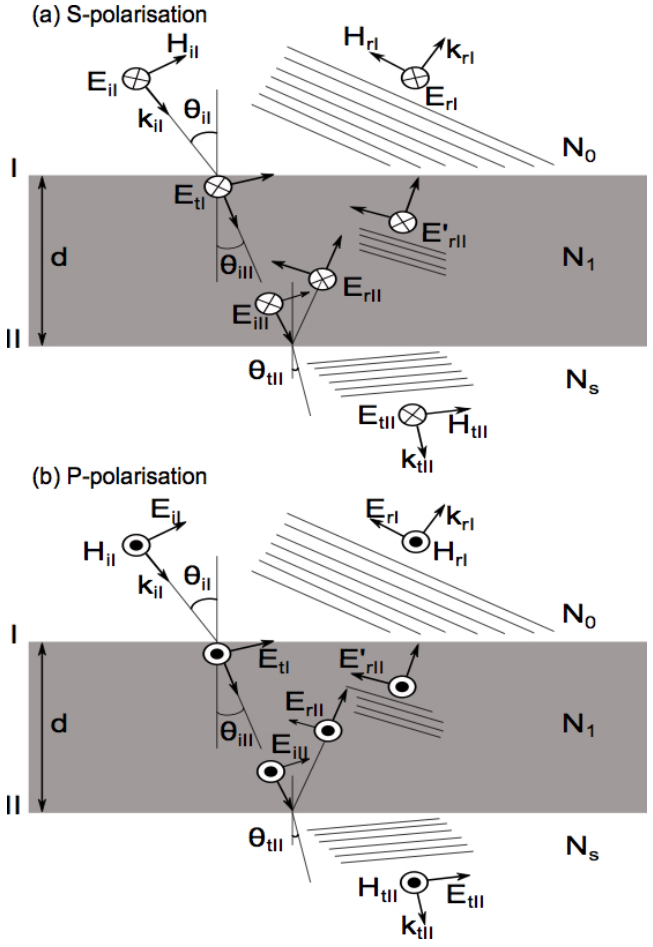

FIGURE 3.5: Transfer matrix deduction for *Ambient/Film/Substrate* optical system: (a) S-polarisation, (b) P-polarisation waves.

3.2.2.1 Mathematical Treatment

The transfer matrix method is an approach used in optics and acoustics to analyse the propagation of electromagnetic or acoustic waves through a stratified medium[95]. For example, this method can be used to design anti-reflective coatings and dielectric mirrors. The mathematical treatment of transfer matrix is based on the Maxwell equations. As we can see in Figure 3.5, the linearly polarised waves are incident on a thin dielectric film, which can be symbolised to the optical structure *Ambient/Film/Substrate*. One important point need to be mentioned that the *total* electric E and magnetic H fields are considered in the whole process. This means, each wave of $E_{iI}, E_{rI}, E_{iII}, E_{rII}, E'_{rII}, E_{tII}$ and so forth, represents the resultant of all possible waves travelling in that direction in that medium. The summation process is therefore smartly built in transfer matrix approach compared to the Fresnel equation method. According to boundary conditions, the tangential components of both electric (E) and magnetic $H = B/\mu$ fields should be continuous across the boundaries from one medium to another one. There is no surface current for continuous B.

For p-polarisation incident waves in Figure 3.5(b), at boundary I we can have

$$E_I = E_{iI} \cdot cos\theta_{iI} - E_{rI} \cdot cos\theta_{iI} = E_{tI} \cdot cos\theta_{iII} - E'_{rII} \cdot cos\theta_{iII} \tag{3.17}$$

and

$$H_I = \sqrt{\frac{\epsilon_0}{\mu_0}} \cdot N_0 \cdot (E_{iI} + E_{rI}) = \sqrt{\frac{\epsilon_0}{\mu_0}} \cdot N_1 \cdot (E_{tI} + E'_{rII}) \tag{3.18}$$

Where use is made of the fact that E and H in nonmagnetic media are related through the complex refractive index and the unit propagation vector:

$$H = \sqrt{\frac{\epsilon_0}{\mu_0}} N \cdot \hat{k} \times E \tag{3.19}$$

At boundary II

$$E_{II} = E_{iII} \cdot cos\theta_{iII} - E_{rII} \cdot cos\theta_{iII} = E_{tII} \cdot cos\theta_{tII} \tag{3.20}$$

and

$$H_{II} = \sqrt{\frac{\epsilon_0}{\mu_0}} \cdot N_1 \cdot (E_{iII} + E_{rII}) = \sqrt{\frac{\epsilon_0}{\mu_0}} \cdot N_s \cdot E_{tII} \tag{3.21}$$

Assuming the substrate has a complex refractive index N_s. Considering phase difference $k_0 h$ between the two interfaces, a wave that traverses the film once undergoes a shift in-phase of

$$k_0 h = k_0 \cdot \frac{2N_1 d \cdot cos\theta_{iI}}{2} \tag{3.22}$$

where k_0 is wavenumber in vacuum: $k_0 = 2\pi/\lambda$, h is the optical path difference, d is the thickness of film, N_1 is the complex refractive index of the film and θ_{iI} is the angle inside the film. So that

$$\begin{aligned} E_{iII} &= E_{tI} \cdot e^{-ik_0 h} \\ E_{rII} &= E'_{rII} \cdot e^{ik_0 h} \end{aligned} \tag{3.23}$$

Then, equations 3.20 and 3.21 for boundary II can now be written as

$$E_{II} = cos\theta_{iII} \cdot (E_{tI} \cdot e^{-ik_0 h} - E'_{rII} \cdot e^{ik_0 h}) \tag{3.24}$$

and

$$H_{II} = \sqrt{\frac{\epsilon_0}{\mu_0}} \cdot N_1 \cdot (E_{tI} \cdot e^{-ik_0 h} + E'_{rII} \cdot e^{ik_0 h}) \tag{3.25}$$

These last two equations can be solved for E_{tI} and E'_{rII},

$$E_{tI} = 1/2 \cdot e^{ik_0 h}(\frac{E_{II}}{cos\theta_{iII}} + \frac{H_{II}}{\sqrt{\frac{\epsilon_0}{\mu_0}} \cdot N_1}) \tag{3.26}$$

and

$$E'_{rII} = 1/2 \cdot e^{-ik_0 h}(\frac{H_{II}}{\sqrt{\frac{\epsilon_0}{\mu_0}} \cdot N_1} - \frac{E_{II}}{cos\theta_{iII}}) \tag{3.27}$$

which are then substituted into equations 3.17 and 3.18, yielding

$$E_I = E_{II} \cdot cosk_0 h + \frac{H_{II} \cdot cos\theta_{iII}}{\sqrt{\frac{\epsilon_0}{\mu_0}} \cdot N_1} \cdot i \cdot sink_0 h \tag{3.28}$$

and

$$H_I = E_{II} \cdot \frac{\sqrt{\frac{\epsilon_0}{\mu_0}} \cdot N_1}{cos\theta_{iII}} \cdot i \cdot sink_0 h + H_{II} \cdot cosk_0 h \tag{3.29}$$

Then, we defined

$$Y_1 = \sqrt{\frac{\epsilon_0}{\mu_0}} \cdot \frac{N_1}{cos\theta_{iII}} \tag{3.30}$$

When E is perpendicular to the incidence plane, which means the incident beam is $s-$ polarisation waves as described in Figure 3.5(a), the above calculations result in similar equations, which have been published in Hecht's *Optics*[93], provided that Y_1 should be defined as

$$Y_1 = \sqrt{\frac{\epsilon_0}{\mu_0}} \cdot N_1 \cdot cos\theta_{iII} \tag{3.31}$$

In matrix notation, the above linear relations for $p-$ polarisation waves can take the form

$$\begin{bmatrix} E_I \\ H_I \end{bmatrix} = \begin{bmatrix} \cos k_0 h & (i \sin k_0 h)/Y_1 \\ Y_1 i \sin k_0 h & \cos k_0 h \end{bmatrix} \cdot \begin{bmatrix} E_{II} \\ H_{II} \end{bmatrix} \tag{3.32}$$

or

$$\begin{bmatrix} E_I \\ H_I \end{bmatrix} = M_I \cdot \begin{bmatrix} E_{II} \\ H_{II} \end{bmatrix} \tag{3.33}$$

For the $s-$ polarisation waves, the matrix expression 3.32 is same as $p-$ polarisation waves. The *characteristic matrix* M_I relates the fields at two adjacent boundaries I and II. Therefore, if there are two overlaying films deposited on the substrate, there will be three boundaries or interfaces. Then, following above matrix expression 3.33 about two adjacent boundaries, we can have matrix M_{II} related to boundary II and III.

$$\begin{bmatrix} E_{II} \\ H_{II} \end{bmatrix} = M_{II} \cdot \begin{bmatrix} E_{III} \\ H_{III} \end{bmatrix} \tag{3.34}$$

Furthermore, the relation between boundary I and III can be build by premultiplying both sides of above expression by M_I. We obtain

$$\begin{bmatrix} E_I \\ H_I \end{bmatrix} = M_I \cdot M_{II} \cdot \begin{bmatrix} E_{III} \\ H_{III} \end{bmatrix} \tag{3.35}$$

Generally speaking, if number of layers is p deposited on a substrate, each layer has its own complex refractive index N_p and thickness d_p, then the first and the last boundaries are related by

$$\begin{bmatrix} E_I \\ H_I \end{bmatrix} = M_I \cdot M_{II} \cdots M_p \cdot \begin{bmatrix} E_{(p+1)} \\ H_{(p+1)} \end{bmatrix} \tag{3.36}$$

The characteristic matrix of the entire multilayer system is the resultant of the product (in the proper sequence) of the individual 2×2 matrices, that is,

$$M = M_I \cdot M_{II} \cdots M_p = \begin{bmatrix} m_{11} & m_{12} \\ m_{21} & m_{22} \end{bmatrix} \tag{3.37}$$

To see how all this fits together with measurements, we will derive expressions for the amplitude coefficients of reflection and transmission using above scheme. In terms of the boundary conditions equations 3.17, 3.18, 3.20 and 3.21, and the settings

$$Y_0 = \sqrt{\frac{\epsilon_0}{\mu_0}} \cdot \frac{N_0}{cos\theta_{tII}}$$

and

$$Y_s = \sqrt{\frac{\epsilon_0}{\mu_0}} \cdot \frac{N_s}{cos\theta_{tII}}$$

and

$$w = \frac{cos\theta_{iI}}{cos\theta_{tII}}$$

The Snell's law can be used to get relationship between incident angle and refractive angles:

$$N_0 sin\theta_{iI} = N_1 sin\theta_{iII} = N_s sin\theta_{tII}.$$

Then we can reformulate the equation 3.33 to obtain

$$\begin{aligned} w \cdot (1-r) &= m_{11} \cdot t + m_{12} \cdot t \cdot Y_s \\ Y_0 \cdot (1+r) &= m_{21} \cdot t + m_{22} \cdot t \cdot Y_s \end{aligned} \tag{3.38}$$

Where these definitions of reflection and transmission coefficients have been used

$$r = E_{rI}/E_{iI} \qquad t = E_{tII}/E_{iI} \ .$$

Consequently for the $p-$ polarised waves in Figure 3.5(b), we can have

$$r_p = \frac{w(m_{21} + m_{22}Y_s) - Y_0(m_{11} + m_{12}Y_s)}{w(m_{21} + m_{22}Y_s) + Y_0(m_{11} + m_{12}Y_s)} \tag{3.39}$$

$$t_p = \frac{2Y_0 w}{Y_0(m_{11} + m_{12}Y_s) + w(m_{21} + m_{22}Y_s)} \tag{3.40}$$

As for the $s-$ polarised waves in Figure 3.5(a), we can get r_s, t_s in the same procedure. But the settings are a little change. They are all listed as following.

$$r_s = \frac{Y_0 m_{11} + Y_0 Y_s m_{12} - m_{21} - Y_s m_{22}}{Y_0 m_{11} + Y_0 Y_s m_{12} + m_{21} + Y_s m_{22}} \tag{3.41}$$

$$t_s = \frac{2Y_0}{Y_0 m_{11} + Y_0 Y_s m_{12} + m_{21} + Y_s m_{22}} \tag{3.42}$$

Where

$$Y_0 = \sqrt{\frac{\epsilon_0}{\mu_0}} \cdot N_0 \cdot cos\theta_{iI} \qquad Y_s = \sqrt{\frac{\epsilon_0}{\mu_0}} \cdot N_s \cdot cos\theta_{tII}$$

In conclusion, to calculate either r or t for any configuration of films, we need only compute the characteristic matrices for each film layer, multiply them and then substitute the resulting matrix elements into the above final r, t equations. More information about $s-$ polarised waves can be found in Hecht Optics[93].

3.2.2.2 Example Illustration

As long as we can get reflection and transmission coefficients through the transfer matrix method calculations, the reflectance and transmittance can also be obtained using equations 3.9 and 3.10. Meanwhile, the ellipsometry parameter ρ can also be found through the ratio between $p-$ and $s-$ polarised reflection coefficient Eq 3.15, or by the ratio between $p-$ and $s-$ transmission coefficient Eq 3.16. In order to illustrate this

convenient calculation method, a thick crystalline silicon (C-Si) sample is used as *ambient/substrate* example firstly. This sample is considered to have parallel boundaries for front and rear surface and is immersed into air. Even though the main purpose of this transfer matrix method is used for analyse of multilayer structure sample, this method can also solve *ambient/substrate* structure samples. One way is just setting the thickness of top layer is zero, then *ambient/film/substrate* is converted to *ambient/substrate* configuration. Actually, this would return the amplitude coefficient equations of reflection and transmission back to the Fresnel equations. Another way is that we can also regard the C-Si sample as *air/C-Si/air* optical system. This would be much understandable referring to transfer matrix method. So we will use the second way to deal with optical problems of C-Si in this example illustration section.

Referring to complex refractive index of crystalline silicon from Aspnes and Studna's[120] experimental data, which is $N_{c-si} = 3.673 - i \cdot 0.005$ at incident beam wavelength $800nm$, we can make use of transfer matrix method to calculate other optical parameters. Firstly, according to the extinction coefficient $k = 0.005$ at $800nm$ light, the absorption coefficient would be $\alpha = 4\pi k/\lambda = 7.854 \times 10^2 cm^{-1}$ and the penetration depth should be $d_p = 1/\alpha = 13\mu m$. N.B. when $I_t/I_0 = 1/e \sim 37\%$, $\alpha d = 1$ from Beer's law

$$I_t = I_0 \cdot e^{-\alpha d}$$

and this depth $d_p = 1/\alpha$ is known as the penetration depth. Taking account of this depth, we assume there are two C-Si samples with different thickness. One $100\mu m$ is bigger than penetration depth and another one $10\mu m$ thickness is smaller than d_p. Then, the optical system should be *Ambient/C-Si/Ambient* structure. Using complex refractive index at $800nm$ light and thickness of C-Si, we can build the characteristic matrix to represent the optical property of C-Si layer. Then, the amplitude coefficients of reflection and transmission can be calculated using equations 3.39, 3.40 for $p-$ polarised waves and equations 3.41, 3.42 for $s-$ polarised waves.

All the left column of Figures 3.6 results are calculated under condition of $100\mu m$ thickness and all the right column of Figures 3.6 results are from $10\mu m$ sample. All of these Figures 3.6 are expressing the variations with incidence angle θ_{iI} from 0° to 90°. Figures 3.6(a) and 3.6(d), show the reflectance (R_s, R_p, R_{45°) variations for $s-, p-$ and 45° linear polarisation incident beam respectively. As we can see in Figure 3.6(a), when incident light is $s-$polarised, R_s is increasing with incident angle and reaching the maximum value at around 90°. While, R_p for $p-$ polarised waves, decreases to almost zero and then dramatically rises up to one with increasing angle. The reason for this minimum $R_p \approx 0$ can be explained from electric dipole radiation at a media interface[99]. In electric dipole radiation, no light radiation occurs toward the oscillating direction of

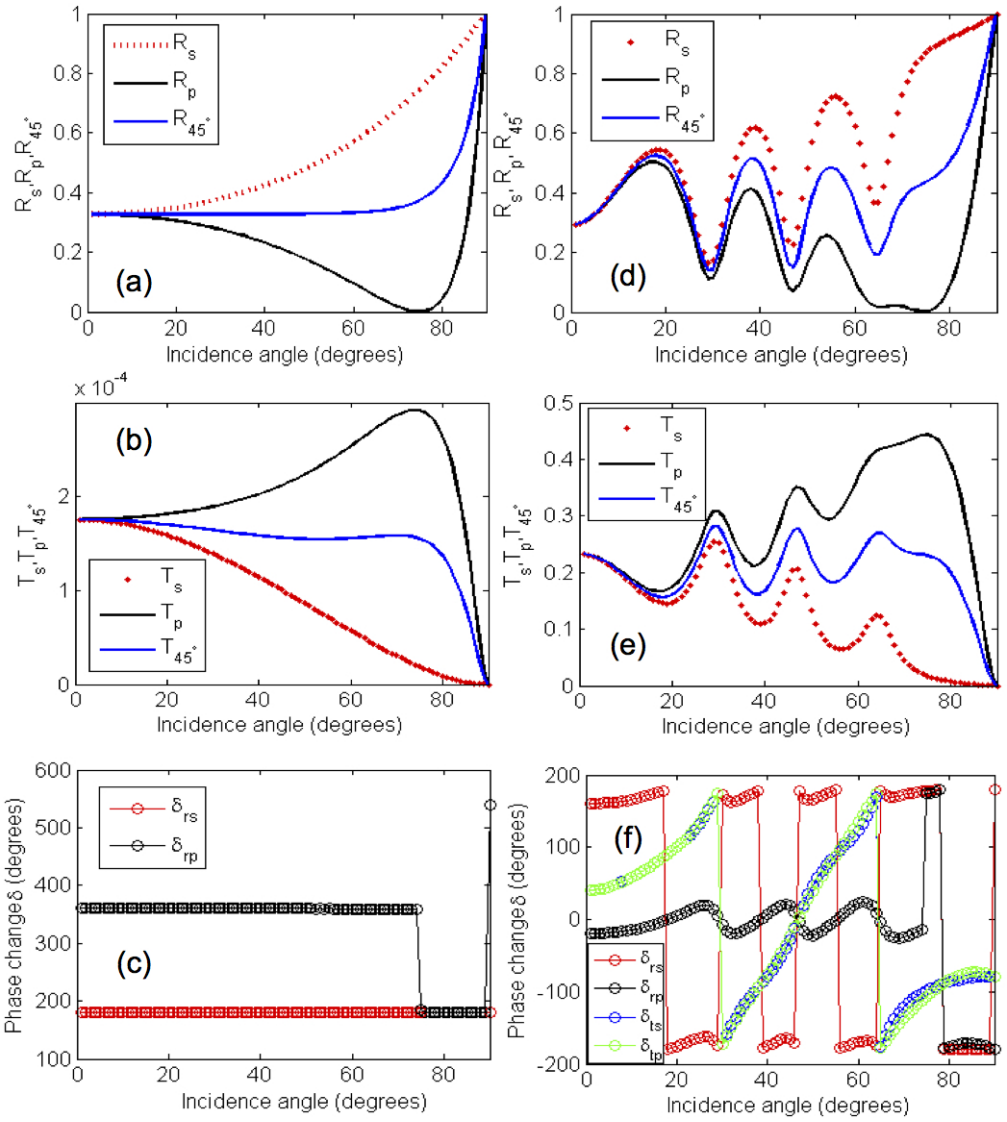

FIGURE 3.6: (a), (b) and (c) are reflectance transmittance and amplitude coefficient phase change respectively as function of incidence angle for $100\mu m$ thick c-Si; Similarly, (d), (e) and (f) are all for $10\mu m$ thick c-Si.

electric dipoles. When the oscillatory direction of electric dipoles near the interface in sample is parallel (perpendicular) to the propagating (vibrational) direction of reflected light, the reflected light would disappear. $p-$ polarised light is just in this condition when incident angle is around 75° for crystalline silicon material. This incidence angle is also known as the *Brewster angle* θ_B. As for the other semiconductor materials, the *Brewster angle* value would be different from C-Si and it depends on the dielectric constants of this material.

The transmittance T_s, T_p, T_{45° variations as function of incidence angle is shown in Figure 3.6(b). Obviously, the trend of transmittance (T_s, T_p, T_{45°) are opposite to the trend of reflectance (R_s, R_p, R_{45°) respectively. But the magnitude unit of transmittance is at 10^{-4}, which is quite smaller comparing to reflectance, and a detector can not detect the

transmitted intensity as accurately. So if the thickness of C-Si is bigger than the $100\mu m$, we definitely can consider it as substrate and Fresnel equations can be used to solve front interface optical problems quickly. Actually, we can also obtain the absorbance A according to energy conservation if we know the reflectance and transmittance simultaneously.

$$A + T + R = 1, \qquad A = \alpha \cdot l$$

And the relation between absorbance and absorption coefficient is also shown in above equation, where l is the light travel distance. From here, we can see most part of $800nm$ light is absorbed apart from the reflected light. From Figure 3.6(c), the phase shifts of reflection coefficients r_s and r_p are described as δ_{rs} and δ_{rp} with incidence angle. (Because the transmittance is so small and the phase shifts are same for t_s, t_p and irregularly vibrating between $-180°$ and $180°$, they are not given in this figure.) We can see that δ_{rs} is always at $180°$ at incidence angles from $0°$ to $90°$. This means C-Si can not influence $s-$ polarised light phase from reflection, even for the thinner C-Si sample with $10\mu m$ thickness in Figure 3.6(f). But the $p-$ polarised light phase shift δ_{rp} experiences a transition from $360°$ for $\theta_{iI} < \theta_B$ to $180°$ for $\theta_{iI} > \theta_B$ shown in Figure 3.6(c). These phase shifts δ_{rs}, δ_{rp} are correlated to the reflection ellipsometry parameter Δ and reflectance R_s, R_p are corresponding to the ψ in term of equations 3.14 and 3.13.

Until now all the basic optical parameters have been discussed for the $100\mu m$ thick c-Si. As for the $10\mu m$ c-Si calculations, we can see the results from all the right column of Figures 3.6, which are reflectance transmittance and amplitude coefficient phase change, separately changing with incidence angle from $0°$ to $90°$. Apparently, as the thickness $10\mu m$ is smaller than penetration depth $13\mu m$, the interference effect is visible in each right-hand column figure. This means a certain intensity of light is multiply reflected between the front and rear surfaces of c-Si. Thus, the destructive and constructive information is shown in the figures under different incidence angle (different optical length). Apart from the interference, the changing behaviours of reflectance and transmittance are still similar as the results of $100\mu m$ thick sample. R_s is gradually increasing, while R_p is slowly decreasing to minimum at around $75°$ and rising up again, which are shown in Figure 3.6(d). Similarity, $T_s, T_p, T_{45°}$ are all opposite to reflectance as shown in Figure 3.6(e). Finally we can discuss the amplitude coefficients phase change $\delta_{rs}, \delta_{rp}, \delta_{ts}, \delta_{tp}$ for $10\mu m$ thick c-Si, which are shown in Figure 3.6(f). Even though δ_{rs} experiences jumping from $180°$ to $-180°$ several times, the phase actually is keeping the same status with respect to spanning incidence angle due to period $360°$. As for δ_{rp}, there is also a $180°$ phase change at around $75°$ incidence angle. δ_{ts} and δ_{tp} are always same and both experiencing $360°$ phase change over the range of incidence angles.

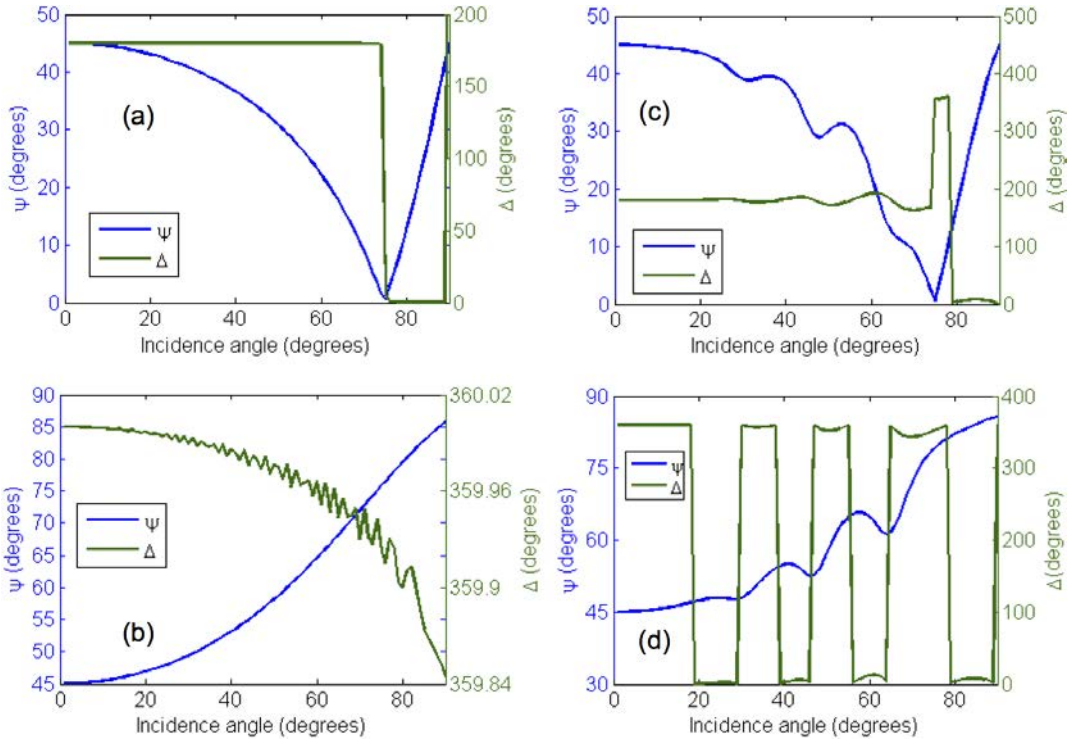

FIGURE 3.7: (a) and (c) are Reflection ellipsometry results (ψ, Δ) changing with incidence angle for $100\mu m$ and $10\mu m$ thick c-Si, respectively; (b) and (d) are transmission ellipsometry data for $100\mu m$ and $10\mu m$ c-Si separately.

Then, the ellipsometry parameters (ψ, Δ) can be derived from the two definitions Equations 3.15 and 3.16: reflection $\rho_r = r_p/r_s$ and transmission $\rho_t = t_p/t_s$ ellipsometry. As shown in Figures 3.7, the left column figures are the reflection and transmission ellipsometry parameters changing with incident angle for $100\mu m$ thick c-Si and the right column figures are for $10\mu m$ c-Si. From reflection ellipsometry results in Figures 3.7(a) and (c), the changing trend is similar with each other. The only difference is the data curves of $10\mu m$ c-Si (c) are not as smooth as $100\mu m$ c-Si (a). One also should note the phase difference Δ between δ_{rp} and δ_{rs} jumps 180° at Brewster incident angle 75°, while ψ experiences a minimum value. Since the difference between r_p and r_s is maximised under this angle θ_B, the sensitivity of ellipsometry measurement is higher under this angle. This is also the reason that ellipsometry measurement is generally performed at the Brewster angle. As for the transmission ellipsometry data, which are described in Figures 3.7(b) and (d), ψ for both samples are gradually increasing from 45° to around 85°. This means the ratio between $|t_p|$ and $|t_s|$ is increasing with rising incidence angle, while the phase difference Δ between δ_{tp} and δ_{ts} is keeping at 0° or 360°. There is no particular variation at Brewster angle for transmission ellipsometry data. Consequently, most of ellipsometry measurements are performed under reflection to utilise Brewster angle and improve the measurement sensitivity.

In summary, we discussed the transfer matrix approach for simulating the basic *ambient/layer/substrate* optical system and illustrated the intrinsic relationships between reflectance transmittance and ellipsometry. The relationship between ellipsometry parameter ρ and experimental conditions can be written as following equation:

$$tan\psi \cdot e^{i\Delta} = \rho(N_0, N_1, N_s, d, \lambda, \theta_{iI}). \tag{3.43}$$

Subsequently, the amplitude and phase components can be split and represented by following equations:

$$\psi = tan^{-1}|\rho(N_0, N_1, N_s, d, \lambda, \theta_{iI})|, \qquad \Delta = arg[\rho(N_0, N_1, N_s, d, \lambda, \theta_{iI})]. \tag{3.44}$$

where $|\rho|$ and $arg(\rho)$ are the absolute value and argument (angle), respectively. Furthermore, it is worth to mention that ρ actually depends on no less than nine arguments: the real and imaginary components of all the three complex refractive indexes (N_0, N_1, N_s), the film thickness d, the incident beam wavelength λ, and the incidence angle θ_{iI}. If the sample structure includes more than one layer, the characteristic matrix of each layer need to be multiplied firstly. Then, the same processes discussed in the above sections can be used to solve out the relevant optical questions. Meanwhile, ellipsometry parameter ρ will depend on more parameters. Anyway, this analysis method is very useful in the simulating experimental data procedure, which will be applied in the following sections. In this thesis, we applied the 45° linear polarised light waves as incident beam for ellipsometry measurements, which can provide equal amplitude components and same initial phase for $s-$ and $p-$ polarised direction. This is also convenient to process ellipsometry measurement data, which will be discussed in detail in the following sections. However, the above theory is based on that the ambient, film and substrate are all homogeneous and optically isotropic structures. If the film is anisotropic, the above theory will not be totally useful any more and some changes need to be considered. As our research samples can be all considered as isotropic structure, so we only confine the theoretical problems for this region. We need to mention that the optical constant of the parallel to PS surface direction, which can be effectively uniform in $x - y$ plane, may be different from that of the perpendicular to surface in z direction.

3.2.3 Ellipsometry Measurement Techniques

Based on the transfer matrix approach, we discussed the calculations of reflectance transmittance and ellipsometry. In this section, we will illustrate the measurement techniques about acquiring the experimental data. As for the spectroscopic reflectance and transmittance measurement techniques, they are quite simple and have been introduced in

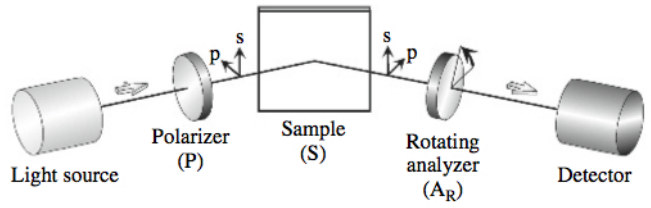

(a)

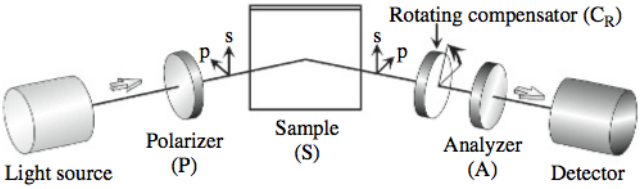

(b)

FIGURE 3.8: Optical configuration of ellipsometry instruments: (a) the rotating analyser ellipsometry (RAE), (b) the rotating compensator ellipsometry (RCE). The Figures and Caption are from[99].

the beginning of this chapter. However, the spectroscopic ellipsometry (SE) technique is not discussed until now. This section contains the further information about how to exactly carry on ellipsometry measurement. In order to simplify the explanation, only reflection ellipsometry is considered in this section. Generally speaking, two kinds of ellipsometry setup are often applied to acquire (ψ, Δ) from a sample and will be introduced one by one in this section. The first one is the simplest and most widely used up to now, rotating analyser ellipsometer (RAE). As shown in Figure 3.8(a), the setup of RAE is composed of light source, polariser (P), sample (S), rotating analyser (A_R) and detector. The symbol PSA_R is used to denote this ellipsometer configuration. The second one is more sophisticated and special for the samples with small extinction coefficients: Rotating compensator ellipsometer (RCE), which is depicted in Figure 3.8(b). The configuration of this ellipsometer includes light source, polariser (P), sample (S), rotating compensator (C_R), analyser (A) and detector. The configuration difference between RAE and RCE setup is obviously shown in the Figure 3.8. When looking against the direction of the beam (looking down the propagation axis toward the origin), the counterclockwise rotation is the positive direction for the optical elements[99]. This definition is very important for analysing (ψ, Δ). Meanwhile, we will see later in this section, ellipsometry basically measures the Stokes parameters (vector) of reflected light waves[104]. The Stokes vector $S = [S_0; S_1; S_2; S_3]$ enables us to describe all types of polarisation, including unpolarised or partially polarised light. The definition of Stokes vector can be seen in Appendix A.1.

Aspnes *et al.* in 1975[121] perfected the RAE system and obtained the optical constants

Optical Element	Symbol	Jones Matrix
polariser (analyser)	P or A	$\begin{bmatrix} 1 & 0 \\ 0 & 0 \end{bmatrix}$
Compensator (Retarder)	C	$\begin{bmatrix} 1 & 0 \\ 0 & e^{-i\delta} \end{bmatrix}$
Coordinate rotation	R(α)	$\begin{bmatrix} cos\alpha & sin\alpha \\ -sin\alpha & cos\alpha \end{bmatrix}$
Sample	S	$\begin{bmatrix} sin\psi e^{i\Delta} & 0 \\ 0 & cos\psi \end{bmatrix}$

TABLE 3.1: Jones matrices for optical elements and coordinate rotation.

of some important materials[120] using this method. However, there is also a drawback that the Stokes parameter S_3 can not be measured in a RAE ellipsometer. When all the Stokes parameters can not be confirmed, the measurement ranges for (ψ, Δ) are restricted. S_3 is not measured and thus measurement range of RAE becomes half ($0° \leq \Delta \leq 180°$) of the full range ($-180° \leq \Delta \leq 180°$). In order to overcome this disadvantage of RAE system, a compensator (quarter wave plate $\lambda/4$) is added into the RAE system between sample and analyser to get rotating analyser ellipsometer with compensator[122–124]. However, if we continue to rotate the analyser, two measurements with different angles setting of the compensator are necessary to obtain all the Stokes parameters. So, rotating compensator ellipsometry (RCE) is the better choice, which is shown in Figure 3.8(b), instead of rotating analyser. The RCE instrument was reported first by Hauge *et al.* in 1975[125]. In RCE, (ψ, Δ) measurement can be performed over the full range since the Stokes parameters can all be obtained from a single measurement.

3.2.3.1 Rotating Analyser Ellipsometry (RAE)

Using Jones (or Mueller) matrices to express the ellipsometry measurement, it can be easy to see the fundamental theory of the ellipsometry technique. These matrices are used to systematically describe the polarisation state of light and the optical elements effect on light's polarisation state. Due to the interaction between the optical elements and light waves in ellipsometry measurement, we apply the simplest Jones matrix formulations[126] to represent the ellipsometry configuration. Table 3.1 summaries the Jones matrix formulation for different optical elements, and a coordinate rotation, with 2×2 matrices. For the compensator, if it is a quarter wave plate , $\delta = \pi/2$. Applying

these symbols of the Jones matrices shown in Table 3.1, the RAE instrument with PSA_R configuration can be expressed as

$$L_{out} = A \cdot R(A) \cdot S \cdot R(-P) \cdot P \cdot L_{in} \tag{3.45}$$

where L_{out} stands for the Jones vector of the detected light by a detector and is given by $L_{out} = \begin{bmatrix} E_A \\ 0 \end{bmatrix}$. L_{in} is the normalised Jones vector corresponding to incident light ($L_{in} = \begin{bmatrix} 1 \\ 0 \end{bmatrix}$). Then, light is transmitting through a polariser, denoted by P. Here, we need to consider a coordinate direction as reference coordinate. Normally, this reference coordinate is defined $x-$ direction as parallel to incident plane, $p-$ polarised direction, and $y-$ direction as perpendicular to incident plane, $s-$ polarised direction, which can be seen in Figure 3.8. Then, as polariser angle is set to P, so we need to rotate the incident light as $R(P)$ firstly. Then, we can multiply the polariser Jones matrix to represent transmitting though polariser. After transmitting, we still need to return the coordinate back to the reference coordinate one, so we multiply $R(-P)$. After interacting with the sample, the polarisation state of reflected light will be changed by Jones matrix S comparing to the incident light. Because the sample defines the incidence plane, which is the same as the reference coordinate, the rotation matrix is not multiplied at here. Finally, the polarisation state of reflected light should be rotated to analyser angle by coordinate rotation matrix $R(A)$ and the light is transmitting though analyser A. After going through analyser, we still need to return the coordinate to the reference coordinate one by $R(-A)$. However, we consider that only the light transmitted though the polariser is taken into account, so the term $R(P)$ can be eliminated from $R(-P)PR(P)$. Similarly, the intensity of light transmitted through the analyser is detected, which is independent on the coordinate rotation. Moreover, a rotation matrix only changes the orientation of the polarised state and does not change the intensity, so $R(-A)$ is also removed from $R(-A)AR(A)$. Using matrix representation, Equation 3.45 can be rewritten as

$$\begin{aligned} \begin{bmatrix} E_A \\ 0 \end{bmatrix} = \begin{bmatrix} 1 & 0 \\ 0 & 0 \end{bmatrix} \cdot \begin{bmatrix} cosA & sinA \\ -sinA & cosA \end{bmatrix} \cdot \begin{bmatrix} sin\psi e^{i\Delta} & 0 \\ 0 & cos\psi \end{bmatrix} \\ \cdot \begin{bmatrix} cosP & -sinP \\ sinP & cosP \end{bmatrix} \cdot \begin{bmatrix} 1 & 0 \\ 0 & 0 \end{bmatrix} \cdot \begin{bmatrix} 1 \\ 0 \end{bmatrix} \end{aligned} \tag{3.46}$$

When $P = 45°$ provides $45°$ linear polarised incident beam, the equation 3.46 is simplified to

$$\begin{bmatrix} E_A \\ 0 \end{bmatrix} = \begin{bmatrix} 1 & 0 \\ 0 & 0 \end{bmatrix} \cdot \begin{bmatrix} cosA & sinA \\ -sinA & cosA \end{bmatrix} \cdot \begin{bmatrix} sin\psi e^{i\Delta} \\ cos\psi \end{bmatrix} \tag{3.47}$$

Neglecting the proportionality term $1/\sqrt{2}$, expansion of equation 3.47 can express the transmitted light amplitude as

$$E_A = cosA \cdot sin\psi \cdot e^{i\Delta} + sinA \cdot cos\psi \tag{3.48}$$

Finally, we can obtain the light intensity measured by a detector as

$$\begin{aligned} I &= |E_A|^2 = I_0(1 - cos2\psi cos2A + sin2\psi cos\Delta sin2A) \\ &= I_0(1 + S_1 cos2A + S_2 cos2A) \end{aligned} \tag{3.49}$$

where I_0 is the proportional constant of reflected light, and the reflected light is proportional to incident light intensity. Meanwhile, the Stokes parameters can be given as:

$$S_1 = -cos2\psi \qquad S_2 = sin2\psi cos\Delta \tag{3.50}$$

we can also see the Stokes parameters S_1 and S_2 are measured as the Fourier coefficients of $cos2A$ and $sin2A$[127]. The light intensity can vary as a function of the analyser angle $2A$ shown in equation 3.49. This means 180° rotation of the analyser corresponds to one optical cycle rotation, and the drawback of RAE originates from this point.

3.2.3.2 Rotating Analyser Ellipsometry with Compensator

As we discussed in Equation 3.49, the Stoke parameter S_3 can not be determined by RAE measurements and the range of Δ is also restricted to $0° \leq \Delta \leq 180°$. The measurement error will become very big at boundary of Δ range: $\Delta \cong 0°$ and 180°. Roseler[122, 123] proposed that adding a compensator into RAE setup allows one to overcome these problems. Using Jones matrixes in Table 3.1, RAE with compensator in $PSCA_R$ configuration can be described as follows:

$$L_{out} = A \cdot R(A) \cdot R(-C) \cdot C \cdot R(C) \cdot S \cdot R(-P) \cdot P \cdot L_{in} \tag{3.51}$$

In order to simplify the equation, we have set the compensator angle to $C = 90°$. This means the fast axis of compensator is chosen in the direction of s-polarisation, which is perpendicular to the incident plane referring to Figure 3.8(b). Moreover, the phase shift of compensator δ is related with compensator angle C and incident beam wavelength λ. Here, we set the polarisation angle as $P = 45°$ and Equation 3.51 is simplified to

$$\begin{aligned} \begin{bmatrix} E_A \\ 0 \end{bmatrix} &= \begin{bmatrix} 1 & 0 \\ 0 & 0 \end{bmatrix} \cdot \begin{bmatrix} cosA & sinA \\ -sinA & cosA \end{bmatrix} \cdot \begin{bmatrix} e^{-i\delta} & 0 \\ 0 & 1 \end{bmatrix} \cdot \begin{bmatrix} sin\psi e^{i\Delta} \\ cos\psi \end{bmatrix} \\ &= \begin{bmatrix} 1 & 0 \\ 0 & 0 \end{bmatrix} \cdot \begin{bmatrix} cosA & sinA \\ -sinA & cosA \end{bmatrix} \cdot \begin{bmatrix} sin\psi e^{i(\Delta-\delta)} \\ cos\psi \end{bmatrix} \end{aligned} \tag{3.52}$$

Compared to equation 3.47, we can notice that the compensator only introduces a shift value δ on Δ without any effect on ψ. This also means the compensator does not influence the amplitude ratio between $p-$ and $s-$ polarised reflected light, but it can change the phase difference between them. Therefore, the final expression for RAE with compensator configuration, I, can be described simply replacing Δ in Equation 3.49 with $\Delta^{'} = \Delta - \delta$. Then, we can obtain

$$I = I_0[1 + S_1 cos2A + (S_2 cos\delta - S_3 sin\delta) sin2A] \tag{3.53}$$

where the Stoke parameter S_3 can be obtained finally as

$$S_3 = -sin2\psi sin\Delta \tag{3.54}$$

Eventually, the determination of all the Stoke parameters S_{1-3} becomes possible when inserting a compensator into RAE setup. Apparently, the two components S_1 and $(S_2 cos\delta - S_3 sin\delta)$ are measured as Fourier coefficients in this technique. To resolve S_2 and S_3 separately, it is necessary to perform more than two measurements with different δ values. We will use quarter wave plate $\lambda/4$ as the compensator in the experiment. So it can produce the phase shift $\delta = 90°$ when the incident polarised light is oriented at 45°, and $\delta = 0°$ when the fast or slow axis of compensator is parallel to the direction of polarised light. Consequently, $\delta = 0°$ at $P = C = 45°$ and $\delta = 90°$ at $P = 45°$ and $C = 90°$. This is convenient so that we can obtain S_2 when $\delta = 0°$ and S_3 when $\delta = 90°$ referring to Equation 3.53.

3.2.3.3 Rotating Compensator Ellipsometry (RCE)

Even though we can get all the Stoke parameters S_{1-3} applying $PSCA_R$ configuration ellipsometry, we still need to do twice measurements with setting different angles of compensator. Actually, we can simplify to only once measurement when rotating the compensator instead of analyser. This RCE instrument configuration PSC_RA can be expressed as following using Jones matrixes.

$$L_{out} = A \cdot R(A) \cdot R(-C) \cdot C \cdot R(C) \cdot S \cdot R(-P) \cdot P \cdot L_{in} \tag{3.55}$$

In order to simplify the above equation, we set polariser and analyser angles to be $P = 45°$ and $A = 0°$ and incident light is also expressed as $L_{in} = \begin{bmatrix} 1 \\ 0 \end{bmatrix}$. So, Equation 3.55

can be expanded as following:

$$\begin{bmatrix} E_A \\ 0 \end{bmatrix} = \begin{bmatrix} 1 & 0 \\ 0 & 0 \end{bmatrix} \cdot \begin{bmatrix} cosC & -sinC \\ sinC & cosC \end{bmatrix} \cdot \begin{bmatrix} 1 & 0 \\ 0 & e^{-i\delta} \end{bmatrix} \cdot \begin{bmatrix} cosC & sinC \\ -sinC & cosC \end{bmatrix} \cdot \begin{bmatrix} sin\psi e^{i\Delta} \\ cos\psi \end{bmatrix} \tag{3.56}$$

As for the compensator C, the rotating zero position is when the fast axis is parallel to the incident plane. The proportionality constant is also eliminated. So, we can get the final electric field amplitude as following by substituting $\delta = 90°$ into the above matrix equation.

$$E_A = (cos^2C - isin^2C)sin\psi e^{i\Delta} + (1+i)cosCsinCcos\psi \tag{3.57}$$

With the helping of Maple software, we can obtain the light intensity formula as following (derivation in appendix A.1), which has also been deduced by Hauge[104, 125].

$$I = I_0(2 + S_1 - 2S_3 sin2C + S_1 cos4C + S_2 sin4C) \tag{3.58}$$

Evidently, if the intensity is measured as a function of rotating the compensator angle C, S_{1-3} can be determined from the Fourier coefficients. The determination of all the Stokes parameters can give a complete description for the polarised state of light waves[93]. Considering this advantage and simply one measurement to acquire (ψ, Δ), we built a RCE setup in our lab to do the ellipsometry and pump-probe spectral ellipsometry for researching ultrafast dynamics property of samples.

Even though we can easily obtain all the Stokes parameters though RCE detection, the purpose of ellipsometry is to realise (ψ, Δ) of the sample. So, we will introduce a convenient method to get (ψ, Δ) from RCE measurement data according to Boer's work[128]. Generally, Equation 3.58 can be reformulated by a general formula[101, 104, 125, 128] :

$$I(C) = A_0 + A_2 cos2C + B_2 sin2C + A_4 cos4C + B_4 sin4C \tag{3.59}$$

This equation obviously illustrates that the intensity is contributed by second and fourth order harmonic oscillation in the compensator azimuth angle C. The Fourier coefficients $A_0 - B_4$ are given by

$$\begin{aligned} A_0 &= \tfrac{1}{\pi}\int_0^\pi I(C)dC \\ A_2 &= \tfrac{2}{\pi}\int_0^\pi I(C)cos2CdC \\ B_2 &= \tfrac{2}{\pi}\int_0^\pi I(C)sin2CdC \\ A_4 &= \tfrac{2}{\pi}\int_0^\pi I(C)cos4CdC \\ B_4 &= \tfrac{2}{\pi}\int_0^\pi I(C)sin4CdC. \end{aligned} \tag{3.60}$$

Further calculation of these Fourier coefficients can be correlated with ellipsometry parameters (ψ, Δ),

$$\begin{aligned} A_0 &= 1 - cos2Pcos2\psi + \tfrac{1}{2}[cos2A(cos2P - cos2\psi) + sin2Asin2Psin2\psi cos\Delta] \\ A_2 &= -sin2Asin2Psin2\psi sin\Delta \\ B_2 &= cos2Asin2Psin2\psi sin\Delta \\ A_4 &= \tfrac{1}{2}[cos2A(cos2P - cos2\psi) - sin2Asin2Psin2\psi cos\Delta] \\ B_4 &= \tfrac{1}{2}[cos2Asin2Psin2\psi cos\Delta + sin2A(cos2P - cos2\psi)]. \end{aligned} \tag{3.61}$$

Then, we still choose the standard setting for RCE detection, in which the polariser angle $P = 45°$ and the analyser angle $A = 0°$ are set to simplify the equations. N.B. $A = 0°$ means the transmission axis of analyser is in the incident plane. So the Equations 3.61 can be simply expressed as

$$\begin{aligned} A_0 &= 1 - \tfrac{1}{2}cos2\psi \\ A_2 &= 0 \\ B_2 &= sin2\psi sin\Delta \\ A_4 &= -\tfrac{1}{2}cos2\psi \\ B_4 &= \tfrac{1}{2}sin2\psi cos\Delta. \end{aligned} \tag{3.62}$$

In the above calculations, we neglect the non ideal behaviour of compensator, which will lead to the errors for the final results. In the following sections, we will focus to reduce the errors and introduce the calibration of RCE system. Obviously, (ψ, Δ) can be found from the above expressions. As we consider that the A_2 would be close to zero for an ideal compensator and applying this coefficient to solve for (ψ, Δ) will therefore introduce large errors. A_0 (the DC component of the intensity) may contain the interference from external light source, so it is also better to avoid this one. Moreover, there is no absolute intensity measured in ellipsometry[128]. Thus we can not determine the absolute values of the Fourier coefficients. Eventually, only the ratio of the Fourier coefficients is more useful for solving the parameters ψ and Δ. Hence, B_2 and B_4 will be scaled to A_4, and two intermediate parameters X_1 and X_2 are introduced, to allow the parameters ψ and Δ can be exactly obtained from the experimental data, as shown in Equations 3.63 and 3.64.

$$\begin{aligned} X_1 &= tan2\psi sin\Delta = -\tfrac{1}{2}\tfrac{B_2}{A_4} \\ X_2 &= tan2\psi cos\Delta = -\tfrac{B_4}{A_4} \end{aligned} \tag{3.63}$$

Consequently, the ellipsometry parameters (ψ, Δ) can be described as

$$\begin{aligned} tan2\psi &= \sqrt{X_1^2 + X_2^2} \\ tan\Delta &= X_1/X_2 \end{aligned} \tag{3.64}$$

Since the value of ψ is determined from a square root and the arctan function returns only values between $-90°$ and $+90°$, the exact values of ψ and Δ have to be determined using

$A_4 > 0 \Rightarrow \psi_2 = 90° - \psi_1$	
$A_4 < 0 \Rightarrow \psi_2 = \psi_1$	
$B_4 > 0 \Rightarrow \Delta_2 = \Delta_1$	$\Delta_2 < 0 \Rightarrow \Delta_3 = \Delta_2 + 360°$
$B_4 < 0 \Rightarrow \Delta_2 = \Delta_1 + 180°$	$\Delta_2 > 0 \Rightarrow \Delta_3 = \Delta_2$

TABLE 3.2: To determine the correct values of ψ and Δ, the signs of Fourier coefficients A_4 and B_4 are required. The sub-indices used in conjunction with ψ and Δ indicate the step in the procedure, e.g. 1 indicates the original value as obtained from equation 3.64, 2 indicates the sign after considering the sign of the Fourier coefficient, etc. The Table and Caption are from[128].

sign information from the Fourier coefficients[128]. This procedure has been proposed by Boer *et. al.*[128] to correct the ellipsometry parameters (ψ, Δ). Table 3.2 is the summary for correction. Due to both parameters (ψ, Δ) having tangent dependence, there are no regions in the $\psi - \Delta$ plane losing accuracy[22, 128].

In conclusion, we introduced the main measurement techniques of ellipsometry. Meanwhile, some disadvantages and advantages of different ellipsometry setups are also illustrated. Comparing to each other, the rotating compensator ellipsometry (RCE) setup can be the best choice for our lab to obtain all the Stokes parameters in once measurement. More importantly, how to deduce the ellipsometry angles (ψ, Δ) from the detected intensity as a function of the compensator angle is described in the final process. In the pump probe techniques, we will combine this RCE setup with pump beam to build the pump probe spectra ellipsometry instrument. Using this instrument will reveal more informations about ultrafast dynamics property of samples.

3.3 Optical Model

The measurement techniques about reflection transmission and ellipsometry have all been introduced in the above sections. The transfer matrix approach is also detailed for simulation. However, the main point of these techniques and simulation methods is to obtain the complex refractive index of the researched material. Even though we mentioned that the complex refractive indexes of some transparent slabs can be determined through reflectance and transmittance measurements, this is not suitable for all the samples. Generally, if we want to obtain the complex refractive index of a material in a spectral range, we need to apply the optical model to fit the measurement data. Then, from the fitting parameters, we can evaluate the complex refractive index or dielectric constant. Basically, the complex refractive index is determined from dielectric polarisation generated in a medium[99]. The dielectric polarisation represents the phenomenon that external electric fields separate electric charges in a medium spatially[99]. The optical constant is used to describe the macroscopic response of a material distorted by

external electric field. This disturbance could separate the positive and negative charges to opposite directions inside the material, but the chemical bond will still hold these opposite charges. Then, the vibration will occur due to external force and internal force. So, the microstructure of a material is a crucial factor to determine the response from the external electromagnetic field. Meanwhile, if the frequency (or wavelength) of electric field is changed, the response of a material will also change. Generally, optical constants depend on the structure of the material and the frequency of external electromagnetic field (light).

There are a number of diagnostic methods to measure the structure of a material, including X-ray diffraction, Raman spectroscopy, scanning electron microscopy, atomic force microscopy etc. From these measurements, we can realise what the chemical element of this material, study the surface of the material and discover how many different phases are in a composite. We can also see the volume fraction of each structure phase or component. Once the basic structure information has been determined, the corresponding dispersion relation model needs to be used to simulate the optical property of this material in a certain spectral range. In order to realise the dielectric function of hydrogenated nano-crystalline silicon (nc-Si:H) and porous silicon (PS), we will introduce the related dispersion models in the following sections.

3.3.1 Dispersion Relations

The hydrogenated nano-crystalline silicon (nc-Si:H) sample is composed of three layers with a c-Si substrate. The configuration is *air/SiO_2/nc-Si:H/SiO_2/C-Si*. The SiO_2 layer is deposited on the C-Si substrate, and the top surface of nc-Si:H layer is natively oxidised to have a thin $\sim 10nm$ SiO_2 film. To simplify the analysis, the optical constants of silicon oxide material (SiO_2) are normally simulated by the classical Lorentz oscillator model in the visible spectral range.

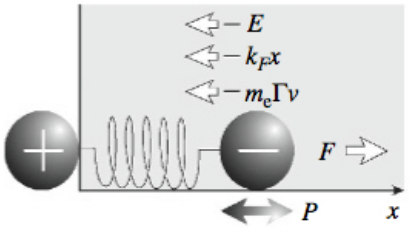

FIGURE 3.9: Physical image of Lorentz model: Distortion of a negative charge with respect to a positive charge in response to an applied E field. The Figure and Caption are from[99].

As we can see in Figure 3.9, Lorentz model can be explained as a simple forced and damped harmonic oscillator. In the electric polarisation shown in Figure 3.9, a negative charged electron is bound to a positive charged atomic nucleus with a spring, which expresses an attractive electric force sustains the oscillator in some sort of equilibrium configuration. This attractive force is formulated by Hooke's law $F = -k_F \cdot x$. When the light is used to disturb the system, the electron bound will oscillate at around its equilibrium position with a resonant frequency given by $\omega_0 = \sqrt{k_F/m_e}$, where m_e is its mass. As the lightwaves impinge on such system, the time varying electric field $E(t) = E_0 \exp(i\omega t)$ will induce the oscillator to be driven in the x-direction. Because the mass of the atomic nucleus is far larger than that of the electron, the position of the nucleus is considered to be fixed. According to Newton's second law, the electron movement in this physical model can be expressed as

$$m_e \frac{d^2x}{dt^2} = -m_e \Gamma \frac{dx}{dt} - m_e \omega_0^2 x - eE_0 \exp(i\omega t) \tag{3.65}$$

where e is the charge of electron and ω is the angular frequency of incident light. Moreover, we also regard the electron as oscillating in a viscous fluid, and the first damping term on the right represents the viscous force. The Γ represents a proportional constant of this viscous force to the speed of the electron's motion. This inclusion of damping is a consequence of the fact that the oscillating dipoles can lose their energy by collisional processes[83]. The second term is mentioned as the restortion force and the third term is the electric driving force $F = qE$ by external light disturbance. Assuming a solution of Equation 3.65 is described by the form $x(t) = a \exp(i\omega t)$, the solution can be found by substituting this assumption into the equation:

$$a = -\frac{eE_0}{m_e} \cdot \frac{1}{(\omega_0^2 - \omega^2) + i\Gamma\omega} \tag{3.66}$$

Considering the unit volume, the number of electrons should be given as N_e and the dielectric polarisation can be expressed as $P = -eN_e x(t)$. And dielectric constant is correlated to dielectric polarisation as $\epsilon = 1 + \chi + P/(\epsilon_0 E)$, where the electric susceptibility χ accounts for all other contributions to the polarisability of the atoms apart from the resonant polarisation. Finally, the dielectric function of Lorentz model is as following[83, 99, 129]:

$$\epsilon = \epsilon_\infty + \frac{(\epsilon_s - \epsilon_\infty)\omega_0^2}{(\omega_0^2 - \omega^2) + i\Gamma\omega} \tag{3.67}$$

Where $\epsilon_\infty = 1 + \chi$ is the dielectric constant at angular frequency far greater than the light frequency $\omega_\infty \gg \omega$, and $\epsilon_s = \epsilon_\infty + N_e e^2/(\epsilon_0 m_e \omega_0^2)$ stands for 'static', which represents the dielectric response to a static electric field[83]. This equation describes

a sharp absorption line centred at ω_0 with full width at half maximum equalling to Γ. As the energy band gap for SiO_2 is quite large at around $9eV$, the corresponding light wavelength range is at around $130nm$ ultraviolet light waves. But the probe light wavelength that will be used is at around $800nm$, so the inter band absorption can not occur, which means the electrons resonance absorption will not happen. Moreover, the lattice vibration from the material background absorption can only happen when probing light waves is in mid-infrared region. Thus, SiO_2 will not display any absorption features in our probing light frequency (around $800nm$). The dispersion is absence of imaginary part: scattering parameter $\Gamma = 0$. Figure 3.10 shows the dielectric constant of SiO_2 over a wavelength range from 400nm to 860nm, with setting the parameters $\epsilon_\infty, \epsilon_s$ and ω_0 at 1, 2.5, 12 separately. In the following discussion, this model and parameter values will be used to express the optical property of SiO_2 layers in nc-Si:H sample, for fitting spectroscopic ellipsometry data of nc-Si:H sample.

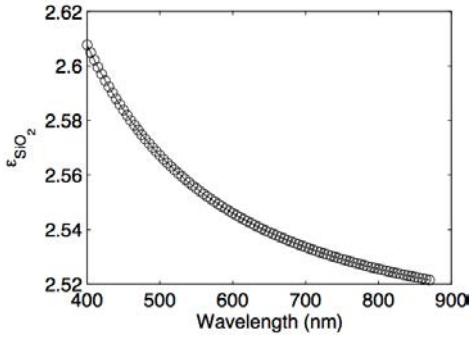

FIGURE 3.10: Dielectric constant of silicon oxide SiO_2 material, which is simulated by Lorentz oscillator model with no absorption, so there is no imaginary part.

As for the c-Si substrate of the nc-Si:H sample, the four term Forouhi-Bloomer (FB) model[130] is used to simulate the complex refractive index of c-Si. This model has demonstrated excellent agreement between modelled (n, k) and published measurement values for crystalline Si, Ge, GaP, GaAs, SiC etc, over a wide range of energies $(0 - 20eV)$. Definitely, the optical property of c-Si substrate is different from nano crystalline silicon clusters (nc-Si) inside of nc-Si:H layer. Sadao Adachi[131] proposed a different way to obtain the optical constant of this kind of micro or nano cluster crystalline silicon. He called this method as Model Dielectric Function-Critical points (MDFCP). The dielectric function in the interband transition region of micro or nano crystalline silicon fundamentally depends on the electronic energy band structure[132]. Normally there are several critical points in the interband transition region. Each critical point corresponds to one imaginary component of dielectric constant. As fitting out all the sub dielectric constant, the adding value will be the imaginary part of dielectric function of this material. Then, according to Kramers-Kronig transformation[133], the real part of dielectric function can be obtained.

Originally, the four terms Forouhi-Bloomer (FB) model[130] was also deduced from the basic semiconductor energy band structure. The extinction coefficient k is derived from one electron model with finite lifetime for the excited electron state and refractive index n is then deduced from the Kramers-Kronig relation as the Hilbert transform of k[130]. The crystalline semiconductors and dielectrics have a periodic crystal structure, and long range order gives rise to the structure in k containing several peaks, which are related to the symmetry points in the Brillouin zone[134, 135] and depicted as calculation terms in the dielectric function. This is similar as critical points for inter band transition region. Generally, four terms are sufficient to describe n and k over a wide spectral range, indicating four dominant critical point transitions[130]. For the nano crystalline silicon clusters (nc-Si), the long range ordered crystal structure could be broken and grain boundaries can also influence the optical properties, but we can continue to use this four terms model as well by just setting different parameter values in the model to indicate the strength of each critical point transition. Moreover, we can also get more information from the difference of each parameter value between c-Si and nc-Si. L.Ding *et. al.*[129] also used a four term Forouhi-Bloomer method to simulate bulk crystalline silicon and nano crystalline silicon materials. The spectroscopic ellipsometry data of both materials can be fitted very well to get reasonable dielectric constant results.

The description of this four terms FB model is expressed as refractive index n and extinction coefficient k as a function of probing light photon energy (E):

$$n(E) = \sqrt{\epsilon_\infty} + \sum_{i=1}^{q} \frac{B_{0_i} \cdot E + C_{0_i}}{E^2 - B_i \cdot E + C_i}, \tag{3.68}$$

$$k(E) = \begin{cases} \sum_{i=1}^{q} \frac{A_i \cdot (E - E_g)^2}{E^2 - B_i \cdot E + C_i} & E > E_g \\ 0 & E \leq E_g \end{cases} \text{,} q\text{=integer} \tag{3.69}$$

where

$$B_{0_i} = \frac{A_i}{Q_i} \cdot (-\frac{B_i^2}{2} + E_g \cdot B_i - E_g^2 + C_i),$$
$$C_{0_i} = \frac{A_i}{Q_i} \cdot [(E_g^2 + C_i) \cdot \frac{B_i}{2} - 2 \cdot E_g \cdot C_i],$$
$$Q_i = \frac{1}{2} \cdot \sqrt{4 \cdot C_i - B_i^2}$$

The state i means different symmetry points for the inter band transition region and the number of these points q is defined by the crystalline semiconductor in question[22]. All parameters $A_i, B_i, C_i, \epsilon_\infty, 4C_i - B_i^2$ should be bigger than zero. E_g is the optical energy band gap and E is the probing light photon energy. Then, we can make use of

this model to simulate the optical properties of nc-Si and c-Si substrate. The values of those parameters for fitting spectroscopic ellipsometry data of nc-Si:H sample are shown in table 3.3 and the modelled dielectric constants for each material are depicted in Figure 3.11. Obviously, the dielectric function of c-Si substrate is different from that of nc-Si. The real and imaginary parts of dielectric constant of nc-Si are both more than two times bigger than the values of c-Si.

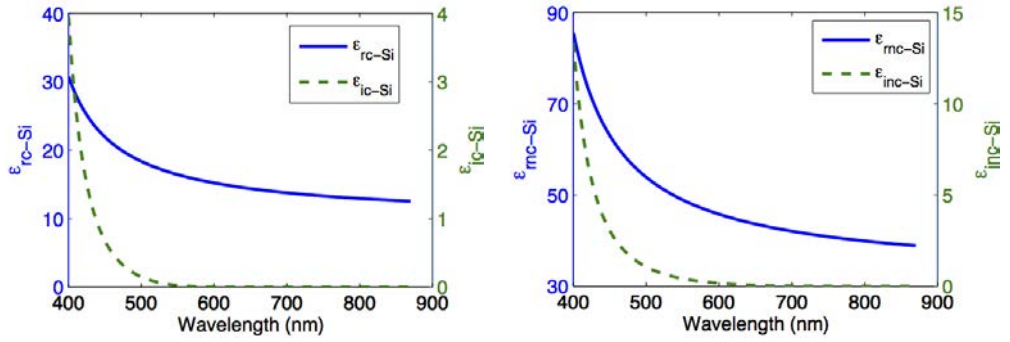

(a) (b)

FIGURE 3.11: Dielectric constant of (a) c-Si substrate of nc-Si:H, and (b) nano clusters nc-Si in nc-Si:H layer, fitted from SE data. The solid lines are the real part and dotted lines are the imaginary parts of dielectric constant.

Apart from the nc-Si phase inside the nc-Si:H layer, the optical property of another phase the amorphous silicon matrix also needs to be simulated. For the amorphous semiconductor material, the dielectric function can be described by Tauc-Lorentz model[131, 133], Cody-Lorentz model[136], band model[137] and tetrahedral model[138]. However, a one term Forouhi-Bloomer model can also be used to simulate the dielectric functions of amorphous semiconductors and amorphous dielectrics. As we mentioned before, the amorphous material will break down the crystal's periodic structure and preserve the short range order. Due to the long range disorder, the symmetry critical points for the inter band transition will also disappear. Meanwhile, the short range order will play a key role in the absorption process for amorphous semiconductor material. Locally, the electronic states of the amorphous solid may be considered to be a broadened superposition of molecular-orbital states[139, 140]. Thus, a one term FB model can be used to stand for this property to express optical function of amorphous silicon (α-Si) material. And it is also quite interesting to compare the parameters between α-Si and c-Si, basing on same original FB model. Actually this dispersion relation model has been extensively verified by lots of experimental measurements, and provides a good fit to the published data for a wide variety of amorphous materials, such as α-Si, α-Si:H, α-Si_3N_4 or α-TiO_2, over a wide range of photon energies[130, 140]. The formulation is listed as following:

$$n(E) = \sqrt{\epsilon_\infty} + \frac{B_0 \cdot E + C_0}{E^2 - B \cdot E + C}, \tag{3.70}$$

$$k(E) = \begin{cases} \frac{A\cdot(E-E_g)^2}{E^2-B\cdot E+C} & E > E_g \\ 0 & E \leq E_g \end{cases} \tag{3.71}$$

where

$$B_0 = \frac{A}{Q}\cdot(-\frac{B^2}{2} + E_g\cdot B - E_g^2 + C),$$
$$C_0 = \frac{A}{Q}\cdot[(E_g^2 + C)\cdot\frac{B}{2} - 2\cdot E_g\cdot C],$$
$$Q = \frac{1}{2}\cdot\sqrt{4\cdot C - B^2}$$

Where A, B, C, ϵ_∞ and E_g are similar to those described in Equation 3.68 and 3.69. These five parameters can fully describe the dispersion relation of an amorphous material, which is represented as the refractive index $n(E)$ and extinction coefficient $k(E)$, and $A, B, C, 4C - B^2$ are all bigger than zero. This is important because $n(E)$ can not be determined from Kramers-Kronig analysis unless these conditions are met[140]. The dielectric function, which will be used for the amorphous silicon matrix in nc-Si:H layer, is shown in Figure 3.12, and the parameters values of the one term Forouhi-Bloomer model are listed in table 3.3, denoted as α-Si. Until now, we have described all the dielectric functions of each material in nc-Si:H sample. These dielectric functions will be integrated together to fit the reflectance and ellipsometry data of nc-Si:H sample, which will be discussed in following sections. In table 3.3, the E_g of C-Si substrate for nc-Si:H sample has relatively high value. This maybe the optical contribution from SiO_2 layer on C-Si substrate, which was deposited, is a little deviation from the standard optical property in Figure 3.10. Moreover, the interfaces in nc-Si:H sample can also increase the error of fitting parameters. In fitting process, we maintained the reasonable fitting parameters for the other materials, so the uncertainty is focused on the C-Si substrate.

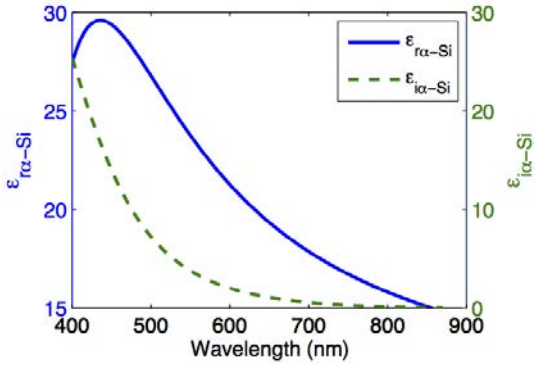

FIGURE 3.12: Dielectric constant of amorphous silicon α-Si modelled by one term Forouhi-Bloomer approach, solid line represents real part and dashed line is for imaginary part.

As for the sample of porous silicon with c-Si substrate, we continue to use the four term FB model to simulate the dielectric constant of c-Si substrate and nano wires c-Si in porous silicon (PS) layer. After fitting the spectroscopic ellipsometry data, we can evaluate the dielectric functions. Figure 3.13(a) illustrates the dielectric constant of c-Si substrate of PS sample in the spectral range from $400nm$ to $870nm$. Figure 3.13(b) describes the dielectric function of nano wires c-Si in PS layer, which is different from the dispersion relation of c-Si substrate due to the quasi one dimensional effect. At moment, all the materials, which are composing nc-Si:H and PS samples, have been modelled by Lorentz oscillator or Forouhi-Bloomer approaches to depict the dielectric functions expressing the optical properties of each sample.

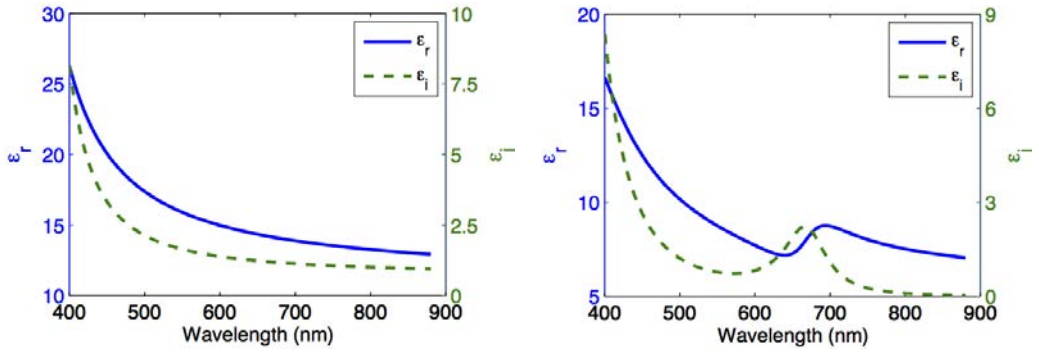

(a) (b)

FIGURE 3.13: Dielectric functions of (a) c-Si substrate of Porous silicon sample and (b) nano wires c-Si in porous silicon layer, solid lines are real part and dashed lines are imaginary part. Both of them are modelled by the four term FB approach.

3.3.2 Effective Medium Theory

Even we used Forouhi-Bloomer model to evaluate the dielectric functions of each component material in nc-Si:H and PS samples, the nc-Si:H layer and porous silicon layer are both irregularly mixing two different phases. For example, nc-Si:H layer is including α-Si matrix and nc-Si clusters, which are inter-twined together to form the nc-Si:H layer. Porous silicon layer consists of nano wires c-Si and the empty voids, which are also intertwined with each other to generate this porous and branched layer. Thus, in order to obtain the dielectric constant of the whole layer, the influence of the microstructure on the macroscopic dielectric response should also be taken into account, apart from the modelling dielectric function of each material. We also need to notice that the diameter of nc-Si clusters is around $\sim 6nm$ and diameter of nano wires c-Si is around $\sim 10nm$, while the probing light wavelength is at around $800nm$. In the cases where the typical length scale characterising feature sizes of the topology is much smaller than the probing light wavelength (long wavelength limit), one can neglect the retardation

Material	ϵ_∞	A_i	B_i	C_i	E_g
C-Si (Substrate nc-Si:H)	5.664	0.011	6.860	11.778	2.065
		0.054	7.361	13.625	
		0.153	8.632	18.817	
		0.047	10.314	26.859	
nc-Si (nano cluster nc-Si:H)	20.520	0.011	6.860	11.778	1.27
		0.054	7.361	13.625	
		0.153	8.632	18.817	
		0.047	10.314	26.859	
$\alpha - Si$ (amorphous-Si)	3.71	1.09	6.67	12.72	1.625
C-Si (Substrate PS)	7.868	0.005	6.857	11.773	1.195
		0.036	7.344	13.622	
		0.049	8.643	18.816	
		0.0025	10.354	26.792	
C-Si (nano wires PS)	3.101	0.008	6.901	11.935	1.111
		0.146	7.408	14.123	
		0.0007	8.343	17.423	
		0.006	3.714	3.457	

TABLE 3.3: Fitting Parameters values of c-Si substrate, nano clusters nc-Si and amorphous phase α-Si in nc-Si:H sample, and c-Si substrate and nano wires c-Si of PS sample, using the four terms and one term Forouhi-Bloomer model, respectively.

effects and apply an effective medium theory to consider the two components mixed system as an effective medium with a macroscopic effective dielectric function ϵ_{eff}[89]. If the length scale characterising feature sizes is larger than the wavelength of probing electromagnetic waves, one can accurately observe the medium and obtain more structural details. So, the size of inclusions in the mixture and the spatial correlation length of the dielectric function needs to be carefully considered with respect to the probing wavelength[141]. In general, the effective medium theory is just a kind of dielectric mixing rule to approximate and predict the effective dielectric response of the composite material. Referring to the constituent dielectric functions, the corresponding volume fraction and probably other microstructure parameters, the different algebraic formulas can be used in the mixing rule and the effective dielectric constant can be calculated. However, in most cases, we do not really know the microstructure of mixing components very well and the mixing rule is just an approximation. Even if the micro structure can be ideally realised, the relation between geometry and mixing rule can still not be computed exactly in realistic cases[89]. In order to explain the different mixing rules more simply, we just consider a two-component mixing system. One component is the host or matrix material with dielectric function ϵ_M and another one is the embedded material with ϵ. Moreover, the factor p is used to describe the volume fraction of matrix material and factor $f = 1 - p$ for the volume fraction of the embedded inclusions.

Bergman representation

A general expression for the effective dielectric function of a two-phase system and the dielectric functions of the constituents was established by Bergman[89, 142–144]. It is called the Bergman representation, involving a function named the spectral density g and the basic quantity matrix volume fraction p. This spectral density g is a normalised distribution function for so-called geometrical resonances. And these resonances illustrate the electric interactions of different parts of the system, which also characterise the micro structure as discussed in W.Theiss' work[89, 145–147]. The Bergman representation is as following:

$$\epsilon_{eff} = \epsilon_M[1 - (1-p)\int_0^1 \frac{g(n,p)}{\frac{\epsilon_M}{(\epsilon_M - \epsilon)} - n} dn] \tag{3.72}$$

In the equation, the spectral density g and the volume fraction p are used to express the influence of the micro structure on the ϵ_{eff}. ϵ_M and ϵ are the another two factors for ϵ_{eff}. n varies from 0 to 1. Moreover, the function $g(n,p)$ does not depend on any material property but only geometry[146], which means it only expresses the micro structure. As we mentioned before, there is no explicit relationship established between $g(n,p)$ and a specific given geometry in most cases. We only can experientially adjust spectral density to reproduce experimental spectra, according to J. Sturm work[148–150]. Basing on this general valid effective medium approximation, D. Stroud researched brine-saturated rocks geometry structure and dielectric permittivity[151], Kunal Ghosh[152] particularly discussed about porous media and some scaling laws were proposed in the context of random resistor networks. Especially for porous media, W.Theiss[89] proposed a three-parameter formula for controlling the shape of the spectral density, which is a rather simple approach to handle the general Bergman representation. The three parameters are porosity, the percolation strength and a broadening parameter d of resonances for almost isolated particles:

$$\begin{aligned} g(n,p) =& g_0\delta(n) + \frac{3\sqrt{3}g_0}{2\pi n(1-p)^2}[p^2|\frac{1-n}{n}|^{1/3} + p(1-p)|\frac{1-n}{n}|^{2/3}] \\ &+ (1 - \frac{g_0}{(1-p)^2})[-\frac{3}{4d^3}(n - \frac{p}{3})^2 + \frac{3}{4d}]\theta(\frac{p}{3} - d + n)\theta(\frac{p}{3} + d - n). \end{aligned} \tag{3.73}$$

Obviously, the spectral density $g(n,p)$ is composed of three parts: (1) the delta-function is used to represent the percolation of the particles; (2) the second term takes into account a broad distribution of resonances to characterise a dense particle system; (3) the third term generates a peak with flexible width d, which represents the isolated particles with weak interaction, θ is the Heaviside step function. The third term is an inverted parabola with a maximum at $p/3$. At the position $n = p/3 - d$ and $n = p/3 + d$, the parabola cuts the n-axis.

Maxwell Garnett & Bruggeman & Looyenga

Apart from the Bergman theory, Maxwell-Garnett[153], Bruggeman[154, 155] and Looyenga[156] also derived expressions for the effective dielectric function of inhomogeneous system. Actually, they are all based on special assumptions about similar topologies: in most cases ensembles of spheres are supposed to interact in a mean local field[150]. Thus, all the formulas of these models are just special cases under the Bergman representation and each formula corresponds to one typical spectral density. Each mixing formula has been expressed with the corresponding spectral density by J. Sturm[150]. We will discuss these simple models one by one and choose the suitable one to evaluate the effective dielectric constant of mixing components layer: nc-Si:H and PS.

(a) Maxwell Garnett

The Maxwell Garnett formula is a very old and excellent mixing rule, which is proposed basing on the Clausius-Mossotti relation[153]. The formula is given by:

$$\frac{\epsilon_{eff} - \epsilon_M}{\epsilon_{eff} + 2\epsilon_M} = f\frac{\epsilon - \epsilon_M}{\epsilon + 2\epsilon_M} \tag{3.74}$$

Where f is the volume fraction of embedded material. In the three dimensional case[157, 158], the formula should be

$$\epsilon_{eff} = \epsilon_M \cdot \frac{\epsilon(1+2f) - \epsilon_M(2f-2)}{\epsilon_M(2+f) + \epsilon(1-f)} \tag{3.75}$$

The corresponding spectral density is featuring as one sharp resonance:

$$g(n, f) = \delta(n - \frac{1-f}{3}) \tag{3.76}$$

This indicates that the Maxwell Garnett model is expected to be valid at low volume fraction of embedded spherical particles, which are sparsely dispersed inside a matrix component. Due to the large distance between particles, the embedded particles can not form an infinite connected network. This particular microstructure restriction precludes the existence of a percolation threshold[159]. Thus, the Maxwell Garnett model is mostly typical for a material with dilute inclusions in the embedding matrix.

(b) Bruggeman

Bruggeman effective medium approximation (EMA) is the most frequently used formula to simulate the effective dielectric constant of a heterogeneous material[160, 161]. The formula is described as

$$(1-f)\frac{\epsilon_M - \epsilon_{eff}}{\epsilon_M + 2\epsilon_{eff}} + f\frac{\epsilon - \epsilon_{eff}}{\epsilon + 2\epsilon_{eff}} = 0 \tag{3.77}$$

The derivation of ϵ_{eff} is based on the assumption of self-consistency, which means the material surrounding the inclusions can be considered as a homogeneous matrix material. Even though the Bruggeman EMA model is relatively simple, this approximation can give a description of percolation phenomenon[162] and this is one of the reasons for its wide use in different kinds of mixed phase materials. Meanwhile, Equation 3.77 also displays that the Bruggeman EMA formula is symmetric with respect to the interchanging between inclusion component and matrix component. The solution of this equation to obtain ϵ_{eff} is expressed as

$$\varepsilon_{eff} = \frac{1}{4}\{\epsilon_M(2-3f) + \epsilon(3f-1) + \sqrt{[\epsilon_M(2-3f) + \epsilon(3f-1)]^2 + 8\epsilon_M \cdot \epsilon}\} \tag{3.78}$$

The spectral density of Bruggeman EMA is as following:

$$\begin{aligned} g(n,f) &= \tfrac{3f-1}{2f}\theta(3f-1)\delta_+(n) + \tfrac{3}{4\pi f n}\sqrt{(n-n_L)(n_R-n)} \\ &\text{with} \\ n_{R/L} &= \tfrac{1}{3}(1+f \pm \sqrt{2f-2f^2}) \end{aligned} \tag{3.79}$$

As we can see the spectral density contains a continuous distribution of resonances and a sharp resonance. The sharp resonance depends on the inclusions volume fraction f. This can be more realistic than just one resonance in Maxwell Garnett model, especially for irregularly shaped particles and high inclusion volume fraction material. Moreover, it can predict the percolation behaviour when the inclusions volume fraction f is high enough to form a continuous network. When $f > 1/3$, the inclusions can form an infinite connected network. At $f < 2/3$, the matrix is in the state of continuous network. When $1/3 < f < 2/3$, both components are connected in the symmetric microstructure and the anomalous dispersion effect is generally absent, which is unlike the dispersion microstructure. In conclusion, the Bruggeman EMA can not only cover the Maxwell Garnett sparsely dispersed microstructure, but also represent the aggregate or random-mixture microstructure. Niklasson[161] and Hongru Ma[159] provided more comparable information about these two models. Goncharenko[162] summarised why Bruggeman EMA is much more preferable than others for predicting effective dielectric functions. In the simulation section, we also chose the Bruggeman EMA to do the fitting for nc-Si:H and PS samples.

(c) Looyenga

Looyenga model only involves just one parameter volume fraction f to determine the effective response in electromagnetic field. The formula is deduced by H.Looyenga[156] as following:

$$\epsilon_{eff}^{1/3} = (1-f)\epsilon_M^{1/3} + f\epsilon^{1/3} \tag{3.80}$$

The spectral density shows a very broad continuum of resonances, which is described as

$$g(n,f) = f^2\delta_+(n) + \frac{3\sqrt{3}}{2\pi}[(1-f)^2|(n-1)/n|^{1/3} + f(1-f)|(n-1)/n|^{2/3}](1-\delta_{0,n}) \quad (3.81)$$

This is advantageous for rather densely packed composites and disadvantageous for dilute particles system.

Comparing all the different effective medium theories, the Bruggeman EMA theory would be a suitable choice. As we mentioned in the above discussion, the model is rather simple compared to Bergman theory. The spectral density and percolation behaviour have both been considered inside of this Bruggeman model. Meanwhile, it can cover the dilute system and densely system with symmetric expression. This model has also been widely proved it can be successfully applied in different fields[160]. But, the Bruggeman model does not predict the plasmon resonance. We will use this Bruggeman EMA to express the effective response of nc-Si:H and PS material in electromagnetic field.

3.3.3 Simulation

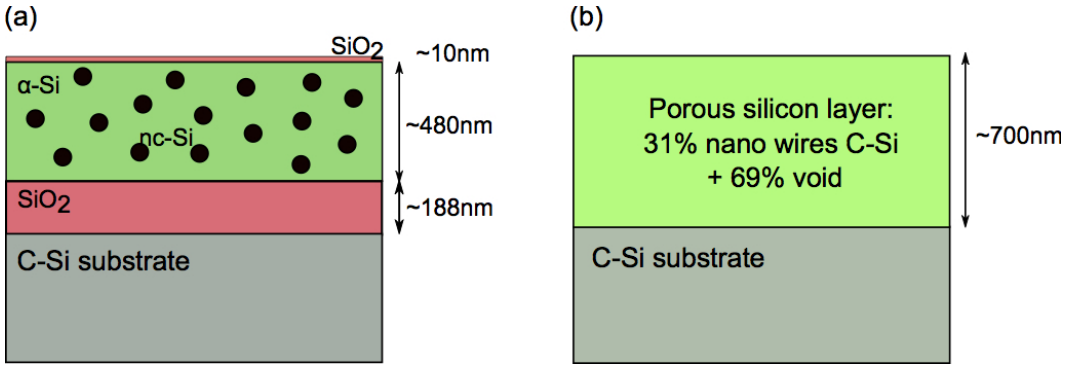

FIGURE 3.14: Schematic structures of (a) nc-Si:H sample and (b) PS on c-Si substrate sample.

Basing on the previous discussions, the optical models of hydrogenated nano crystalline silicon (nc-Si:H) sample and porous silicon (PS) on c-Si substrate sample can be constructed. Through simulating and fitting the measurement data of reflectance transmittance and ellipsometry, the dielectric function of researched material can be evaluated.

Figure 3.14(a) schematically describes the basic structure of nc-Si:H sample. The top layer and third layer are both silicon oxide material, SiO_2, whose dielectric constant is modelled by the classical Lorentz model. The corresponding parameters are same for these two layers, which are illustrated in Section 3.2.1. The c-Si substrate and nc-Si inclusions are simulated by the four term Forouhi-Bloomer model, with different parameters values due to the different microstructure. Meanwhile, the dielectric function

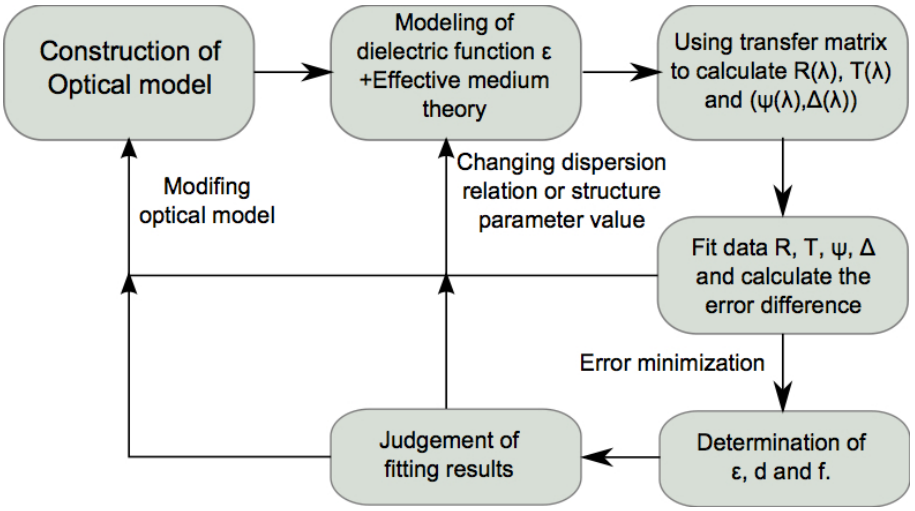

FIGURE 3.15: Flowchart of simulation procedure for fitting reflectance, transmittance and spectroscopic ellipsometry data.

of amorphous phase silicon (α-Si) is defined by the one term Forouhi-Bloomer model. Eventually, the Bruggeman EMA model is applied to express the effective dielectric response of second layer by mixing the dielectric constants of nc-Si and α-Si components. According to Raman scattering measurement data, the volume fraction f of nc-Si inclusions is estimated as around 0.35. To this end, the simulated optical model for nc-Si:H sample is constructed. This means the optical property of each layer in nc-Si:H sample is depicted as the corresponding dispersion relation, and the structure information about thickness for each layer has been confirmed by SEM measurement. Finally, we can calculate reflectance $R^{cal}(\lambda)$, transmittance $T^{cal}(\lambda)$ and ellipsometry parameters $(\psi^{cal}(\lambda), \Delta^{cal}(\lambda))$ with the help of transfer matrix method under a fixed incident angle. Then, comparing to the experimental data $R^{exp}(\lambda)$, $T^{exp}(\lambda)$ and $(\psi^{exp}(\lambda), \Delta^{exp}(\lambda))$, the fitting process is carried on by adjusting the parameters of optical model to minimise the mean square error (MSE) between calculation and measurement values. For example, the MSE for fitting ellipsometry data can be expressed as following:

$$MSE = \frac{1}{2N - M} \sum_{i=1}^{N} [(\frac{\psi_i^{cal} - \psi_i^{exp}}{\sigma \psi_i^{exp}})^2 + (\frac{\Delta_i^{cal} - \Delta_i^{exp}}{\sigma \Delta_i^{exp}})^2] \ , \tag{3.82}$$

where N is the number of data points in the spectral region of ellipsometry measurement. M is the number of variable parameters in the model, which we set to constant value 6. σ is the standard deviation on the experimental data points. This is assumed to be 1, meaning there is no deviation for measurement results. ψ^{exp} and Δ^{exp} are the measurement values, while ψ^{cal} and Δ^{cal} are the corresponding calculation values[129]. From this way, the loop of fitting program can be built to minimise the MSE and optimise the fitting results in an iterative fitting procedure, as shown in Figure 3.15 with

a flowchart of the simulation procedure. After we determined the dielectric function of each material and thickness d for each layer and volume fraction of inclusions f, we also need to check whether the simulated parameter values are physically reasonable. For example, all the values should be bigger than zero and E_g energy gap should be in the reasonable range. This corresponds to the 'Judgement' section in the flowchart, Figure 3.15. If the parameter values are not reasonable, we need to modify the optical model to make it much more realistic, or we can also choose other dielectric function models such as Tauc-Lorentz, Sellmeier and Cauchy models.

As for the spectroscopic ellipsometry measurement, a commercial ellipsometer, Horiba Jobin-Yvon UVISEL, has been applied firstly to measure the $(\psi(\lambda), \Delta(\lambda))$ of nc-Si:H sample in the spectral range from $400nm$ to $870nm$. Moreover, the lab built RCE system was also used to measure the sample and check the accuracy of RCE system. As the probe centred at around $800nm$, the spectrum range can only be available from $760nm$ to $820nm$. The lab built RCE system is specially used for the pump probe ellipsometry measurement, but it can also be used as the common ellipsometry by blocking the pump beam. The next section will provide more information about calibration and detection of the pump-probe RCE system.

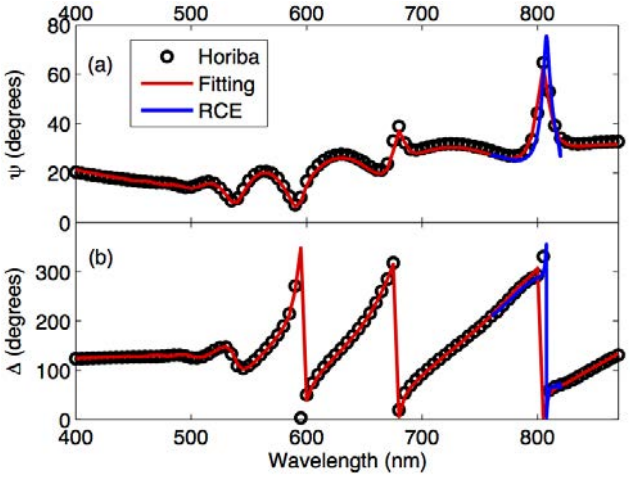

FIGURE 3.16: Ellipsometry data $(\psi(\lambda), \Delta(\lambda))$ and fitting results between $400nm$ and $870nm$ for nc-Si:H sample; circle dotted lines are the data from Horiba commercial ellipsometer; blue solid lines are measured by lab built RCE, covering from $760nm$ to $820nm$, both of them are measured under 70° incident angle; red solid lines are the optical model fitting results.

Figure 3.16 shows the black circle dotted data $(\psi(\lambda), \Delta(\lambda))$ of nc-Si:H sample from Horiba commercial ellipsometer measurement, in the spectral region between $400nm$ and $870nm$. The blues lines data are measured by the lab built RCE system, which only covers the spectral range from $760nm$ to $820nm$. The incident angle is fixed at 70° for both of them. The blue lines are almost coincident with black circle dots between $760nm$ and $820nm$. So, the accuracy of lab built RCE system can be verified that it is good

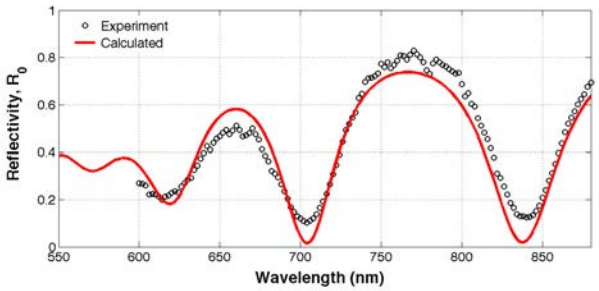

FIGURE 3.17: Spectral reflectance measurement under normal incident angle, dotted line is the data and red solid line is the calculated results from optical model.

enough to measure the ellipsometry (ψ, Δ) of a sample. Then, the optical model fitting results are shown as red solid lines, which are overlapped with the Horiba and RCE measurement data. From the fitting, we finally identified the parameters values of each dielectric function. These parameters are listed in table 3.3, which have been discussed in dispersion relation section. And the corresponding dielectric functions are also plotted in figures of section 3.2.1. As for the structure parameters, thickness d and inclusions volume fraction f are listed in table 3.4. We can see the thickness value of each layer for nc-Si:H sample is around same as the value obtained from SEM. The inclusions volume fraction is also around same as the obtained value from Raman scattering. Furthermore, we can also get the effective dielectric function of the mixing components layer, which is shown in Figure 3.18 within the spectral range from $400nm$ to $870nm$. The results of the ellipsometry are also cross-checked by spectral reflectance measurement at near normal incident angle. The same structure parameters and dielectric function for each material are used in the optical model to fit the spectral reflectance data. The reflectance fitting curve and measurement data are shown in Figure 3.17. Both of two lines are almost coincident with each other, which also demonstrates that the optical model is precise to describe the optical properties of nc-Si:H sample. In the ultrafast dynamics research, the pump probe time resolved measurement will be performed on the nc-Si:H sample, basing on the retrieved effective dielectric function in spectral range from $760nm$ to $820nm$, as shown the subfigure in Figure 3.18. In this range, the real part ϵ_{reff} drops monotonically from 12.25 to 11.8 and the imaginary part ϵ_{ieff} decreases from 0.05 to 0.02. This estimation result is consistent with the previously published works on nc-Si:H and μc-Si:H[85, 86, 163, 164].

Regarding the sample of PS layer on c-Si substrate, the same simulation process can be done to evaluate the effective dielectric constant of PS layer. Figure 3.14(b) depicts the basis structure of the sample. The PS layer is composed of void inclusions and nano wires c-Si matrix. The porosity or void volume fraction is estimated at 69% by gravimetric method and c-Si nano wires diameter is estimated as $\ll 50nm$ by SEM images. The

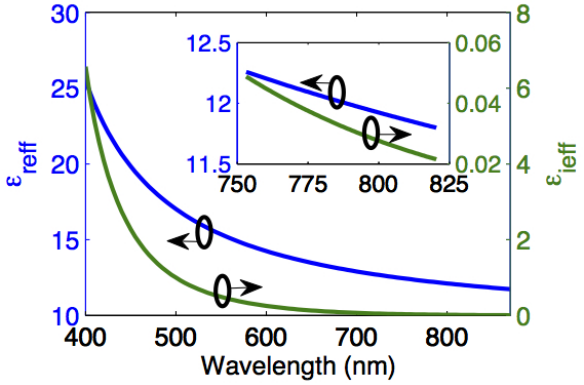

FIGURE 3.18: Effective dielectric function of the nc-Si:H layer, which is composed by nc-Si inclusions and α-Si matrix, $\epsilon_{eff} = \epsilon_{reff} - i \cdot \epsilon_{ieff}$, obtained from measurements shown in Figure 3.16 and simulations of the multilayer optical model. Left and right axes correspond to the real and imaginary parts of the complex dielectric function, respectively. Inset: an enlarged portion of the spectra between 750 and 825nm.

thickness of PS layer is around 700nm from SEM cross-section images. The void dielectric constant $\epsilon_{void} = 1$. The dielectric function of nano wires c-Si and c-Si substrate are both modelled by four terms Forouhi-Bloomer method. The Bruggeman EMA model is applied to express the effective dielectric function of the PS layer, which involves void inclusions and nano wires c-Si matrix. So, referring to the simulation Flowchart 3.15, the experimental data $(\psi^{exp}(\lambda), \Delta^{exp}(\lambda))$ can be fitted by the constructed optical model and transfer matrix method. Figure 3.19 shows the measurement data from the Horiba and RCE systems as black circle dots and blue solid lines, respectively. The fitting results from the optical model are displayed as red solid lines. The accuracy of RCE system is verified again and the optical model has nearly identical $(\psi^{cal}(\lambda), \Delta^{cal}(\lambda))$ to the measured data. Thus, the corresponding parameters of dielectric functions for c-Si substrate and nano wires c-Si are obtained and listed in table 3.3. Moreover, the structure parameters in fitting are expressed in table 3.4. The thickness d of PS layer is fitted as 800nm, which is a little bigger than SEM measured value 700nm. This could because the interface between PS layer and substrate is hard to be ideally identified, which leads to the error of the thickness measurement. The porosity f is fitted as 0.7517, which is also a little bigger than gravimetric measurement value 0.69. Meanwhile, the effective dielectric constant of PS layer was obtained using the Bruggeman EMA model, which is shown in Figure 3.20. Actually, the value of the real part of effective dielectric function is close to that of SiO_2 material. Comparing to previous published work on the dielectric constant of porous silicon[90, 165–167], the dielectric function obtained from fitting the ellipsometry data is reasonable in the wavelength range from 750nm to 850nm. ϵ_{reff} is dropping from 1.82 to 1.76 and ϵ_{ieff} decreases from 0.017 to 0.003. We will focus on this spectral range in the ultrafast dynamics research.

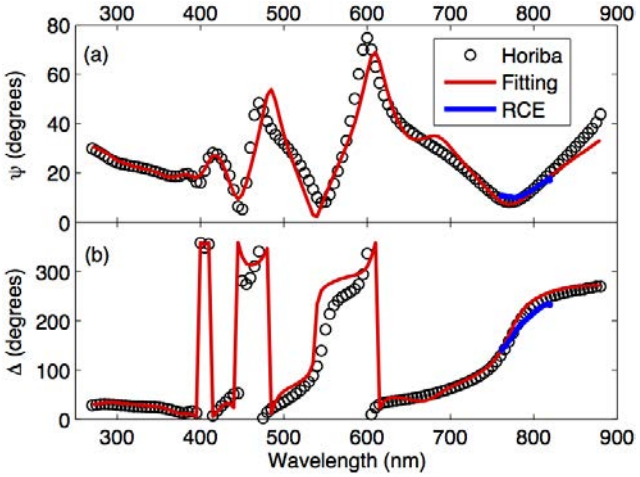

FIGURE 3.19: Ellipsometry data $(\psi(\lambda), \Delta(\lambda))$ and fitting results in spectral region between $200nm$ and $880nm$ for the sample of PS layer on c-Si substrate; circle dotted lines are the data from Horiba ellipsometer; blue solid lines are measured by lab built RCE, covering from $760nm$ to $820nm$. 70° incident angle is fixed for both of them; red solid lines are the fitting results.

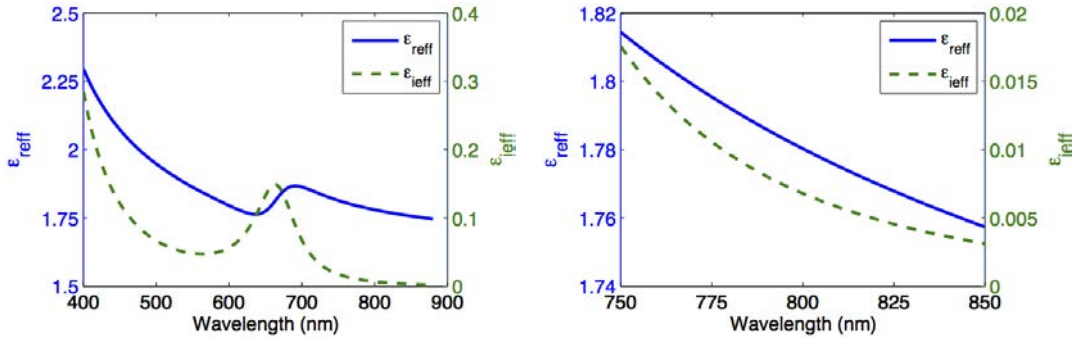

FIGURE 3.20: Effective dielectric constant of PS layer in (a) spectral range from $400nm$ to $880nm$ and (b) spectral range from $750nm$ to $850nm$.

Sample	d_1	d_2	d_3	f	MSE
nc-Si:H	10.045nm	475.28nm	188nm	0.3537	0.0008
PS	800nm	-	-	0.7517	0.0025

TABLE 3.4: Structure parameters: thickness d and volume fraction f, obtained from fitting ellipsometry data. For nc-Si:H sample, f is the nc-Si inclusions volume fraction; for PS sample, f is the porosity.

In conclusion, the dielectric functions and sample structure parameters all can be estimated from fitting the spectroscopic ellipsometry data. Meanwhile, the Bruggeman EMA model is good enough to express the effective dielectric constant of material with mixing phases. From this way, we can realise the basic optical properties of a sample under the probing light frequency. If we use another higher intensity pump pulse to interact with the semiconductor sample, the sample would be activated and free carriers

(electrons and holes) would be excited during the interaction. These excited carriers will result in the variation of the optical properties of the sample. Then, a decay process of this optical property change will be followed. In order to detect the optical properties variation after pump excitation, a weaker probe pulse is applied. The optical path length of the probe pulse is precisely controlled comparing to the pump pulse, for the time resolved of monitoring the decay process of the optical property change. Obviously, reflection transmission and ellipsometry are still the general approaches to be performed on monitoring the dielectric function variation after pump pulse excitation. From this detecting process, the ultrafast dynamics information of researched samples can be fully revealed.

3.4 Ultrafast Time-Resolved Spectroscopy

The optical spectroscopic measurements and analysis methods have been illustrated in the above sections. As shown, the information about the electronic band structure of semiconductors and the properties of surfaces and interfaces can all be explored by optical spectroscopy methods, which include the detections of the reflection, transmission and ellipsometry. Actually, when combined with the ultrafast laser system, the optical spectroscopy approaches can reveal more informations about non-equilibrium, nonlinear, relaxation and transport dynamics of semiconductors[2], termed 'ultrafast time-resolved spectroscopy'. In the following sections, we will make an overview of the ultrafast time-resolved research techniques based on the optical spectroscopic methods.

Ultrafast laser pulses are a unique tool for the excitation and 'stop-action' measurements of ultrafast microscopic and quantum mechanical processes in materials[168]. Here, a femtosecond pulsed laser is used to do time resolved spectroscopic studies of ultrafast dynamics processes in solid state materials. Generally, the pump probe approach is the main method to do the ultrafast time resolved research. The ultrafast laser beam is split into two beams by a beamsplitter, one with high intensity, used to excite the semiconductor sample, and coined the pump beam. Another one with low intensity, is termed the probe beam, and is used to detect the variation of the sample's properties after pump excitation. By controlling the optical path length of the probe pulse compared to that of pump pulse, the phenomena induced by the pump can be time-resolved on femtosecond time-scales by the probe beam. This is just like a high-speed electronic flash to make stop-action photographs of rapid mechanical motions of macroscopic objects[168].

Figure 3.21 shows the schematic non-collinear pump probe approach. An intense pump pulse firstly excites the medium into non-equilibrium state. Generally, for the semiconductor material, as long as the pump photon energy is bigger than the energy band gap

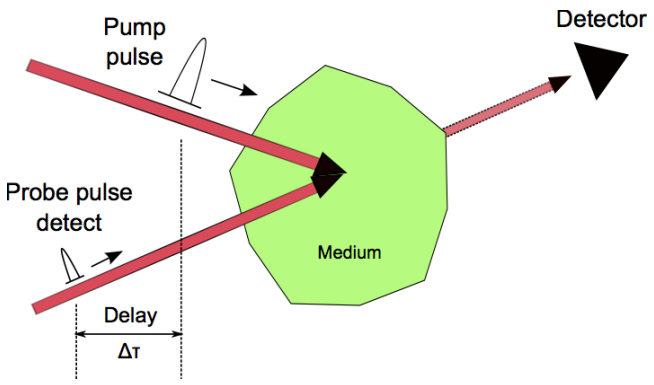

FIGURE 3.21: Schematic non-collinear pump probe approach. A pump pulse with high intensity excites a medium. After a time delay Δt, a weak probe pulse impinges upon the excited area to detect the variation of excited state medium.

of material, the absorption of pump photons will induce dense free carriers inside the material. The dense excited carriers may also result in variations of the band gap and lattice temperature, etc.[169]. As the excited state of the medium is probed by another, weaker, external electromagnetic field, the dielectric function is the first physical parameter to be considered in describing the pump induced internal dipoles polarisation. In brief, the optical properties of the excited state are monitored by the probe beam and described using the dielectric function. So, all the excited phenomena can be summarised into the variation of dielectric function. To explain it more clearly, the optical property of the excited state is represented by $\epsilon(t)$, which can be expressed as following formula

$$\epsilon(t) \rightarrow \epsilon_{t<t_0} + \Delta\epsilon(t - t_0) \ . \tag{3.83}$$

Here, ϵ_{t-t_0} expresses the unperturbed optical property of the medium and $\Delta\epsilon(t - t_0)$ means the induced variation of optical property at time t following the pump excitation time t_0. In order to detect the optical property of the excited state medium at different time, $\epsilon(t)$, a probe pulse is arriving at the excited area with time delay Δt after the pump pulse, which is shown in Figure 3.21. This time delay Δt is actually the time difference between the detection time t and excitation time t_0. Normally, the intensity of the probe pulse is kept low to avoid inducing any further perturbation to medium. With precise control of the optical path length of the probe pulse, the transient change of the optical properties can be mapped as a function of time delay, $\epsilon(\Delta t)$, through detecting the probe pulses.

Similarly, to realise the dielectric function of the medium at different time delay after the pump excitation, the basic optical spectroscopy methods can be applied, such as measuring the reflection, transmission and ellipsometry of the probe beam. Basically, $\epsilon(\Delta t)$ is dependent on the excited carrier concentration, carrier-carrier scattering rate, etc. To reveal the physical meaning of the values of $\epsilon(\Delta t)$, a theoretical modelling

approach needs to be proposed to indicate the interpretation of dynamics process from the time resolved measurement data[47].

We will use the time-resolved spectroscopic pump-probe reflection, transmission and ellipsometry methods, to investigate the ultrafast dynamics process of nano structured silicon. For instance, the pump probe transmission measurement can be used to reveal the changes in time-resolved absorption, pump probe reflection tends to be more sensitive to the changes in refractive index as well as changes in the absorption[168]. As for the spectroscopic pump probe ellipsometry, it can not only provide the amplitude ratio between reflected $p-$ and $s-$ polarised light waves, but also afford the phase difference between those two, from the excited sample. Finally, through exploring dielectric function $\epsilon = \epsilon_r - i \cdot \epsilon_i$ of excited sample, we can surmise key facts about ultrafast carrier dynamics.

3.4.1 Pump-probe Reflection and Transmission

In this subsection, the time-resolved pump probe reflection and transmission measurements will be introduced to investigate the dielectric constant of excited state evolving on the femtosecond time scale. Generally, the setup is constructed to measure the reflection and transmission incorporating the pump probe setup. The pump beam is used to create the perturbation for the medium and probe beam is for detecting the optical properties of the excited state. Moreover, in the pump-probe system geometry, the incident angle and the photons energy should be considered carefully. We also need to notice that the response time of detector is $\sim 1ns$ and the time width of laser pulse is $\sim 60fs$, moreover the laser pulse period is $1ms$ and the detected signal is integrated and averaged. The one dimensional steper motor can control the minimum step distance of the retroreflector in less than one micrometer ($1fs \rightarrow 0.15\mu m$). The time resolution was determined by the time width of laser pulse. A schematic of the pump probe setup, which was built in our lab, is shown in Figure 3.22.

A Coherent Ti: sapphire femtosecond laser system is used in our lab. The ultrafast seed pulses are first generated by a mode-locked Micra oscillator. These seed pulses have $80MHz$ repetition rate, around 400mW average power and spectral centre at $\sim 800nm$. Then, the seed pulses are provided into stretcher to broaden the pulses time width. This is done to avoid the breakdown of the optics inside the regenerator when amplifying the pulses power. In the regenerator, the stretched seed pulses are amplified by another Ti:sapphire laser system, which is pumped by evolution Q-switched Nd:YLF laser with $527nm$ wavelength. After the amplification, the average power of produced pulses can reach up to $4.3W$. Then, the time width of amplified pulses are compressed as short

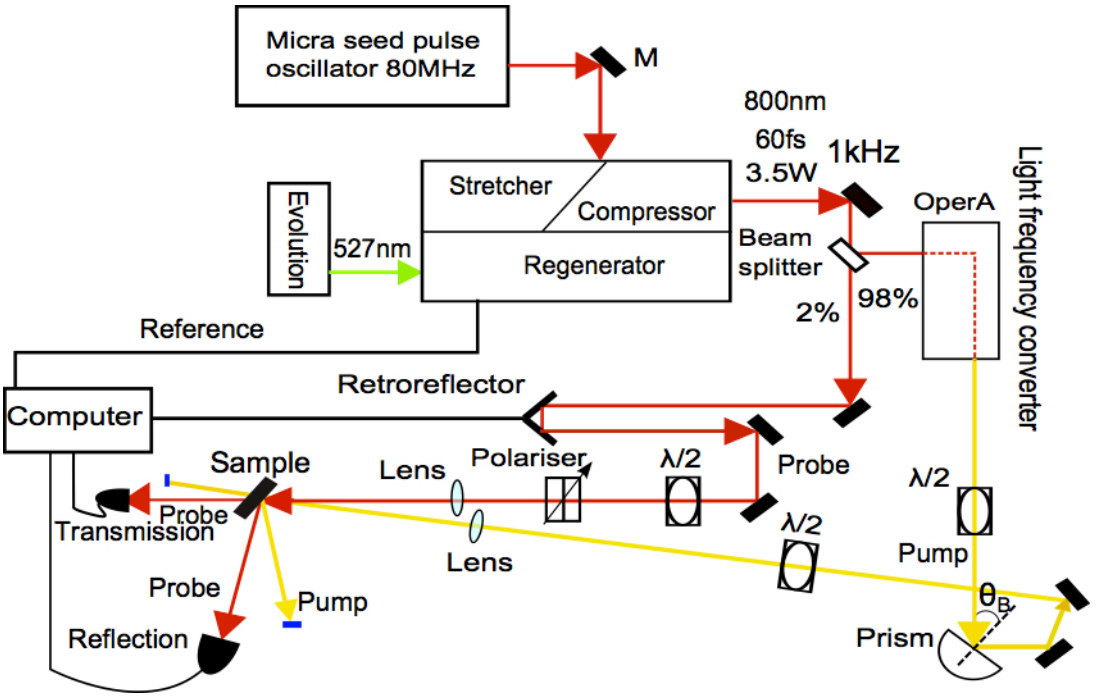

FIGURE 3.22: Schematic time-resolved pump probe reflection and transmission measurement setup. The output laser from compressor is split into pump and probe beam. A retroreflector is mounted on an automated translation stage to control the optical length of probe beam and generate the time delay (Δt) comparing to pump beam. Finally, the pump and probe beam are spatially overlapped on the sample surface. One detector is used to measure the reflection and another one for transmission. A LabView program is set to control the setup by computer.

as possible in the compressor. The final output laser pulses have average power value at around $3.5W$, the repetition rate at $1kHz$ and pulse time width of about $60fs$. The centre spectra of output pulses is still at around $800nm$. With the help of commercial intensity autocorrelator, the time width of output pulses can be measured, which is displayed in Figure 3.23(a). From a Gaussian fit, we can know the full width at half maximum (FWHM) in time is $\sim 60fs$. Moreover, we can use a spectrometer to check the output spectra of laser pulses, which is shown in Figure 3.23(b). From this figure, we can see the output spectral region of laser beam has a Gaussian shape distribution and the spectral range is from around $760nm$ to $830nm$, which is also the detecting range in the spectral pump probe experiments.

Then, a beamsplitter is used to split the source laser into two parts. The reflection part has 98% power and transmitted part has around 2% power. The transmited beam is used as the probe and the reflected beam as the pump. The optical path length of the probe pulses can be automatically adjusted by a retroreflector, which is mounted on a motorised, one dimensional translation stage with sub-μm control. As we know the light velocity is 3.0×10^8m/s, $1fs$ corresponds to a $0.15\mu m$ movement of the retroreflector. Considering the time width of pulses $60fs$, the scanning step is set as $50fs$, corresponding

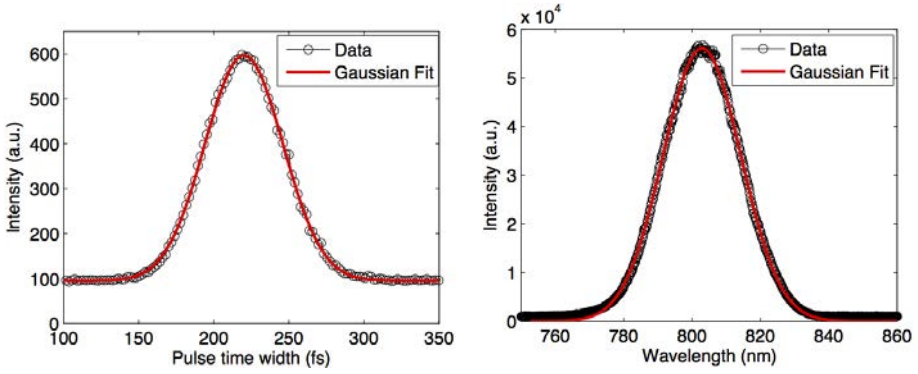

(a) (b)

FIGURE 3.23: (a)Time width of laser pulse data shown as black circle line and Gaussian fitting shown as red line; (b) Spectral distribution of the output laser: black circle line is the data and red line is the Gaussian fit.

to $7.5\mu m$ step distance for retroreflector. Through this method, we can precisely control the time delay between probe pulse and pump pulse. Then, the probe beam is attenuated to be less than $5\mu W$ by a neutral density filter. The polarisation of probe beam is adjusted through a polariser. The pump beam traverses a fixed optical path. We can also utilise the light frequency converter (TOPAS) to convert the $800nm$ of the input laser into other spectral laser pulses in the optical path of pump beam. As laser beam need pass through several nonlinear crystals inside of TOPAS, the time width of pump pulse was stretched. Then, the average power of pump beam can be adjusted using an attenuator, basing on a combination of a rotatable half wave plate and near Brewster angle reflection from a prism. After the prism reflection, the pump beam is $s-$ polarised. But, the final polarisation of pump beam can be determined by another half wave plate.

If the spectra of the pump and probe beam are identical with each other, we set the polarisation to be orthogonal to each other to avoid interference. Moreover, the transmitted and reflected pump beam are both blocked. The sample is mounted on a holder, which can be rotated to perform different incident angle measurements. The pump and probe spots diameter are focused to $\sim 500\mu m$ and $\sim 50\mu m$ respectively on the sample surface by different lenses. Their non-collinear spatial overlap is checked using a CCD camera with magnifying lens. The angle difference between probe and pump beam is set at $\sim 20°$. Then, the transmitted and reflected probe beam are measured by biased silicon photodiodes connected to separate lock-in amplifiers. We can also replace the two photodiode detectors with two spectrometers to perform the spectroscopic reflection and transmission measurements in the probing spectral range from $770nm$ to $820nm$. The measured signal intensity as the function of time delay and spectra can indicate the interesting observations on sample's properties, including the electronic band structure, plasma frequency, absorption and scattering dynamics[22, 170].

3.4.2 Pump-probe Ellipsometry

From the pump probe reflection and transmission measurements, we can only detect the information about amplitude variation of the probe beam as a function of the time delay and the probe wavelength. However, as we mentioned before, the spectroscopic ellipsometry can not only get the amplitude ratio information between $p-$ and $s-$ polarised components, but also reveal the phase difference between them. If we can combine the ellipsometry technique with the pump-probe approach, the dielectric function $\epsilon = \epsilon_r - i \cdot \epsilon_i$ of the excited state medium can be determined more precisely. The technique of rotating compensator ellipsomety (RCE), which has been illustrated in section 3.2.3.3, is combined into pump probe measurement and PSC_RA (polariser-sample-rotating compensator-analyser) configuration is set into probe beam. The pump beam is still used to excite the sample. The schematic is shown in Figure 3.24.

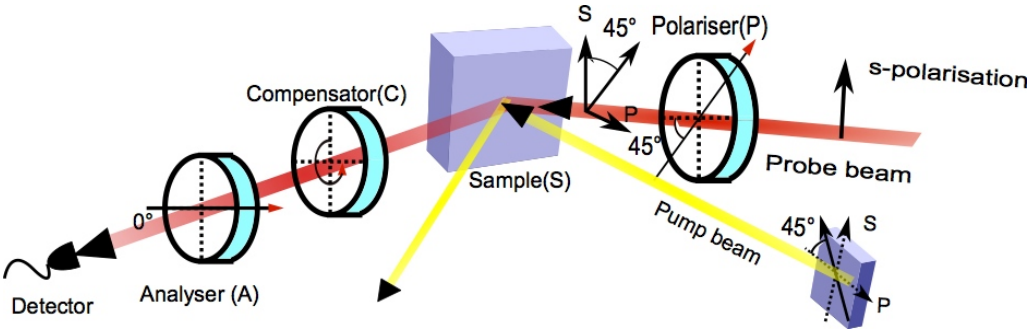

FIGURE 3.24: Schematic of pump probe rotating compensator ellipsometry system. After the pump beam excites the sample, the 45° linear polarised probe beam, which is defined by a polariser, interacts with the excited state of sample under a fixed time delay (t). Then, the residual of reflected probe beam transmits through a compensator ($\lambda/4$ wave plate) and an analyser before being detected by a photodiode or spectrometer. After detecting the reflected light intensity with rotating compensator angle from 0° to 360°, the $\psi(\lambda, t), \Delta(\lambda, t)$ can be obtained finally for this fixed time delay.

After the pump beam excites the sample, the time delay between probe and pump can be fixed at a value (t) by controlling the optical path length of probe beam. Then, the non-collinear incident probe beam with $s-$ polarised sate is firstly adjusted to 45° linear polarisation by an Edmund optics linear high-contrast (10000 : 1) glass broadband ($750nm - 1400nm$) polariser, which is prior to impinging upon the excited area of sample. The 45° linearly polarised state is necessary to simplify the progress of processing measurement data, which provides the equal amplitudes and equal phases of light waves in $p-$ and $s-$ polarised directions. After interacting with the excited area of sample, the residual of reflected probe beam will pass through a combination of rotating compensator and 0° analyser. Then, the signal is detected by a photodiode or spectrometer. The compensator is an Edmund Optics broadband ($700 - 1000nm$) achromatic quarter ($\lambda/4$) wave plate, precisely controlled by a New Focus motorised 'ground-worm gear'

rotation mount, providing the accurate rotation of the optic to 0.01°[22]. The analyser is a Thorlabs Glan-Thompson polariser with an extinction ratio of 100000 : 1 and the operating spectral range can be from $350nm$ to $2.3\mu m$. Finally, while rotating the compensator from 0° to 360° and identifying with the analyser, the intensity of reflected probe beam is detected by a spectrometer. In summary, the detected intensity is the function of probing spectrum, compensator angle and time delay, which denotes as $I_{probe}(\lambda, C, t)$. Data $I_{probe}(\lambda, C, t)$ will be further processed to obtain the ellipsometry parameters $(\psi(\lambda, t), \Delta(\lambda, t))$ according to the Boer's method[128] in section 3.2.3.3. Then, the time delay can be moved to another value and the same process is still applied to find the corresponding ellipsometry parameters. It is also worth mentioning that the polarisation of pump beam should be orthogonal to the probe in pump probe ellipsometry measurement to avoid interference.

As we discussed in section 3.2.3, the pump probe ellipsometry approach has more advantages. Especially for multilayer structured opaque sample with low absorption coefficient, the pump probe ellipsometry can be an ideal choice to monitor the variation of the dielectric function. As the phase difference Δ has a large change at around Brewster's angle, the incident angle of probe beam is set at around Brewster angle of sample for the accurate ellipsometry measurement[99]. However, the pump probe ellipsometry is not always useful for all samples. When the sample is hard to be excited, the high pump fluence is normally needed. The RCE system needs around ten minutes to rotate the compensator from 0° to 360° in one measurement. This long time detection at each time delay could destroy the sample due to the accumulation of heating from the pump excitation. The porous silicon material is quite easy to damage with long detection time, due to the low thermal conductivity[171, 172]. So, the pump probe reflection and transmission will be the better choices to research ultrafast dynamics property of this material.

3.4.2.1 Polariser and Analyser Calibration

From the setup, we can see the polariser angle should be at 45° and analyser angle should be exactly at 0°. Thus, before performing the measurements, it is necessary to calibrate the analyser (A), polariser (P) and compensator (C) scales for reducing the systematic errors in RCE system and ensuring the reliability of measurement[173]. The calibration is particularly important. Because a very small deviation of the optical element can lead to a large error in ellipsometry parameters (ψ, Δ), especially when the sample in question has a low absorption coefficient[174].

The method for calibrating the polariser (P) and analyser (A) is discussed by McCrackin *et.al.*[100] and then improved by Ghezzo[175]. Firstly, the compensator is taken out of the probe beam PSC_RA configuration and the pump beam is blocked. Then the polariser angle (P) is rotated to approximately 0°, of which fast axis is parallel to the plane of incidence. The analyser angle (A) is rotated to about 90°, of which fast axis is approximately perpendicular to the incident plane. A highly reflective surface sample is put into the sample holder, which normally is a chemically-mechanically polished crystalline silicon slice. We know the ellipsometry parameter Δ of c-Si experiences a big change of π when the incidence angle is at Brewster's angle 75°, which is shown as Figure 3.7(a). This property is applied to calibrate P and A. The incident angle of probe beam is chosen to be below the silicon Brewster angle 75° in the first case. Referring to McCrackin[100], the intensity of detected light can be written as

$$I = 4L^2 + \frac{4\chi^2}{tan^2\psi sin^2\delta} - \frac{8L\chi}{tan\psi}(\frac{cos\Delta}{tan\delta} - sin\Delta) \ . \tag{3.84}$$

Where $L = A - \pi/2$, δ is the phase difference between $p-$ and $s-$ components of the transmitted light waves from polariser and χ is related to the polariser angle as[100]:

$$P = \chi/tan\delta \ . \tag{3.85}$$

Using above two equations 3.84 and 3.85, the expression of intensity I can be rewritten as

$$I = 4L^2 + \frac{4}{tan^2\psi}(\chi^2 + P^2) - \frac{8L}{tan\psi}(Pcos\Delta - \chi sin\Delta) \ . \tag{3.86}$$

As the analyser angle A is at around 90°, a minimum detected light intensity can be acquired by requiring the polariser angle P satisfies $\partial I/\partial P = 0$. Thus, the following equation 3.87 can obtained with considering $\delta = 0$:

$$P = (A - \pi/2)tan\psi cos\Delta \ . \tag{3.87}$$

Regarding the equation 3.87, where ψ, Δ are both constant values, if the polariser angle P and analyser angle A are satisfied in this relation, the minimum detected intensity can be obtained. Thus, a set of data (A, P) can be found under one probing incident angle, which are shown as one of linear lines in Figure 3.25. This procedure is repeated for three different incident angles, where red black and pink lines data are acquired under $55°, 65°, 80°$ respectively. As another incident angle is used, another new set of linear curve data can be obtained, which can formulate as following equation

$$P = (A - \pi/2)tan\bar{\psi}cos\bar{\Delta} \ . \tag{3.88}$$

Eliminating the $A - \pi/2$ from equation 3.87 and 3.88, we can get

$$P(1 - \frac{tan\psi cos\Delta}{tan\bar{\psi} cos\bar{\Delta}}) = 0 \tag{3.89}$$

If the one incident angle is bigger than Brewster's angle of the polished c-Si and another one is smaller, the following relation can be obtained[100]

$$\frac{tan\psi cos\Delta}{tan\bar{\psi} cos\bar{\Delta}} < 0 \ . \tag{3.90}$$

As we have realised that the relation $(tan\psi cos\Delta)/(tan\bar{\psi} cos\bar{\Delta}) \neq 1$ can be satisfied under the any two different incident angles detection for polished c-Si, so the $P = 0$ is the only solution of equation 3.89, which corresponds to $A = 90°$ in term of equation 3.87 or 3.88. The acquired data curves will be intersected in one point, which looks like in Figure 3.25. From this crossing point, both of the polariser and analyser are accurately calibrated. The true position of polariser and analyser can be aligned with the scale readings on the housing of these optics. Moreover, it will be difficult to align P and A when incidence angle is at Brewster's angle, which is shown as the flat blue line relationship between P and A under 75° Brewster angle of c-Si in Figure 3.25.

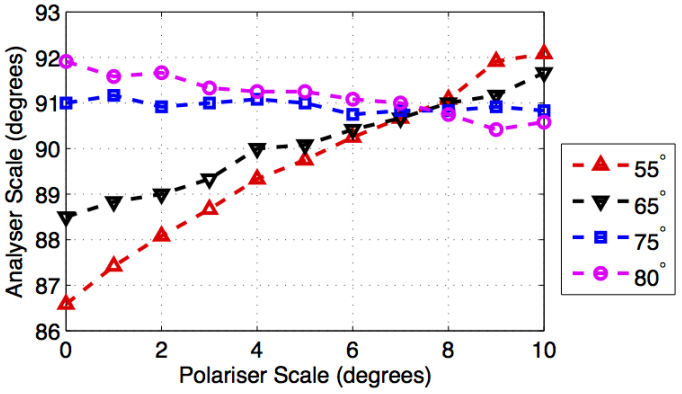

FIGURE 3.25: Calibration of the azimuths of polariser and analyser for pump probe RCE system. The four lines correspond to different incident angles of probe beam, and the exactly orthogonal point between $P = 0°$ and $A = 90°$ is picked from the four lines crossing point, of which housing scales read $P^{'} = 7.5°$ and $A^{'} = 90.85°$.

3.4.2.2 Compensator Calibration

After calibrating the polariser and analyser, the polariser angle $P = 45°$ and analyser angle $A = 0°$ can be accurately fixed. Next, we need to calibrate the compensator $\lambda/4$ wave plate. Firstly, the compensator is put back to the original position and the sample is removed from the PSC_RA configuration. Then, the reflective arm is moved to the straight line with the incident arm of probe beam. At the moment, the probe beam setup looks like PC_RA configuration and pump beam is still blocked. The probe

beam intensity is measured by a photodiode with rotating the compensator angle from 0° to 360°, which shows data as $I(C)$. The positive rotating direction is defined as counterclockwise rotation when looking down the propagation axis toward the light origin, which is shown in Figure 3.24. Meanwhile, we can also simulate this measurement results by an optical model calculation using Jones Matrixes in table 3.1.

$$L_{out} = A \cdot R(A) \cdot R(-C) \cdot C \cdot R(C) \cdot R(-P) \cdot P \cdot L_{in} \tag{3.91}$$

As $P = 45°$ and $A = 0°$, the theoretical simulation results can be compared to the experimental data, which is displayed by red solid line and black dot line in Figure 3.26. The difference of first minimum point between data and simulation results demonstrates a small shifting is needed for the scale alignment of compensator to make the two curves overlapping with each other, which shows the shifting of scale is $\sigma = 4.58°$. The appendix A.2 introduces more information about compensator calibration model in Matlab program.

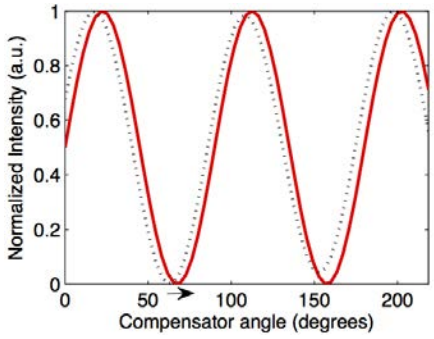

FIGURE 3.26: Calibration of compensator ($\lambda/4$ wave plate) angle. The intensity of light is measured in a PC_RA configuration without sample. Comparing the theoretically predicted value (red solid line) with experimental data (black dotted line), the mismatch $\sigma = 4.58°$ in the aligning compensator angle C can be obtained.

3.4.2.3 Accuracy of the Ellipsometry Setup

As the polariser analyser and compensator of probe beam RCE system have been fully calibrated, the final step is to obtain the $(\psi(\lambda), \Delta(\lambda))$ through fitting Fourier coefficients from detected data $I(\lambda, C)$. The data of $I(C)$ under each probe spectra corresponds to the (ψ, Δ) of a sample under this wavelength and the detailed derivation process for $I(C)$ to (ψ, Δ) has been illustrated in Section 3.2.3.3. The intensity I shows the harmonic contributions of second and fourth order[128] as the compensator azimuth angle C rotating from 0° to 360°, which can be expressed as equation 3.59. From fitting Fourier coefficients, the corresponding (ψ, Δ) can be obtained according to equation 3.64.

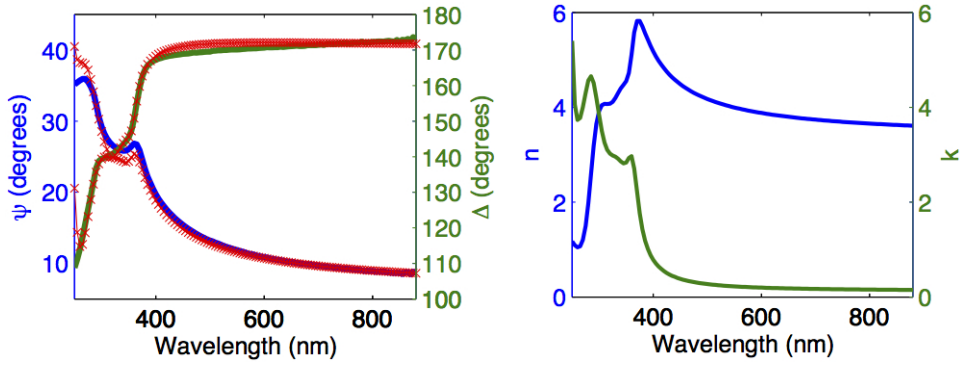

(a) (b)

FIGURE 3.27: (a)Data (ψ, Δ) measured from commercial ellipsometry under 70° incident angle for polished c-Si, blue line is ψ and green line is Δ, the red lines are the Forouhi-Bloomer optical model fitting; (b)complex refractive index $N = n - i \cdot k$ of polished c-Si from optical model fitting.

In order to demonstrate the accuracy of the probe beam RCE system, we measured a polished crystal silicon (c-Si) sample with our ellipsometer and compared to the data from the commercial ellipsometer. $(\psi(\lambda), \Delta(\lambda))$ were obtained from Horiba commercial ellipsometry under 70° incident angle in the spectral range from $250nm$ to $900nm$. Using the four terms Forouhi-Bloomer optical model simulation, which has been described in section 3.3.1, the complex refractive index $N = n - i \cdot k$ of polished c-Si can be fitted. Figure 3.27(a) describes the data and red lines fitting results, and Figure 3.27(b) is the complex refractive index from optical model fitting. Then, the same polished c-Si is remeasured by the probe beam ellipsometry under the same conditions. Meanwhile, the incident angle 70° needs to be precisely identified. Considering the (ψ, Δ) of c-Si has the big change at Brewster angle 75°, the incident angle of probe beam is spanning from around 55° to 80° for measuring (ψ, Δ). The photodiode is used to detect the intensity at compensator angle $I(C)$ and the data is shown in Figure 3.28. As we can see, the (ψ, Δ) experienced big changes at 75° incident angle, which calibrates the accurate incident angle of the probe beam. Applying the (n, k) values at $800nm$ from Figure 3.27(b), the theoretical (ψ, Δ) values can be calculated at increasing incidence angle, which are shown as red solid lines in Figure 3.28. The experimental data match very well with the theoretical red lines.

After checking the incident angle of probe beam, the polished c-Si can be remeasured by this probe beam RCE system with a spectrometer as the detector at a 70° incidence angle. The obtained results from probe beam ellipsometry are plotted together with the data from commercial ellipsometry, which are shown in Figure 3.29. The dotted lines representing probe beam ellipsometry data are coincident very well with commercial ellipsometry data (solid lines). From this, the accuracy of probe beam ellipsometry is demonstrated, and it is good enough to precisely exploit the ellipsometry information

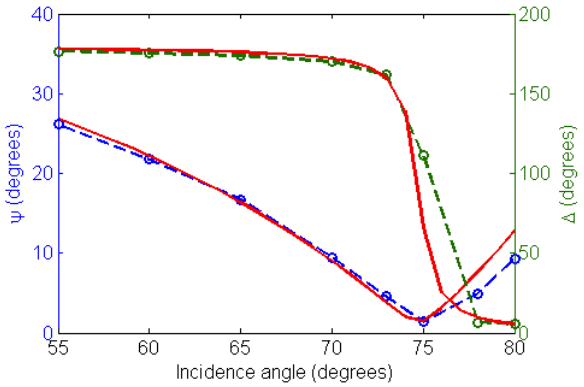

FIGURE 3.28: Data (ψ, Δ) of polished c-Si measured by probe beam ellipsometry with spanning incident angle from 55° to 80°; the circle dashed blue line is ψ and green line is Δ and red solid lines are from theoretical calculation.

from a sample. Actually, in the Figures 3.16 and 3.20 of Section 3.3.3, the probe beam ellipsometry has been applied to measure the (ψ, Δ) of nc-Si:H and PS samples, which are both consistent with the data from the commercial ellipsometer relevant to the probe spectral range.

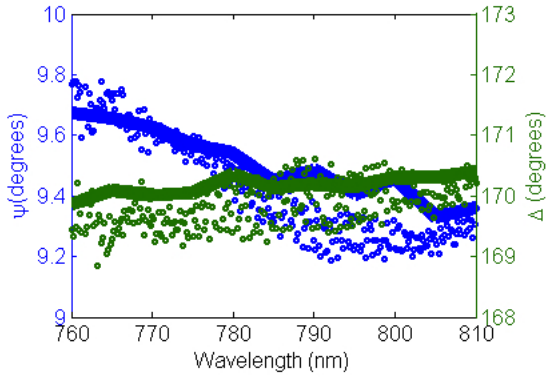

FIGURE 3.29: Accuracy calibration of probe beam ellipsometry. Blue and green solid lines are measured by commercial ellipsometry; blue and green dotted lines are from probe beam ellipsometry.

Finally, combining the probe RCE ellipsometer and pump excitation, the time resolved pump probe ellipsometry system is created. The probe beam ellipsometry can measure the $(\psi(\lambda), \Delta(\lambda))$ of a sample under different time delays after the pump beam excitation. By controlling the time delay t between pump and probe pulses, the final ellipsometry parameters $\psi(\lambda, t)$ and $\Delta(\lambda, t)$ can be obtained. From observing ellipsometry parameters variation as increasing time delay, the decay process of excited state sample can be depicted.

3.4.3 Pump Probe Data Analysis

Once we obtained the data to express the optical properties of excited state sample, through measurements of the pump probe reflection, transmission and ellipsometry, the data analysis process needs to be done to reveal the ultrafast dynamics information. As the pump photons energy is bigger than the energy band gap of the sample, the pump beam excites the sample creating the free carriers (electron-hole) plasma by the pump photons absorption via the inter-band transition. Sometimes, especially at low temperature and in pure samples, excitons can be mainly excited in the material. While, in our case, the excited dense quasi free carriers screen the Coulomb interaction of the exciton and make them dissociate, producing free electron-hole pairs. Moreover, the experiment is performed under room temperature, which also inhibits the formation of excitons. Thus, the optical properties of excited sample are mainly influenced by the free carriers.

A lot of previous works have been done to investigate the generation and the optical properties of dense electron-hole plasma, among them published works by K.Sokolowski *et al*, A.J. Sabbah *et al* and others[9, 17, 42, 176, 177]. When a semiconductor is excited by a high intensity of the pump beam, the probed signal variation in the dielectric function can be attributed to two physical effects, which are associated with free-carrier absorption and an energy band change. Moreover, the energy band change can be due to inter band transition and nonlinear absorption of pump beam, including three separate parts: (i) state and band filling, (ii) lattice temperature changes, (iii) band gap renormalisation. So, the total four mechanisms contribute independently to the dielectric constant ϵ of the excited material, which can be described by the following expression:

$$\epsilon = \epsilon_{back} + \Delta\epsilon_{fcr} + \Delta\epsilon_{sbf} + \Delta\epsilon_{ltc} + \Delta\epsilon_{bgs}. \tag{3.92}$$

Where ϵ_{back} is the background dielectric constant of the material without pump excitation, which illustrates the optical properties of inter band transitions and lattice vibration absorption. Through the common optical spectroscopic measurement methods and the corresponding optical model simulation, which have been discussed in section 3.2 and 3.3, the ϵ_{back} can be obtained. The $\Delta\epsilon_{fcr}, \Delta\epsilon_{sbf}, \Delta\epsilon_{ltc}$ and $\Delta\epsilon_{bgs}$ are corresponding to the four physical mechanisms induced by the pump excitation: free carriers response, state band filling, lattice temperature change, band gap renormalisation respectively. Furthermore, from the theoretical predictions on optical measurement of crystalline silicon as a function of excited electron-hole density in the Sokolowski *et al* work[17], we can

see that free carriers response dominates the optical property of the excited state, especially under the higher excited carriers concentration. This means that the only effect of the free carrier response can be sufficient to interpret the optical measurement results of the probe beam followed excitation by the pump. This has also been demonstrated in other works on crystalline silicon, amorphous silicon, and other semiconductor materials, in which the free carrier response gives a great contribution to the optical properties of excited material[4, 18, 42, 178].

As the pump beam excited the semiconductor material, the inter band transition process can happen and lead to the generation of free carriers (electrons and holes), which are moving in the conduction band or valence band. In order to consider the band structure and Coulomb interaction effects on carrier movement, the effective mass m^* rather than the free electron or hole mass m_e, m_h is assumed for the carriers. Then, the probe beam is applied to reveal the following intra band process of free carriers by detecting optical property of the excited material. As the electrons (holes) are excited into the conduction (valence) band, the carrier-carrier scattering process will happen and the excess energy will also be lost gradually by emitting phonons. Generally, these intra band quasi free carriers processes yield values of the effective mass, the scattering mechanism of carriers and of collective excitations like plasmons[135].

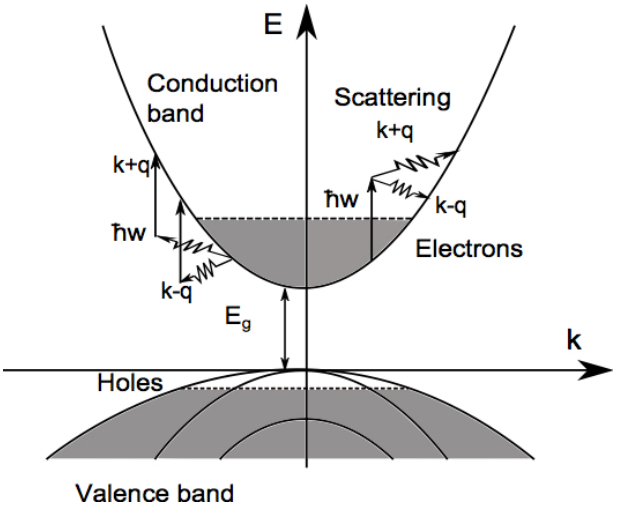

FIGURE 3.30: Schematic of two steps free carriers absorption process in the conduction band of semiconductor material, k wave vector represents the momentum of particles and E is energy level of the energy band. The absorption of a photon can only lead to a electron transition in vertical E axis; the absorption or emission of a phonon or scattering by a impurity can realise the horizontal k axis change.

Figure 3.30 shows some basic intra band processes of the excited free carriers. The direct intra band transitions between two states k and k' (wave vectors) can not be possible unless the absorbing or emitting a photon $\hbar\omega$ occurs simultaneously. Because the photon absorption or emission is only a vertical process in the $E_n - k$ (energy

and momentum) plane and the photon only has a very small momentum comparing to carriers. Therefore, in order to change the carrier's momentum significantly and realise the intra-band transition between occupied states below the Fermi level to an unoccupied energy state above Fermi energy level, some momentum conservation is involved. The mechanisms, which can contribute to the momentum conservation process in the intra-band free carrier transition, include phonon scattering and scattering from the ionised impurities. As shown in Figure 3.30, an electron can absorb a photon first and then emit $(k-q)$ or absorb $(k+q)$ a phonon to realise the intra band transition. Or, an electron can also scatter by absorbing or emitting a phonon to change the momentum. Then, it can absorb a photon to realise energy level transition. Similarly, in the valence band, the free hole intra band transition can also occur with help of photons and phonons. As a simple approximation, Drude model is applied here to illustrate the free carriers optical property in the presence of the probe electric field[83, 88, 99, 135, 179].

3.4.3.1 Free Carriers Absorption

Actually, the Drude model is typically applied for researching the optical properties of the free electron gas, such as metals containing dense free electrons. Free electron systems do not experience a restoring force in the medium when driven by the electric field of the probe. As for the excited semiconductors, we need to consider the fact that the electrons or holes are moving in the conduction or valence band. This is taken into account by assuming the carriers behave as particles with an effective mass m^* rather than the free electron mass m_e. In order to derive the Drude equation for describing the dielectric function of free electrons system, the classical Lorentz oscillator model (Equation 3.65) is used without the restoring force term, which has been discussed in section 3.3.1. Thus, the oscillation of a free electron induced by the probe beam AC electric field $E(t) = E_0 e^{i\omega t}$ can be expressed as the following equation:

$$m_e \frac{d^2x}{dt^2} + m_e \Gamma \frac{dx}{dt} = -eE(t) = -eE_0 e^{i\omega t}, \tag{3.93}$$

where ω is the angular frequency of the probe light and E_0 is its amplitude. The damping rate is Γ. The first term represents the acceleration of the electron and second term is the frictional damping force of the medium. The right hand side term is the driving force exerted by the probe. Considering the electron velocity $v = \dot{x}$, the equation 3.93 can be rewriten as

$$m_e \frac{dv}{dt} + m_e \Gamma v = -eE(t)\ . \tag{3.94}$$

Then, the momentum p can substitute $m_e v$ to give

$$\frac{dp}{dt} = -\frac{p}{\tau} - eE(t), \tag{3.95}$$

where damping time $\tau = 1/\Gamma$, which means the electron loses its momentum in time τ. So, τ is also termed as momentum scattering time. By looking for the solutions of motion with $x = x_0 e^{i\omega t}$ and $v = v_0 e^{i\omega t}$, we can obtain

$$x = \frac{eE_0}{m_e(\omega^2 - i\Gamma\omega)}, \qquad v(t) = \frac{-e\tau}{m_e}\frac{1}{1+i\omega\tau}E(t)\ . \tag{3.96}$$

As for the semiconductor, m^* should replace the m_e. Furthermore, the background relative permittivity, due to inter band transition or lattice vibration absorption, need also to be considered. The free carriers polarisation is described as $P_{free\ carrier} = -N_{eh}ex$, where N_{eh} is the number of carriers per unit volume. The electric displacement can be formulated as:

$$\begin{aligned} D &= \epsilon\epsilon_0 E \\ &= \epsilon_0 E + P_{back} + P_{free\ carrier} \\ &= \epsilon_{back}\epsilon_0 E - \tfrac{N_{eh}e^2 E}{m^*(\omega^2 - i\Gamma\omega)}. \end{aligned} \tag{3.97}$$

The term P_{back} accounts for the background polarisability of bound electrons, apart from free carriers polarisation $P_{free\ carrier}$. The effective mass m^* represents the band structure's influence on excited free carriers in the semiconductor, which is approximated as $m^* = (m_e^{*-1} + m_h^{*-1})^{-1}$, where m_e^{*-1} and m_h^{*-1} are the effective masses of electrons and holes. N_{eh} is the free carrier concentration (of electron-hole pairs) generated by the pump beam excitation. Therefore, the dielectric constant of a photon excited semiconductor, which is also dependent on the angular frequency of probe beam, is finally given by

$$\epsilon = \epsilon_{back} - \frac{N_{eh}e^2}{m^*\epsilon_0}\frac{1}{\omega^2 - i\Gamma\omega} \tag{3.98}$$

The plasma frequency ω_p is defined as

$$\omega_p^2 = \frac{N_{eh}e^2}{m^*\epsilon_0}. \tag{3.99}$$

So, the final dielectric function of excited semiconductor can be briefly formulated as

$$\epsilon = \epsilon_{back} + \Delta\epsilon_{fca} = \epsilon_{back} - \frac{\omega_p^2}{\omega^2 - i\Gamma\omega} \tag{3.100}$$

Consequently, from the dielectric constant expression, the two important parameters plasma frequency, ω_p, and the scattering rate, Γ, are used to describe the ultrafast dynamics of photon excited free carriers plasma. ω_p involves the information about the

excited carriers concentration and effective mass, and Γ reveals the carrier-carrier or carrier-phonon scattering mechanism of photon excited semiconductor. The complex dielectric function variation, due to free carriers absorption response $\Delta\epsilon_{fca} = \Delta\epsilon_1 - i \cdot \Delta\epsilon_2$, can be split into real part and imaginary part as following formulas:

$$\Delta\epsilon_1 = -\frac{\omega_p^2}{\Gamma^2 + \omega^2} \ , \qquad \Delta\epsilon_2 = \frac{\omega_p^2 \Gamma}{\omega(\Gamma^2 + \omega^2)} \ . \tag{3.101}$$

As we can see from above equations, ω_p and Γ both influence the real part and imaginary part of $\Delta\epsilon_{fca}$. In the pump probe work here, the angular frequency ω of probing light is fixed at around $2.36 \times 10^{15} rad/s$ corresponding to the probing wavelength $800nm$. The damping time $\tau = 1/\Gamma$ can be dependent on the excited carriers concentration and lattice temperature. At low carrier concentration, the carrier-phonon collisions ($\tau = 10^{-13}s$) dominate carrier relaxation[17]. For higher concentration, the carrier-carrier collisions, in which the total momentum is conserved, are considered to be responsible for the lower damping time ($\tau = 10^{-15}s$) in femtosecond time scale, which is observed in previous high-carrier concentration experiments[180]. In the next step, using these equations, we will introduce the new fitting program to fit the data from pump probe reflection transmission and ellipsometry measurements. Then, from the obtained ω_p and Γ, we can realise the ultrafast dynamics property of the material.

3.4.3.2 Fitting Process

Until now, the optical properties of a photo excited semiconductor can be simply represented as dielectric function equation 3.100. In the equation 3.100, the ϵ_{back} expresses the dielectric constant of unexcited state material, considering the inter band transition or lattice vibration absorption properties. It can be obtained through the flowchart of simulation procedure for fitting spectroscopic ellipsometry or reflection and transmission measurement data in section 3.3.3. $\Delta\epsilon_{fca}$ indicates the dielectric constant variation, induced by the free carriers absorption response due to pump photons excitation. Furthermore, in order to fit the pump probe measurement data, we need to modify the simulation program of the fitting flowchart in section 3.3.3.

Figure 3.31 illustrates the new flowchart of fitting pump probe data procedure. Firstly, the optical model of excited state sample is constructed considering the background optical property ϵ_{back} and free carriers absorption respnse (FCA) induced optical property $\Delta\epsilon_{fca}$. So, the modelling of dielectric function of this excited state can be expressed as $\epsilon = \epsilon_{back} + \Delta\epsilon_{fca}(\omega_p, \Gamma)$. As we mentioned before, ϵ_{back} can be identified from common optical spectroscopy measurement methods, such as reflectance, transmittance and ellipsometry. Then, $\Delta\epsilon_{fca}(\omega_p, \Gamma)$ is simply formulated by the Drude model, which is shown

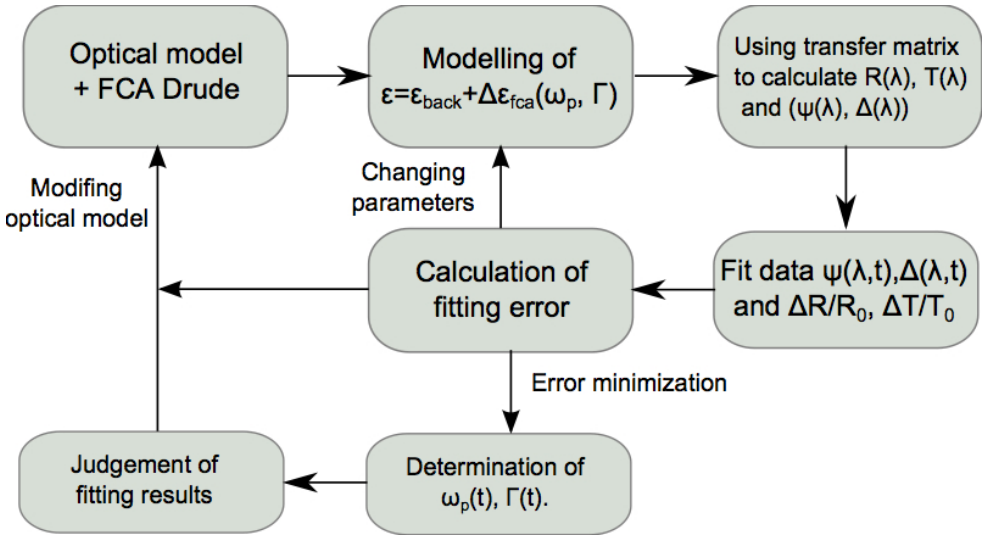

FIGURE 3.31: Flowchart of fitting pump probe measurement data procedure. The optical model of excited state semiconductor includes the background dielectric constant ϵ_{back}: inter band transition or lattice vibration absorption, and dielectric constant variation $\Delta\epsilon_{fca}$, induced by free carriers absorption response (FCA). The modelling of optical property is described as $\epsilon = \epsilon_{back} + \Delta\epsilon_{fca}(\omega_p, \Gamma)$. Applying the transfer matrix method, the reflectance $R(\lambda)$, transmittance $T(\lambda)$ and ellipsometry data $(\psi(\lambda), \Delta(\lambda))$ can all be calculated. Then, fitting the pump probe data,$\psi(\lambda,t), \Delta(\lambda,t), \Delta R/R_0, \Delta T/T_0$, and minimising the error at each time delay, the $\omega_p(t), \Gamma(t)$ can be finally determined.

as equation 3.101. As long as setting the reasonable values of two parameters ω_p and Γ in Drude equation, the dielectric function of excited state sample can be retrieved. The reflectance $R(\lambda)$, transmittance $T(\lambda)$ and ellipsometry $\psi(\lambda), \Delta(\lambda)$ of excited state sample can be all calculated out regarding the information of incident angle and sample structure. The transfer matrix method is still used in the calculation, which has been introduced in section 3.2.2.

However, the pump probe reflection and transmission measurement data are expressed as $\Delta R/R_0 = [R(\lambda,t) - R(\lambda,0)]/R(\lambda,0)$ and $\Delta T/T_0 = [T(\lambda,t) - T(\lambda,0)]/T(\lambda,0)$ respectively. $R(\lambda,0)$ and $T(\lambda,0)$ are the reflectance and transmittance of characterised sample before the pump beam excitation. This means the $R(\lambda,0), T(\lambda,0)$ can be calculated out only using ϵ_{back} in the transfer matrix method and they can also be measured from the common optical spectroscopy methods. The subscript 0 here is just used to indicate there is no pump beam perturbation. Then, after the pump beam excitation, the reflectance and transmittance of probe beam are represented by $R(\lambda,t)$ and $T(\lambda,t)$ separately under each time delay. Combining the free carrier absorption induced variation $\Delta\epsilon_{fca}$ with ϵ_{back} to express the new dielectric constant of excited state sample, the new $R(\lambda,t), T(\lambda,t)$ can also be calculated and the final simulation results of $\Delta R/R_0, \Delta T/T_0$ can be obtained. Finally, these calculated results $\Delta R/R_0, \Delta T/T_0$ are used to fit the measurement data and minimise the fitting error by adjusting the Drude model parameters $(\omega_p(t), \Gamma(t))$ for each time delay.

In the pump-probe experimental setup, only the reflection intensity, $I_r(\lambda, t)$, and transmission intensity, $I_t(\lambda, t)$, are measured. So, the final results of the reflectance and transmittance changes are expressed as following formula 3.102, where $I_r(\lambda, 0), I_t(\lambda, 0)$ are the detected probe intensity before the pump pulse excitation.

$$\Delta R/R_0 = \frac{I_r(\lambda, t) - I_r(\lambda, 0)}{I_r(\lambda, 0)} \ , \qquad \Delta T/T_0 = \frac{I_t(\lambda, t) - I_t(\lambda, 0)}{I_t(\lambda, 0)} \ . \tag{3.102}$$

The ellipsometry data $\psi(\lambda, t)$ and $\Delta(\lambda, t)$ can be obtained from the pump probe RCE system measurement. Then, the calculation results and measurement data of $\psi(\lambda, t), \Delta(\lambda, t)$ can be compared with each other straightforwardly. From the minimisation of fitting errors between the calculation and the measurement values, the ultrafast dynamics parameters $\omega_p(t), \Gamma(t)$ can be determined as a function of the time delay. If the final fitting results are not reasonable, the optical model should be modified to improve the fitting process. For example changing the structure parameters, then, the fitting errors are iteratively minimised again by adjusting $\omega_p(t)$ and $\Gamma(t)$. After judging the reasonableness of the fitting results, the decay processes of $\omega_p(t), \Gamma(t)$ are eventually realised.

3.5 Summary

In summary, to characterise the ultrafast dynamics of semiconductor samples, the dielectric function of unexcited state sample ϵ_{back} need to be found first. Thus, the common optical spectroscopy methods are used here, such as the measurements of reflectance R, transmittance T and ellipsometry (ψ, Δ). So, the principles of these techniques are introduced. Then, to determine the ϵ_{back}, a corresponding optical model need to be constructed referring to the optical structure of the sample. Applying the transfer matrix calculation method, the measurement data can be simulated. As the ϵ_{back} is obtained, the pump probe measurement data can be analysed. In the pump probe measurement, after the pump beam excites the sample, the reflection, transmission and ellipsometry methods can still be applied for the probe beam to monitor the optical property variation of the excited sample for each time delay. This excited state optical property can be simply described by $\epsilon = \epsilon_{back} + \Delta\epsilon_{fca}(\omega_p, \Gamma)$, where the second term is induced by the excited free carrier absorption response and formulated by Drude model. After modifying the optical model with Drude equation, the transfer matrix method is applied again to fit the pump probe data and acquire the ultrafast dynamics parameters $\omega_p(t)$ and $\Gamma(t)$ as function of time delay. From these two parameters decay process, we can discuss the ultrafast dynamics property of the sample, such as the mechanisms of excited carriers relaxation and the excess energy release.

As the researched samples in this thesis are hydrogenated nano crystalline silicon (nc-Si:H) and porous silicon (PS), there are two phases composing the material nc-Si:H (nano clusters c-Si embedding into amorphous silicon matrix α-Si) and Porous silicon (nano wires c-Si mixing with voids). The Bruggeman effective medium approximation (EMA) is used for both of them in the optical model simulation to represent the effective dielectric response for the probe. With the help of these measurement techniques and simulation methods, the ultrafast dynamics properties of nano semiconductor samples can be discussed more deeply.

Chapter 4

Pump Probe Reflection and Ellipsometry of nc-Si:H

4.1 Introduction

In this Chapter, we characterise the ultrafast dynamical properties of a nc-Si:H sample using the pump probe reflection and ellipsometry techniques. Firstly, we discuss the influence of the probe beam polarisation on the intensity of the reflected signal, which is also related to the probing incidence angle. The 45° linear polarised state is used in both pump probe reflection and ellipsometry measurements. Then, multiple probing incident angle experiments were performed to precisely determine the ultrafast dynamics parameters plasma frequency ω_p and scattering rate Γ with changing time delay. We found that Γ is dependent on ω_p when the carrier-carrier scattering mechanism dominates the scattering process. Then, the pump fluence was gradually increased, to estimate the effective mass of excited free carriers as $m^* \approx 0.17m_e$. Furthermore, from the extracted carrier concentration change as a function of the time delay, the carrier recombination process is discussed and analysed to determine the carrier recombination coefficients. Apart from the discussion of the relaxation mechanism, the DC (direct current) conductivity change as a function of the pump photon energy is also researched for nc-Si:H sample using a light frequency converter (TOPAS). The analysis of the conductivity revealed that the carrier thermal dynamic distribution can be better described by the classical Maxwell Boltzmann statistics. Lastly, the pump probe ellipsometry technique is used to characterise the excited state nc-Si:H sample as well. We realise the decay processes of dielectric constant and absorption coefficient of nc-Si:H material, and the conductivity decay process is also accurately determined.

4.2 Influence of Probe Beam Polarisation

In order to see the influence of the probe beam polarisation on the measurement results, the polarised state of probe beam is adjusted to $s-, p-$ and 45° linear polarisation through rotating the polariser respectively, in the pump probe reflection measurement of nc-Si:H sample. The experimental setup is shown in Figure 3.22. The pump beam spectra are identical with probe beam at $800nm$ and its polarisation is always kept to be orthogonal with probe beam to avoid interference on the sample surface. The pump fluence is fixed at $2.5mJ/cm^2$ and incident angle of probe beam is at near Brewster's angle of silicon 70°. A CCD camera is used to check the spatial overlap on the sample surface between pump and probe spot and the temporal overlap between pump and probe pulse is checked using a BBO crystal to perform a non-collinear intensity autocorrelation measurement[169]. Then, the reflected intensity of the probe beam is measured by a spectrometer as a function of time delay. The time width of pulse is around $60fs$ and step size of time delay is retained at $50fs$.

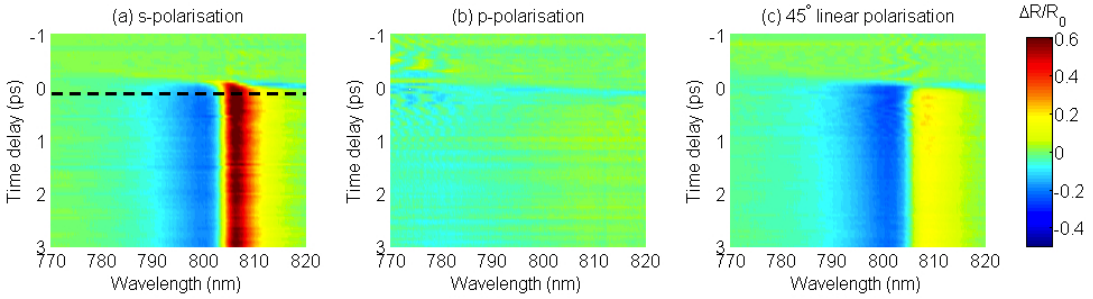

FIGURE 4.1: $\Delta R/R_0$ as a function of the time delay (ps) and the probe wavelength (nm). The probe beam polarisation is adjusted to $s-, p-$ and 45° linear polarised state and pump beam polarisation is always orthogonal to the probe beam, separately. The incident angle of probe beam is 70° and pump fluence is kept as $2.5mJ/cm^2$.

The measurement data of $\Delta R/R_0$ were plotted as the function of the time delay and probe wavelength, which are shown in Figure 4.1. As we can see, the zero time delay ($0ps$) is identified from the starting variation point of data $\Delta R/R_0$, which is induced by the pump excitation. When the probe beam was $s-$ polarised state, the data $\Delta R/R_0$ had a strong change after zero time delay. Then, there was a slow decay process of the signal from $0ps$ to $3ps$, which is shown in Figure 4.1(a). Moreover, we focused onto the data $\Delta R/R_0$ at fixed time delay $350fs$, which is marked as the dashed black line in Figure 4.1(a). It can be seen that the data $\Delta R/R_0$ is not monotonously changing as a function of the probe wavelength from $770nm$ to $820nm$. The value of $\Delta R/R_0$ is dropping to around -0.35 firstly, and then rising up to around 0.55. Actually, this interference fringe is the result from pump excitation and multilayer structured nc-Si:H sample. We will analyse this fringe in detail in the next section, multiple incident angle measurements. In Figure 4.1(b), when the $p-$ polarised state of probe beam was used

to detect the excited state sample, there is almost no change of $\Delta R/R_0$. This should be related to the Brewster's angle incidence of the probe beam. As the probe angle was at 70°, most of the $s-$ polarised light will be reflected from the sample. Thus, the $s-$ polarised incident beam can provide more information about the excited state. If the $p-$ polarised light waves are used, the most of light waves were absorbed by the sample and only a little part of $p-$ polarised light can be reflected back bringing the optical information of excited state sample. Thus, we can not easily see anything when applying $p-$ polarised probe beam.

Considering that the pump probe ellipsometry is performed with 45° linear polarised probe beam, the pump probe reflection measurement for nc-Si:H sample is also done under the same condition. The result is shown in Figure 4.1(c). The amplitude range of data $\Delta R/R_0$ is varying from around -0.3 to 0.3 at around $350fs$ time delay, which is a little smaller than $s-$ polarised probing results in Figure 4.1(a). And the 45° linear polarisation of the probe beam can also provide equal magnitude of the electric field and same original phase for $s-$ and $p-$ polarisations. So, the ultrafast dynamics properties of sample can be analysed more precisely, which will be discussed in the following sections.

4.3 Multiple Incident Angle Measurements

The part of discussion and results in this subsection had been published in paper: **Enhanced carrier-carrier interaction in optically pumped hydrogenated nanocrystalline silicon. Applied Physics Letters, 101(14):141904, 2012.**[164] Part of text is from the publication.

In order to accurately determine the ultrafast dynamics parameters of the plasma frequency ω_p and scattering rate Γ of excited state sample nc-Si:H, the incident angle of the probe beam spanned from 40° to 80° in the pump-probe reflection measurements. This multiple incident angle measurements method was previously reported by Roeser[18] to realise the dielectric function of the excited state, who also mentioned that the pump probe ellipsometry can be another best choice to characterise the dielectric function of the excited sample. In our multi-incident angle measurements, the polarisation of the probe beam was fixed at 45° linear polarised state and pump beam fluence was kept constant at around $2.5 \pm 0.5 mJ/cm^2$ for each probing incident angle measurement. Here the error $\pm 0.5 mJ/cm^2$ mainly comes from the variation of projected area on sample surface at different probing angles. The pump probe measurement results are shown in Figure 4.2.

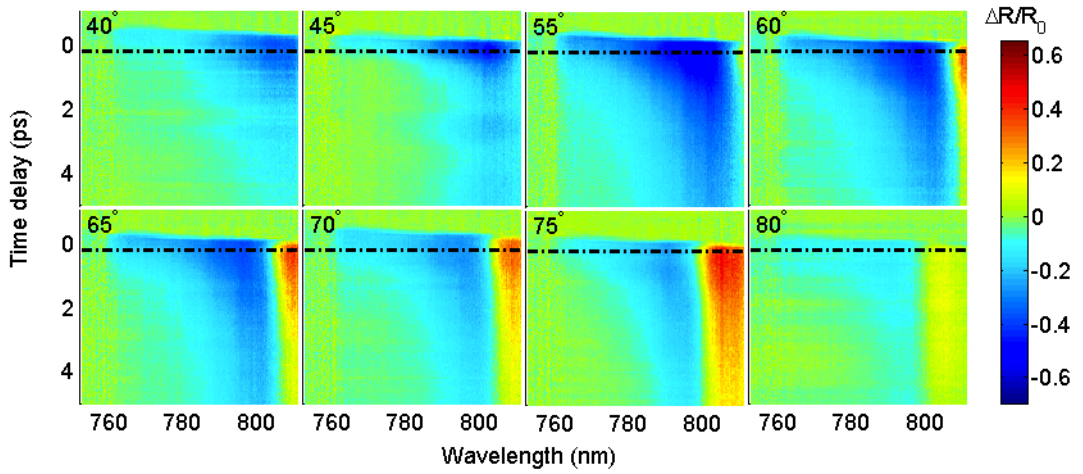

FIGURE 4.2: Pump probe reflection data $\Delta R(t)/R_0$ as the function of probing spectra (nm) and time delay (picoseconds) under each probing incident angle measurement. The dash-dotted lines mark the data $\Delta R/R_0$ at $\sim 350fs$ time delay following excitation.

Apparently, as the probing incident angle was spanning from 40° to 80°, a Fabry-Perot fringe was gradually appeared in the spectral range between $780nm$ and $820nm$. As we can see the 60° incident angle measurement results, a rising edge of the fringe was occurred at the around $815nm$ of probing spectra. And the fringe shifted to shorter wavelengths as the probing incident angle was increasing up to 80°. As the pump photons were absorbed by the nc-Si:H material to generate the free carriers plasma, the dielectric constant variation of nc-Si:H layer occured, which resulted in the change of the reflected probing signal. We also checked that there is no reflection signal variation when pumping the underlaying SiO_2 layer with c-Si substrate.

Thus, in order to analyse these measurement results and explain the fringe shifting, the corresponding multilayer optical model needs to be constructed. As the effective dielectric constant of the nc-Si:H layer ϵ_{eff0}, shown in Figure 3.18, has been obtained through the spectroscopic ellipsometry measurement and simulation, which is mentioned in Section 3.3.3, the excited state can be estimated by applying classical Drude model to represent the excited free carriers contribution. In this case, the new effective dielectric function of nc-Si:H layer after pump excitation can be described as $\epsilon_{eff} = \epsilon_{eff0} + \Delta\epsilon_{fca}$. Then, according to the flowchart of fitting process in Figure 3.31, the physical meaning of this multi angle experimental results can be explained.

Firstly, we focus on the data $\Delta R/R_0$ as a function of probe wavelength and incident angle for a fixed time delay $t \sim 350fs$, which are marked as the dash-dot lines in Figure 4.2. This time delay is chosen as it permits a sufficient time for the carriers in the plasma to build up and achieve a thermal equilibrium, while it is still short enough to avoid significant population decay due to the recombination or diffusion of the carriers. Then, the optical model and simulation process are introduced here. With

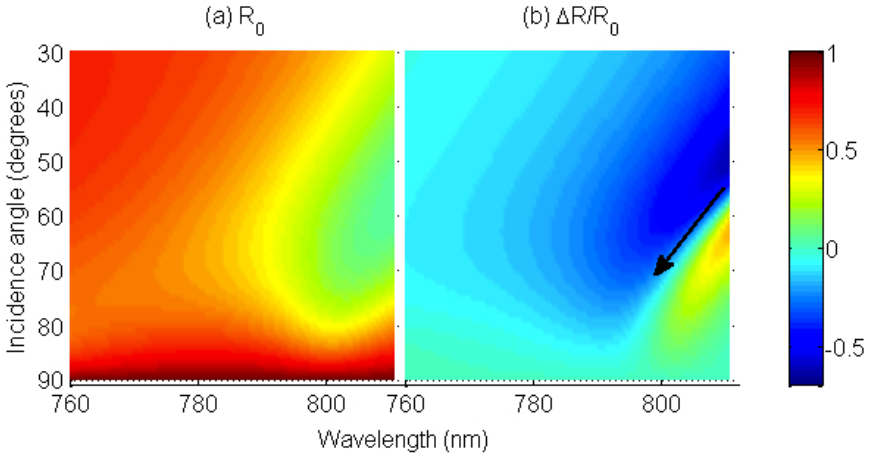

FIGURE 4.3: (a)Simulation of reflectance R_0 with changing wavelength and incident angle for unexcited state, (b) Simulation of $\Delta R/R_0$ with reasonable Drude parameters $\omega_p = 1.0 \cdot 10^{15} sec^{-1}$ and $\Gamma = 2.0 \cdot 10^{15} sec^{-1}$ to express the fringe shifting, shown as black arrow line, for excited state nc-Si:H sample.

the help of the transfer matrix method and ϵ_{eff0} from ellipsometry measurement in Figure 3.18(b), the reflectance R_0 can be calculated as a function of probe wavelength and incidence angle. As shown in Figure 4.3(a), the interference fringe is blue shifting as incident angle is increasing due to the multilayer structure of sample. Then, the dielectric function of nc-Si:H layer was replaced by $\epsilon_{eff} = \epsilon_{eff0} + \Delta\epsilon_{fca}(\omega_p, \Gamma)$ to express the optical property of the excited state of nc-Si:H material. The reasonable values of $\omega_p = 1.0 \cdot 10^{15} sec^{-1}$ and $\Gamma = 2.0 \cdot 10^{15} sec^{-1}$ were used here to obtain R_t. The final calculated data $\Delta R/R_0 = (R_t - R_0)/R_0$ were described in Figure 4.3(b). As indicated by the black arrow line in Figure 4.3(b), the fringe is also shifting to the shorter wavelength with increasing incidence angle. This behaviour is consistent with the dash dot lines of measurement results in Figure 4.2. So, in this way, the dash dotted lines data can be fitted simultaneously by adjusting the parameters ω_p and Γ. Because the dash-dotted lines data are picked out under the same time delay and around same pump fluence, the optical property of excited state should also be around same for each probing incident angle. Thus, simultaneous fitting all the data lines can obtain the accurate parameters ω_p and Γ.

Figure 4.4 shows the pump probe data curves $\Delta R/R_0$ and fitting results for each probing incident angle under a fixed time delay $\sim 350fs$, which are depicted as black dotted lines and red solid lines respectively. It is obvious that the data $\Delta R/R_0$ was flipped on the red side of the probing spectrum and this flip shifted to the shorter wavelength as the optical path inside the sample increases with rising incident angle from 40° to 80°. This observation is consistent with the blue-shift of the Fabry-Perot interference fringes [19], which is due to the induced dielectric function variation of the nc-Si:H film and multilayer structured sample. As we mentioned in the above paragraph, the

simultaneously iterative fitting was done basing on the modification of optical model with Drude equation. The red solid fitting lines in Figure 4.4 for each incident angle are all coincident with the data curves. Eventually, the two fitting parameters were determined from the fitting procedures, plasma frequency $\omega_p = 1.2^{+0.3}_{-0.2} \times 10^{15} s^{-1}$ and scattering rate $\Gamma = 2^{+1.2}_{-1} \times 10^{15} s^{-1}$.

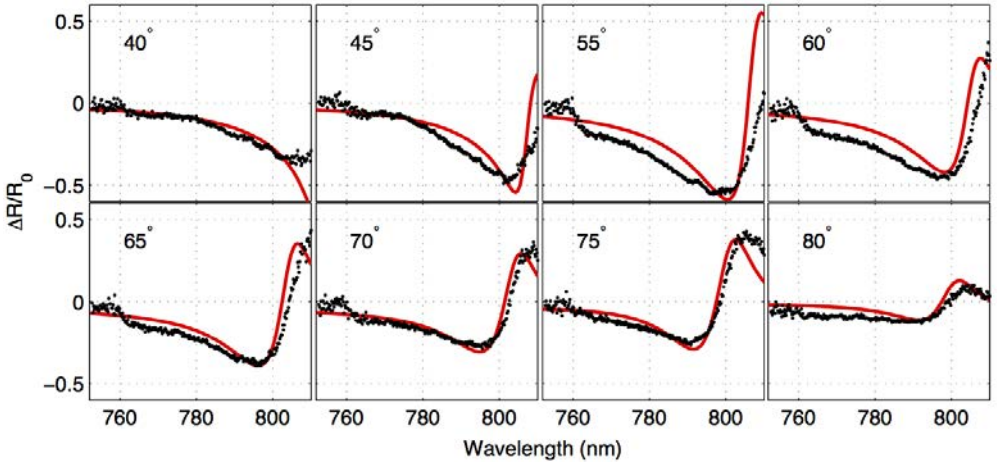

FIGURE 4.4: Transient pump probe data $\Delta R/R_0$ at fixed time delay $350fs$ under the probing incident angle from 40° to 80°. Black dotted lines depict data $\Delta R/R_0$, extracted from the measurement results in Figure 4.2. Red solid lines represent the Drude model fitting results.

Comparison of the values ω_p and Γ to other published literatures for bulk silicon and embedded nano Si clusters can result in some interesting conclusions. Sokolowski-Tinten *et al.*[17] estimated a scattering frequency of $\Gamma = 9.9 \times 10^{14} s^{-1}$ from pump probe reflectivity measurements, which attributed to the collision between free carriers, although the plasma frequency from this measurement is almost an order of magnitude higher than in our experiments. Sabbah *et al.*[42] estimated the scattering rate $\Gamma = 1.25 \times 10^{13} s^{-1}$ at plasma frequencies well below the one in our study. It is important to note that the procedures from which the values were quoted are based on signal angle reflectivity measurements. Moreover, a number of works using terahertz pump-probe spectroscopy methods have also been published to investigate the Drude parameters in similar materials[10, 13, 58]. They proposed the scattering rates in the range from 3×10^{13} to $1.25 \times 10^{14} s^{-1}$ at nearly the same plasma frequency as in our experiments. As the scattering rate Γ can be dependent on the probing frequency[58], the above mentioned values should be considered carefully. Even though the different scattering rates proposed from these studies, the damping of excited carriers is governed by carrier-carrier collisions is acceptable for all of them. Apparently, the estimation of the scattering rate of nc-Si:H sample in this work is by an order of the magnitude faster than previously reported ones.

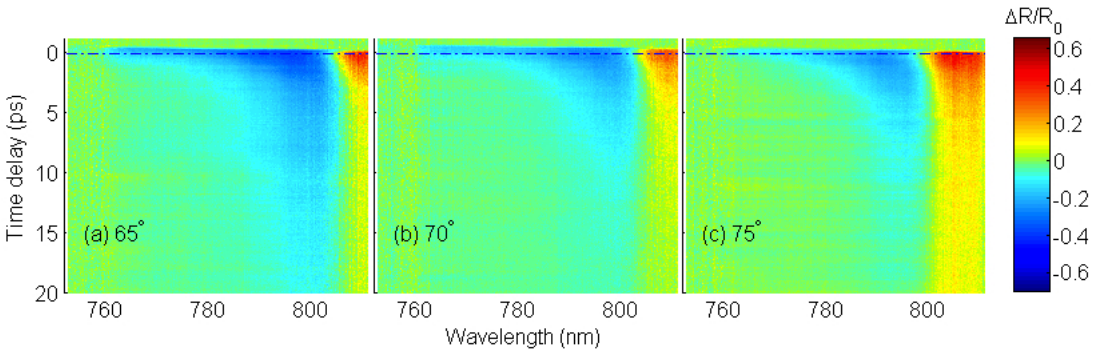

FIGURE 4.5: Time-resolved pump probe reflection data at three different incident angles: 65°, 70° and 75°. The time delay is scanning from 0*ps* to 20*ps* to reveal the signal decay process.

In order to explore the decay processes of plasma frequency $\omega_p(t)$ and scattering rate $\Gamma(t)$, the pump probe data $\Delta R/R_0$ under three incident angles $65°, 70°$ and $75°$ measurements were used again to be fitted separately as time delay was scanning from $0ps$ to $20ps$. As shown in Figure 4.5, all of these results consisted of a fast and a somewhat slower components in decay process. This seems to indicate the contribution to decay process results from two different relaxation mechanisms: a fast one is lasting a few picoseconds and a slow one is in the range of tens of picoseconds. Considering the nc-Si:H layer is composed of α-Si matrix and nc-Si clusters, the two decay channels of excited carriers can be proposed. In other words, these two decay channels represent different life time of excited carriers. The more detailed discussions about life time of excited carriers in this material had been researched by our group through pump probe scattering measurements[57]. Here, we are analysing the pump probe reflection data, which provides the spatially averaged information about the effective dielectric function variation. The optical model is also based on the effective dielectric function change.

By adjusting the plasma frequency ω_p and scattering rate Γ for each time delay, the experiment data $\Delta R/R_0$ can be fitted by the Drude model. In the Figure 4.6, data at logarithm increment of time delay were chosen to show the fitting results. As we can see, the fitting red solid lines matched very well with the measurement black dotted lines $\Delta R/R_0$ at each time delay. Obviously, as the time delay is increasing from $0ps$ to $20ps$, ω_p and Γ need to be adjusted precisely to control the trend of red lines to be consistent with the data for $\Delta R/R_0$. In fitting process, we found that adjusting ω_p value can control the amplitude of red lines and Γ mainly regulate the flipping trend in the spectral range between $790nm$ and $810nm$. However, when the data $\Delta R/R_0$ amplitude is very low in the longer time delays, the noise can strongly influence the accuracy of fitting results. As we can see the data in time delay range from $12ps$ to $20ps$ in Figure 4.6, the data uncertainty directly results in the significant fitting errors for ω_p and Γ. Despite these

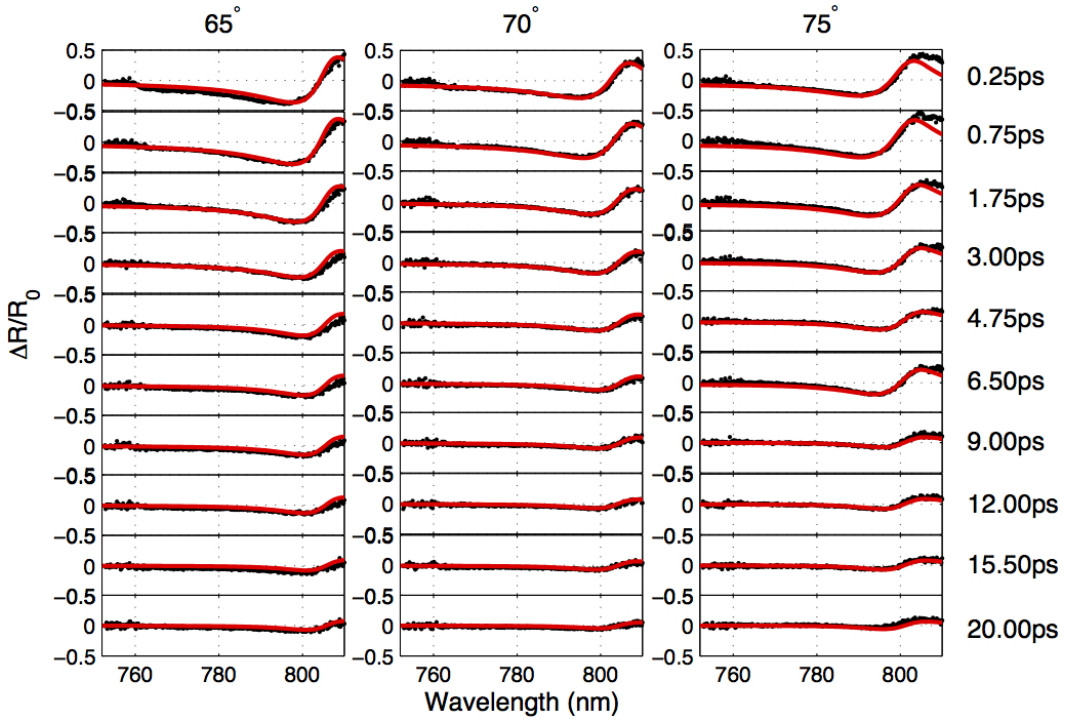

FIGURE 4.6: Time-resolved pump probe data $\Delta R/R_0$ (black dotted lines) with Drude optical model fitting results (red solid lines). The data at logarithm increment of time delay were picked out to be analysed.

big fitting errors in longer time delay range, the general behaviour of Drude parameters can still be obtained through this continuous fitting.

Figure 4.7 depicts the behaviour of the fitting results $\omega_p(t)$ and $\Gamma(t)$ with increasing time delay. The $\omega_p(t), \Gamma(t)$ for different incidence angles measurements have almost same decreasing trends with each other, which also illustrates the same excited state under the three probing angles. As the plasma frequency ω_p is correlated to the carrier concentration N_{eh} referring to Eq 3.99, the carriers concentration decay process $N_{eh}(t)$ can be derived out from the decay of $\omega_p(t)$ if the effective mass m^* is known. Thus, the reducing of $\omega_p(t)$ also indicates the carriers concentration $N_{eh}(t)$ is also decreasing as a function of time delay. Actually, lots of mechanisms can lead to the reducing of the pump excited carrier concentration, including electron-hole recombination, inter valley transition, defect capture etc. Due to the decrease of the carrier concentration, the carrier-carrier scattering and carrier-phonon scattering will also be gradually diminished. Consequently, this results in the reducing trend of $\Gamma(t)$. In order to find the relationship between ω_p and Γ, the carrier-carrier scattering is believed to be the main damping reason firstly. According to Eq 3.99, we can see the plasma frequency $\omega_p^2 \propto N_{eh}$. And the scattering rate can be described as $\Gamma = \frac{v_f}{l_0}$, where v_f is the Fermi velocity and l_0 is

the average distance between carriers.

$$v_f = \frac{\hbar}{m^*} \cdot (3\pi^2 N_{eh})^{1/3} \ , \qquad l_0 = (\frac{3}{4\pi N_{eh}})^{1/3} \tag{4.1}$$

Thus, the relation $\Gamma \propto (N_{eh})^{2/3}$ can be obtained. Finally, the relation between ω_p and Γ can be simply represented as

$$\frac{\omega_p^2}{\Gamma^{3/2}} = Constant \ .$$

Thus, we plotted the $\omega_p^2/\Gamma^{3/2}$ as function of time delay in Figure 4.7. Before $7ps$ time delay, all of those three lines are kept at around constant 10^7. Then, in the longer time delay, the ratio becomes unstable, which can be due to the inaccuracy of fitting values ω_p and Γ. We believe that the carrier-phonon interaction starts to play a role and covers the carrier-carrier contribution, which results in the thermal effect in this longer time delay. This ratio relation is also discussed through pump probe measurement research in Roger's thesis[22]. In conclusion, as the carrier-carrier scattering mechanism is the main scattering process in the initial decay, it is reasonable to assume the scattering rate is dependent on the plasma frequency.

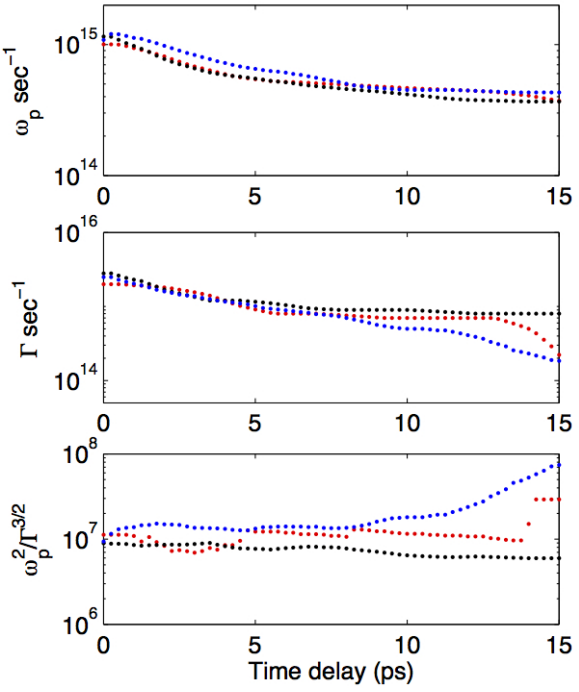

FIGURE 4.7: Drude parameters $\omega_p(t), \Gamma(t)$ with increasing time delay, obtained from fitting three incident angles measurements data; ratio $\omega_p^2/\Gamma^{3/2}$ indicates the relation between ω_p and Γ; the red dotted lines are from fitting 65° data, black for 70° and blue for 75°.

4.4 Pump Fluence Dependent Measurements

The discussion and results in this subsection have also been published in paper: **Enhanced carrier-carrier interaction in optically pumped hydrogenated nanocrystalline silicon. Applied Physics Letters, 101(14):141904, 2012.**[164] Part of text is from the publication.

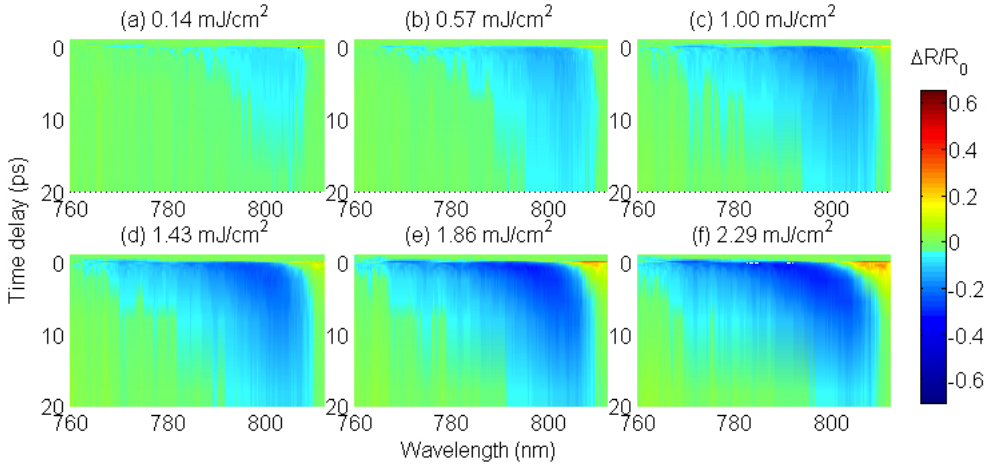

FIGURE 4.8: Time resolved pump probe measurement data $\Delta R/R_0$ as function of time delay and probing wavelength were recorded under 70° incident angle with increasing pump fluence from 0.14 to $2.29 mJ/cm^2$.

In order to realise the initial excited carrier concentration N_{eh} and carrier-carrier scattering mechanism, the effective mass m^* of excited carriers should be estimated first. This was done by measuring the pump probe spectra reflection $\Delta R(\lambda, t)/R_0$ with fixed incident angle of 70° and increasing pump fluence F from 0.14 to $2.3 mJ/cm^2$. The Figure 4.8 expresses the time resolved measurement results under different pump fluence. There is also an interference fringe observed in the red side of the probe spectra, especially under the high pump fluence excitation. Similarly, we analysed the data $\Delta R/R_0$ at the initial time delay $\sim 350 fs$, applying the fitting procedure with Drude optical model. The analysed data and fitting results are all illustrated in Figure 4.9. Then, the fitted plasma frequencies were plotted as a function of the pump fluence, which is shown in Figure 4.10. The linear relation can be seen between ω_p^2 and pump fluence. As for the value of intercept on ω_p^2 axis, it doe not correspond to the plasma frequency in the absence of pumping, but indicates the detection limit of the experimental setup. The slope of the graph was obtained by a linear fitting to be $6.1 \times 10^{29} cm^2/(mJs^2)$, which is used to estimate the effective mass m^*. Because the plasma frequency ω_p^2 is related to carriers concentration N_{eh} though Eq 3.99 and the carriers concentration can be estimated through the absorption property of excited state sample via following relation:

$$N_{eh} = \frac{A \cdot F}{\hbar \omega d} \ , \tag{4.2}$$

where A is the absorbance of the sample and d is the thickness of nc-Si:H layer and ω is angular frequency of probing light. Thus, the relation between plasma frequency ω_p^2 and pump fluence F can be constructed as following

$$\omega_p^2 = \frac{1}{m^*} \cdot \frac{AF}{d} \cdot \frac{e^2}{\epsilon_0 \hbar \omega} \ . \tag{4.3}$$

The absorbance $A = 0.4$ is calculated from the optical model for excited state of sample[164]. Thus, the effective mass can be estimated from the linear fit slope, which is $m^* = 0.17^{+0.05}_{-0.03} \cdot m_e$. This value is very close to the previously used value for analysing bulk silicon[17, 42]. They used $m^*_{opt} = 0.15 \cdot m_e$ to express the band edge reduced optical effective mass for analysing the time-resolved pump probe reflectivity measurements. Thus, we can conclude that the non-parabolicity effects[181] are not significant here.

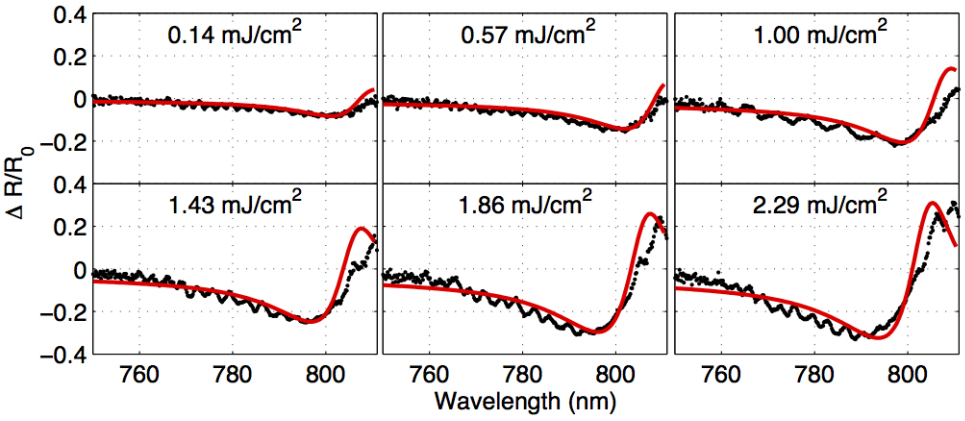

FIGURE 4.9: Pump probe data $\Delta R/R_0$ under the fixed time delay $\sim 350fs$ and different pump fluence between 0.14 and $2.29mJ/cm^2$. Black dots depict the data $\Delta R/R_0$, which are extracted from measurement data in Figure 4.8. Red solid lines represent the Drude model fitting.

Using the determined optical effective mass and the fitting values of plasma frequency, the carriers concentration at $\sim 350fs$ time delay for each pump fluence can be calculated out, which is shown referring to right axis of Figure 4.10. The carrier concentration represents the effective value averaging over the whole probe beam spot, which has been defined inside the fitting model. In the pump probe scattering measurements and analysis for this nc-Si:H material[57], we realised that the majority of the excited carriers are localised in the nano crystals at this time delay. Thus, the concentration in the nc-Si clusters should be greater by a factor of $1/f$, where $f = 0.35$ is the volume fraction of nc-Si clusters in the layer. With the help of optical effective mass and carriers concentration, the mean free path of excited carriers can be calculated. This ambipolar electron-hole plasma is classically given by $l = v_f/\Gamma$, where v_f is Fermi velocity. The data from Figure 4.4 are used and the mean free path is obtained about 0.3nm. This short distance can lead to important conclusions: the carrier is self confined inside of the nc-Si clusters. Due to the strong carriers mutual interaction and carrier-carrier scattering, the

escape from the excitation volume is limited. Apparently, because the mean diameters of nc-Si cluster is by an order of magnitude greater than the mean free path, the scattering with nano crystalline boundaries can not contribute to the damping constant. Moreover, the obtained scattering rate is too fast to fit the mechanisms for collisions with defects and phonon assisting the carriers scattering[182]. Therefore, it is reasonable to assume the carrier-carrier collision is the main reason for this fast scattering rate.

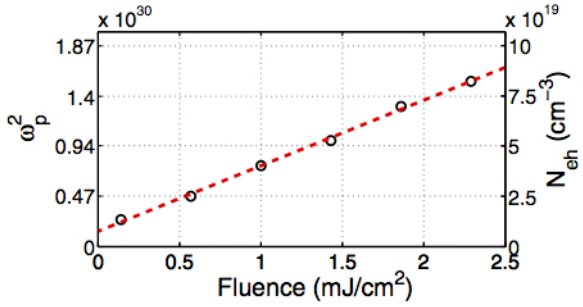

FIGURE 4.10: Plasma frequency ω_p^2 from Drude model fitting is shown as the empty circle with increasing pump fluence. The carriers concentration N_{eh} is derived corresponding to each ω_p^2 value. The dashed red line is linear fit.

To further elaborate, the average distance between carriers r_0 can be calculated using the modified carrier concentration in nc-Si clusters $2.9 \times 10^{20} cm^{-3}$, providing $r_0 = (3/4\pi N_{eh})^{1/3} = 1.3nm$. However, the scattering radius $r_s = (\pi N_{eh} l)^{-1/2} = 3nm$. This is greater than the average distance between carriers, which indicates the strong carrier-carrier interaction. Regarding the Fermi liquid theory, the scattering cross-section scales with temperature[164, 183] as $(k_B T/E_f)$. Thus, this factor is approaching unity at $\sim 10^4 K$ in our experimental conditions. At this temperature, Coulomb interaction is completely unscreened and limitation due to the Pauli exclusion principle is ineffective. This high temperature of the electronic sub-system is in the range with the high concentrations achieved by femtosecond pumping[184]. As for a classical electron gas at Fermi temperature, the screening radius can be approximated[185] by $(\epsilon_0 k_B T/N_{eh} e^2)^{1/2}$, providing an estimation of $1.7nm$. This supports the argument of strong interaction in a confined hot carriers system. Meanwhile, the spatial confinement[186] is another factor to contribute to the enhancement of carriers interaction, which is well known as increasing the Coulomb interaction. Even though this factor has not been explored in this experiment, a similar influence is expected to effect the scattering mechanism.

In summary, we have measured the pump-probe reflectivity change induced by free carriers pumped into nano-crystalline silicon embedded in an amorphous hydrogenated silicon matrix (nc-Si:H). Using multi-angle pump probe reflectivity change measurements, we have determined the values of the plasma frequency, ω_p, its corresponding concentration, and the scattering rate Γ from fitting of the Drude model. The plasma frequency,

shown to be linear with the pumping fluence, and the reduced optical mass was found to be slightly different from that of the bulk silicon. The scattering mechanism was attributed to carrier-carrier scattering with a remarkably large scattering cross-section, not reported previously in similar experiments.

4.5 Determining the Carrier Recombination Coefficients

Even though nc-Si:H material has excellent optoelectronics properties, one of the critical points in developing optoelectronics applications is characterising and understanding the decay process of the excited free carriers. Basically, after optical pump excitation, the electrons and holes undergo spatial and temporal evolution with characteristic times dependent on the various relaxation processes[187]. The carriers recombination in the relaxation process mainly dominates the decay process of excited carriers and also influences optical property of excited state material as increasing time delay. As we can see in Figure 4.8, the amplitude of $\Delta R/R_0$ for different pump fluence were gradually returning back to zero as time delay was scanning from $0ps$ to $20ps$. Using transfer matrix method and Drude model, the data $\Delta R/R_0$ under pump fluence from $0.14mJ/cm^2$ to $2.29mJ/cm^2$ in Figure 4.8 can be fitted as a function of time delay to extract the excited carriers concentration decay process. Then, a recombination model, including the linear, quadratic and cubic term, is applied to fit the carriers concentration decay process and three recombination coefficients can be identified through the fitting procedures. From this way, the recombination property of excited carriers in nc-Si:H material was characterised.

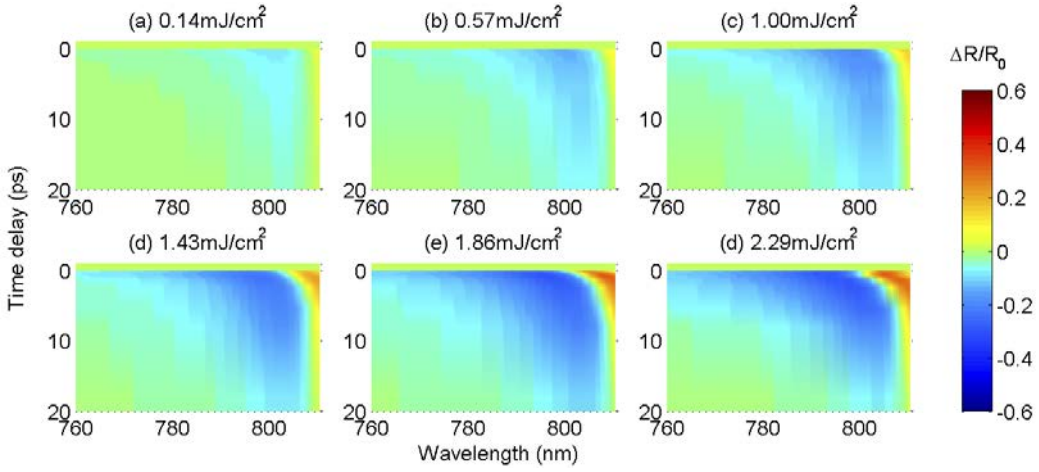

FIGURE 4.11: Simulation results $\Delta R/R_0$ as the function of time delay and probing wavelength under each pump fluence. The measurement data can be seen in Figure 4.8.

Adjusting the plasma frequency $\omega_p(t)$ and scattering rate $\Gamma(t)$ of Drude model under each time delay, the data in Figure 4.8 can be simulated. Figure 4.11 shows the fitting

results $\Delta R/R_0$ as a function of time delay and probing wavelength for each pump fluence. Comparing to the original measurement data in Figure 4.8, they are roughly coincident with each other. As probe time delay is increasing, the signal $\Delta R/R_0$ is gradually returning back to zero. And the Fabry-Perot fringes in the red side of spectrum are also appeared in the simulation results. As we have estimated optical effective mass is around $m^* = 0.17m_e$, the excited carriers concentration decay process $N_{eh}(t)$ can be extracted from $\omega_p(t)$ according to Eq 3.99.

Figure 4.12 shows the decay of $N_{eh}(t)$ and $\Gamma(t)$ for different pump fluence. At higher pump fluence, there are more photons irradiating the sample, creating higher initial carriers concentration at around $0ps$. Moreover, as the scattering rate represents the frictional damping force of the material[83], the higher initial carriers concentration can cause the higher initial scattering rate. Then, as the time delay is increasing and $\Delta R/R_0$ is decaying, the $N_{eh}(t)$ shows a reasonable reducing trend and $N_{eh}(t)$ at $20ps$ time delay for each pump fluence almost reaches the same value. As for the $\Gamma(t)$ decay process, the general behaviour is still logical reducing as a function of increasing time delay due to the decreasing $N_{eh}(t)$. But, the error of $\Gamma(t)$ in the longer time delay is significantly bigger due to the fitting of the weaker signal data of $\Delta R/R_0$. Moreover, the scattering rate will not only depend on the carrier concentration any more, but also involves the carrier-phonon and carrier-defect scattering mechanisms at lower pump fluence. Consequently, we will simply focus on the decay process of $N_{eh}(t)$ in the following discussion. We need to notice that the pump fluence in this subsection is smaller than that in multiple incidence angle measurements, so the relationship $\Gamma \propto N_{eh}^{2/3}$ is not ideally satisfied.

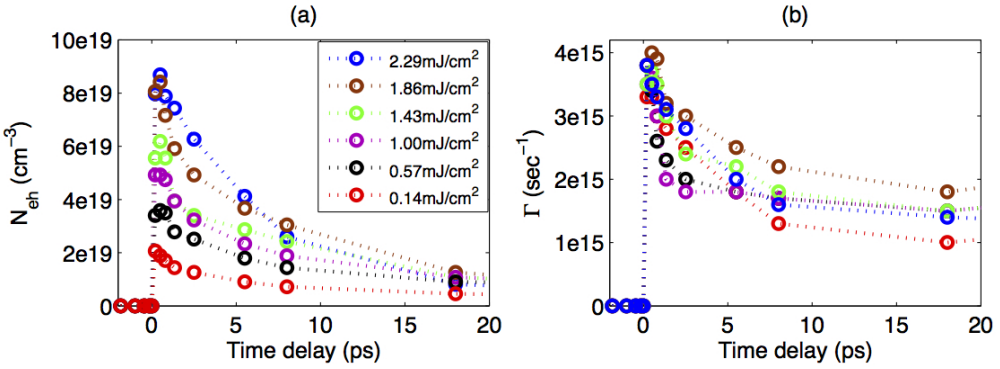

FIGURE 4.12: (a) carriers concentration N_{eh} and (b) scattering rate Γ as the function of time delay under each pump fluence measurement.

To study the non-radiative recombination processes of photo excited carriers in the time domain, pump probe optical techniques are invaluable tools[5]. So far, some basic relaxation mechanisms of carriers in semiconductors were described previously[188], especially for crystalline silicon. After the optical excitation, the various relaxation processes lead

to the excited electrons and holes undergoing spatial and temporal evolution with characteristic times. Ellen J. Yoffa[188] claimed that carriers thermalisation due to carriers collisions can be achieved in time order of $10^{-14} sec$ $(= 0.01 ps)$. Then, both electrons and holes can be described by quasi-Fermi levels[188] with a single temperature $T_e = T_h$. Then, the recombination process will dominate the next relaxation step for the carriers. Generally speaking, the recombination process of the excited carriers can be formulated as the following equation[189]:

$$-\frac{dN(t)}{dt} = cN(t) + bN^2(t) + aN^3(t) \ . \tag{4.4}$$

The first linear term is called Shockley-Read-Hall (SRH) recombination, which is associated with recombination via deep energy levels[190, 191]. The second quadratic term indicates the direct (or radiative) band-to-band recombination, or the trap assisted Auger recombination[192]. In our case, there is no luminescence after pump excitation, so this quadratic term may be the direct bimolecular recombination or the trap assisted Auger recombination. The released energy may be dissipated by phonon emission or transferred to a neighbouring carrier. The third cubic term normally represents the Auger recombination, which means that an electron recombines with a hole and the released energy is taken up by a third carrier. The parameters a, b, c are the recombination coefficients for the corresponding terms. As long as the recombination coefficients can be determined, the recombination property of excited carriers in nc-Si:H material can be realised.

Hopkins[193] mentioned that Auger process mainly dominates the excited carriers recombination when the carriers concentration is bigger than $5 \times 10^{17} cm^{-3}$ for crystalline silicon[194, 195]. And he used the pump probe thermal reflectance technique to determine the cubic term Auger recombination coefficient for Silicon. Furthermore, Hopkins also used the Drude model to get the carrier concentration from his experiment, but his research is only for the pure crystalline silicon, and neglected the other recombination mechanisms. Only the three particle Auger recombination process contributes for c-Si, as expressed by the only cubic term in Eq 4.4. This is probably because the band-to-band recombination in this indirect gap c-Si is a weak process, which requires phonon participation. The Auger coefficient for c-Si has been measured to span the range from 10^{-31} to $10^{-30} cm^6 s^{-1}$[196–198]. In his research, when excited carriers accumulate in the conduction band by the high repetition rate pump pulses, the Auger recombination coefficient can reach $5.35 \times 10^{-28} cm^6 s^{-1}$.

While nc-Si:H material is composed by amorphous silicon (α-Si) and nc-Si clusters,

this heterostructure removes the restrictions that the energy and momentum conservation laws impose on the inter-electron processes[199]. Furthermore, the strong three dimensional confinement for nano c-Si clusters leads to the relaxation of translational momentum conservation[200]. So, the recombination process could be including other mechanisms, such as band to band bimolecular recombination and trap assisted Auger recombination[201] etc, apart from the three particles Auger recombination. Consequently, the recombination Eq 4.4 is applied to consider all the possible mechanisms.

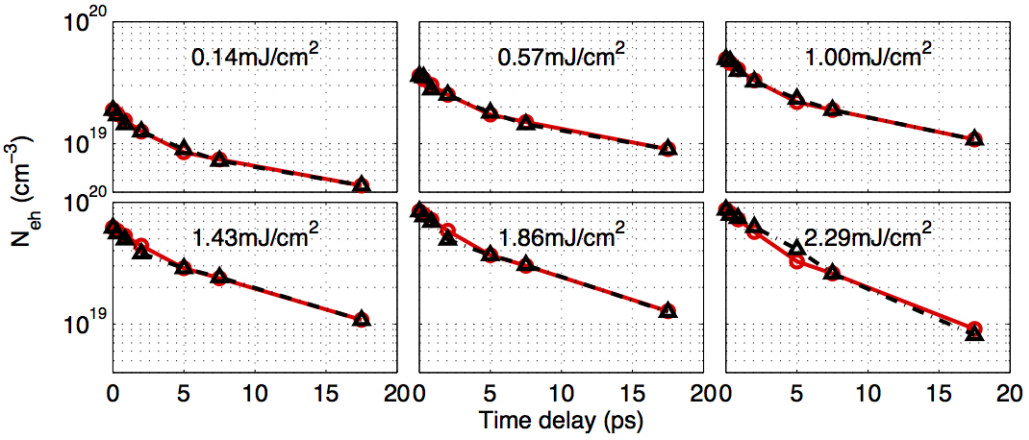

FIGURE 4.13: Decay processes $N_{eh}(t)$ under each pump fluence, which are shown as black triangle lines, are fitted by recombination Eq 4.4 expressing as red circle lines.

So far, the decay process of the carriers concentration $N_{eh}(t)$ has been extracted through the optical model simulation of $\Delta R/R_0$ for each pump fluence measurement, which is shown in Figure 4.12(a). Then, referring to the recombination Eq 4.4, $N_{eh}(t)$ can be fitted as a function of increasing time delay. Figure 4.13 shows the fitting results and extracted data of $N_{eh}(t)$ decay process, which are depicted as red circles and black triangles respectively. They are matched with each other very well in the $20ps$ decay process. The little deviation can be attributed to the measurement errors.

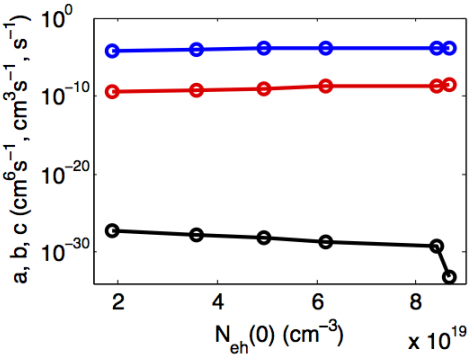

FIGURE 4.14: Recombination coefficients a, b, c changing as increment of initial carriers concentration $N_{eh}(0)$, which corresponds to the pump fluence increasing from 0.14 to $2.29mJ/cm^2$. The black, red and blue lines represent coefficients a, b, c respectively.

Eventually, the recombination coefficients a, b, c are derived out through the fitting of carrier concentration decay processes. Figure 4.14 expresses the coefficients as a function of initial excited carriers concentration $N_{eh}(0)$. And the $N_{eh}(0)$ is correlated to the pump fluence increasing from 0.14 to $2.29 mJ/cm^2$. The black, red and blue lines are representing the coefficients a, b, c separately. Firstly, the linear term coefficient c is kept constant at around $10^{-4}s^{-1}$ with increasing $N_{eh}(0)$. This value is quite lower than the other published paper, of which linear term coefficient is at around $10^{9}s^{-1}$[202]. Moreover, regarding to the decay range of carriers concentration $N_{eh}(t)$ is in the magnitude from $10^{19}cm^{-3}$ to around $10^{18}cm^{-3}$, the linear term $cN_{eh}(t)$ changing region is from 10^{15} to $10^{14}cm^{-3}s^{-1}$ with increasing time delay. Then, the quadratic term coefficient b is fitted out at around $10^{-9}cm^{3}s^{-1}$. This coefficient magnitude is similar to the published non-radiative bimolecular recombination coefficient[4, 53, 201] about amorphous silicon (α-Si) material, which is also interpreted as Auger recombination of spatially overlapping $e-h$ paris[53]. The nc-Si:H film includes amorphous phase silicon as matrix material, which may determine the magnitude of quadratic coefficient. Furthermore, the quadratic term $bN_{eh}^{2}(t)$ is varying between 10^{29} and $10^{27}cm^{-3}s^{-1}$. Lastly, for the cubic term coefficient a, even though there is a little decreasing as the increasing $N_{eh}(0)$, the magnitude of a is still around $10^{-29}cm^{6}s^{-1}$, except the highest pump fluence point at magnitude 10^{-33}. This cubic term coefficient is bigger than that of bulk crystalline silicon, of which is in the region from 10^{-31} to $10^{-30}cm^{6}s^{-1}$[193]. But, the nc-Si:H material is also including nano clusters c-Si phase. For the nano cluster semiconductor materials, the cubic term coefficient is greater than the bulk material[200], which can be from 10^{-29} to $10^{-28}cm^{6}s^{-1}$. Thus, the coefficient a is reasonable comparing to the published cubic term coefficient. Meanwhile, the cubic term $aN_{eh}^{3}(t)$ variation is from 10^{28} to $10^{25}cm^{-3}s^{-1}$ as increasing time delay. From the estimation of each term changing region in the time domain, we can see the linear term value is much smaller than the quadratic and cubic term. The quadratic and cubic term have almost equal contributions to the recombination process of photo excited carriers in nc-Si:H material. Thus, we can ideally ignore the linear term in the carriers recombination process. Until now, we can make a summary that the recombination process of $N_{eh}(t)$ in nc-Si:H material is mainly controlled by the quadratic and cubic recombination term. The quadratic coefficient value is in the magnitude of around $10^{-9}cm^{3}s^{-1}$ and the cubic coefficient value is at around $10^{-29}cm^{6}s^{-1}$.

4.6 Pump Spectra Dependent Measurements

The discussion and results in this subsection have been published in paper: **High-frequency conductivity of optically excited charge carriers in hydrogenated**

nanocrystalline silicon investigated by spectroscopic femtosecond pump probe reflectivity measurements. Thin Solid Films, 2015.[69] Most part of text is from the publication.

In this section, we report a first attempt to understand the high-frequency conductivity as a function of the pump photon energy. The idea is to establish the dependence of the conductivity immediately (a few hundred femtoseconds) after excitation on the excess energy provided by the pump photons to the carriers. This short time is sufficient to allow the carrier subsystem to thermalise and settle at a certain thermodynamics distribution characterised by a temperature proportional to the excess energy, but still too short for it to exchange energy with another subsystem of the lattice ions. In the investigation, we recorded 25 pump-probe spectra, each of which corresponds to a pump wavelength between 580 and 820nm. The reflectance is probed by a broadband probe in the range between 765 and 815nm. The results are analysed using the Drude conductivity and Boltzmann transport theories. We show that the thermal distribution of the nascent carriers can be described as that of a classical hot non-degenerate gas. The conductivity of the gas monotonically decreases as the excess energy provided by the pump photons decreases. Here, the investigated sample is the nc-Si:H material.

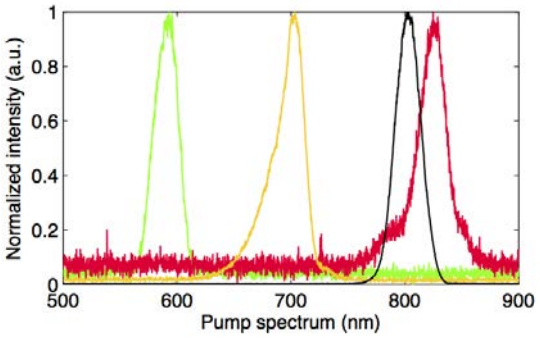

FIGURE 4.15: Representative pump beam spectra is spanning from 580nm to 820nm, which are depicted as colour lines. The probe beam is fixed at the spectrum between 760nm and 820nm, showing as black line.

The spectroscopic pump probe setup is shown on the Figure 3.22. An ultrafast laser system (Coherent) was used to deliver $1kHz, 50fs$ laser pulses centred around 790nm. Then, the main beam is split into high-intensity pump pulses and low-intensity probe pulses by a pellicle beam splitter. Using a light frequency converter (OPA), the pump wavelength can be converted to any wavelength between 580 and 820nm. The pump fluence was fixed at $0.6mJ/cm^2$ and the probe intensity of the fundamental beam frequency was further attenuated by a neutral density filter. Figure 4.15 illustrates representative range of the pump spectrum as colour lines and the probe spectrum as a black line. The incident angle of probe beam was set to 70°, whereas the angle of pump was set

to around 50°. The polarisation of the probe beam was adjusted to provide equal contributions of the $s-$ and $p-$ polarised components, and the pump beam was always in the $s-$ polarised state. The spatial overlap between probe and pump spots on sample surface was checked by a CCD camera equipped with a magnifying lens. The temporal overlap between probe and pump pulses was checked by detecting the sum frequency generation on a BBO crystal. By using a computer controlled retroreflector, the probe time delay with respect to the pump was fixed at $300fs$. Finally, the wavelength of the reflected probe beam was analysed by a spectrometer (Ocean Optics QE65 Pro), and the collected data are presented here as $\Delta R(\lambda)/R_0$, where R_0 is the reflectance without pumping. Further, $\Delta R = R(t) - R_0$ is the change in reflectance induced by the pump excitation[4, 17], where $R(t)$ is the reflectance measured at a certain delay time ($300fs$ in this work) by the probe. The $300fs$ delay was chosen because it is sufficiently long for the excited free carrier plasma to build up in the nc-Si:H layer but still short enough to avoid significant population decay[57, 164] and the carrier-lattice interaction[195].

The fixed pump fluence $0.6mJ/cm^2$ allows to keep the roughly same average energy of pump beam irradiating on the sample surface per unit time crossing a unit area when choosing the different pump spectra. So, the pump photon energy is the only changing factor to influence the reflection signal response of probing beam, which is corresponding to the pump photons energy between $1.51eV$ and $2.14eV$. And the probe photon energy is constant at around $1.55eV$. The application of the pump pulse generates a free carrier plasma inside the nc-Si:H layer. These excited carriers change the effective dielectric function of the nc-Si:H layer and the detected intensity of the reflected probe. The excited carrier concentration can generally be derived from the measured intensity change of the reflected probe. The relation between the concentration and the reflectance can be obtained using the classical Drude model[4, 17, 19]. According to the Drude model, the dielectric function of the excited layer after pump excitation, ϵ_{eff}, can be approximated as follow: $\epsilon_{eff} = \epsilon_{eff0} + \Delta\epsilon_{fca}$, which is detailed in Eq 3.100. An optical mass of $m^* \approx 0.17$ has been estimated for this material in section 4.4 [164]. Thus, the excited carrier concentration N_{eh} can be deduced from plasma frequency ω_p referring to Eq 3.99. However, there is another important factor affecting the conductivity, that is, the scattering rate Γ. Thus, the main task is to obtain Γ and N_{eh} for each pump spectrum and establish the DC conductivity according to the relation $\sigma_0 = e^2 N_{eh}/(\Gamma m^* m_e)$. Note that at a relatively short delay time of around $300fs$, carrier-carrier collisions are the main scattering process contributing to Γ. The carrier-phonon collision contribution to the scattering can be neglected, as it is realised on much longer timescales.

Simultaneous experimental determination of Γ and N_{eh} is a complex task that generally requires at least two independent measurements, such as a combination of the transmittance and reflectance[29], or determination of different polarisation states of the probe.

However, this task can be simplified when Γ has a known dependence on N_{eh}. Here we refer to known models of carrier-carrier scattering published elsewhere[203]. Briefly, these models allow us to calculate the scattering rate as a function of the carrier concentration and carrier temperature as a parameter for the Maxwell-Boltzmann (MB) and Fermi-Dirac (FD) distributions. In this work, we assumed the MB distribution. We note that we independently verified that the FD distribution provides unsatisfactory results. According to the model, the scattering rate can be estimated as follows:

$$\hbar\Gamma = k_B T_{ryd}(\frac{T_n}{T})^{3/2}(ln\frac{T^2}{T_n^{3/2}T_{ryd}^{1/2}}) \cdot M \ , \tag{4.5}$$

where k_B is the Boltzmann constant; T_n is the Fermi temperature, which is directly related to the carrier concentration as $k_B T_n = \frac{\hbar^2}{2m^* m_e}(3\pi^2 N_{eh})^{2/3}$; and T_{ryd} and M are the Rydberg temperature and band structure factor, respectively. The band structure factor can be approximated as close to that of bulk silicon[203]. The value of the Rydberg temperature is less well known because of the enhanced carrier-carrier interaction at high carrier concentrations[164]; in our calculation procedure, it was left as an unknown, but fixed, parameter (that is, it is the same for all pump and probe wavelengths). Finally, for the MB distribution, the temperature of the nascent carriers can be evaluated according to the equipartition theorem, $\frac{3}{2}k_B T = \frac{\hbar\omega_{pump} - E_g}{2}$, where $\hbar\omega_{pump}$ and E_g are the pump photon energy and energy gap of the material, respectively. The latter in our experiment was about $1.2eV$, whereas the former was varied. Thus, in our fitting procedure we simulate 25 reflectance pump-probe spectra taken at different pump photon frequencies ω_{pump} (corresponding to different carrier temperatures T) for which the carrier concentration N_{eh} is an unknown free parameter, and the Rydberg temperature T_{ryd} is an unknown fixed parameter. The confidence of the simulation procedure is ensured by the small number of fitting parameters and their independence of the probing wavelength in each particular spectrum.

Figure 4.16 shows the pump-probe change in the reflectance data, $\Delta R/R_0$, as a function of the probe wavelength taken at different pump wavelengths. The probe spectrum spans 770 to $810nm$, whereas the pump wavelength covers the region from 580 to $820nm$ at $10nm$ intervals. All the spectra show a Fabry-Perot fringe on the red side, similar to that observed elsewhere[19, 164]. This fringe originates from the interference effect induced by the change in the dielectric function of the layer following excitation by the pump. However, the contrast of the fringe varies with the pump. This clearly indicates that the excitation efficiency and carrier concentration depend on the pump wavelength for this system. This effect has, however, a simple explanation: the absorbance of the pump pulse depends on the conditions of constructive and destructive interference of the incoming and internally reflected light components within the layer.

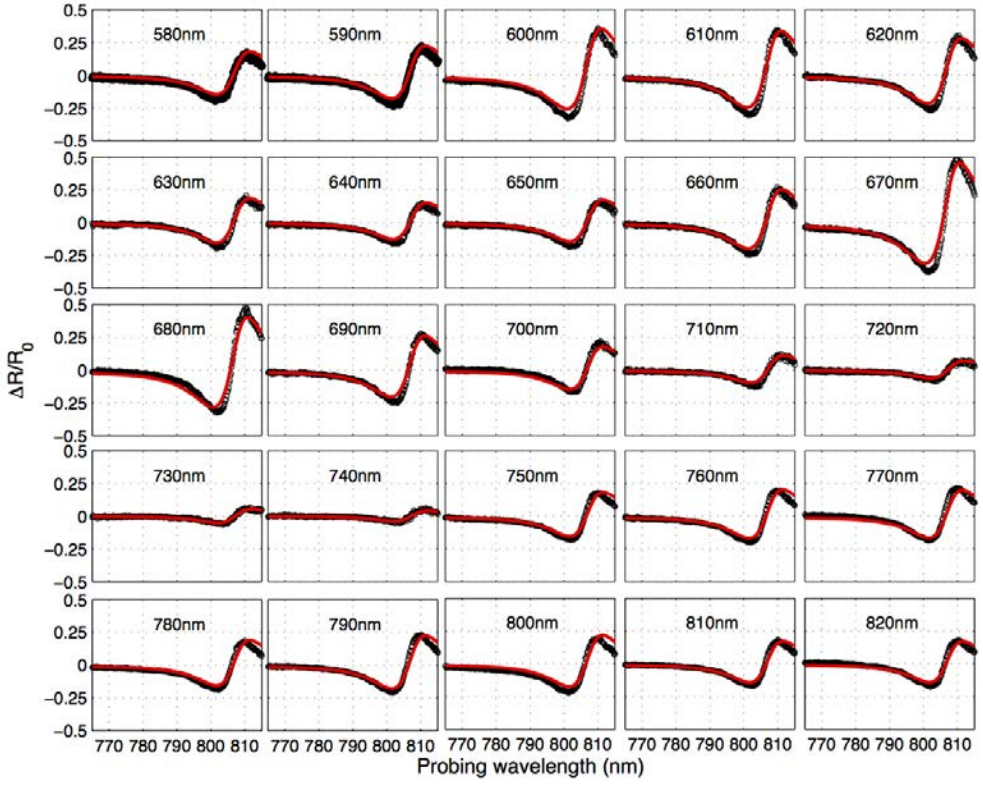

FIGURE 4.16: Transient pump probe experimental data (black dots) for $\Delta R/R_0$ as a function of the probe wavelength taken at different pump wavelengths. Red lines denote simulated results.

Using Eqs. 3.100 and 4.5 in the multilayer optical model discussed in previous sections, the data $\Delta R/R_0$ can be fitted to retrieve N_{eh} and Γ as functions of the pump wavelength. The fitting results are shown as red solid lines in Figure 4.16, which coincide well with the black data points. The retrieved N_{eh} and Γ are shown in Figure 4.17(a) and (b), respectively. The Rydberg temperature used in the calculation, given by $m_e m^* e^4/4\pi\hbar^2(\epsilon\epsilon_0)^2$, was calculated with the standard constants and optical mass given above, except for ϵ, which is a fixed fitting parameter here. The dielectric constant indicates screening of the carrier-carrier interaction. Unlike the ϵ value for silicon bulk material, which lies between 12 and 13, the value producing the best fit is somewhat lower than 2, demonstrating a tenfold carrier-carrier interaction enhancement, in agreement with a previous work[164]. (Please note that in the previous work the scattering rate estimate provided a higher value because the pumped carrier density was higher). The N_{eh} and Γ retrieved from the simulation show synchronous oscillation as a function of the pump wavelength. The oscillations originate in the constructive and destructive interference of the multiple reflections of the pump beam from the multilayer interfaces.

The synchronous behaviour of N_{eh} and Γ is in agreement with a conductivity model of a non-degenerate electron-hole gas in which the scattering rate increases with the carrier density. However, N_{eh} and Γ behave differently as a function of the pump wavelength.

That is, N_{eh} oscillates around a constant value, whereas Γ tends to increase. This is because N_{eh} depends only on the absorbance, whereas Γ has an additional dependence on the carrier temperature, which in turn depends on the excess energy provided by the pump photons. According to Eq 4.5, a lower temperature (smaller photon energy) causes an increase in the scattering rate.

Finally, with the obtained N_{eh} and Γ values, we calculated the conductivity σ_0, as shown in Figure 4.17(c). Remarkably, the conductivity decreases monotonically as a function of the decreasing excitation energy. This result indicates that for the MB distribution, the nascent carrier conductivity simply depends on the excess energy (temperature) provided by the pump photons.

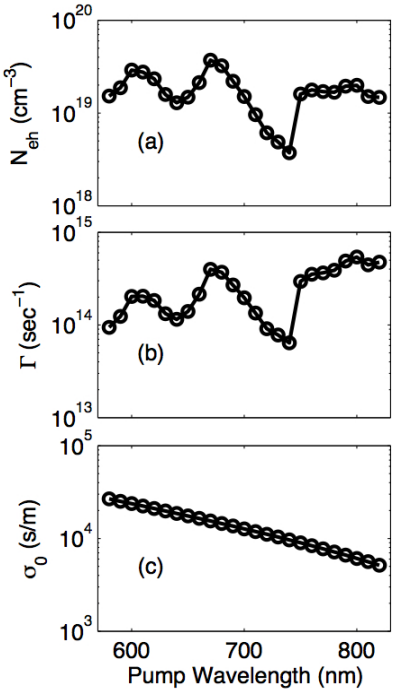

FIGURE 4.17: Excited carrier concentration N_{eh}, scattering rate Γ, and conductivity σ_0 as functions of pump centre wavelength, obtained using Drude model and MB limitation fitting data $\Delta R/R_0$.

In conclusion, in this work we measured and analysed the pump-probe wavelength-dependent reflectivity of nc-Si:H sample at a fixed delay time of $300\,fs$. To establish the optical model of the sample, we investigated their composition with Raman and XRD methods and studied the optical properties using ellipsometry in the previous sections. To find the high-frequency conductivity at this short time, we simulated the pump-probe results using an optical model modified by the Drude contribution of the free carriers excited by the pump. The analysis revealed that the carrier thermodynamic distribution is better described by the classical MB statistics. We found that the conductivity decreases monotonically as the excitation photon energy decreases, as expected for a

classical electron-hole plasma. Our work shows that in the design of optoelectronic devices one should carefully consider the effect of the balance between the carrier density and the excess energy in order to achieve a desired conductivity.

4.7 Pump Probe Ellipsometry

In order to accurately characterise the decay processes of dielectric constant, absorption coefficient and conductivity of excited nc-Si:H sample, the pump probe ellipsometry method is introduced and applied to measure the $\psi(\lambda, t), \Delta(\lambda, t)$ as the function of probe time delay and probing wavelength. The experimental setup can be seen in Figure 3.24. Actually, the pump probe ellipsometry setup is constructed basing on the pump probe reflection and rotating compensator ellipsometry configuration. The only difference is that the reflected probe beam is analysed by rotating compensator and analyser prior to be detected by the spectrometer. The polarised state of incident probe beam is adjusted by a polariser to $P = 45°$ linear state and the analyser is fixed as $A = 0°$. Here we defined the angle of the optical element is between transmission axis of optics and the incident plane's direction. Moreover, the positive rotating direction of each optical element is defined as the counterclockwise rotation when looking against the direction of the incident source beam. The detailed setup and rotating angle of each optical element have been illustrated in section 3.4.2. From this way, the detected intensity $I(\lambda, C)$ as the function of probing wavelength and compensator angle from 0° to 360°, can be obtained for each time delay after pump excitation. Then, the Fourier analysis procedure needs to be done to extract the ellipsometry data $\psi(\lambda, t)$ and $\Delta(\lambda, t)$. This procedure has been introduced in section 3.2.3.3 referring to Boer's publication[128].

In the experiment, the pump fluence is fixed at around $2.5 mJ/cm^2$ and the incident angle of probe beam is kept at 70° near Brewster angle. The angle difference between probe and pump beam is around 20°. As the pump and probe beam have the identical spectrum, the polarisation of pump beam is adjusted to be orthogonal with the polarised state of probe beam to avoid interference. And the pump spot is overlapped with the probe spot on the sample surface. Precisely controlling the optical path length of probe beam with retroreflector, the decay process of data $I(\lambda, C, t)$ can be detected. Before we did the pump probe ellipsometry, the only probe beam is used to measure the ellipsometry ψ, Δ of nc-Si:H sample without excitation. The results is described in figure 3.16. As we can see, the obtained results are matched very well with the data from commercial ellipsometer in the probing spectra range between around $760 nm$ and $820 nm$. From the fitting, the effective dielectric function ϵ_{eff0} of nc-Si:H layer can be identified, which is shown in figure 3.18.

Then, we can start the pump probe ellipsometry for nc-Si:H sample with varying the time delay from $-0.7ps$ to around $13ps$. The measurement data are the detected spectra intensity as function of rotating compensator angle and time delay, $I(\lambda, C, t)$. In order to extract $\psi(\lambda, t), \Delta(\lambda, t)$ for each time delay, the Fourier fitting needs to be done to get the Fourier coefficients. Then, the $\psi(\lambda, t), \Delta(\lambda, t)$ can be obtained referring to equation 3.64 under each time delay. For example, the data under $1ps$ time delay and $800nm$ probing wavelength have been picked out from the measurement results, which are shown as black circle line in figure 4.18. According to the equation 3.59, the detected intensity under $800nm$ probe wavelength and fixed time delay $1ps$ is contributed by second and fourth order harmonic oscillation in the compensator angle C. Thus, the Fourier coefficients can be obtained by Fourier fitting, which is shown as red solid line in figure 4.18. Finally, the $\psi = 32.78°$ and $\Delta = 312.46°$ are derived out according to equation 3.64 under this $800nm$ probing wavelength and $1ps$ time delay.

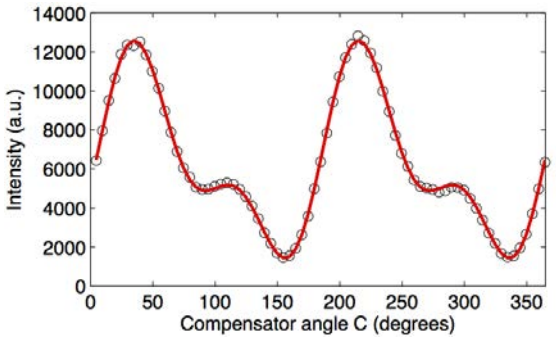

FIGURE 4.18: Pump probe ellipsometry measurement data for $1ps$ time delay and $800nm$ probing wavelength. The detected intensity is a function of the compensator angle from 0° to 360°. The circle dotted line is the raw data and the red solid line is the Fourier fitting line according to equation 3.59. Thus, from obtained Fourier coefficients, the $\psi = 32.78°$ and $\Delta = 312.46°$ can be derived out.

Similarity, the whole time resolved pump probe spectra ellipsometry measurement data $I(\lambda, C, t)$ can be converted to $\psi(\lambda, t)$ and $\Delta(\lambda, t)$ at all probing wavelength and time delay according to the above mentioned method. Figure 4.19(a) and (b) represent the obtained ellipsometry data $\psi(\lambda, t)$ and $\Delta(\lambda, t)$, which are both plotted as a function of the probing wavelength and time delay in 3D picture. When the time delay is smaller than zero, $t < 0$, which indicates the unexcited state of the nc-Si:H sample, the data $\psi(\lambda)$ and $\Delta(\lambda)$ are both roughly same as the obtained data in figure 3.16 from the commercial ellipsometry measurement. At the time delay $t \approx 0$, the $\psi(\lambda)$ and $\Delta(\lambda)$ are both experiencing the strong variations, which are depicted as the sudden reduction of $\psi(\lambda)$ and shifting of $\Delta(\lambda)$ to shorter probing wavelength in figure 4.19(a) and (b) respectively. Then, for $t \gg 0$, the $\psi(\lambda)$ is gradually recovering back to the around original amplitude values and $\Delta(\lambda)$ is also trying to shift back to the original longer wavelength. This recovering phenomena is similar to the previous pump probe reflection

results of $\Delta R/R_0$. As time delay is going on, the data $\Delta R/R_0$ recovered back to zero, which means the reflectance returns to original value of unexcited state of sample.

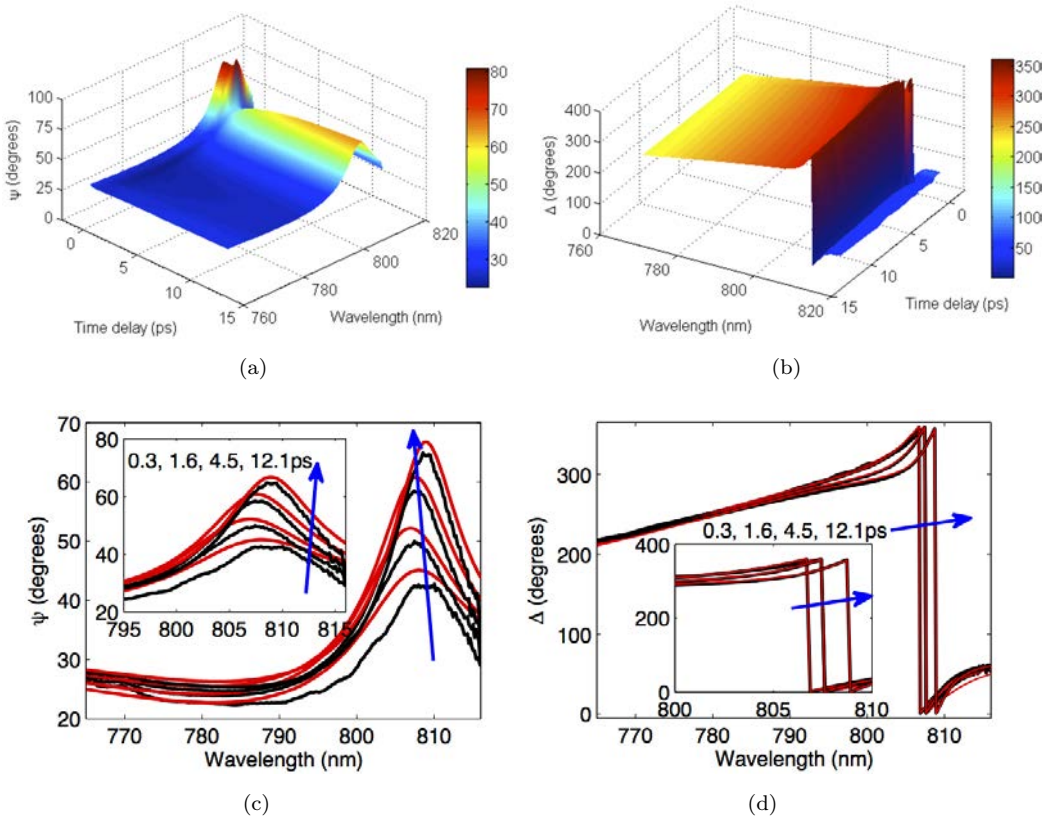

FIGURE 4.19: Time resolved pump probe ellipsometry measurement data for nc-Si:H sample under 70° incident angle, (a) $\psi(\lambda, t)$ and (b) $\Delta(\lambda, t)$, which are both plotted as the function of probing wavelength and time delay. Figures (c) and (d) depict the detected data (ψ, Δ) as black lines and the modified optical model simulation results as red solid lines under $0.3, 1.6, 4.5, 12.1ps$ time delay respectively.

The definition of reflection ellipsometry is defined as[99]: $\rho \equiv tan\psi e^{i\Delta} \equiv \frac{r_p}{r_s}$, where r_p and r_s are the reflection coefficients of $p-$ and $s-$ polarised light waves respectively. Moreover, $tan\psi = |r_p|/|r_s|$ and $\Delta = \delta_{rp} - \delta_{rs}$ express the amplitude ratio and phase difference between reflected $p-$ and $s-$ polarised light waves, separately. Consequently, in order to reveal the optical property of nc-Si:H sample in excited sate, the corresponding optical model should be constructed for nc-Si:H sample to fit data $\psi(\lambda, t)$ and $\Delta(\lambda, t)$. For the unexcited sate, the multilayer optical model in section 3.3.3 has been introduced and constructed to reveal the optical property of nc-Si:H sample. Meanwhile, we used $800nm$ pump beam to excite the SiO_2 film with crystalline silicon substrate under same pump fluence and we can not get the variation of reflected probe signal. We can confirm that the photon excited nc-Si:H film is the main reason for the probing signal change.

As in the previous sections, the Drude model was used in the analysis of the free carrier contribution to the change of the dielectric function, which has been discussed in section

3.4.3. So, $\epsilon_{eff} = \epsilon_{eff0} + \Delta\epsilon_{fca}(\omega_p, \Gamma)$ is applied to formulate the new effective dielectric constant of excited state nc-Si:H film. Then, in term of analysing flowchart 3.31, ϵ_{eff} substituted ϵ_{eff0} into the multilayer optical model. Adjusting (ω_p, Γ), the decay process of data $\psi(\lambda, t)$ and $\Delta(\lambda, t)$ can be fitted very well. Figure 4.19 (c) and (d) display the fitting results with the detected data under $0.3, 1.6, 4.5, 12.1ps$ time delay, which were shown as red lines and black lines respectively, and they were also coincident with each other very well. From here, we also clearly see that there is a strong influence on ψ and a weak effect on Δ after pump pulse excitation. As the time delay was increasing from $0.3ps$ to $12.1ps$, the values of ψ at each probing wavelength was also increasing to return to ground state values and Δ was shifting to the original longer wavelength, which are indicated by the blue arrow lines in figures.

Consequently, the decay process of effective dielectric function $\epsilon(\lambda, t)$ of nc-Si:H film from unexcited state to excited state can be identified after fitting $\psi(\lambda, t)$ and $\Delta(\lambda, t)$. Figure 4.20(a) and (b) depict the real part and imaginary part of $\epsilon_{eff}(\lambda, t)$ as the function of probing wavelength from $760nm$ to $820nm$ and time delay between $-0.7ps$ and $13ps$. As we can see, both of $\epsilon^r_{eff}(\lambda, t)$ and $\epsilon^i_{eff}(\lambda, t)$ are not strongly dependent on the probing wavelength, which is expected as for the free carriers response measured away from the resonance. But, they express a big dependence on the time delay t. So the general decay trend can be more clearly observed after averaging the ϵ^r_{eff} and ϵ^i_{eff} over the whole probing wavelength, which are shown as subfigures in figure 4.20(a) and (b). As we can see, the subfigure (a) $\epsilon^r_{eff}(t)$ decreases after the photons excitation and then gradually recoveres back to the original unexcited state value. The subfigure (b) $\epsilon^i_{eff}(t)$ indicates that there is a suddenly distinct positive rising after the pump excitation. Then, the $\epsilon^i_{eff}(t)$ gradually decreases to the unexcited state. Moreover, the fractional change of ϵ^r_{eff} is quite small in comparison to that of imaginary part ϵ^i_{eff}, during the excitation process $t \approx 0ps$. Such a relation is demonstrated for the free carrier absorption when the plasma frequency and scattering rate are of the same order[185].

According to relationship $N^2 = (n - i \cdot k)^2 = \epsilon$, the absorption coefficient of nc-Si:H film can also be acquired, $\alpha = 4\pi k/\lambda$. As we can see in figure 4.21, the absorption coefficient is also experiencing the dramatic rising after excitation and then is gradually decreasing as time delay is increasing, which is similar to the changing behaviour of $\epsilon^i_{eff}(t)$ in figure 4.20(b). Referring to the α value from $t < 0$ to $t > 0$, the absorption coefficient has increased more than 4 times under every probing spectra after pump photons excitation. This sudden distinctive rise in the absorption coefficient is mainly due to the induced absorption property of the excited free carriers. The dynamic behaviours of the absorption coefficient and dielectric function of the nc-Si:H film as increasing time delay are also corresponding very well with the other published measurements on nc-Si:H material[5, 10, 58, 204, 205].

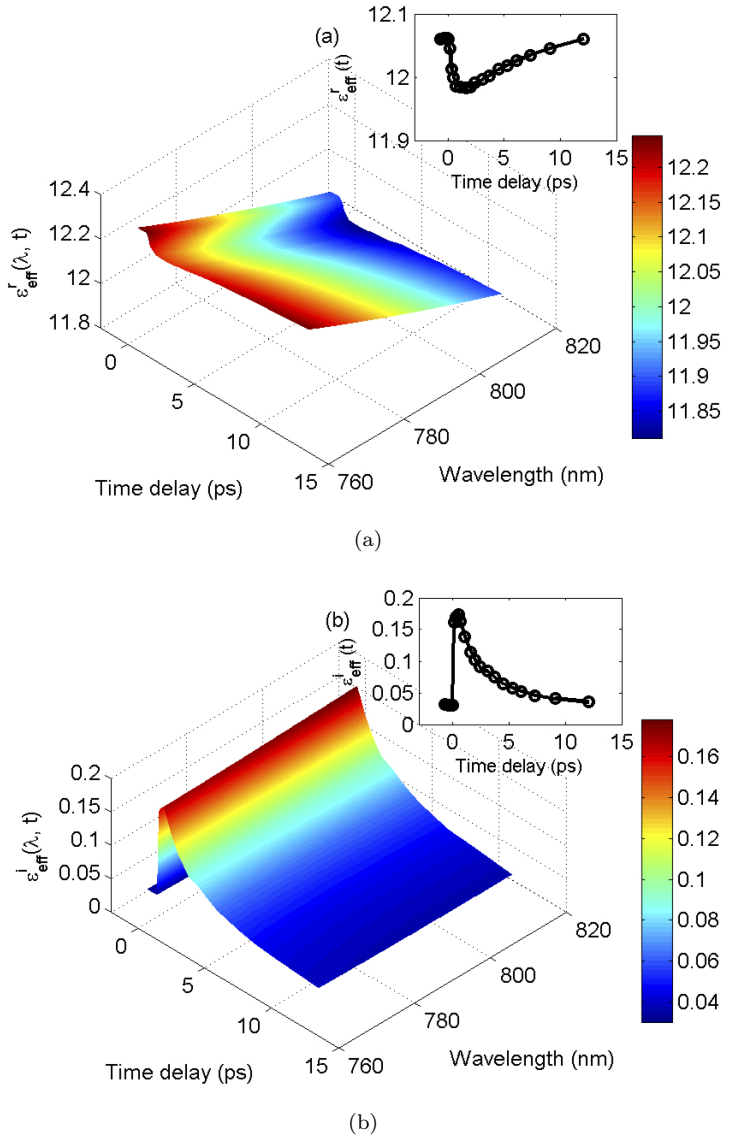

(a)

(b)

FIGURE 4.20: Dielectric constant $\epsilon_{eff}(\lambda, t)$ of nc-Si:H film as the function of probing wavelength from 760nm to 820nm and time delay between $-0.7ps$ and $13ps$. (a) shows the real part of ϵ_{eff}, (b) shows the imaginary part of ϵ_{eff}. The subfigures in (a) and (b) are the averaging real part and imaginary part of dielectric constant over whole probe spectrum as increasing time delay.

Meanwhile, the decay processes of plasma frequency $\omega_p(t)$ and scattering rate $\Gamma(t)$ in the Drude equation can also be obtained by the new multilayer optical model simulating $\psi(\lambda, t), \Delta(\lambda, t)$ of excited state nc-Si:H sample under each time delay. Furthermore, in section 4.4, the effective mass has been estimated by pump fluence dependent measurements, which is $m^* \approx 0.17m_e$. So, the $\omega_p(t)$ can be converted to the decay process of excited carriers concentration $N_{eh}(t)$. Figure 4.22(a) and (b) illustrate the $N_{eh}(t)$ and $\Gamma(t)$ decay processes between $0ps$ and $13ps$ respectively. The magnitudes of $N_{eh}(t)$ and $\Gamma(t)$ are roughly coincident as the values obtained in section 4.5, where recombination

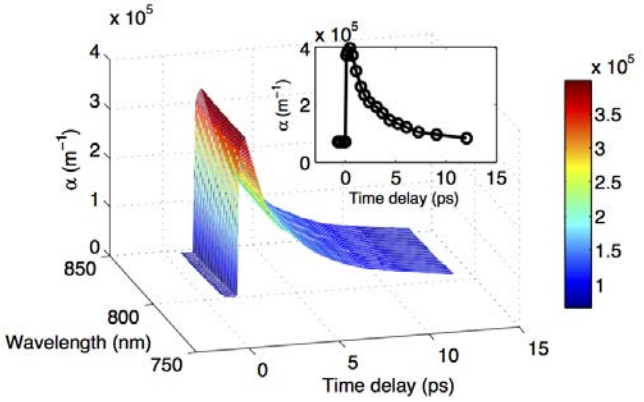

FIGURE 4.21: Absorption coefficient $\alpha(\lambda, t)$ (m^{-1}) as a function of the probing wavelength and time delay, which is deduced from $\epsilon_{eff}(\lambda, t)$ of nc-Si:H film. The subfigure is the $\alpha(t)$ averaging over the probing spectra.

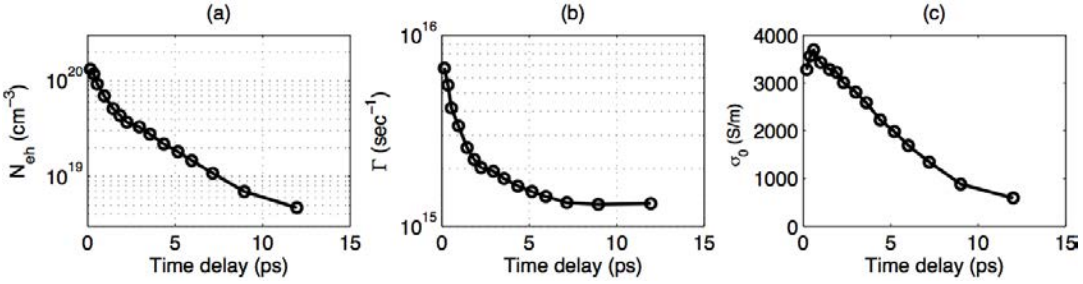

FIGURE 4.22: Decay processes of carriers concentration $N_{eh}(t)$, scattering rate $\Gamma(t)$ and conductivity σ_0 of excited state nc-Si:H, obtained from fitting pump probe ellipsometry data $\psi(\lambda, t), \Delta(\lambda, t)$.

coefficients were discussed. This demonstrates the reliability of the pump probe ellipsometry technique for precise identification of N_{eh} and $\Gamma(t)$. From here, the conductivity decay process of excited state nc-Si:H film can also be solved, which is deduced according to $\sigma_0(t) = e^2 N_{eh}(t)/(\Gamma(t) m^* m_e)$ and shown in Figure 4.22(c). The conductivity σ_0 is decreasing from around $3500 S/m$ to $600 S/m$ with increasing time delay between $0ps$ and $13ps$. These high frequency conductivity values are reasonable when comparing to the obtained conductivity value in section 4.6 under $800nm$ pump light excitation. As we can see, the pump probe ellipsometry technique is a good method to realise the decay process of optical property of excited state material. Applying the appropriate optical model simulation, the ultrafast dynamics information of researched material can be understood precisely.

4.8 Summary

In conclusion, the pump probe reflection and ellipsometry techniques are discussed and applied to research the ultrafast dynamics properties of hydrogenated nano-crystalline

silicon (nc-Si:H) material in this chapter. Firstly, the influence of probe beam polarisation on the pump probe reflection is discussed under the around Brewster's angle of probing light. And the 45° linear polarised state is finally chosen to do the pump probe research. Then, regarding to the multilayer structure of nc-Si:H sample, the multiple incident angles measurements are done to reveal the two important ultrafast dynamics parameters: plasma frequency ω_p and scattering rate Γ under each time delay. We found that Γ is dependent on ω_p when the carrier-carrier scattering mechanism dominates the scattering process. Furthermore, to realise the excited carrier concentration N_{eh} and discuss the carrier-carrier scattering mechanism, the effective mass m^* of excited carriers is estimated as $m^* \approx 0.17m_e$ through the pump fluence dependent measurements. Then, the recombination property of $N_{eh}(t)$ under different pump fluences is analysed through the fitting of the decay process of $N_{eh}(t)$ and determining the recombination coefficients. We found the recombination process of excited carriers in nc-Si:H material is mainly controlled by the quadratic and cubic recombination terms. The quadratic coefficient value is in the magnitude of around $10^{-9}cm^3s^{-1}$ and cubic coefficient is at around $10^{-29}cm^6s^{-1}$. Moreover, the DC (direct current) conductivity as a function of pump photon energy in initial decay time ($\sim 300fs$) is detected, and analysed using the Drude conductivity and Boltzmann transport theory. The analysis shows that the thermal distribution of excited nascent carriers can be described as that of a classical hot non-degenerate gas. The conductivity of the gas decreases monotonically as the excitation photon energy decreases. Finally, the pump probe ellipsometry technique is introduced and applied to measure the $\psi(\lambda, t)$ and $\Delta(\lambda, t)$ for precise characterisation of the decay processes of the dielectric function and absorption coefficient and conductivity of excited state nc-Si:H material.

Chapter 5

Pump Probe Transmission and Reflection of PS

5.1 Introduction

In this chapter, a free standing porous silicon (PS) membrane is researched through pump probe transmission and reflection measurements. Firstly, we introduce the basic preparation and characterisation methods for the PS membrane sample. Then, the reflectance and transmittance of the PS membrane are both measured and the optical model is constructed to fit these data. From the fitting, the dielectric constant of nano wires c-Si in PS material can be evaluated. Moreover, the porosity and thickness of PS membrane can also be estimated. After that, we simultaneously did the time resolved pump probe spectral transmission and reflection measurements. In the analysing procedure, we develop an analytical model based on the Wentzel-Kramers-Brillouin (WKB) approach and Drude equation to simulate the pump probe transmission and reflection data simultaneously. The model allows us to retrieve a pump-induced nonuniform complex dielectric function change along the membrane depth and increasing time delay. We show that the model fitting to the pump probe data requires a minimal number of fitting parameters while still complying with the restriction imposed by the Kramers-Kronig relation. Moreover, referring to the Drude equation in analytical model, the excited carriers concentration and scattering rate can also be estimated as functions of the PS membrane depth and time delay from fitting the data. Finally, the diffusion coefficient D and recombination time τ of excited carriers in PS membrane material are discussed through the simulation of a carrier transport equation. We realised the developed model has a broad range of applications for experimental data analysis and practical implementation in the design of devices involving a spatially nonuniform dielectric function, such

as in biosensing, wave-guiding, solar energy harvesting, photonics and optoelectronic devices.

5.2 PS Membrane Preparation and Characterisation

The discussion and results in this subsection had been published in paper: **Determination of excitation profile and dielectric function spatial nonuniformity in porous silicon by using wkb approach. Optics express, 22(22):2712327135, 2014.**[29] Most part of text is from the publication.

The porous silicon layer was fabricated by electrochemical anodisation of the surface of a $3''$ diameter (100) silicon wafer (B-doped, $5 - 15m\Omega cm$), using an electrolyte comprised of methanol and 40% HF in a ratio 1 : 1; a current density of $30mA/cm^2$ and anodisation time of 11 min was chosen to yield a layer with $\sim 60\%$ porosity and $11\mu m$ depth (calculated using a gravimetric calibration curve); the layer was detached from the underlying substrate, after anodisation, by applying a $120mA/cm^2$ pulse (10s) before removed from the electrolyte; the free standing membrane was then rinsed in methanol and air-dried. On the other hand, the porosity of $> 50\%$ and the thickness of $\sim 13\mu m$ of the PS membrane were also estimated from the images of the surface and cross section obtained by SEM, showing in Figure 5.1(a)-(c). The surface of PS membrane is shown in Figure 5.1(a), which is like a sponge or a honey comb plate, and the irregular holes are mixing with the nano c-Si wires. The cross section of PS membrane in Figure 5.1(b) describes the nano c-Si cylinders were constructing the main structure and the branches are interweaving with each other to generate the voids inside of PS membrane.

Apart from the structure information, it is necessary to describe the dielectric constant of the sample at ground state without pump pulse perturbation, which is also fundamental process to investigate the optical property of excited state of PS membrane in the following discussion. The distinguished method to determine the dielectric constant of PS membrane is to evaluate the Fabry-Perot interference fringes from transmission or reflection measurements. The periodical distance of interference fringes relates to the thickness of sample d and probing light wavelength, and the contrast of fringes between peak and valley has a relation with the penetration depth of probing light $d_p = 1/\alpha$, where α is absorption coefficient. If $d \ll d_p$, the interference fringes can be clearly observed in the transmission or reflection measurements. Applying an approximate optical model to fit them, the optical properties of the sample can be identified. This method is quite common to be used to research the optical property of PS membrane samples[90, 166, 167, 206–208]. In our case, we measured transmittance T_0, and reflectance R_0, of the membrane using the probe beam in the region of interest between

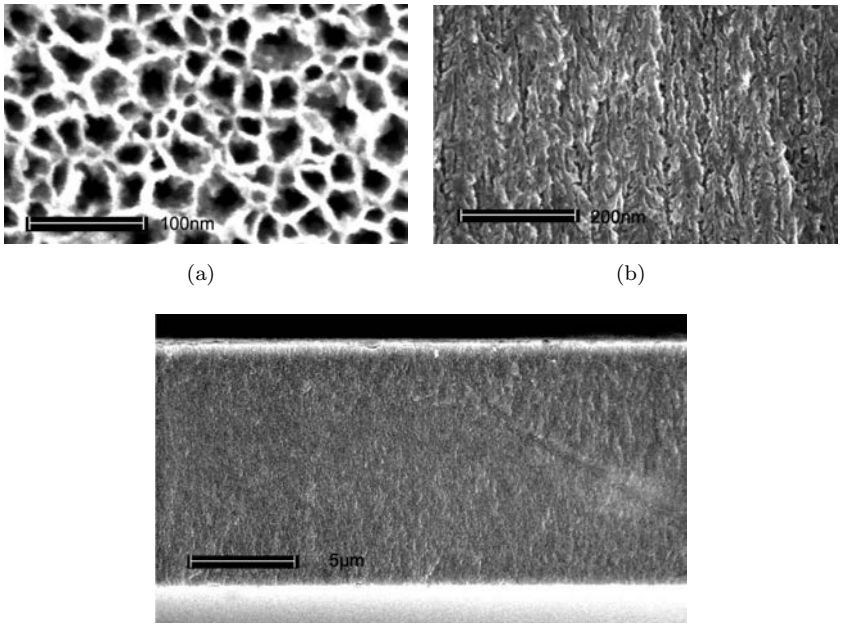

(a) (b)

(c)

FIGURE 5.1: SEM images of the porous silicon (PS) membrane sample, showing (a) the surface of the sample; and (b) and (c) cross sections of the sample.

760 and 810nm. The polarisation of probe beam is fixed at $s-$ polarised state and incident angle is kept at 45°. The results are shown in Figure 5.2. The interference fringes of T_0 and R_0 can be clearly seen in this figure.

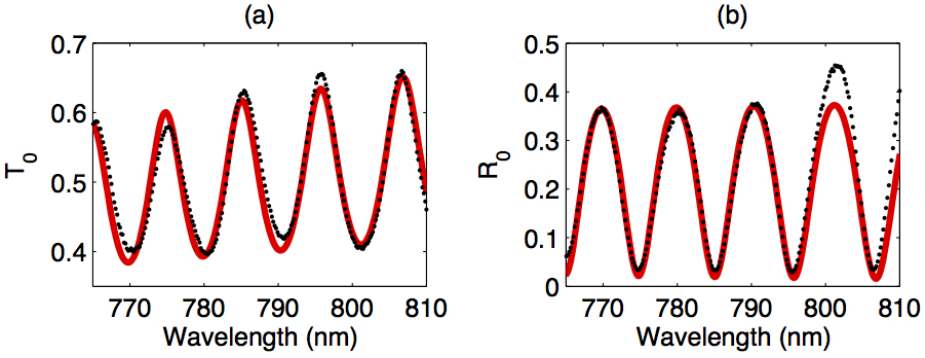

FIGURE 5.2: (a) Transmittance, T_0 and (b) reflectance R_0, of the PS membrane, which are both measured under 45° incident angle and $s-$ polarised state of probe beam. The black dots show the experimental data; the red solid lines correspond to the best fitting.

According to the measurement condition, the $air/membrane/air$ optical configuration can be constructed for fitting T_0 and R_0. As for describing the optical response of the PS membrane, we used Forouhi-Bloomer model combining with the Bruggeman effective medium approximation. The four terms Forouhi-Bloomer (FB) inter-band model[130] is applied to simulate the complex refractive index of the nano crystalline silicon constituent of the membrane, which is written as Equation 3.68 and 3.69 for real and imaginary parts respectively. Then, $\epsilon_{c-Si} = (n - ik)^2$ assigns the dielectric function of

the nano crystalline silicon. This model is based on the crystalline silicon energy band structure and satisfies the Kramers-Kronig relations. In the FB model, E_g is the energy band gap and E is the probing photon energy, ϵ_∞ is the dielectric constant corresponding to probing photon energy $E \to \infty$, and the A_i, B_i and C_i are the phenomenological parameters related to the optical transitions around the critical points where the conduction and valence bands are approximately parallel to each other and the optical absorption is enhanced. Generally, four dominant critical point transitions can sufficiently describe the c-Si optical property[130]. Thus, four terms, $q = 4$, can be used to describe the optical property of crystalline silicon (c-Si) over a wide spectral range. A similar approach was also used in the previous works to simulate nano crystalline silicon materials[129, 209].

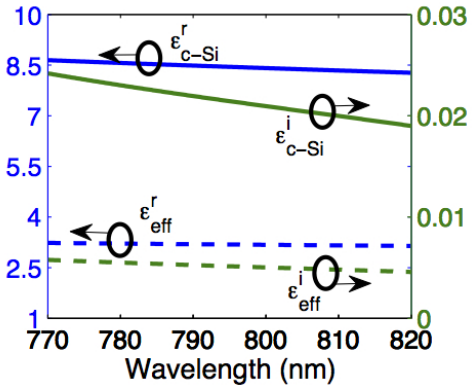

FIGURE 5.3: Real and imaginary parts of the dielectric functions of the crystalline silicon constituent (c-Si) of the PS membrane (solid lines) and the effective medium approximation (dashed lines). The left axis corresponds to the real parts; the right axis corresponds to the imaginary parts.

Then, the Bruggeman effective medium approximation[160] is used to mix the phase of nano c-Si with voids to express the effective dielectric function, ϵ_{eff}, of the PS membrane, which is given as

$$\begin{aligned}\epsilon_{\mathit{eff}} = \frac{1}{4}\{&\epsilon_v(3p-1) + \epsilon_{c-Si}(2-3p) \\ &+ \sqrt{[\epsilon_v(3p-1) + \epsilon_{c-Si}(2-3p)]^2 + 8\epsilon_{c-Si}\epsilon_v}\} \ .\end{aligned} \tag{5.1}$$

where $\epsilon_v = 1$ is the dielectric constant of voids and p is the porosity of the PS membrane. Referring to the experimental conditions and sample structure information, the effective dielectric constant ϵ_{eff} can be used in the transfer matrix method[93, 164] to calculate out T_0^{cal} and R_0^{cal}, denoting the modelled transmittance and reflectance, respectively. We note that ϵ_{eff} was assumed to be uniform across the membrane depth (an assumption that holds for membranes thinner than $30 \to 50\mu m$). The more details about using transfer matrix to calculate transmittance and reflectance can be found in Equations 3.41 and 3.42. The fitting parameters in the optical model were iteratively adjusted to

minimise the difference between the calculated and measured values to obtain the best fits shown in Figure 5.2. The best fits were obtained by setting the energy band gap, E_g, of nano c-Si at $1.3eV$; the composition and thickness used in the calculation are very similar to those obtained experimentally (a porosity is 54.5% and a thickness of $13.2\mu m$). The phenomenological parameters, A_i, B_i, and C_i are close to the values published in the original paper for the crystalline silicon[130]. The values of ϵ_{c-Si} and ϵ_{eff} obtained in the fitting process for the whole PS membrane are shown in Figure 5.3. We note that the dielectric function of the nano-crystalline silicon constituent is slightly different from that of bulk silicon owing the presence of native silicon oxide and nanoscopic dimensions affecting the band structure of silicon crystallites[210, 211]. We also note that the absolute change of the values of ϵ_{c-Si} over the observed spectrum is greater than that of the corresponding effective dielectric functions ϵ_{eff}. This effect is owed to the dilution of the crystalline silicon phase and decreased contribution to the optical response. However, the relative change is same for both functions. The detailed flowchart of simulation procedure has been illustrated in figure 3.15. Then, we can do the pump probe transmission and reflection measurements and analysis the data basing on the optical property of ground state PS membrane. Actually, it has been reported that a significant response can be observed in pump-probe measurements, and this technique was widely used in the previous works to study the excited state of the PS[20, 61, 62]. It was shown that the excitation of the free carriers can be described sufficiently well by the Drude response.

5.3 Determination of Excitation Profile in PS Membrane

The discussion and results in this subsection have also been published in paper: **Determination of excitation profile and dielectric function spatial nonuniformity in porous silicon by using WKB approach. Optics express, 22(22):2712327135, 2014.**[29] Most part of text is from the publication.

To obtain the experimental results we used pump-probe femtosecond pulses with identical spectrum spanning through the region between 770 and $820nm$. All the measurements were done at a $5ps$ time delay between the pump and probe, recording simultaneously the changes of transmittance and reflectance induced by the pump. The analysis focused on the retrieving of the complex dielectric function alteration caused by the pump excitation. We show that the assumption of uniform excitation and uniform dielectric function alteration is insufficient for constructing an optical model able to successfully describe the observed results. Therefore, we developed an analytical approach that allows us to find a non-uniformity of the excitation. This method is based

on the Wentzel-Kramers-Brillouin approach (WKB) and allows us to find a smooth change of the dielectric function between the membrane facets. Using this method, we retrieved the depth-dependent change of the complex dielectric function induced by the pump. The optical model developed in this study can be used for more complex analysis of optical pump-probe measurements, such as determination of the excitation lifetime, reconstruction of carrier diffusion, and establishing the conductivity.

The optical properties of optically excited PS membranes were investigated by using the traditional optical pump-probe method to measure induced reflection and transmission change at a $5ps$ delay time after pump excitation. A relativity long time delay was set here to allow the nascent, hot, excited charge carriers to cool and relax to the bottom of the band edge, the delay time was also sufficiently short to allow the recombination process to be neglected as it proceeds on a much longer time scale. For the measurements, a Coherent ultrafast laser system was used to provide ultrashort laser pulses. The system delivers $\sim 50fs$ pulses of nearly Gaussian shape, covering the spectral range between $760nm$ and $830nm$. The source beam was split by a pellicle beam splitter into intensive pump pulses and weak probe pulses in a ratio of $\sim 100:1$. With the help of a computer-controlled retroreflector, the optical path length of the probe pulse can be precisely delayed with respect to that of the pump pulse, generating a difference between arrival times of the pulses on the surface of the sample. The pump fluence was adjusted by using an attenuator based on a combination of a rotatable half-wave plate and a near-Brewster angle reflection, which was set to $1.5mJ/cm^2$. The polariser and half-wave plate were used to set the probe and pump beams to the $s-$ and $p-$ polarisation states, respectively, to avoid interference. The incident angle of the probe beam was set to 45°. The difference between the pump and probe beam incident angles was 15°. The probe and pump were focused to ~ 50 and $\sim 500\mu m$ spot diameters, respectively, on the surface of the PS membrane. The spatial overlap between the pump and probe was checked by a CCD camera equipped with a magnifying lens. The temporal overlap between the pump and probe pulses was determined by a second harmonic generation from a BBO crystal positioned at the place of the sample. For measurements of the transmission and reflection of the probe beam, the same spectrometer (Ocean Optics QE65 Pro) was used. Further information about the experimental setup can be found in section 3.4.1 and Figure 3.22. The measurements presented here are in the form of a fractional change of the reflectance and transmittance: $\Delta T/T_0 = (T_t - T_0)/T_0$ and $\Delta R/R_0 = (R_t - R_0)/R_0$, where T_t and R_t are the transmittance and reflectance respectively, of the excited sample at a time delay t after the pump excitation; T_0 and R_0 are the transmittance and reflectance of the sample without excitation, which have been characterised in Figure 5.2. Figure 5.4 shows the experimental results of the transient

pump-probe fractional change of the transmission and reflection, $\Delta T/T_0$ and $\Delta R/R_0$, respectively, as a function of the probe wavelength.

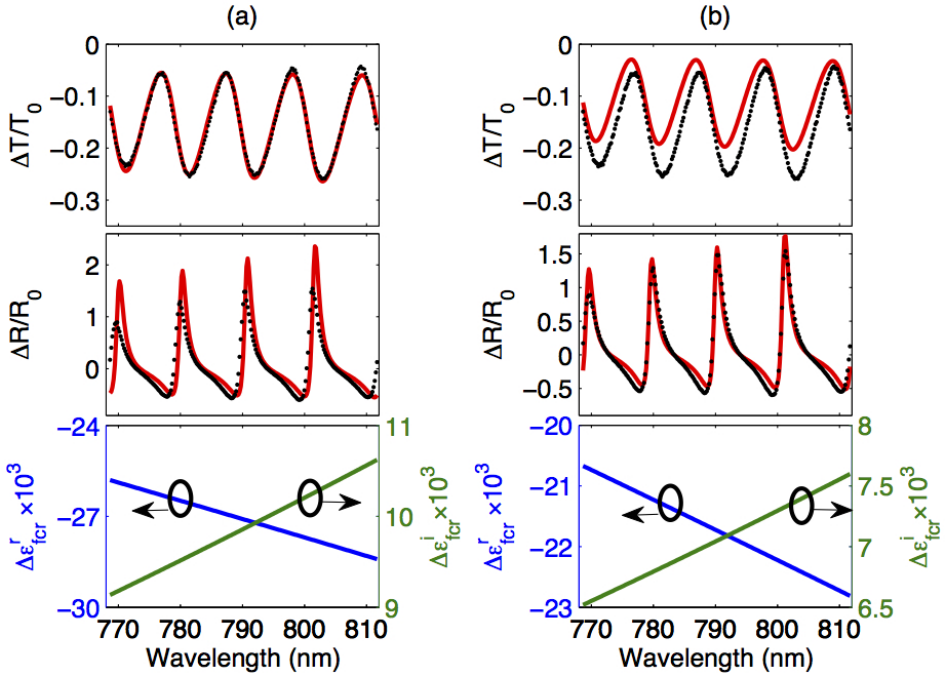

FIGURE 5.4: Transient pump-probe transmission and reflection, $\Delta T/T_0$ and $\Delta R/R_0$, measured on the PS membranes at a time delay of $5ps$. The black dots represent the experimental results. The red solid lines show the fitting results using the uniform optical model. The bottom plots show the change to the dielectric function induced by the pump and used for the calculation of $\Delta T/T_0$ and $\Delta R/R_0$. (a) A uniform model provides good fitting to $\Delta T/T_0$, but shows a discrepancy in the fitting to $\Delta R/R_0$; (b) a uniform model fits well $\Delta R/R_0$, but fails to describe $\Delta T/T_0$.

5.3.1 Uniform Excitation Model

We attempted to simulate the experimental pump-probe results by assuming a uniform change of the complex dielectric function across the membrane depth induced by the pump. The dielectric function of the nano-silicon fraction excited by the pump, $\epsilon_{Si-pump}$, can be described as a sum of the dielectric functions at the ground state (shown in Figure 5.3), ϵ_{c-Si}, and the response of the free carrier, $\Delta\epsilon_{fcr}$, excited by the pump:

$$\epsilon_{Si-pump} = \epsilon_{c-Si} + \Delta\epsilon_{fcr} \ . \tag{5.2}$$

In general, there are additional possible physical effects expected to contribute to the change of the linear optical properties of an optically excited semiconductor, such as band filling, band structure renormalisation and phonon excitation, but in our experimental conditions these effects are negligible [17].

The Bruggeman model was then implemented again to express the effective dielectric function of the excited PS membrane and the transfer matrix method was used to evaluate the change of the transmittance and reflectance, $\Delta T/T_0$ and $\Delta R/R_0$, respectively, induced by the excitation. However, we were unable to fit simultaneously $\Delta T/T_0$ and $\Delta R/R_0$. Figure 5.4(a) shows the cases where a uniform change of the dielectric function provides a good fitting of $\Delta T/T_0$, but was not satisfactory for $\Delta R/R_0$. In contrast, on Figure 5.4(b) $\Delta R/R_0$ was reasonably well-fitted, but $\Delta T/T_0$ was not. Any attempts to simultaneously fit the change in reflectance and transmittance resulted in discrepancies between the experiment and calculations. We concluded that no unique solution exists for a uniform $\Delta\epsilon_{fcr}$ that can describe the optical response of the optically excited PS membrane. This conclusion is well-founded on a simple argument that, in the first instance after the excitation, the spatial profile of the excited carriers reproduces the absorption profile of the pump and, thus, it is not uniform because the pump intensity drops along the propagation path through the membrane. Therefore, we developed a new procedure to analyse the results and calculate the variation of the optical properties as a function of the membrane depth.

5.3.2 Nonuniform Model

The model we used to describe the optical response of the optically excited membrane is based on the WKB method, in which a smooth nonuniform change of the dielectric properties as a function of the depth is assumed[212]. In our case, this change is related to the alteration of the density of excited charge carriers as a function of the membrane depth along the coordinate z. Therefore, the dielectric function of the membrane is given by $\epsilon'_{Si-pump}(z) = \epsilon_{c-Si} + \Delta\epsilon_{fcr}(z)$. This function was used in the Bruggeman model to obtain the effective dielectric function $\epsilon'_{eff}(z)$ and calculate $\Delta T/T_0$ and $\Delta R/R_0$ by fitting the experimental results. Hence, in this fitting procedure $\Delta\epsilon_{fcr}(z)$ can be retrieved. We note that, in general, one may expect nontrivial oscillations as a function of the angle of diffusively scattered light[213], but here we will concentrate on the specular reflection and transmission only, which are well described by a model with a dielectric function depending exclusively on the perpendicular coordinate.

5.3.2.1 Definition of Boundary Characteristic Matrix

First, we derive the boundary transfer matrix method that is used to calculate the transmittance and reflectance of the membrane. Figure 5.5(a) shows a boundary between media i and j. The complex amplitudes of light incoming from the left and right are expressed as a_i^{in} and a_j^{in}, respectively, while the outgoing amplitudes are given by a_i^{out}

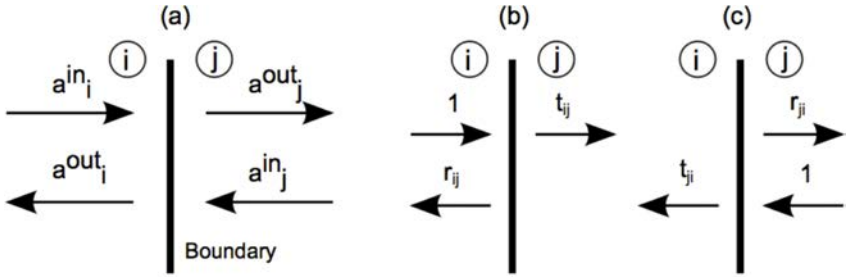

FIGURE 5.5: (a) Complex amplitudes of the electric fields of light crossing a boundary; amplitude coefficients for light incoming in the forward (b) and reverse (c) directions.

and a_j^{out}. a_j^{out} denotes the summation of the transmission part of a_i^{in} and the reflection part of a_j^{in}, and a_i^{out} represents the summation of the reflection part of a_i^{in} and the transmission part of a_j^{in}. Neglecting surface roughness, which causes cross-polarised scattering[43], we may define a characteristic (transfer) boundary matrix $\hat{T_{ij}}$ for $s-$ polarisation only that relates the fields on both sides of the boundary, i and j:

$$\begin{bmatrix} a_i^{in} \\ a_i^{out} \end{bmatrix} = \hat{T_{ij}} \cdot \begin{bmatrix} a_j^{out} \\ a_j^{in} \end{bmatrix} = \begin{bmatrix} T_{ij}^{11} & T_{ij}^{12} \\ T_{ij}^{21} & T_{ij}^{22} \end{bmatrix} \cdot \begin{bmatrix} a_j^{out} \\ a_j^{in} \end{bmatrix} . \tag{5.3}$$

The Equation 5.3 reveals that the boundary transfer matrix $\hat{T_{ij}}$ includes four elements and the directivity is from medium i to j. To obtain the elements of the matrix $\hat{T_{ij}}$, the two special cases shown in Figure 5.5(b) and Figure 5.5(c) are considered. Figure 5.5(b) depicts the case of light with a unitary field amplitude crossing the boundary from i to j. So, the reflection from the boundary can be described as r_{ij}, which is the reflection coefficient from medium i to j and a negative value. The positive direction can be defined as the direction from left to right side. The transmission is represented as the transmission coefficient t_{ij}, which is a positive value. The Equation 5.3 for such a case can be presented as

$$\begin{bmatrix} 1 \\ r_{ij} \end{bmatrix} = \hat{T_{ij}} \cdot \begin{bmatrix} t_{ij} \\ 0 \end{bmatrix} . \tag{5.4}$$

Similarity, for the field crossing the boundary from j to i, which is shown in Figure 5.5(c), the expression can be formulated as

$$\begin{bmatrix} 0 \\ t_{ji} \end{bmatrix} = \hat{T_{ij}} \cdot \begin{bmatrix} r_{ji} \\ 1 \end{bmatrix} . \tag{5.5}$$

Then, considering the four elements in boundary transfer matrix $\hat{T_{ij}}$, we can expand the equation 5.4 and equation 5.5 to following equations 5.6 and 5.7 respectively.

$$\begin{aligned} 1 &= T_{ij}^{11} \cdot t_{ij} \\ r_{ij} &= T_{ij}^{21} \cdot t_{ij} \end{aligned} \tag{5.6}$$

$$\begin{aligned} 0 &= T_{ij}^{11} r_{ji} + T_{ij}^{12} \\ t_{ji} &= T_{ij}^{21} r_{ji} + T_{ij}^{22} \end{aligned} \tag{5.7}$$

From equation 5.6, we can get transmission and reflection coefficients from medium i to medium j, which are expressed in equation 5.8.

$$t_{ij} = \frac{1}{T_{ij}^{11}} , \qquad r_{ij} = \frac{T_{ij}^{21}}{T_{ij}^{11}} \tag{5.8}$$

Combining equation 5.6 and 5.7, the boundary transfer matrix $\hat{T_{ij}}$ can be written as following

$$\hat{T_{ij}} = \begin{bmatrix} \frac{1}{t_{ij}} & -\frac{r_{ji}}{t_{ij}} \\ \frac{r_{ij}}{t_{ij}} & t_{ji} - \frac{r_{ij} r_{ji}}{t_{ij}} \end{bmatrix} . \tag{5.9}$$

Furthermore, we can simplify this boundary transfer matrix $\hat{T_{ij}}$ to more brief expression 5.10, referring to relations $r_{ij} = -r_{ji}$ and $t_{ij} = 1 + r_{ij}, t_{ji} = 1 + r_{ji}$. And the relationship $\hat{T_{ij}}^{-1} = \hat{T_{ji}}$ can also be confirmed when considering the directivity for boundary transfer matrix. As we can see in this general boundary transfer matrix expression, the four elements only depend on the reflection and transmission coefficients r_{ij}, t_{ij} respectively between the medium i and medium j.

$$\hat{T_{ij}} = \frac{1}{t_{ij}} \cdot \begin{bmatrix} 1 & r_{ij} \\ r_{ij} & 1 \end{bmatrix} \tag{5.10}$$

5.3.2.2 Nonuniform Optical Property in WKB Approximation

Using the boundary transfer matrix developed above, we will derive a characteristic matrix based on the WKB method to calculate the transmittance and reflectance of light propagating through a membrane with a spatially nonuniform optical response.

Figure 5.6 shows a schematic cross-section of a membrane with the thickness d. There are three regions denoted as ①, ② and ③ from the left to the right hand side. The interfaces between the regions ① and ②, and between ② and ③ can be described by the boundary transfer matrices $\hat{T_{12}}$ and $\hat{T_{23}}$, respectively. According to Equation 5.10, these matrices can be presented as the following:

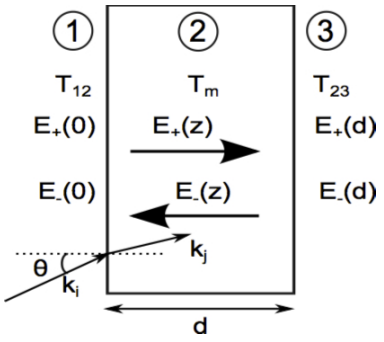

FIGURE 5.6: Schematic representation of a membrane cross-section. Regions ① and ③ represent the membrane interfaces; ② denotes the membrane region with a nonuniform dielectric function.

$$\hat{T_{12}} = \frac{1}{t_{12}} \begin{bmatrix} 1 & r_{12} \\ r_{12} & 1 \end{bmatrix} \; ; \quad \hat{T_{23}} = \frac{1}{t_{23}} \begin{bmatrix} 1 & r_{23} \\ r_{23} & 1 \end{bmatrix} \tag{5.11}$$

Then, to derive the matrix, $\hat{T_m}$, describing the optical response of $s-$polarised light propagating between the interfaces, we assign the total electric field of light inside of the medium as $E(z) = E_+(z) + E_-(z)$ for every depth between 0 and d, where $E_+(z)$ and $E_-(z)$ represent the fields of light propagating from left to right and in the reverse directions, respectively. k_i and k_j are the wave vectors of light outside and inside the membrane. Referring to the Wentzel-Kramers-Brillouin (WKB) approximation[214–217], the electric field $E_\pm(z)$ at any depth position z is given by the following:

$$\begin{aligned} E_\pm(z) &= \frac{a_\pm}{\sqrt{q(z)}} \cdot e^{\pm i \int_0^z dz' q(z')} \\ \text{where} & \\ q(z) &= \sqrt{\tfrac{\omega^2}{c^2}\epsilon'_{eff}(z) - k_x^2} \; . \end{aligned} \tag{5.12}$$

Here the total wave vector $k_j(z)$ at any depth position inside the medium is representing as

$$k_j(z)^2 = \frac{\omega^2}{c^2}\epsilon'_{eff}(z) = \frac{\omega^2}{c^2}[\Re(\epsilon'_{eff}(z)) + i\Im(\epsilon'_{eff}(z))] \; . \tag{5.13}$$

And the term $k_x = \frac{\omega}{c} sin\theta$ defines the tangential component of the wave vector, which is parallel to the surface of medium. θ is the incident angle of the probing beam. $\epsilon'_{eff}(z)$ is the effective dielectric constant of membrane under excited state, which is also a function of depth position z. According to the Snell's law $n_i sin\theta_i = n_j sin\theta_j$ and probing angular frequency $\omega = \omega_i = \omega_j$, we can multiply both sides of Snell's Equation by ω/c to obtain $k_i sin\theta_i = k_j sin\theta_j$. Consequently, tangential component $k_x = \frac{w}{c} sin\theta$ should always be constant at any depth position z as the tangential component of incident wave

vector $k_i sin\theta_i = \frac{\omega_i}{c} sin\theta_i$. So the parameter $q(z)$ actually describes the perpendicular component of wave vector at any depth position z inside the medium.

Finally, the electric field $E_{\pm}(z)$ at the arbitrary depth position in the region between 0 and d can be formulated using the WKB approximation method. And $a_{\pm}/\sqrt{q(z)}$ is the magnitude of electric field at any depth position. The exponential term $e^{\pm i \int_0^z dz^{'} q(z^{'})}$ actually includes a real part component to attenuate the magnitude of electric field and an imaginary part to express the absorption property at each depth position of membrane.

Eventually, the matrix $\hat{T_m}$ relating the fields between the interfaces inside the membrane, can be expressed as the following:

$$\begin{bmatrix} E_+(0) \\ E_-(0) \end{bmatrix} = \hat{T_1}\hat{T_2}\hat{T_3}\cdots\hat{T_n} \begin{bmatrix} E_+(d) \\ E_-(d) \end{bmatrix} = \hat{T_m} \begin{bmatrix} E_+(d) \\ E_-(d) \end{bmatrix} \tag{5.14}$$

Where $\hat{T_1}, \hat{T_2}, \hat{T_3}, \cdots \hat{T_n}$ can be considered as the boundary transfer matrixes corresponding to every depth position from the denoting number 1 to n between front interface 0 and rear interface d. In another word, we can assume the medium is composed by infinite boundaries between the two interfaces and each boundary can be expressed as a transfer matrix. The $\hat{T_m}$ is obtained from multiplying all these matrixes from left first one $\hat{T_1}$ to the right final one $\hat{T_n}$, which can be used to represent the whole medium property and make a bridge between the $(E_+(0), E_-(0))$ and $(E_+(d), E_-(d))$. Using equation 5.12, $(E_+(0), E_-(0))$ and $(E_+(d), E_-(d))$ can be formulated as following:

$$\begin{aligned} E_+(0) &= \frac{a_+}{\sqrt{q(0)}} \cdot e^{i \int^0 dz^{'} q(z^{'})} \\ E_-(0) &= \frac{a_-}{\sqrt{q(0)}} \cdot e^{-i \int^0 dz^{'} q(z^{'})} \\ E_+(d) &= \frac{a_+}{\sqrt{q(d)}} \cdot e^{i \int^d dz^{'} q(z^{'})} \\ E_-(d) &= \frac{a_-}{\sqrt{q(d)}} \cdot e^{-i \int^d dz^{'} q(z^{'})} \end{aligned} \tag{5.15}$$

Substituting these equations 5.15 into the medium expression 5.14, the matrix for whole membrane $\hat{T_m}$ can be obtained as following

$$\begin{aligned} \hat{T_m} &= \sqrt{\frac{q(d)}{q(0)}} \begin{bmatrix} e^{-i\psi} & 0 \\ 0 & e^{i\psi} \end{bmatrix} \\ \text{where} & \\ \psi(z, \lambda, \theta) &= \int_0^d dz\ q(z) = \frac{\omega}{c} \int_0^d dz\ \sqrt{\epsilon^{'}_{eff}(z, \lambda) - sin^2\theta}\ . \end{aligned} \tag{5.16}$$

We define the phase as $\psi(z, \lambda, \theta)$ in above Equation and the phase ψ is a function of depth z, probing wavelength λ and incident angle θ.

Finally, the characteristic matrix for the entire membrane system, shown in Figure 5.6, can be expressed as a product of the individual matrixes: $\hat{T_{12}}$ for front interface, $\hat{T_m}$ for the medium and $\hat{T_{23}}$ for the rear interface, which is written as:

$$\begin{aligned}\hat{T} &= \hat{T_{12}} \cdot \hat{T_m} \cdot \hat{T_{23}} \\ &= \frac{1}{t_{12}} \begin{bmatrix} 1 & r_{12} \\ r_{12} & 1 \end{bmatrix} \cdot \sqrt{\frac{q(d)}{q(0)}} \begin{bmatrix} e^{-i\psi} & 0 \\ 0 & e^{i\psi} \end{bmatrix} \cdot \frac{1}{t_{23}} \begin{bmatrix} 1 & r_{23} \\ r_{23} & 1 \end{bmatrix} \\ &= \frac{1}{t_{12}t_{23}} \sqrt{\frac{q(d)}{q(0)}} \cdot \begin{bmatrix} e^{-i\psi} + r_{12}r_{23}e^{i\psi} & e^{i\psi}r_{12} + e^{-i\psi}r_{23} \\ e^{-i\psi}r_{12} + e^{i\psi}r_{23} & e^{i\psi} + r_{12}r_{23}e^{-i\psi} \end{bmatrix}\end{aligned} \tag{5.17}$$

According to equations 5.8, the reflection and transmission coefficients are given by $r_{ij} = \frac{T_{ij}^{21}}{T_{ij}^{11}}$ and $t_{ij} = \frac{1}{T_{ij}^{11}}$. So they can be obtained from the final matrix expression 5.17 for the membrane system, which are given as following

$$t = \frac{1}{\sqrt{\frac{q(d)}{q(0)}}} \cdot \frac{t_{12}t_{23}}{e^{-i\psi} + r_{12}r_{23}e^{i\psi}} \ , \qquad r = \frac{e^{-i\psi}r_{12} + e^{i\psi}r_{23}}{e^{-i\psi} + r_{12}r_{23}e^{i\psi}} \ . \tag{5.18}$$

Then, according to the Fresnel equation 3.8 for $s-$ polarised light, we can obtain the r_{12} and r_{23}, which are shown as following

$$r_{12} = r_0 = \frac{cos\theta - \sqrt{\epsilon'_{eff}(0) - sin^2\theta}}{cos\theta + \sqrt{\epsilon'_{eff}(0) - sin^2\theta}} \ , \qquad r_{23} = -r_d = -\frac{cos\theta - \sqrt{\epsilon'_{eff}(d) - sin^2\theta}}{cos\theta + \sqrt{\epsilon'_{eff}(d) - sin^2\theta}} \ . \tag{5.19}$$

Furthermore, the reflection coefficients r_0 and r_d can be briefly formulated using the definition 5.12 of $q(z)$ and wave vector $k_z = \frac{w}{c}cos\theta$, which are shown as following

$$r_0 = \frac{k_z - q(0)}{k_z + q(0)} \ , \qquad r_d = \frac{k_z - q(d)}{k_z + q(d)} \ . \tag{5.20}$$

Substituting these reflection coefficients of the front interface and rear interface into the equation 5.18 and combing the relations $t_{12} = 1 + r_{12}, t_{23} = 1 + r_{23}$, we can get the total reflection and transmission coefficients of the whole PS membrane as following

$$r = \frac{r_0e^{-i\psi} - r_de^{i\psi}}{e^{-i\psi} - r_0r_de^{i\psi}} \ , \qquad t = \frac{1}{\sqrt{\frac{q(d)}{q(0)}}} \cdot \frac{(1 + r_0)(1 - r_d)}{e^{-i\psi} - r_0r_de^{i\psi}} \ . \tag{5.21}$$

If we make a parameter definition as $E = e^{i\psi}$, the total reflection and transmission coefficients equations 5.21 can be further simplified as following

$$r = \frac{E^{-2}r_0 - r_d}{E^{-2} - r_0 r_d}\ , \qquad t = \frac{1}{\sqrt{\frac{q(d)}{q(0)}}} \cdot \frac{(1+r_0)(1-r_d)E^{-1}}{E^{-2} - r_0 r_d}\ . \tag{5.22}$$

Then, to calculate the reflectance and transmittance of excited state membrane, one can use the definition: $R_t = |r|^2$ and $T_t = |t|^2$ referring to equations 5.22. (PS membrane is detected in the air atmosphere.) As long as we realised the incident angle θ of probing beam and effective dielectric constant of the excited state PS membrane $\epsilon'_{eff}(z,\lambda)$, we can calculate out R_t, T_t and fit the measurement data $\Delta T/T_0, \Delta R/R_0$ simultaneously. The incident angle θ can be set in the experimental conditions. As the $\epsilon'_{eff}(z,\lambda)$ is derived from $\Delta\epsilon_{fcr}(z,\lambda)$, one can see that the only unknown in our experiment is a complex function $\Delta\epsilon_{fcr}(z)$, which can be reasonably well retrieved from a simultaneous fitting of the $\Delta T/T_0$ and $\Delta R/R_0$.

5.3.2.3 Fitting and Determination of $\Delta\epsilon_{fcr}(z)$

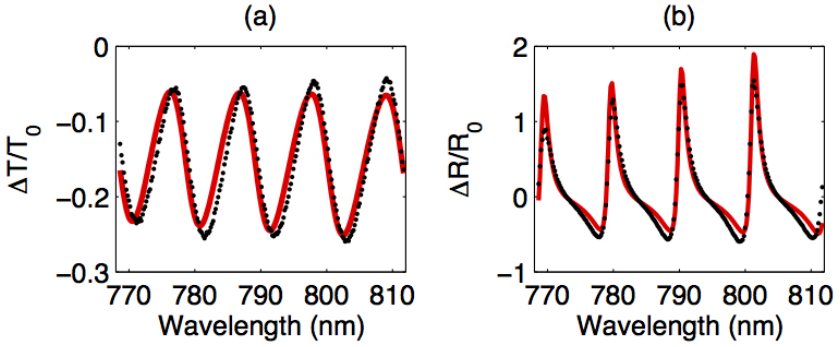

FIGURE 5.7: Simultaneous fitting of the transmittance (a) and reflectance (b) change using the nonuniform model. The black dots show the experimental results of the pump-probe experiment at the 5*ps* time delay; the red-line denotes the fitting of the nonuniform model.

To simplify the fitting process, the fitting parameters were defined as $\Delta\epsilon_{fcr}(0,\lambda)$ and $\Delta\epsilon_{fcr}(d,\lambda)$ for the front surface and rear surfaces of the PS membrane, respectively, and a smooth decaying function with depth of membrane joining these points. The fitting parameters and function are located in the complex plane; their real and imaginary parts are related by the Kramers-Kronig bidirectional relations. By using these parameters, the front and rear surface reflection coefficients r_0 and r_d and the accumulated phase ψ can be estimated and iteratively adjusted minimising the difference between the calculated and the measurement results of $\Delta T/T_0$ and $\Delta R/R_0$. Figure 5.7 shows the best fitting results for the optical model with a nonuniform complex dielectric function. The

results of the fitting represented by the red solid lines reproduce well the measurements denoted by the black dots. It is clearly seen that the nonuniform model provides better fitting to the results than the uniform one.

Actually, the free carrier response, $\Delta\epsilon_{fcr}(z,\lambda)$, is formulated by the Drude equation 3.100 under the restriction of Kramers-Kronig relation, which expresses the dielectric constant changing as probing light wavelength. Inside the Drude equation 3.100, the plasma frequency $\omega_p(z)$ and scattering rate $\Gamma(z)$ represent the nonuniform property as the function of membrane depth position z. The WKB method has assumed a smooth decaying function between $\Delta\epsilon_{fcr}(0,\lambda)$ and $\Delta\epsilon_{fcr}(d,\lambda)$. Moreover, referring to the Beer's law: $I_t = I_0 \cdot e^{-\alpha d}$, the light intensity passing the medium also performs the exponential function with increasing depth. Consequently, the $\omega_p(z)$ and $\Gamma(z)$ are simplified as the exponential functions to reproduce the exponential decaying of $\Delta\epsilon_{fcr}(z)$.

Regarding to the assumed smoothly exponential functions for $\omega_p(z)$ and $\Gamma(z)$ separately, the front surface $\omega_p(0), \Gamma(0)$ and rear surface $\omega_p(d), \Gamma(d)$ can be proposed to produce the $\Delta\epsilon_{fcr}(0,\lambda)$ and $\Delta\epsilon_{fcr}(d,\lambda)$. These four parameters are used for simultaneously fitting pump probe reflection and transmission data $(\Delta R/R_0, \Delta T/T_0)$, meanwhile the exponential functions of $\omega_p(z)$ and $\Gamma(z)$ can be identified as long as the values of four parameters are obtained.

$$\omega_p(z) = \omega_p(0) \cdot e^{-a_1 \cdot z} \ , \quad \text{where} \quad a_1 = -\frac{1}{d} \cdot ln\frac{\omega_p(d)}{\omega_p(0)} \ ; \tag{5.23}$$

$$\Gamma(z) = \Gamma(0) \cdot e^{-a_2 \cdot z} \ , \quad \text{where} \quad a_2 = -\frac{1}{d} \cdot ln\frac{\Gamma(d)}{\Gamma(0)} \ . \tag{5.24}$$

As adjusting the four parameters $(\omega_p(0), \Gamma(0))$ and $(\omega_p(d), \Gamma(d))$, which represent the changing of the front surface $\Delta\epsilon_{fcr}(0,\lambda)$ and rear surface dielectric functions $\Delta\epsilon_{fcr}(d,\lambda)$ respectively, we can minimise the difference between calculation and measurement, and complete the fitting process. The criterion for judging the best fitting results is constructed according to the weighted least squares method, which can be formulated as following

$$\chi = \frac{1}{2N-M}\sum_{i=1}^{N}\{w_1[(\frac{\Delta R}{R_0})^{cal} - (\frac{\Delta R}{R_0})^{exp}]^2 + w_2[(\frac{\Delta T}{T_0})^{cal} - (\frac{\Delta T}{T_0})^{exp}]^2\} \ . \tag{5.25}$$

Where N is the number of data points of probing spectrum in the measurements and M is the number of variable parameters in the fitting model, $M = 4$. The weighted coefficients w_1, w_2 can be used to weight the balance of contributions from pump probe reflection fitting and transmission fitting. Here, $w_1 = 15\%$ and $w_2 = 85\%$ are used referring to the scale of Figure 5.7. We note here that this linear regression algorithm

provides the fitting error of $\chi = 0.0016$. On the other hand, the fitting errors for the uniform model (shown in Figure 5.4) is by an order of magnitude greater.

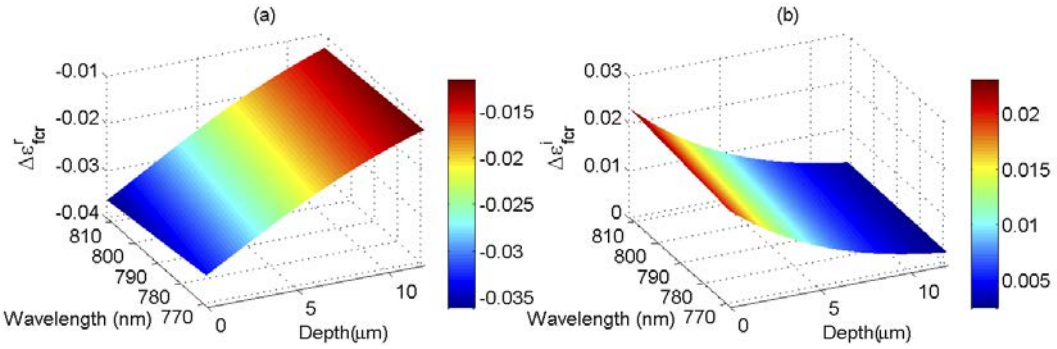

FIGURE 5.8: Wavelength-dependent lateral distribution of the real (a) and imaginary (b) parts of the dielectric function change induced by the pump excitation, retrieved from the optical model based on the WKB approach.

From the model fitting, we retrieved the real and imaginary parts, $\Delta\epsilon^r_{fcr}(z,\lambda)$ and $\Delta\epsilon^i_{fcr}(z,\lambda)$, of the dielectric function change 5 ps after the excitation by the pump. These functions are shown in Figure 5.8. It can be seen that $\Delta\epsilon^r_{fcr}$ and $\Delta\epsilon^i_{fcr}$ are only weakly dependent on the probe wavelength, as expected for the free carrier response measured away from the resonance. However, these functions depend strongly on the position, z: $\Delta\epsilon^r_{fcr}(z)$ is changing from around -0.035 to -0.012, while $\Delta\epsilon^i_{fcr}(z)$ is shifting from around 0.022 to 0.003 as a function of the depth between $0\mu m$ and $13\mu m$. The observed change corresponds to the excitation profile decaying as a function of the distance from the front surface. Moreover, by comparing $\Delta\epsilon_{fcr}$ with the dielectric function of nano c-Si without pump excitation ϵ_{c-Si} in Figure. 5.3, it can be seen that the fractional change of the real part, $\Delta\epsilon^r_{fcr}$, is quite small in comparison to that of the imaginary part, $\Delta\epsilon^i_{fcr}$. Such a relation is characteristic for the free carriers response when the plasma frequency and scattering rate are of the same order[218]. In order to clearly illustrate the changing behaviour of $\epsilon_{fcr}(z)$ as increasing the depth position from 0 to d, the real and imaginary part of $\Delta\epsilon_{fcr}(z,\lambda)$ can be simply averaged over the whole probing wavelength from around $770nm$ to $820nm$, which is displayed in Figure 5.9.

We note here that the profile of the excitation strength (the dielectric function change) is in general different from that expected for a semi-infinite solid because of the pump pulse absorbance enhancement resulting from bouncing inside the membrane between the rear and front surfaces. It can be estimated that the pump pulse travels $2 \rightarrow 3$ round trips before its intensity decays by a factor of $1/e$.

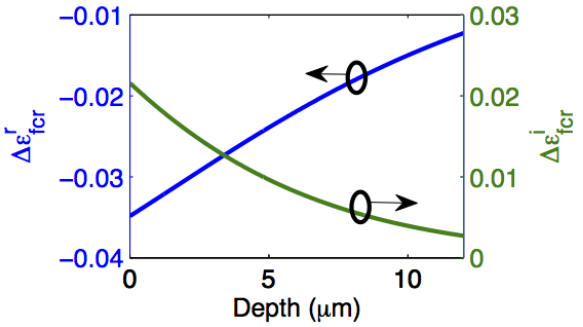

FIGURE 5.9: Averaging over the probing spectrum to obtain the real part $\Delta\epsilon^r_{fcr}(z)$ and imaginary part $\Delta\epsilon^i_{fcr}(z)$ of dielectric constant variation for excited state PS membrane at $5ps$ time delay.

5.3.3 Conclusion

In conclusion, we investigated and developed an analytical calculation method to estimate the spatial distribution along the membrane depth of the dielectric function of porous silicon membranes excited optically by a femtosecond laser pulse. We found that a model with a uniform excitation is inadequate as it does not provide a solution to reconstruct the observed experimental results and neglects the spatial excitation profile of the free charge carriers. To overcome this problem we developed an analytical method based on the WKB approximation. Using this method, we obtained the spatial distribution of the real and imaginary parts of the dielectric function bidirectionally coupled by the Kramers–Kronig relation. The results confirm that the main contribution to the change of the dielectric function induced by the optical pump can be attributed to the excited free carrier response. Thus, the obtained spatial distribution conveys the distribution of the excited carriers as a function of the membrane depth. Moreover, it seems possible to manipulate and to engineer the dielectric function by tuning the pump pulse intensity.

The modelling results provided an insight that the fractional change of the imaginary part, associated with the free carrier absorption, is significantly stronger than that of the real one. It also suggests that the excitation profile of the membrane differs from that of its semi-infinite solid counterpart because for the former the round trips and constructive interference of the pump pulse enhance the absorbance.

We believe that the method of reconstructing the spatial dielectric function distribution is useful not only for optically pumped materials but can be applied to biosensing where the PS refractive index is sensitive to the binding of biological and chemical molecules for which adsorption and distribution inside a thin film are strongly non-uniform, solar cells and detectors with a nonuniform structure and morphology, and a variety of

optoelectronic devices with induced or permanent nonuniform dielectric function modulation. In general, this model is applicable for the samples sufficiently transparent and reflective to measure the transmittance and reflectance, respectively.

5.4 Discussion on Carriers Transport Property of PS Membrane

Because of the excellent optoelectronic applications for porous silicon material, the transportation property of excited carriers in PS membrane is necessary to be studied, which mainly involves the carriers recombination time and diffusion coefficient. Generally, the experimental method to investigate the charge carriers transport in PS is studying current-voltage $(I-V)$ curves or steady-state photoconductivity measurements. But, the problem of fabricating efficient and stable contacts on PS surface remains still to be unsolved[79]. Moreover, the ordinary PS sample usually is composed of the porous silicon layer with c-Si substrate. In this case, the influence of c-Si substrate avoids to realise the accurate transport properties of PS material[219, 220]. So, in our research, the free standing thin membrane of PS is researched directly and time resolved pump probe method is applied to analyse the transport property, which is an optical non-contacted approach.

Actually, it has been reported that the diffusion coefficient D can be evaluated from the decay process of laser induced transient grating experiments[221–223]. Tomasiunas[223] estimated the value of diffusion coefficient $D \approx 40 cm^2/s$ for around 60% porosity PS, which is even higher than generally anticipated diffusion coefficient of crystalline Si [224]. While, another value $\sim 10^{-6} cm^2/s$ of the ambi-polar diffusion constant in PS by Schwarz *et al*[222] was obtained using the same method under low injection measurements. This huge difference was explained as the different injection level for PS material. To clarify the diffusion coefficient D of PS material more precisely, we proposed to use time resolved pump probe method with simultaneous detecting reflection and transmission. The measurements were scanning from $-20ps$ to $210ps$, recording simultaneous changes of transmittance and reflectance included by the excitation. In the analysis, the pump induced carrier concentration as the function of PS membrane depth and time delay is extracted from the data, basing on the WKB method and Drude equation. Then, the life time of excited carriers is estimated assuming the general linear recombination process. Finally, the diffusion coefficient D is evaluated through fitting the decay process of excited carriers concentration according to the Fick's second law, where the diffusion coefficient D is assumed to be constant at any membrane depth.

5.4.1 Time Resolved Pump Probe Measurements and Analysis

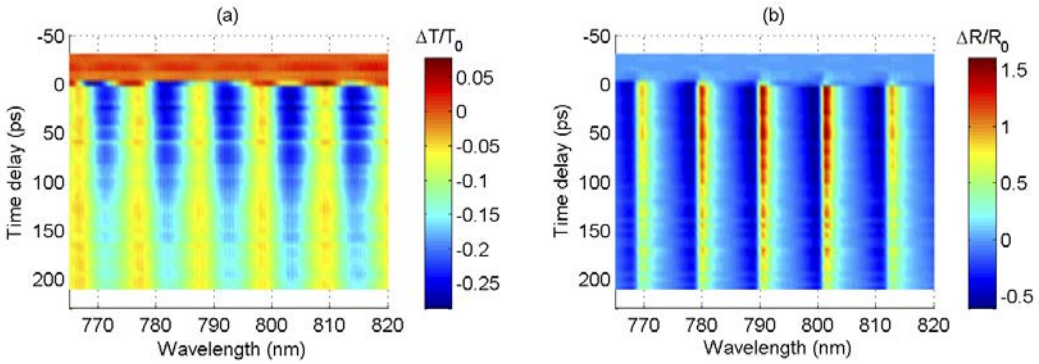

FIGURE 5.10: Time resolved pump probe (a) transmission $\Delta T/T_0$ and (b) reflection $\Delta R/R_0$ simultaneous measurement data as the function of time delay from $-20ps$ to $210ps$ in the probing spectrum region between $760nm$ and $820nm$.

In order to evaluate the excited carriers diffusion coefficient of PS membrane, the time resolved pump probe transmission and reflection are measured simultaneously under the fixed experimental conditions firstly, $1.5mJ/cm^2$ pump fluence and 45° probing incident angle. The time delay was scanning from around $-20ps$ to $210ps$, with $5ps$ step size. Figure 5.10 (a) and (b) described the measurement results $\Delta T/T_0$ and $\Delta R/R_0$ changing with probing wavelength and time delay. In the negative time delay region, the values of measurement data $\Delta T/T_0$ and $\Delta R/R_0$ were just around zero, which corresponded to the unexcited state PS membrane. In the positive time delay region, the Fabry-Perot interference fringes were induced after the pump photons excitation[19], of which amplitude was decaying as increasing the time delay from around $0ps$ to $210ps$. Referring to the amplitude of these interference fringes under each time delay, the dielectric constant of excited state PS membrane can be precisely deduced out. Meanwhile, the decay processes of data $\Delta T/T_0$ and $\Delta R/R_0$ seem to indicate that it takes more than $200ps$ for the excited state of PS membrane to return back to the ground state. Maly[61] estimated around $500ps$ decay time through detecting positive differential absorbance decay process, which corresponds to the recombination process of excited carriers in nano wires c-Si. Tang[225] used the optical pump-terahertz (THz) probe spectroscopy method to obtain the excited carriers life time as $\sim 700ps$. And Mizeikis[221] applied transient light-induced grating experiment to realise the excited carriers life time as around $430ps$ corresponding to the about same porosity as our researched PS membrane. As the life time of excited carriers is correlated with the doping level[221] of c-Si, pore size and pump intensity[61], it can only say that the magnitude of carriers life time is around several hundred picoseconds. Even though the whole decay process seems not totally to be covered in the measurements, we will estimate the life time of excited carriers in our PS membrane from detected data for evaluating carriers diffusion coefficient.

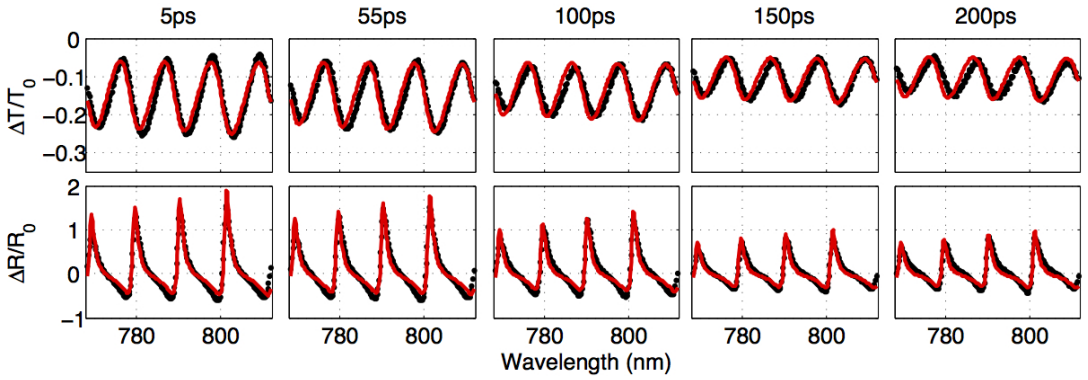

FIGURE 5.11: Applying WKB approach, black dots data $\Delta T/T_0$ and $\Delta R/R_0$ decay processes were simultaneously fitted, which were shown as red solid lines in the above figure.

The WKB method is applied to describe the optical response of the optically excited PS membrane, in which a smooth nonuniform change of the dielectric properties as a function of the depth is assumed[212]. As this change is related to the variation of the excited charge carriers concentration as a function of the membrane depth, the Drude equation 3.100 is used to express the influence of this excited free carriers response on dielectric constant variation of nano wires c-Si, $\Delta\epsilon_{fcr}(z)$. Moreover, the restriction of Kramers-Kronig relation is also obeyed in the fitting process. Therefore, the dielectric constant of excited state nano wires c-Si can be described as $\epsilon'_{Si-pump}(z) = \epsilon_{c-Si} + \Delta\epsilon_{fcr}(z)$, where ϵ_{c-Si} has been mentioned as the dielectric constant of unexcited state nano wires c-Si and characterised in Figure 5.3. Then, the Bruggeman model is applied to mix this excited state c-Si with void for expressing the effective response of excited state PS membrane $\epsilon'_{eff}(z)$. Finally, the decay process of pump probe transmission $\Delta T/T_0$ and reflection $\Delta R/R_0$ data can be simultaneously fitted using transfer matrix method calculation. To illustrate the fitting results, the data at different time delay, such as $5ps, 55ps, 100ps, 150ps, 200ps$, were picked out and shown in Figure 5.11. As we can see, the amplitudes of interference signal, shown as black dots lines, are gradually becoming weaker. And the fitting results, displayed as red solid lines, are coincident with the data very well.

From the fitting procedure, the dielectric constant variation of nano wires c-Si, $\Delta\epsilon_{fcr}(z,\lambda)$ can be obtained. As the $\Delta\epsilon_{fcr}(z,\lambda)$ weakly depends on the probing spectrum between $760nm$ and $820nm$, which has been illustrated in Figure 5.9, $\Delta\epsilon_{fcr}(z)$ is expressed with averaging over the whole probing wavelength. Figure 5.12(a) and (b) describe the real part $\Delta\epsilon^r_{fcr}(z)$ and imaginary part $\Delta\epsilon^i_{fcr}(z)$ as the function of PS membrane depth from $0\mu m$ to $12\mu m$ under the different time delay. As we can see, the amplitudes of $\Delta\epsilon^r_{fcr}(z)$ and $\Delta\epsilon^i_{fcr}(z)$ are both gradually decreasing as increasing the time delay from $5ps$ to $200ps$. This phenomenon is reasonable considering the decay process of measurement

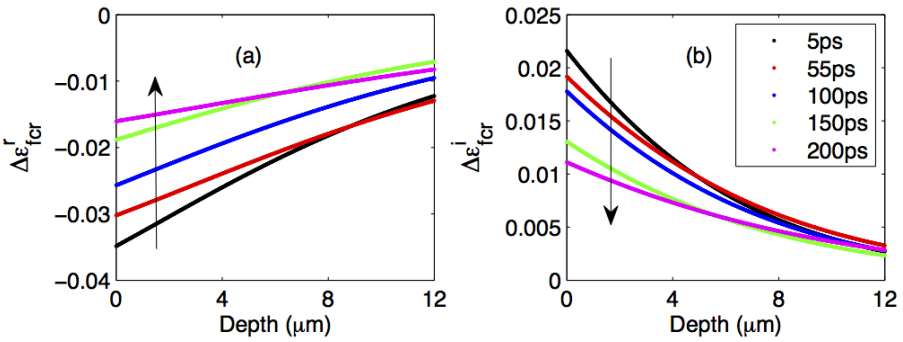

FIGURE 5.12: Dielectric constant variation of nano wires c-Si in PS membrane $\Delta\epsilon_{fcr}(z)$, which is induced by excited free carriers response, (a) real part and (b) imaginary part, changing with PS membrane depth under each time delay.

data $\Delta T/T_0$ and $\Delta R/R_0$ in Figure 5.10, which indicates the dissipation of excited free carries in membrane and nonuniform property is gradually returning back to the uniform optical property.

5.4.2 Solving Recombination and Diffusion Processes

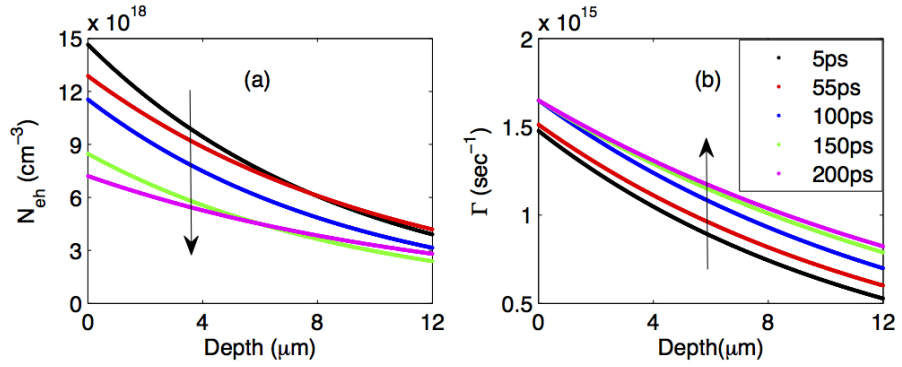

FIGURE 5.13: (a) The excited carriers concentration N_{eh} and (b) scattering rate Γ changing with the PS membrane depth between $0\mu m$ and $12\mu m$ under different time delay, which were marked as the different colour lines.

Due to $\Delta\epsilon_{fcr}(z)$ is defined by Drude equation, the plasma frequency ω_p and scattering rate Γ have been characterised as well in the fitting process. From the theoretical calculation about optical properties of quantum wires c-Si in porous silicon by G. D. Sanders[211], the optical effective mass for excited carriers can be estimated as $m^* = 0.17m_e$. Even though this is a estimation value, the decay process of the excited carrier concentration $N_{eh}(t)$ can be analytically deduced out from plasma frequency $\omega_p(t)$ according to Equation 3.99. Figure 5.13 (a) and (b) express the deduced excited carriers concentration N_{eh} and scattering rate Γ changing with the PS membrane depth position between $0\mu m$ and $12\mu m$ under different time delay. Apparently, as the time delay is increasing from $5ps$ to $200ps$, the amplitude of excited carriers concentration

$N_{eh}(z)$ is gradually decreasing, especially for the front surface value $N_{eh}(0)$, which is dropping from around $15 \times 10^{18} cm^{-3}$ to $7 \times 10^{18} cm^{-3}$. As for the scattering rate $\Gamma(z)$, the amplitude seems to have a little rising trend with increasing time delay, which can be due to the enhancement of carrier-phonon collisions in the longer time delay. As long as the $N_{eh}(z,t)$ can be estimated as the function of depth and time delay, the diffusion coefficient D of excited carriers in porous silicon membrane can be evaluated.

After the free carriers were excited through pump photon absorption, the free carriers recombination and diffusion have started with increasing the time delay. In contrast to carrier recombination, diffusion does not actually decrease the number of free carriers in material[226]. As we know, the carriers diffusion process means removing the excited carriers in real space from the high density area to low density area. Meanwhile, the carriers recombination process occurs with increasing time delay. Thus, the transport property of excited carriers in PS membrane is mainly composed by carriers diffusion and recombination in the whole decay process. According to the Fick's second law, the carriers transport equation for PS membrane can be written as:

$$\frac{dN_{eh}(z,t)}{dt} = D \cdot \frac{d^2 N_{eh}(z,t)}{dz^2} - \frac{N_{eh}(z,t)}{\tau} \ , \tag{5.26}$$

where D is the diffusion coefficient and the unit is cm^2/s; $N_{eh}(z,t)$ is the free carriers concentration as the function of depth position z and time delay t; τ is the recombination time of free carriers or non-equilibrium carrier lifetime. Here, we neglect the pump induced thermal affect on the diffusion coefficient and assume the diffusion coefficient D is a constant value for the carriers at any depth position and time delay, which simplified the transport problem as the Equation 5.26. Referring to the obtained results $N_{eh}(z,t)$ in Figure 5.13(a), the second derivative term $d^2 N_{eh}(z,t)/dz^2$ can be deduced out under each time delay t. However, in order to find the solution of Equation 5.26, we also need to know the carrier recombination time τ. To estimate the recombination time τ of PS membrane, the recombination process in the whole excited carriers transport procedure has been simplified into an exponential equation with increasing time delay t: $N_{eh}(t) = C_0 \cdot e^{-\frac{t}{\tau}}$, where C_0 is a constant value. Then, the natural logarithm is applied for both sides and a linear equation, $ln(N_{eh}(t)) = -\frac{t}{\tau} + C_0$, is got to express the relationship between $ln\langle N_{eh}(t)\rangle$ and t. Here, we used the mean value $\langle N_{eh}(t)\rangle$, which is averaging over the whole membrane depth for N_{eh} in Figure 5.13(a). Applying a linear equation to fit the data $ln\langle N_{eh}(t)\rangle$ with time delay t, the recombination time τ can be obtained from the slope of this linear fitting line. Figure 5.14 (a) depicts the data $ln\langle N_{eh}(t)\rangle$ under each time delay by black circle line and linear fitting results as red solid line. Finally, the recombination time $\tau \approx 350 ps$ is acquired.

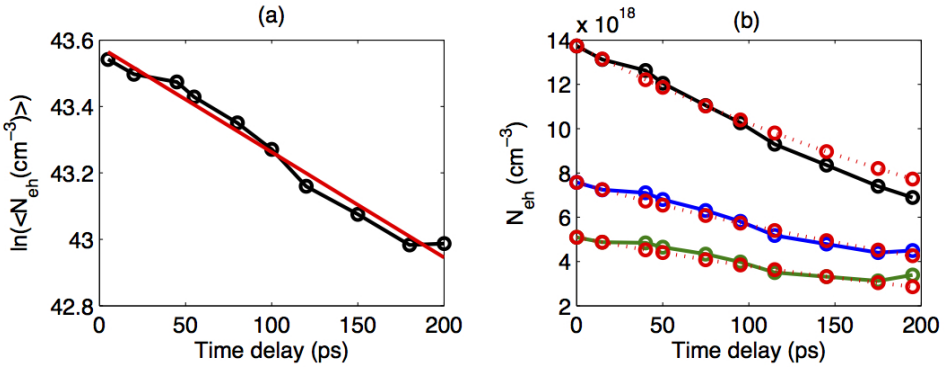

FIGURE 5.14: (a) The black circle data line is natural logarithm of mean carriers concentration $ln(\langle N_{eh}\rangle)$ changing with time delay t from $0ps$ to $200ps$, the red solid line is the linear fitting results; (b) carriers concentration N_{eh} changing with time delay from $0ps$ to $200ps$ under the three depth position of PS membrane, $z = 0.5\mu m, z = 6\mu m$ and $z = 10\mu m$, showing as black, blue and green lines respectively, which were fitted by Equation 5.26, expressing as red lines for each other.

Then, the diffusion coefficient D can be estimated through fitting the data $N_{eh}(z,t)$ with time delay t from $0ps$ to $200ps$ at any membrane depth position, referring to Equation 5.26. Here, we chose three depth positions of PS membrane at $z = 0.5\mu m, z = 6\mu m$ and $z = 10\mu m$. The decay process of data $N_{eh}(z,t)$ at these three depth position are illustrated in Figure 5.14 (b) as black, blue and green lines respectively. From the red lines fitting, we found that the diffusion coefficient at any value of $D < 10^{-1}cm^2/s$ can satisfy the decay process of data N_{eh} at all these three positions, which generally represents that the transportation property of PS membrane is mainly dominated by the recombination process and the diffusion property has little influence on excited carriers distribution in PS membrane.

In conclusion, we investigated the diffusion coefficient of porous silicon membrane through the non-contact time resolved pump probe method, of which pump probe reflection and transmission were measured simultaneously. Then, the nonuniform optical model, which combined the WKB approach and Drude equation, was applied to fit the reflection and transmission data. From the fitting, the dielectric constant variation of nano wires c-Si was characterised firstly and excited carriers concentration was also estimated out changing with membrane depth and time delay. Assuming the linear recombination process of excited carriers, the carrier lifetime was obtained, $\tau \approx 350ps$. Then, using the Fick's second law, the diffusion coefficient D of excited carriers in PS membrane can be evaluated by fitting the carriers concentration decay process at any membrane depth. The diffusion coefficient $D < 10^{-1}cm^2/s$ is found out, which indicates the transport property of of $N_{eh}(t)$ in PS membrane is mainly controlled by carrier recombination and the carrier diffusion has little effect on the $N_{eh}(t)$ decay.

5.5 Summary

In summary, we applied the pump probe transmission and reflection simultaneous measurements to research a free standing porous silicon (PS) membrane. The preparation and characterisation of PS membrane were introduced firstly and the dielectric function of nano wires c-Si is obtained through the transmittance and reflectance detections and optical model simulation. Then, basing on these basic ground state information, we develop an analytical model combing the WKB approach and Drude equation to simulate the pump probe transmission and reflection data simultaneously. A pump induced nonuniform complex dielectric constant variation along the membrane depth and increasing time delay can be retrieved by this analysing model. We show that the model fitting to pump probe data requires a minimal number of fitting parameters while still complying with the restriction imposed by the Kramers-Kronig relation. Moreover, the excited carrier concentration and scattering rate can also be estimated as changing membrane depth and time delay. Finally, the diffusion coefficient D and recombination time τ of excited carriers in PS membrane are discussed through fitting a carriers transport equation. We found that the transport property of excited carriers in PS membrane is mainly dominated by the carriers recombination and the carriers diffusion has little influence on the optical response of the excited state.

Chapter 6

Conclusions

This thesis has mainly achieved two distinctive goals: (1) developing a set of novel ultrafast optical pump probe spectroscopy techniques to monitor the optical response of the photo-excited state of composite nano semiconductor materials; (2) constructing a suitable optical model to simulate the pump probe measurement data and reveal the ultrafast dynamics properties of the excited carriers in corresponding materials. The conclusions drawn for each step are shown as following:

Referring to the multilayer structured nc-Si:H opaque sample, the multiple probing angles of the pump probe reflection measurements were done firstly to precisely determine the plasma frequency ω_p and scattering rate Γ for each time delay. We found that Γ is dependent on ω_p when the carrier-carrier scattering mechanism dominates the scattering process. Then, the effective mass m^* of excited carriers is estimated as $m^* \approx 0.17m_e$ via the pump fluence dependent measurements. So, the decay process of excited carriers concentration $N_{eh}(t)$ can be evaluated out and the recombination property of $N_{eh}(t)$ is analysed by fitting $N_{eh}(t)$ decay with a recombination equation. From the coefficients, we found that the recombination process of the excited carriers is mainly controlled by the quadratic and cubic recombination terms, which give the coefficients as $10^{-9}cm^3s^{-1}$ and $10^{-29}cm^6s^{-1}$ respectively. Thirdly, the high-frequency conductivity as a function of pump photon energy was investigated via the pump probe wavelength dependent reflection measurements under the fixed $300fs$ time delay, and analysed by an optical model combining the Drude contribution of excited carriers with the Maxwell-Boltzmann transport theory. The analyse shows the thermal distribution of excited nascent carriers can be described as that of a classical hot non-degenerate gas. The conductivity of gas decreases monotonically as the excitation photon energy decreases. Finally, the pump probe ellipsometry technique is applied to accurately monitor the decay of the dielectric constant, absorption coefficient and conductivity of the excited nc-Si:H material.

As for the investigation of a free standing PS membrane, we applied the pump probe spectroscopic transmission and reflection measurements simultaneously. According to the detected data, we found that a model with a uniform excitation is inadequate to simulate the experimental results. Considering the spatial profile of the excited charge carriers, we developed an analytical approach based on the WKB approach and the Drude expression for a simultaneous fitting of the pump probe transmission and reflection data. A pump induced nonuniform complex dielectric constant variation along the increasing of membrane depth and time delay can be obtained. Moreover, the excited carrier concentration and scattering rate can also be estimated, corresponding to each membrane depth position and time delay. Finally, the diffusion coefficient D and recombination time τ of excited carriers in PS membrane are both discussed through fitting of carriers transport equation. We found that the transport property of the excited carriers in PS membrane is mainly dominated by the carrier recombination and the carrier diffusion has little influence on the optical response.

The work done in this thesis not only gives insights on different ultrafast optical pump probe spectroscopy approaches to monitor the optical response of photo excited semiconductor materials, but also, more importantly, demonstrates the corresponding analytical models can be useful in studying the ultrafast dynamics properties of the excited carriers. Meanwhile, this work paves the way that, when designing the optoelectronic devices, one should carefully consider the diffusion coefficient and recombination property of excited carriers, and also need to notice the effect of the balance between the carrier concentration and the excess energy in order to achieve a desired conductivity.

Appendix A

Ellipsometry

A.1 Derivation of RCE intensity with Mueller matrixes

With the help of Stokes parameters and Mueller matrix, we can derive the detected reflective intensity of rotating compensator ellipsometry (RCE) system with compensator rotation angles using Maple software. The final intensity expression should be like as equation 3.58. Firstly, we need to introduce the advantages of Stokes parameters. The Stokes parameters can describe all kinds of the polarisation state light waves, including the unpolarised and partially polarised light waves. So, to determine the polarised state of a light wave, all the Stokes parameters must be realised. Fujiwara[99] used the light intensity of polarised light to define these four Stokes parameters and gave detailed explanations about them as following:

$$\begin{aligned} S_0 &= I_x + I_y \ ; \\ S_1 &= I_x - I_y \ ; \\ S_2 &= I_{+45^\circ} - I_{-45^\circ} \ ; \\ S_3 &= I_R - I_L \ . \end{aligned} \tag{A.1}$$

Here, S_0 stands for the total light intensity and S_1 expresses the light intensity determined by subtracting the light intensity of linear polarisation in the y direction (I_y) from that in the x direction (I_x) [Figure A.1(a)]. Furthermore, S_2 shows the light intensity obtained through subtracting the light intensity of linear polarisation at $-45°(I_{-45^\circ})$ from that at $+45°(I_{+45^\circ})$ [Figure A.1(b)]. Regarding to the parameter S_3, the light intensity of left-circular polarisation (I_L) is subtracted from that of right-circular polarisation (I_R) [Figure A.1(c)]. Therefore, the parameters S_{1-3} illustrate the relative difference in light intensity between each state of polarisation. These parameters can also be described by

using electric fields. The more details about these Stokes parameters can be found in Fujiwara's publication[99].

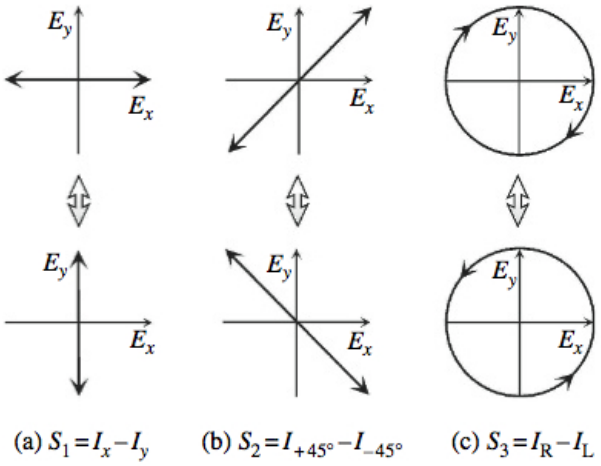

FIGURE A.1: Definitions of Stokes parameters (S_{1-3}) based on light intensity. The Figure and Caption are from[99].

Then, the Mueller matrices are illustrated in table A.1 by Stokes parameters. The δ is equal to $\pi/2$ referring to quarter wave plate for compensator and c indicates the rotating angle, $A = (r_p r_p^* + r_s r_s^*)/2$. Then according to the RCE system equation 3.55 and polariser and analyser angles $P = 45°, A = 0°$, we can calculate the L_{out} with $Lin = [1, 0, 1, 0]^T$, using Stokes parameters for ψ, Δ equations A.2 and trigonometric functions.

$$\begin{aligned} S_1 &= sin(\psi)^2 - cos(\psi)^2 = -cos(2\psi) \\ S_2 &= 2sin(\psi)cos(\psi)cos(\Delta) = sin(2\psi)cos(\Delta) \\ S_3 &= -2sin(\psi)cos(\psi)sin(\Delta) = -sin(2\psi)sin(\Delta) \end{aligned} \tag{A.2}$$

Eventually through Maple software calculation, we can obtain the output for RCE system as Muller matrix including Stokes parameters as following:

$$L_{out} = \frac{A}{8} \cdot \begin{bmatrix} 2 + S_1 - 2S_3 sin(2c) + S_1 cos(4c) + S_2 sin(4c) \\ 2 + S_1 - 2S_3 sin(2c) + S_1 cos(4c) + S_2 sin(4c) \\ 0 \\ 0 \end{bmatrix} \tag{A.3}$$

Through Stokes parameters definition, we know the output intensity variation formula for the RCE system as following, which is almost identical with Equation 3.58.

$$I = I_x = \frac{A}{8} \cdot [2 + S_1 - 2S_3 sin(2c) + S_1 cos(4c) + S_2 sin(4c)]. \tag{A.4}$$

Optical Element	Symbol	Muller matrix
Polariser (*Analyser*)	P (A)	$1/2\begin{bmatrix}1&1&0&0\\1&1&0&0\\0&0&0&0\\0&0&0&0\end{bmatrix}$
Compensator (*Retarder*)	C	$\begin{bmatrix}1&0&0&0\\0&1&0&0\\0&0&cos(\delta)&sin(\delta)\\0&0&-sin(\delta)&cos(\delta)\end{bmatrix}$
Coordinate rotation	R(c)	$\begin{bmatrix}1&0&0&0\\0&cos(2c)&sin(2c)&0\\0&-sin(2c)&cos(2c)&0\\0&0&0&1\end{bmatrix}$
Sample	S	$A\begin{bmatrix}1&-cos(2\psi)&0&0\\-cos(2\psi)&1&0&0\\0&0&sin(2\psi)cos(\Delta)&sin(2\psi)sin(\Delta)\\0&0&-sin(2\psi)sin(\Delta)&sin(2\psi)cos(\Delta)\end{bmatrix}$
Depolarizer	D	$\begin{bmatrix}1&0&0&0\\0&0&0&0\\0&0&0&0\\0&0&0&0\end{bmatrix}$

Table A.1: Muller matrices for optical elements and coordinate rotation

A.2 Matlab model for compensator calibration

```
% Jones Matrix;
% Polarizer(Analyzer)
Polar=[1,0;0,0]; Analy=[1,0;0,0];
% Compensator(Retarder), Quarter wave plate
Compen=[1,0;0,exp(-i*pi/2)];

% Coordinate rotation, All the Angles are corresponding to the incident Plane;
alphaA=0;
RadianA=pi*alphaA/180;
alphaP=45;
RadianP=pi*alphaP/180;
for C=1:360;
```

```
alphaC=C;
RadianC=pi*alphaC/180;

% Sample
% Sampl=[sin(ψ)*exp(i * Δ),0;0,cos(psi)]
% rotating compensator ellipsometry (RCE)
Lin=[1;0];
RotatA=[cos(RadianA),sin(RadianA);-sin(RadianA),cos(RadianA)];
RotatC=[cos(RadianC),sin(RadianC);-sin(RadianC),cos(RadianC)];
RotatMC=[cos(-RadianC),sin(-RadianC);-sin(-RadianC),cos(-RadianC)];
RotatMP=[cos(-RadianP),sin(-RadianP);-sin(-RadianP),cos(-RadianP)];
% Without Sample
Lout=Analy*RotatA*RotatMC*Compen*RotatC*RotatMP*Polar*Lin;
Iten(C)=abs(Lout(1))^2;
end

C=[1:360];
RadC=C.*pi/180;

figure(1)
plot(C,Iten)
xlabel('Compensater Angle (degrees)')
ylabel('Output Normalised Intensity')
```

Bibliography

[1] Andreas Othonos. Probing ultrafast carrier and phonon dynamics in semiconductors. *Journal of Applied Physics*, 83(4):1789–1830, 1998.

[2] Jagdeep Shah. *Ultrafast spectroscopy of semiconductors and semiconductor nanostructures*, volume 115. Springer, 1999.

[3] Zenghu Chang. *Fundamentals of attosecond optics*, volume 1. CRC Press Boca Raton, 2011.

[4] A. Esser, H. Heesel, H. Kurz, C. Wang, G. N. Parsons, and G. Lucovsky. Femtosecond spectroscopic study of ultrafast carrier relaxation in hydrogenated amorphous silicon a-si:h. *J. Appl. Phys.*, 73(3):1235–1239, 1993. ISSN 00218979.

[5] Emmanouil Lioudakis, Andreas Othonos, and A. G. Nassiopoulou. Ultrafast transient photoinduced absorption in silicon nanocrystals: Coupling of oxygen-related states to quantized sublevels. *Applied Physics Letters*, 90(17):171103, 2007.

[6] J. von Behren, Y. Kostoulas, K. Burak Üçer, and P.M. Fauchet. The femtosecond optical response of porous, amorphous and crystalline silicon. *Journal of Non-Crystalline Solids*, 198–200, Part 2(0):957 – 960, 1996. ISSN 0022-3093.

[7] PM Fauchet, D Hulin, R Vanderhaghen, A Mourchid, and WL Nighan Jr. The properties of free carriers in amorphous silicon. *Journal of non-crystalline solids*, 141:76–87, 1992.

[8] V Grivickas and J Linnros. Free-carrier absorption and luminescence decay of porous silicon. *Thin solid films*, 255(1):70–73, 1995.

[9] Ronald Ulbricht, Euan Hendry, Jie Shan, Tony F Heinz, and Mischa Bonn. Carrier dynamics in semiconductors studied with time-resolved terahertz spectroscopy. *Reviews of Modern Physics*, 83(2):543, 2011.

[10] L. Fekete, P. Kužel, H. Němec, F. Kadlec, A. Dejneka, J. Stuchlík, and A. Fejfar. Ultrafast carrier dynamics in microcrystalline silicon probed by time-resolved terahertz spectroscopy. *Phys. Rev. B*, 79:115306, Mar 2009.

[11] Matthew C Beard, Gordon M Turner, and Charles A Schmuttenmaer. Subpicosecond carrier dynamics in low-temperature grown gaas as measured by time-resolved terahertz spectroscopy. *Journal of Applied Physics*, 90(12):5915–5923, 2001.

[12] Matthew C Beard, Gordon M Turner, and Charles A Schmuttenmaer. Transient photoconductivity in gaas as measured by time-resolved terahertz spectroscopy. *Physical Review B*, 62(23):15764, 2000.

[13] D. G. Cooke, A. N. MacDonald, A. Hryciw, J. Wang, Q. Li, A. Meldrum, and F. A. Hegmann. Transient terahertz conductivity in photoexcited silicon nanocrystal films. *Phys. Rev. B*, 73:193311, May 2006.

[14] Marek Samoc, Anna Samoc, Barry Luther-Davies, Zhenan Bao, Luping Yu, Bing Hsieh, and Ullrich Scherf. Femtosecond z-scan and degenerate four-wave mixing measurements of real and imaginary parts of the third-order nonlinearity of soluble conjugated polymers. *JOSA B*, 15(2):817–825, 1998.

[15] Jiangwei Wang, Mansour Sheik-Bahae, AA Said, David J Hagan, and Eric W Van Stryland. Time-resolved z-scan measurements of optical nonlinearities. *JOSA B*, 11(6):1009–1017, 1994.

[16] Y. J. Ma, J. I. Oh, D. Q. Zheng, W. A. Su, and W. Z. Shen. Tunable nonlinear absorption of hydrogenated nanocrystalline silicon. *Opt. Lett.*, 36(17):3431–3433, Sep 2011.

[17] K. Sokolowski-Tinten and D. von der Linde. Generation of dense electron-hole plasmas in silicon. *Phys. Rev. B*, 61(4):2643–2650, Jan 2000.

[18] C. A. D. Roeser, A. M.-T. Kim, J. P. Callan, L. Huang, E. N. Glezer, Y. Siegal, and E. Mazur. Femtosecond time-resolved dielectric function measurements by dual-angle reflectometry. *Review of Scientific Instruments*, 74(7):3413–3422, 2003.

[19] M. C. Downer and C. V. Shank. Ultrafast heating of silicon on sapphire by femtosecond optical pulses. *Phys. Rev. Lett.*, 56:761–764, Feb 1986.

[20] P Malỳ, F Trojanek, A Hospodkova, V Kohlova, and I Pelant. Transmission study of picosecond photocarrier dynamics in free-standing porous silicon. *Solid state communications*, 89(8):709–712, 1994.

[21] W-Z Lin, RW Schoenlein, JG Fujimoto, and EP Ippen. Femtosecond absorption saturation studies of hot carriers in gaas and algaas. *Quantum Electronics, IEEE Journal of*, 24(2):267–275, 1988.

[22] Thomas Roger. *Time Resolved Ultrafast Dynamic Excitations in Semiconductors.* Doctor Thesis, University of Birmingham, 2012.

[23] S. K. Sundaram and E. Mazur. Inducing and probing non-thermal transitions in semiconductors using femtosecond laser pulses. *Nat Mater*, 1(4):217–224, 12 2002.

[24] Saravanapriyan Sriraman, Sumit Agarwal, Eray S. Aydil, and Dimitrios Maroudas. Mechanism of hydrogen-induced crystallization of amorphous silicon. *Nature*, 418 (6893):62–65, 07 2002.

[25] A. Shah, P. Torres, R. Tscharner, N. Wyrsch, and H. Keppner. Photovoltaic technology: the case for thin-film solar cells. *Science*, 285:692, 1999.

[26] A.V. Shah, J. Meier, E. Vallat-Sauvain, N. Wyrsch, U. Kroll, C. Droz, and U. Graf. Material and solar cell research in microcrystalline silicon. *Solar Energy Materials and Solar Cells*, 73(1-4):469–491, 2003.

[27] Sungwook Jung and Junsin Yi. Nanocrystalline-silicon thin-film nonvolatile memory devices for display applications. *Electron Device Letters, IEEE*, 31(9):981–983, 2010.

[28] C.-H. Lee, A. Sazonov, A. Nathan, and J. Robertson. Directly deposited nanocrystalline silicon thin-film transistors with ultra high mobilities. *Appl. Phys. Lett.*, 89:252, 2006.

[29] Wei He, Igor V Yurkevich, Leigh T Canham, Armando Loni, and Andrey Kaplan. Determination of excitation profile and dielectric function spatial nonuniformity in porous silicon by using wkb approach. *Optics express*, 22(22):27123–27135, 2014.

[30] L. Canham. *Handbook on Porous Silicon*. Springer, 2014.

[31] L. Khriachtchev. *Silicon Nanophotonics: Basic Principles, Present Status and Perspectives*. World Scientific, Singapore, 2008.

[32] K. Reddy and X. Fan. Self-referenced composite fabry-perot cavity vapor sensors. *Opt. Express*, 20(2):966–971, 2012.

[33] G. Q. Lu and X. S. Zhao. *Nanoporous Materials: Science and Engineering*. Imperial College Press, 2005.

[34] V. Agarwal, M. E. Mora-Ramos, and B. Alvarado-Tenorio. Optical properties of multilayered period-doubling and rudin-shapiro porous silicon dielectric heterostructures. *Photon. Nanostruct.: Fundam. Appl.*, 7(2):63–68, 2009.

[35] Kyowon Kim and Thomas E. Murphy. Porous silicon integrated mach-zehnder interferometer waveguide for biological and chemical sensing. *Opt. Express*, 21 (17):19488–19497, Aug 2013.

[36] I. Suarez, V. Chirvony, D. Hill, and J. Martinez-Pastor. Simulation of surface-modified porous silicon photonic crystals for biosensing applications. *Photon. Nanostruct.: Fundam. Appl.*, 9:304–311, 2011.

[37] P. Lalanne and G. M. Morris. Design, fabrication and characterization of subwavelength periodic structures for semiconductor anti-reflection coating in the visible domain. *Proc. SPIE*, 2776:300–309, 1996.

[38] H. Ouyang, C. C. Striemer, and P. M. Fauchet. Quantitative analysis of the sensitivity of porous silicon optical biosensors. *Appl. Phys. Lett.*, 88(16):163108, 2006.

[39] U. C. Hasar, I. Y. Ozbek, E. A. Oral, T. Karacali, and H. Efeoglu. The effect of silicon loss and fabrication tolerance on spectral properties of porous silicon fabry-perot cavities in sensing applications. *Opt. Express*, 20(20):22208–22223, Sep 2012.

[40] A. Najar, J. Charrier, P. Pirasteh, and R. Sougrat. Ultra-low reflection porous silicon nanowires for solar cell applications. *Opt. Express*, 20(15):16861–16870, Jul 2012.

[41] C.V. Shank, R. Yen, and C. Hirlimann. Time-resolved reflectivity of femtosecond-optical-pulse-induced phase transitions in silicon. *Physical Review Letters*, 50(6): 454–457, February 1983.

[42] A.J. Sabbah and D. M. Riffe. Femtosecond pump-probe reflectivity study of silicon carrier dynamics. *Phys. Rev. B*, 66:165217, 2002.

[43] V Freilikher, VI Tatarskii, M Pustilnik, and I Yurkevich. Polarization of light scattered from slightly rough dielectric film. *Optics letters*, 19(18):1382–1384, 1994.

[44] Charles Kittel and Ching-yao Fong. *Quantum theory of solids*, volume 24. Wiley New York, 1963.

[45] Charles Kittel and By Charles Kittel. *Introduction to solid state physics*. Wiley New York, 1986.

[46] Dimitri Chekulaev. *Experimental Study of Ultrafast Carrier Dynamics and Plasmons in Nanostructures*. Doctor Thesis, University of Birmingham, 2012.

[47] Jean-Claude Diels and Wolfgang Rudolph. Ultrashort laser pulse phenomena: fundamentals, techniques, and applications on a femtosecond time scale (optics and photonics). *Academic, New York*, 1996.

[48] Takayuki Tanaka, Akira Harata, and Tsuguo Sawada. Subpicosecond surface-restricted carrier and thermal dynamics by transient reflectivity measurements. *Journal of applied physics*, 82(8):4033–4038, 1997.

[49] D. H. Reitze, T. R. Zhang, Wm. M. Wood, and M. C. Downer. Two-photon spectroscopy of silicon using femtosecond pulses at above-gap frequencies. *J. Opt. Soc. Am. B*, 7(1):84–89, Jan 1990.

[50] V. R Almeida, C. A Barrios, R. R. Panepucci, and M. Lipson. All-optical control of light on a silicon chip. *Nature*, 431(1081), 2004.

[51] S. Godefroo, M. Hayne, M. Jivanescu, A. Stesmans, M. Zacharias, O. I. Lebedev, G. VanTendeloo, and V. V. Moshchalkov. Classification and control of the origin of photoluminescence from si nanocrystals. *Nat. Nano*, 408(440), 2008.

[52] Hitoki Yoneda, Hidetoshi Morikami, Ken-ichi Ueda, and Richard M More. Ultrashort-pulse laser ellipsometric pump-probe experiments on gold targets. *Physical review letters*, 91(7):075004, 2003.

[53] A. Esser, K. Seibert, H. Kurz, G. N. Parsons, C. Wang, B. N. Davidson, G. Lucovsky, and R. J. Nemanich. Ultrafast recombination and trapping in amorphous silicon. *Phys. Rev. B*, 41:2879–2884, Feb 1990.

[54] A. Esser, H. Heesel, H. Kurz, C. Wang, G. N. Parsons, and G. Lucovsky. Transport properties of optically generated free carriers in hydrogenated amorphous silicon in the femtosecond time regime. *Phys. Rev. B*, 47:3593–3597, Feb 1993.

[55] K. E. Myers, Q. Wang, and S. L. Dexheimer. Ultrafast carrier dynamics in nanocrystalline silicon. *Phys. Rev. B*, 64(16):161309, Oct 2001. doi: 10.1103/PhysRevB.64.161309.

[56] J Kudrna, P Malỳ, F Trojánek, J Štěpánek, T Lechner, I Pelant, Johannes Meier, and U Kroll. Ultrafast carrier dynamics in undoped microcrystalline silicon. *Materials Science and Engineering: B*, 69:238–242, 2000.

[57] J. Barreto, T. Roger, and A. Kaplan. Resolving the ultrafast dynamics of charge carriers in nanocomposites. *Applied Physics Letters*, 100(24):241906, 2012.

[58] K. Shimakawa, T. Itoh, H. Naito, and S. O. Kasap. The origin of non-drude terahertz conductivity in nanomaterials. *Applied Physics Letters*, 100(13):132102, 2012.

[59] AA Bugayev, A Khakhaev, and AS Zubrilov. Picosecond time-resolved reflectivity of porous silicon. *Optics communications*, 106(1):65–68, 1994.

[60] Martynas Beresna, Roland Tomašiūnas, János Volk, György Kádár, et al. Picosecond reflectance recovery dynamics of porous silicon multilayer. *JOSA B*, 26(2): 249–253, 2009.

[61] P Malỳ, F Trojánek, J Kudrna, A Hospodková, S Banáš, V Kohlová, J Valenta, and I Pelant. Picosecond and millisecond dynamics of photoexcited carriers in porous silicon. *Physical Review B*, 54(11):7929, 1996.

[62] F Trojanek, P Malỳ, I Pelant, A Hospodkova, V Kohlova, and J Valenta. Picosecond dynamics of photoexcited carriers in free-standing porous silicon. *Thin Solid Films*, 255(1):77–79, 1995.

[63] S Vepřek and V Mareček. The preparation of thin layers of ge and si by chemical hydrogen plasma transport. *Solid-State Electronics*, 11(7):683–684, 1968.

[64] Stan Vepřek and Maritza GJ Vepřek-Heijman. Open questions regarding the mechanism of plasma-induced deposition of silicon. *Plasma chemistry and plasma processing*, 11(3):323–334, 1991.

[65] S Veprek, M Heintze, FA Sarott, M Jurcik-Rajman, P Willmott, A Mada, MJ Thompso, PC Taylo, PG Le Comber, and Y Hamakaw. Amorphous silicon technology. In *Materials Research Society Symposium Proceedings*, volume 118, pages 3–17, 1988.

[66] S Usui and M Kikuchi. Properties of heavily doped gd si with low resistivity. *Journal of Non-Crystalline Solids*, 34(1):1–11, 1979.

[67] WE Spear, G Willeke, PG Le Comber, and AG Fitzgerald. Electronic properties of microcrystalline silicon films prepared in a glow discharge plasma. *Le Journal de Physique Colloques*, 42(C4):C4–257, 1981.

[68] Evelyne Vallat-Sauvain, U Kroll, J Meier, A Shah, and J Pohl. Evolution of the microstructure in microcrystalline silicon prepared by very high frequency glow-discharge using hydrogen dilution. *Journal of Applied Physics*, 87(6):3137–3142, 2000.

[69] Wei He, Igor V Yurkevich, Ammar Zakar, and Andrey Kaplan. High-frequency conductivity of optically excited charge carriers in hydrogenated nanocrystalline silicon investigated by spectroscopic femtosecond pump–probe reflectivity measurements. *Thin Solid Films*, 2015.

[70] E Bustarret, MA Hachicha, and M Brunel. Experimental determination of the nanocrystalline volume fraction in silicon thin films from raman spectroscopy. *Applied Physics Letters*, 52(20):1675–1677, 1988.

[71] O Vetterl, F Finger, R Carius, P Hapke, L Houben, O Kluth, A Lambertz, A Mück, B Rech, and H Wagner. Intrinsic microcrystalline silicon: A new material for photovoltaics. *Solar Energy Materials and Solar Cells*, 62(1):97–108, 2000.

[72] B. E. Warren and B. L. Averbach. The effect of cold-work distortion on x-ray patterns. *Journal of Applied Physics*, 21(6):595–599, 1950.

[73] H.P.King and L.E.Alexander. *X-ray Diffraction Procedures*. Wiley, New York, 1981.

[74] C. E. Bouldin, E. A. Stern, B. von Roedern, and J. Azoulay. Structural study of hydrogenated a-ge using extended x-ray absorption fine structure. *Phys. Rev. B*, 30:4462–4469, Oct 1984.

[75] L Houben, M Luysberg, P Hapke, R Carius, F Finger, and H Wagner. Structural properties of microcrystalline silicon in the transition from highly crystalline to amorphous growth. *Philosophical Magazine A*, 77(6):1447–1460, 1998.

[76] Paul Scherrer. Bestimmung der grösse und der inneren struktur von kolloidteilchen mittels röntgenstrahlen. *Nachrichten von der Gesellschaft der Wissenschaften zu Göttingen, mathematisch-physikalische Klasse*, 1918:98–100, 1918.

[77] AL Patterson. The scherrer formula for x-ray particle size determination. *Physical review*, 56(10):978, 1939.

[78] Furu Zhong, Xiao-yi Lv, Zhen-hong Jia, and Jiaqing Mo. Fabrication of porous silicon-based silicon-on-insulator photonic crystal by electrochemical etching method. *Optical Engineering*, 51(4):040502–1, 2012.

[79] Giampiero Amato, Christophe Delerue, and HJ VonBardeleben. *Structural and optical properties of porous silicon nanostructures*, volume 5. CRC Press, 1998.

[80] C Pickering, MIJ Beale, DJ Robbins, PJ Pearson, and R Greef. Optical studies of the structure of porous silicon films formed in p-type degenerate and non-degenerate silicon. *Journal of Physics C: Solid State Physics*, 17(35):6535, 1984.

[81] L_T Canham. Silicon quantum wire array fabrication by electrochemical and chemical dissolution of wafers. *Applied Physics Letters*, 57(10):1046–1048, 1990.

[82] K. H. Jun, R. Carius, and H. Stiebig. Optical characteristics of intrinsic microcrystalline silicon. *Phys. Rev. B*, 66:115301, 2002.

[83] Anthony Mark Fox. *Optical properties of solids*, volume 3. Oxford university press, 2001.

[84] M Vanecek, J Kocka, J Stuchlik, Z Kozisek, O Stika, and A Triska. Density of the gap states in undoped and doped glow discharge a-si: H. *Solar Energy Materials*, 8:411–423, 1983.

[85] A. Poruba, A. Fejfar, Z. Remes, J. Springer, M. Vanecek, J. Kocka, J. Meier, P. Torres, and A. Shah. Optical absorption and light scattering in microcrystalline silicon thin films and solar cells. *Journal of Applied Physics*, 88(1):148–160, 2000.

[86] M. Vaněček, A. Poruba, Z. Remeš, N. Beck, and M. Nesládek. Optical properties of microcrystalline materials. *Journal of Non-Crystalline Solids*, 227–230:967 – 972, 1998.

[87] Nobuyoshi Koshida, Hideki Koyama, Yoshiyuki Suda, Yuko Yamamoto, Minoru Araki, Tadashi Saito, Katsuaki Sato, Noriko Sata, and Shik Shin. Optical characterization of porous silicon by synchrotron radiation reflectance spectra analyses. *Applied physics letters*, 63(20):2774–2776, 1993.

[88] Frederick Wooten. *Optical properties of solids*, volume 111. Academic Press New York, 1972.

[89] Wolfgang Theiß. Optical properties of porous silicon. *Surface Science Reports*, 29 (3):91–192, 1997.

[90] L. Canham and L.T. Canham. *Properties of porous silicon*. EMIS datareviews series. INSPEC, 1997. ISBN 9780852969328.

[91] F Koch, V Petrova-Koch, and T Muschik. The luminescence of porous si: the case for the surface state mechanism. *Journal of Luminescence*, 57(1):271–281, 1993.

[92] V Klimov, D McBranch, and V Karavanskii. Strong optical nonlinearities in porous silicon: Femtosecond nonlinear transmission study. *Physical Review B*, 52(24): R16989, 1995.

[93] Eugene Hecht. *Optics*. Addison Wesley Longman, 1998.

[94] Krishna Seshan. *Handbook of thin film deposition*. Access Online via Elsevier, 2012.

[95] M. Born and Wolf. *Principles of Optics*. Pergamon, Oxford, 1980.

[96] Enrico Nichelatti. Complex refractive index of a slab from reflectance and transmittance: analytical solution. *Journal of Optics A: Pure and Applied Optics*, 4 (4):400, 2002.

[97] MA Khashan and AM El-Naggar. A new method of finding the optical constants of a solid from the reflectance and transmittance spectrograms of its slab. *Optics communications*, 174(5):445–453, 2000.

[98] O Stenzel, V Hopfe, and P Klobes. Determination of optical parameters for amorphous thin film materials on semitransparent substrates from transmittance and reflectance measurements. *Journal of Physics D: Applied Physics*, 24(11):2088, 1991.

[99] Hiroyuki Fujiwara. *Spectroscopic ellipsometry: principles and applications*. John Wiley and Sons Ltd, 2007.

[100] Robert R. Stromberg Frank L. McCrackin, Elio Passaglia and Harold L. Steinberg. Measurement of the thickness and refractive index of very thin films and the optical properties of surfaces by ellipsometry. *JOURNAL OF RESEARCH of the National Bureau of Standards—A. Physics and Chemistry*, 67A(4):363–377, April 1963.

[101] Joungchel Lee, P. I. Rovira, Ilsin An, and R. W. Collins. Rotating-compensator multichannel ellipsometry: Applications for real time stokes vector spectroscopy of thin film growth. *Review of Scientific Instruments*, 69(4):1800–1810, 1998.

[102] Jr. G. E. Jellison and F. A. Modine. Optical constants for silicon at 300 and 10 k determined from 1.64 to 4.73 ev by ellipsometry. *Journal of Applied Physics*, 53 (5):3745–3753, 1982.

[103] G.E. Jellison Jr. Data analysis for spectroscopic ellipsometry. *Thin Solid Films*, 234(1–2):416 – 422, 1993. ISSN 0040-6090.

[104] P.S. Hauge. Recent developments in instrumentation in ellipsometry. *Surface Science*, 96(1–3):108 – 140, 1980. ISSN 0039-6028.

[105] RW Collins, AS Ferlauto, GM Ferreira, Chi Chen, Joohyun Koh, RJ Koval, Yeeheng Lee, JM Pearce, and CR Wronski. Evolution of microstructure and phase in amorphous, protocrystalline, and microcrystalline silicon studied by real time spectroscopic ellipsometry. *Solar Energy Materials and Solar Cells*, 78(1):143–180, 2003.

[106] Ilsin An, YM Li, CR Wronski, HV Nguyen, and RW Collins. In situ determination of dielectric functions and optical gap of ultrathin amorphous silicon by real time spectroscopic ellipsometry. *Applied physics letters*, 59(20):2543–2545, 1991.

[107] Hiroyuki Fujiwara, Michio Kondo, and Akihisa Matsuda. Real-time spectroscopic ellipsometry studies of the nucleation and grain growth processes in microcrystalline silicon thin films. *Physical Review B*, 63(11):115306, 2001.

[108] RW Collins, Ilsin An, H Fujiwara, Joungchel Lee, Yiwei Lu, Joohyun Koh, and PI Rovira. Advances in multichannel spectroscopic ellipsometry. *Thin Solid Films*, 313:18–32, 1998.

[109] RW Collins, Joohyun Koh, H Fujiwara, PI Rovira, AS Ferlauto, JA Zapien, CR Wronski, and R Messier. Recent progress in thin film growth analysis by multichannel spectroscopic ellipsometry. *Applied surface science*, 154:217–228, 2000.

[110] HL Maynard, N Layadi, and JTC Lee. Plasma etching of submicron devices: in situ monitoring and control by multi-wavelength ellipsometry. *Thin Solid Films*, 313:398–405, 1998.

[111] Sang-Jun Cho, PG Snyder, CM Herzinger, and B Johs. Etch depth control in bulk gaas using patterning and real time spectroscopic ellipsometry. *Journal of Vacuum Science & Technology B: Microelectronics and Nanometer Structures*, 20 (1):197–202, 2002.

[112] EA Irene. Applications of spectroscopic ellipsometry to microelectronics. *Thin Solid Films*, 233(1):96–111, 1993.

[113] James Clerk Maxwell and Joseph John Thompson. *A treatise on electricity and magnetism*, volume 2. Clarendon, 1904.

[114] Glenn S Smith. *An introduction to classical electromagnetic radiation*. Cambridge University Press, 1997.

[115] Harland Tompkins and Eugene A Irene. *Handbook of ellipsometry*. Access Online via Elsevier, 2005.

[116] Hans W Verleur. Determination of optical constants from reflectance or transmittance measurements on bulk crystals or thin films. *JOSA*, 58(10):1356–1361, 1968.

[117] Valeri P Tolstoy, Irina V Chernyshova, and Valeri A Skryshevsky. *Handbook of Infrared Spectroscopy of Ultrathin Films*. Wiley Online Library, 2003.

[118] OS Heavens. Optical properties of thin films. *Reports on Progress in Physics*, 23 (1):1, 1960.

[119] AJ El-Haija. Effective medium approximation for the effective optical constants of a bilayer and a multilayer structure based on the characteristic matrix technique. *Journal of applied physics*, 93(5):2590–2594, 2003.

[120] D. E. Aspnes and A. A. Studna. Dielectric functions and optical parameters of si, ge, gap, gaas, gasb, inp, inas, and insb from 1.5 to 6.0 ev. *Phys. Rev. B*, 27: 985–1009, Jan 1983.

[121] DE Aspnes and AA Studna. High precision scanning ellipsometer. *Applied Optics*, 14(1):220–228, 1975.

[122] A Röseler and W Molgedey. Improvement in accuracy of spectroscopic ir ellipsometry by the use of ir retarders. *Infrared physics*, 24(1):1–5, 1984.

[123] A Röseler. Ir spectroscopic ellipsometry: instrumentation and results. *Thin Solid Films*, 234(1):307–313, 1993.

[124] A Röseler. Spectroscopic ellipsometry in the infrared. *Infrared Physics*, 21(6): 349–355, 1981.

[125] P.S. Hauge. Generalized rotating-compensator ellipsometry. *Surface Science*, 56 (0):148 – 160, 1976. ISSN 0039-6028.

[126] R Clark Jones. A new calculus for the treatment of optical systems. *JOSA*, 31(7): 500–503, 1941.

[127] Wolfgang Budde. Photoelectric analysis of polarized light. *Applied Optics*, 1(3): 201–205, 1962.

[128] J H W G den Boer, G M W Kroesen, and F J de Hoog. Spectroscopic rotating compensator ellipsometry in the infrared: retarder design and measurement. *Measurement Science and Technology*, 8(5):484, 1997.

[129] Liang Ding, TP Chen, Yang Liu, Chi Yung Ng, and S Fung. Optical properties of silicon nanocrystals embedded in a sio_ {2} matrix. *Physical Review B*, 72(12): 125419, 2005.

[130] A. R. Forouhi and I. Bloomer. Optical properties of crystalline semiconductors and dielectrics. *Phys. Rev. B*, 38:1865–1874, Jul 1988.

[131] Sadao Adachi and Hirofumi Mori. Optical properties of fully amorphous silicon. *Physical Review B*, 62(15):10158, 2000.

[132] Sadao Adachi. *Optical constants of crystalline and amorphous semiconductors: numerical data and graphical information.* Springer, 1999.

[133] Jr. G. E. Jellison and F. A. Modine. Parameterization of the optical functions of amorphous materials in the interband region. *Applied Physics Letters*, 69(3): 371–373, 1996.

[134] David L Greenaway and Günther Harbeke. *Optical properties and band structure of semiconductors*. Pergamon Press Oxford, 1968.

[135] P.K.Basu. *Theory of optical processes in semiconductors*. Oxford university press, 1997.

[136] A. S. Ferlauto, G. M. Ferreira, J. M. Pearce, C. R. Wronski, R. W. Collins, Xunming Deng, and Gautam Ganguly. Analytical model for the optical functions of amorphous semiconductors from the near-infrared to ultraviolet: Applications in thin film photovoltaics. *Journal of Applied Physics*, 92(5):2424–2436, 2002.

[137] J. Leng, J. Opsal, H. Chu, M. Senko, and D.E. Aspnes. Analytic representations of the dielectric functions of materials for device and structural modeling. *Thin Solid Films*, 313–314(0):132 – 136, 1998. ISSN 0040-6090.

[138] H.R. Philipp. Optical properties of non-crystalline si, sio, siox and sio2. *Journal of Physics and Chemistry of Solids*, 32(8):1935 – 1945, 1971. ISSN 0022-3697.

[139] Richard Zallen. *The Physics of Amorphous Solids*. John Wiley & Sons, 1983.

[140] A. R. Forouhi and I. Bloomer. Optical dispersion relations for amorphous semiconductors and amorphous dielectrics. *Phys. Rev. B*, 34:7018–7026, Nov 1986.

[141] Ari H Sihvola. *Electromagnetic mixing formulae and applications*. Number 47. Iet, 1999.

[142] David J. Bergman. The dielectric constant of a composite material—a problem in classical physics. *Physics Reports*, 43(9):377 – 407, 1978. ISSN 0370-1573.

[143] David J. Bergman. Hierarchies of stieltjes functions and their application to the calculation of bounds for the dielectric constant of a two-component composite medium. *SIAM Journal on Applied Mathematics*, 53(4):915–930, Aug 1993.

[144] David J Bergman. Rigorous bounds for the complex dielectric constant of a two-component composite. *Annals of Physics*, 138(1):78 – 114, 1982. ISSN 0003-4916.

[145] W Theiss. The dielectric function of porous silicon — how to obtain it and how to use it. *Thin Solid Films*, 276(1–2):7 – 12, 1996. ISSN 0040-6090. Papers presented at the European Materials Research Society 1995 Spring Conference, Symposium I: Porous Silicon: Material, Technology and Devices.

[146] W. Theiss, S. Henkel, and M. Arntzen. Connecting microscopic and macroscopic properties of porous media: choosing appropriate effective medium concepts. *Thin Solid Films*, 255(1–2):177 – 180, 1995. ISSN 0040-6090. ¡ce:title¿European Materials Research Society 1994 Spring Conference, Symposium F: Porous Silicon and Related Materials¡/ce:title¿.

[147] M. Evenschor, P. Grosse, and W. Theiss. Optics of two-phase composites. *Vibrational Spectroscopy*, 1(2):173 – 177, 1990. ISSN 0924-2031.

[148] J Sturm, P Grosse, S Morley, and W Theiss. Far infrared optical properties of metal-insulator composites. *Zeitschrift für Physik D Atoms, Molecules and Clusters*, 26(1):195–197, 1993.

[149] E Gorges, P Grosse, J Sturm, and W Theiss. A parameterization of the effective dielectric function of a two-phase composite medium. *Zeitschrift für Physik B Condensed Matter*, 94(3):223–226, 1994.

[150] J Sturm, P Grosse, and W Theiss. Effective dielectric functions of alkali halide composites and their spectral representation. *Zeitschrift für Physik B Condensed Matter*, 83(3):361–365, 1991.

[151] D Stroud, GW Milton, and BR De. Analytical model for the dielectric response of brine-saturated rocks. *Physical Review B*, 34(8):5145, 1986.

[152] Kunal Ghosh and Ronald Fuchs. Spectral theory for two-component porous media. *Phys. Rev. B*, 38:5222–5236, Sep 1988.

[153] JC Maxwell Garnett. Colours in metal glasses, in metallic films, and in metallic solutions. ii. *Philosophical Transactions of the Royal Society of London. Series A, Containing Papers of a Mathematical or Physical Character*, pages 237–288, 1906.

[154] Von DAG Bruggeman. Berechnung verschiedener physikalischer konstanten von heterogenen substanzen. i. dielektrizitätskonstanten und leitfähigkeiten der mischkörper aus isotropen substanzen. *Annalen der Physik*, 416(7):636–664, 1935.

[155] Rolf Landauer. The electrical resistance of binary metallic mixtures. *Journal of Applied Physics*, 23(7):779–784, 1952.

[156] H Looyenga. Dielectric constants of heterogeneous mixtures. *Physica*, 31(3):401–406, 1965.

[157] Henrik Wallén, Henrik Kettunen, and Ari Sihvola. Composite near-field superlens design using mixing formulas and simulations. *Metamaterials*, 3(3-4):129–139, 2009.

[158] Peter Uhd Jepsen, Bernd M. Fischer, Andreas Thoman, Hanspeter Helm, J. Y. Suh, René Lopez, and R. F. Haglund. Metal-insulator phase transition in a vo2 thin film observed with terahertz spectroscopy. *Phys. Rev. B*, 74:205103, Nov 2006.

[159] Hongru Ma, Rongfu Xiao, and Ping Sheng. Third-order optical nonlinearity enhancement through composite microstructures. *JOSA B*, 15(3):1022–1029, 1998.

[160] Dali Zhang, Elena Cherkaev, and Michael P. Lamoureux. Stieltjes representation of the 3d bruggeman effective medium and padé approximation. *Applied Mathematics and Computation*, 217(17):7092 – 7107, 2011. ISSN 0096-3003.

[161] G. A. Niklasson, C. G. Granqvist, and O. Hunderi. Effective medium models for the optical properties of inhomogeneous materials. *Appl. Opt*, 20(1):26–30, 1981.

[162] Anatoliy V Goncharenko. Generalizations of the bruggeman equation and a concept of shape-distributed particle composites. *Physical review E*, 68(4):041108, 2003.

[163] R. Krankenhagen, M. Schmidt, S. Grebner, M. Poschenrieder, W. Henrion, I. Sieber, S. Koynov, and R. Schwarz. Correlation between structural, optical and electrical properties of c-si films. *Journal of Non-Crystalline Solids*, 198–200: 923 – 926, 1996.

[164] Thomas W. Roger, Wei He, Igor V. Yurkevich, and Andrey Kaplan. Enhanced carrier-carrier interaction in optically pumped hydrogenated nanocrystalline silicon. *Applied Physics Letters*, 101(14):141904, 2012.

[165] MH Chan, SK So, and KW Cheah. Optical absorption of free-standing porous silicon films. *Journal of applied physics*, 79(6):3273–3275, 1996.

[166] D Kovalev, G Polisski, M Ben-Chorin, J Diener, and F Koch. The temperature dependence of the absorption coefficient of porous silicon. *Journal of applied physics*, 80(10):5978–5983, 1996.

[167] G Mauckner, W Rebitzer, K Thonke, and R Sauer. Quantum confinement effects in absorption and emission of freestanding porous silicon. *Solid state communications*, 91(9):717–720, 1994.

[168] A. Weiner. *Ultrafast Optics*. Wiley Series in Pure and Applied Optics. John Wiley & Sons, 2009. ISBN 9780470473450.

[169] J-C.Diels and W.Rudolph. *Ultrafast Laser Pulse Phenomena: Fundamentals, Techniques and Applications on a Femtosecond TIme Scale*. Academic Press, 1995.

[170] L. Bagolini, A. Mattoni, G. Fugallo, L. Colombo, E. Poliani, S. Sanguinetti, and E. Grilli. Quantum confinement by an order-disorder boundary in nanocrystalline silicon. *Phys. Rev. Lett.*, 104:176803, Apr 2010.

[171] S Lettieri, U Bernini, E Massera, and P Maddalena. Optical investigations on thermal conductivity in n-and p-type porous silicon. *physica status solidi (c)*, 2 (9):3414–3418, 2005.

[172] U Bernini, S Lettieri, P Maddalena, R Vitiello, and G Di Francia. Evaluation of the thermal conductivity of porous silicon layers by an optical pump-probe method. *Journal of Physics: Condensed Matter*, 13(5):1141, 2001.

[173] L. Kuntzler R. Kleim and A. El Ghemmaz. Systematic errors in rotating-compensator ellipsometry. *Journal of the Optical Society of America A*, Vol. 11, Issue 9(Issue 9):pp. 2550–2559, September 1994.

[174] T.W.Roger and A.Kaplan. Time-resolved ellipsometry to study extreme non-equilibrium electron dynamics in nanostructured semiconductors. *MRS Proceedings*, 1426:6, 2012.

[175] M.Ghezzo. Method for calibrating the analyser and the polarizer in an ellipsometer. *BRIT. J. APPL. PHYS. (J. PHYS. D)*, 2(2):1483–1485, 1969.

[176] SS Mao, Fabien Quéré, Stéphane Guizard, X Mao, RE Russo, Guillaume Petite, and Philippe Martin. Dynamics of femtosecond laser interactions with dielectrics. *Applied Physics A*, 79(7):1695–1709, 2004.

[177] Fausto Rossi and Tilmann Kuhn. Theory of ultrafast phenomena in photoexcited semiconductors. *Reviews of Modern Physics*, 74(3):895, 2002.

[178] Bo E. Sernelius. Intraband relaxation time in highly excited semiconductors. *Phys. Rev. B*, 43:7136–7144, Mar 1991.

[179] Neil W Ashcroft and N David Mermin. Solid state physics. *Rinehart and Winston, New York*, 19761, 1976.

[180] D. Hulin, M. Combescot, J. Bok, A. Migus, J. Y. Vinet, and A. Antonetti. Energy transfer during silicon irradiation by femtosecond laser pulse. *Phys. Rev. Lett.*, 52: 1998–2001, May 1984.

[181] H. M. van Driel. Optical effective mass of high density carriers in silicon. *Applied Physics Letters*, 44(6):617–619, 1984.

[182] JB Roy and PK Basu. Free carrier absorption in in0. 47ga0. 53as due to alloy disorder. *physica status solidi (b)*, 167(1):K69–K72, 1991.

[183] Philippe Nozières and David Pines. *The theory of quantum liquids*, volume 6. Perseus Books Cambridge, Massachusetts, 1999.

[184] Sergei Ivanovich Anisimov and BS Luk'yanchuk. Selected problems of laser ablation theory. *Physics-Uspekhi*, 45(3):293–324, 2002.

[185] John M Ziman. *Principles of the Theory of Solids*. Cambridge university press, 1972.

[186] Louis E Brus. Electron–electron and electron-hole interactions in small semiconductor crystallites: The size dependence of the lowest excited electronic state. *The Journal of chemical physics*, 80(9):4403–4409, 1984.

[187] Peter Y Yu, Manuel Cardona, and Lu J Sham. Fundamentals of semiconductors: physics and materials properties. *Physics Today*, 50:76, 1997.

[188] Ellen J Yoffa. Dynamics of dense laser-induced plasmas. *Physical Review B*, 21 (6):2415, 1980.

[189] PC Findlay, CR Pidgeon, R Kotitschke, A Hollingworth, BN Murdin, CJGM Langerak, AFG van Der Meer, CM Ciesla, J Oswald, A Homer, et al. Auger recombination dynamics of lead salts under picosecond free-electron-laser excitation. *Physical Review B*, 58(19):12908, 1998.

[190] Per Jonsson, Henry Bleichner, Mats Isberg, and Edvard Nordlander. The ambipolar auger coefficient: Measured temperature dependence in electron irradiated and highly injected n-type silicon. *Journal of applied physics*, 81(5):2256–2262, 1997.

[191] KG Svantesson, NG Nilsson, and L Huldt. Recombination in strongly excited silicon. *Solid State Communications*, 9(3):213–216, 1971.

[192] Alicia W Cohn, Alina M Schimpf, Carolyn E Gunthardt, and Daniel R Gamelin. Size-dependent trap-assisted auger recombination in semiconductor nanocrystals. *Nano letters*, 13(4):1810–1815, 2013.

[193] Patrick E Hopkins, Edward V Barnat, Jose L Cruz-Campa, Robert K Grubbs, Murat Okandan, and Gregory N Nielson. Excitation rate dependence of auger recombination in silicon. *Journal of Applied Physics*, 107(5):053713, 2010.

[194] OB Wright and VE Gusev. Acoustic generation in crystalline silicon with femtosecond optical pulses. *Applied physics letters*, 66(10):1190–1192, 1995.

[195] Henry M van Driel. Kinetics of high-density plasmas generated in si by 1.06 and 0.53μm picosecond laser pulses. *Physical Review B*, 35(15):8166, 1987.

[196] Chun-Mao Li, Theodore Sjodin, and Hai-Lung Dai. Photoexcited carrier diffusion near a si (111) surface: Non-negligible consequence of carrier-carrier scattering. *Physical Review B*, 56(23):15252, 1997.

[197] KG Svantesson and NG Nilsson. The temperature dependence of the auger recombination coefficient of undoped silicon. *Journal of Physics C: Solid State Physics*, 12(23):5111, 1979.

[198] W Gerlach, H Schlangenotto, and H Maeder. On the radiative recombination rate in silicon. *physica status solidi (a)*, 13(1):277–283, 1972.

[199] GG Zegrya and VA Kharchenko. New mechanism of auger recombination of nonequilibrium current carriers in semiconductor heterostructures. *Soviet physics, JETP*, 74(1):173–181, 1992.

[200] István Robel, Ryan Gresback, Uwe Kortshagen, Richard D Schaller, and Victor I Klimov. Universal size-dependent trend in auger recombination in direct-gap and indirect-gap semiconductor nanocrystals. *Physical review letters*, 102(17):177404, 2009.

[201] Ilya A. Shkrob and Robert A. Crowell. Ultrafast charge recombination in undoped amorphous hydrogenated silicon. *Phys. Rev. B*, 57:12207–12218, May 1998.

[202] M Capizzi, S Modesti, A Frova, JL Staehli, M Guzzi, and RA Logan. Electron-hole plasma in direct-gap ga 1-x al x as and k-selection rule. *Physical Review B*, 29(4): 2028, 1984.

[203] Monique Combescot and Roland Combescot. Conductivity relaxation time due to electron-hole collisions in optically excited semiconductors. *Phys. Rev. B*, 35: 7986–7992, May 1987.

[204] Emmanouil Lioudakis, Andreas Othonos, and A. G. Nassiopoulou. Probing carrier dynamics in implanted and annealed polycrystalline silicon thin films using white light. *Appl. Phys. Lett.*, 88(18):181107, 2006. ISSN 00036951.

[205] Emmanouil Lioudakis, Andreas Othonos, A. G. Nassiopoulou, Ch. B. Lioutas, and N. Frangis. Influence of grain size on ultrafast carrier dynamics in thin nanocrystalline silicon films. *Applied Physics Letters*, 90(19):191114, 2007.

[206] Vytautas Grivickas and Pierre Basmaji. Optical absorption in porous silicon of high porosity. *Thin Solid Films*, 235(1):234–238, 1993.

[207] I Sagnes, A Halimaoui, G Vincent, and PA Badoz. Optical absorption evidence of a quantum size effect in porous silicon. *Applied physics letters*, 62(10):1155–1157, 1993.

[208] J Von Behren, T Van Buuren, M Zacharias, EH Chimowitz, and PM Fauchet. Quantum confinement in nanoscale silicon: The correlation of size with bandgap and luminescence. *Solid state communications*, 105(5):317–322, 1998.

[209] Emmanouil Lioudakis, Andreas Othonos, GC Hadjisavvas, PC Kelires, and AG Nassiopoulou. Quantum confinement and interface structure of si nanocrystals of sizes 3–5nm embedded in a-sio2. *Physica E: Low-dimensional Systems and Nanostructures*, 38(1):128–134, 2007.

[210] C. Delerue, G. Allan, E. Martin, and M. Lannoo. *Porous Silicon Science and Technology*. Springer Verlag (Germany), Les Editions de Physique (France), 1995.

[211] GD Sanders and Yia-Chung Chang. Theory of optical properties of quantum wires in porous silicon. *Physical Review B*, 45(16):9202, 1992.

[212] J. J. Sakurai. *Modern Quantum Mechanics*. Addison-Wesley, 1993.

[213] V Freilikher, M Pustilnik, I Yurkevich, and AA Maradudin. Wave scattering from a thin film with volume disorder: reflection and transmission. *Optics communications*, 110(3):263–268, 1994.

[214] JM White and PF Heidrich. Optical waveguide refractive index profiles determined from measurement of mode indices: a simple analysis. *Applied Optics*, 15(1):151–155, 1976.

[215] H Bremmer. The wkb approximation as the first term of a geometric-optical series. *Communications on pure and applied mathematics*, 4(1):105–115, 1951.

[216] Katsunari Okamoto. *Fundamentals of optical waveguides*. Academic press, 2010.

[217] MJ Adams. An introduction to optical waveguides. *Mir, Moscow*, 1984.

[218] J. M. Ziman. *Principles of the theory of solids*. Cambridge University Press, 1972.

[219] M Ben-Chorin, F Möller, and F Koch. Band alignment and carrier injection at the porous-silicon–crystalline-silicon interface. *Journal of applied physics*, 77(9): 4482–4488, 1995.

[220] M Ben-Chorin, F Möller, and F Koch. Nonlinear electrical transport in porous silicon. *Physical Review B*, 49(4):2981, 1994.

[221] V Mizeikis, K Jarašiūnas, M Sūdžius, and L Subačius. Contactless characterization of porous silicon structures by four-wave mixing and microwave techniques. *Journal of Porous Materials*, 7(1-3):303–306, 2000.

[222] R Schwarz, F Wang, M Ben-Chorin, S Grebner, A Nikolov, and F Koch. Photocarrier grating technique in mesoporous silicon. *Thin Solid Films*, 255(1):23–26, 1995.

[223] R Tomasiunas, I Pelant, J Kočka, P Knápek, R Lévy, P Gilliot, JB Grun, and B Hönerlage. Carrier diffusion in porous silicon studied by transient laser-induced grating spectroscopy. *Journal of applied physics*, 79(5):2481–2486, 1996.

[224] Jan Linnros and Vytautas Grivickas. Carrier-diffusion measurements in silicon with a fourier-transient-grating method. *Physical Review B*, 50(23):16943, 1994.

[225] Hao Tang, Li-Guo Zhu, Liang Zhao, Xuejin Zhang, Jie Shan, and Shuit-Tong Lee. Carrier dynamics in si nanowires fabricated by metal-assisted chemical etching. *ACS nano*, 6(9):7814–7819, 2012.

[226] K.T. Tsen. *Ultrafast Physical Processes in Semiconductors*. Number v. 67 in Semiconductors and Semimetals. Academic Press, 2001. ISBN 9780127521763.